

UNIVERSITY OF OKLAHOMA
GRADUATE COLLEGE

FUNDAMENTAL HYDRAULIC FRACTURING CONCEPTS FOR POORLY
CONSOLIDATED FORMATIONS

A DISSERTATION

SUBMITTED TO THE GRADUATE FACULTY

in partial fulfillment of the requirements for the

Degree of

DOCTOR OF PHILOSOPHY

By

DAVID MARTINEZ
Norman, Oklahoma
2012

FUNDAMENTAL HYDRAULIC FRACTURING CONCEPTS FOR POORLY
CONSOLIDATED FORMATIONS

A DISSERTATION APPROVED FOR THE
MEWBOURNE SCHOOL OF PETROLEUM AND GEOLOGICAL ENGINEERING

BY

Dr. Jean-Claude Roegiers, Chair

Dr. Roger Slatt

Dr. Faruk Civan

Dr. Subhash Shah

Dr. Yucel Akkutlu

© Copyright by DAVID MARTINEZ 2012
All Rights Reserved.

To my wife, Julieta, whose love and support lightened the load during this journey

To my daughter, Laura, an incessant source of pride that inspires me to aim higher

To Mom and Grandma, for teaching me the value of hard work, patience, and persistence

To Jorge and Hernan, for their constant words of encouragement and advice

To my Family, for backing up my projects, even when they seem out of reach

ACKNOWLEDGEMENTS

I would like to express my heartfelt appreciation to my advisor, Dr. Jean-Claude Roegiers, for steering me into the fascinating field of Rock Mechanics, for his guidance to (hopefully) grasp its intricacies, for his invaluable insight on its practical applications in the field, and most of all, for his friendly and timely advice to advance further into my professional endeavors.

Special gratitude is extended to Itasca Consulting Group for generously providing the code PFC3D[®], and for the assistance and support during the stages of this work.

The help from the doctorate committee members to improve the clarity of this dissertation is sincerely appreciated.

TABLE OF CONTENTS

ABSTRACT	xiii
1 INTRODUCTION	1
1.1 OBJECTIVES	2
1.2 SCOPE OF WORK AND ASSUMPTIONS.....	3
1.3 PROCEDURE	4
2 ASPECTS OF POORLY CONSOLIDATED FORMATIONS	6
2.1 SEDIMENTATION AND LITHIFICATION	6
2.2 PETROPHYSICS.....	9
2.3 MECHANICAL PROPERTIES.....	11
2.3.1 Stress-Strain Curve	15
2.3.2 Elastic Parameters	22
2.3.3 Failure Characteristics	28
2.3.4 Other Properties	28
2.4 IMPLICATIONS FOR THE SIMULATION MODEL SETUP	29
3 CONVENTIONAL HYDRAULIC FRACTURING MODELING.....	31
3.1 MODEL COMPONENTS	31
3.2 FRACTURE MECHANICS FUNDAMENTALS.....	34
3.2.1 Linear Elastic Fracture Mechanics (LEFM)	35
3.2.2 Non-Linear Elastic Fracture Mechanics (NEFM).....	48

3.2.3	Statistical Fracture Mechanics	53
3.3	HYDRAULIC FRACTURE PROPAGATION MODELS	57
3.4	COMPARISON OF FRACTURE PROPAGATION MODELS	61
4	NUMERICAL SIMULATION SETUP	64
4.1	DEM OVERVIEW	65
4.2	DEM THEORETICAL BACKGROUND (Itasca Consulting Group, 2005c)...	66
4.3	DEM SPECIMEN DEFINITION	69
4.4	MECHANICAL TESTING AND CALIBRATION	72
4.5	FLUID COUPLING	74
4.6	FLUID PROPERTIES CALIBRATION	76
4.7	FLOW GRID DEFINITION	79
4.8	SIMULATION MONITORING	81
4.9	SIMULATION SETUP	82
4.9.1	Model Genesis	82
4.9.2	Mechanical Calibration	83
4.9.3	Boundary Layer	85
4.9.4	Flow Grid	87
4.9.5	Supporting Algorithms	88
5	DISCRETE ELEMENT HYDRAULIC FRACTURING SIMULATION RESULTS	90
5.1	METHODOLOGY	91

5.2	MECHANICAL PROPERTIES EFFECTS	95
5.2.1	Uniaxial Compressive Strength (UCS) (Runs 2A to 5A)	96
5.2.2	Young's Modulus, E (Runs 6A to 9A)	106
5.2.3	Poisson's Ratio Effects	116
5.2.4	Ductility Effects	125
5.2.5	Strength Heterogeneity Effects	137
5.3	STRESS BOUNDARY CONDITIONS EFFECTS	140
5.3.1	Anisotropy	140
5.3.2	Deviatoric Stress	150
5.4	MOHR DIAGRAM ANALYSIS	161
5.5	SOME PRACTICAL IMPLICATIONS	164
6	CONCLUSIONS AND RECOMMENDATIONS	166
7	REFERENCES	169
	APPENDIX A: ALTERNATIVE METHODS FOR FLUID FLOW COUPLING IN DISCRETE ELEMENT SPECIMENS	176
	APPENDIX B: SETUP AND MONITORING ALGORITHMS	186

LIST OF TABLES

Table 2-1. Representative properties of a poorly consolidated synthetic rock.....	15
Table 2-2. Results of triaxial testing data of various unconsolidated sandstones.....	23
Table 4-2. List of variables within the driver	80
Table 4-3. Fluid flow input information	81
Table 4-4. Parameter tracking list.....	81
Table 4-5 . Input information for the base-case specimen.....	83
Table 4-6. Micro-properties derived from virtual mechanical testing.....	84
Table 4-7. Fluid set-up information.....	87
Table 4-8 Brief description of scripts used to set-up and execute the simulations.....	88
Table 5-1 Mechanical properties of the specimens constructed for the simulations	96
Table 5-2. Parameters of the specimens used to investigate the Poisson's ratio effect..	116
Table 5-3 Properties of specimens used to determine ductility effects	125
Table 5-4 Strength heterogeneity runs	137
Table 5-5 Stress values used to evaluate stress anisotropy effect.....	140
Table 5-6 Stress values used to evaluate deviatoric stress effect.....	150

LIST OF FIGURES

Figure 2-1. Basic types of grain contacts.....	9
Figure 2-2. Deere and Miller's rock strength classification	12
Figure 2-3. Stress-strain schematic of an uniaxial compression test	14
Figure 2-4. Isostatic compression of GOM unconsolidated samples	17
Figure 2-5. Pore volume compressibility of GOM unconsolidated samples	18
Figure 2-6. Compressibility of GOM unconsolidated reservoir samples	18
Figure 2-7. SEM picture of slot shaped pore network in a well consolidated rock.....	20
Figure 2-8. Uniaxial compressive testing of unconsolidated material.....	21
Figure 2-9. Triaxial compressive testing of unconsolidated material of the Adriatic Sea	22
Figure 2-10. Triaxial compressive testing of weak North Sea samples	24
Figure 2-11. Dependence of elastic modulus on effective mean stress for different stress paths in unconsolidated sands.....	24
Figure 2-12. Dependence of Poisson's ratio on applied shear stress.....	26
Figure 2-13. Dependence of Poisson's ratio on shear stress and confining pressure	26
Figure 2-14. Effect of stress dependent Young's modulus on fracture properties	27
Figure 3-1. Schematic representation of a hydraulic fracture.....	33
Figure 3-2. Components of a conventional hydraulic fracture model	33
Figure 3-3. Fracture extension modes.....	35
Figure 3-4. Finite element grid of a propagating fracture.....	41
Figure 3-5. Energy balance used for fracture increment calculation.....	48
Figure 3-6. FPZ for the maximum normal stress criterion	51

Figure 3-7. FPZ cohesive crack model	52
Figure 3-8. Abou-Sayed's model	60
Figure 3-9. Rummel and Winter model	61
Figure 4-1. PFC3D® calculation process	68
Figure 4-2. Unconfined testing of the virtual (left side) and real (right side) samples	73
Figure 4-3. Fluid flow implementation in PFC3D.....	75
Figure 4-4. Deere and Miller's classification of base-case rock specimen.....	84
Figure 4-6. Group of particles acting as boundary layer.	86
Figure 4-7. Fluid grid depiction.....	88
Figure 5-1 Cracks representation	94
Figure 5-2 Representation of compressive forces chains	95
Figure 5-3 Curves of injection pressure vs. flowrate for various UCS runs.....	99
Figure 5-4 Shear to total cracks vs. injection flowrate for various UCS runs	100
Figure 5-5 Curves of injection pressure vs. volumetric strain for various UCS runs.....	101
Figure 5-7 Compressive forces for Runs1A and 2A.....	104
Figure 5-8 Displacements for Runs1A and 2A.....	105
Figure 5-9 Curves of injection pressure vs. flowrate for various Young's modulus runs	110
Figure 5-10 Shear to total cracks vs. injection flowrate for various E runs.....	111
Figure 5-11 Curves of injection pressure vs. volumetric strain for various E runs	112
Figure 5-12 Crack agglomeration for Runs 8A and 7A	113
Figure 5-14 Displacements for Runs 8A and 7A.....	115
Figure 5-15 Curves of injection pressure vs. flowrate for various Poisson's ratio runs.	118

Figure 5-16 Shear to total cracks vs. injection flowrate for various PR runs	119
Figure 5-17 Curves of injection pressure vs. volumetric strain for various PR runs.....	120
Figure 5-18 Crack agglomeration for Runs 1A-PR1 and 1A-PR4	122
Figure 5-19 Compressive forces for Runs 1A-PR1 and 1A-PR4	123
Figure 5-20 Shear forces for Runs 1A-PR1 and 1A-PR4	124
Figure 5-21 Stress-strain curves of specimens used to determine ductility effects	127
Figure 5-22 Curves of injection pressure vs. flowrate for various ductility runs	128
Figure 5-23 Curves of cracks formed vs. injection flowrate for various ductility runs..	131
Figure 5-24 Curves of injection pressure vs. volumetric strain for various ductility runs	132
Figure 5-25 Crack agglomeration for Runs 1A-PR4 and Duc3	134
Figure 5-26 Compressive forces for Runs 1A-PR4 and Duc3.....	135
Figure 5-27 Shear forces for Runs 1A-PR4 and Duc3	136
Figure 5-28 Curves of injection pressure vs. volumetric strain for various heterogeneity levels	138
Figure 5-29 Crack agglomeration for Run SD44 and base-case PR4.....	139
Figure 5-30 Curves of injection pressure vs. flowrate for various stress anisotropy runs	143
Figure 5-31 Curves of shear to total cracks vs. injection flowrate for various stress anisotropy runs.....	144
Figure 5-32 Curves of injection pressure vs. volumetric strain for various stress anisotropy runs.....	145
Figure 5-34 Back view of crack agglomeration for Runs 1A and 1E.....	147

Figure 5-35 Top view of compressive forces for Runs 1A and 1E	148
Figure 5-36 Top view of displacements for Runs 1A and 1E.....	149
Figure 5-37 Curves of injection pressure vs. flowrate for various deviatoric stresses ...	152
Figure 5-38 Curves of shear to total cracks vs. flowrate for various deviatoric stresses	153
Figure 5-39 Curves of injection pressure vs. volumetric strain for various deviatoric stresses	154
Figure 5-40 Crack agglomeration for Runs 1A and 1A2.....	157
Figure 5-41 Crack agglomeration for Runs 1A and 1A6.....	158
Figure 5-42 Compressive forces for Runs 1A and 1A2.....	159
Figure 5-43 Displacements for Runs 1A and 1A6.....	160
Figure 5-44 Representation of stress, failure criteria, and pressure injection effect on the Mohr diagram.....	161
Figure 5-45 Mohr diagram representation of the effect of decreasing UCS on shear cracking.....	162
Figure 5-46 Mohr diagram representation of the effect of Young's modulus and Poisson's ratio on shear cracking.....	163
Figure 5-47 Mohr diagram representation of the effect of stress anisotropy on shear cracking.....	164

ABSTRACT

This dissertation examines –by means of the discrete element method- the mechanisms that govern hydraulic fracturing in poorly consolidated formations. The motivation to take on this project was the widely reported discrepancies between values predicted by conventional hydraulic fracturing simulators and the values encountered in the field, in formations of this type. The proposed numerical framework integrates dissimilar methodologies for the simulation of the solid and fluid components. The solid material – the rock- was represented as a collection of discrete particles that interact with each other by linear, spring-like contacts; this method is known as the Discrete Element Method (DEM). Meanwhile, the fluid was modeled by finite-difference discretization of the equations of conservation, applied to fluid flow in porous media (i.e. Navier-Stokes equations in porous media). A coupling mechanism conveys information about the interactions between the fluid and solid components.

The results of this study suggest that conventional simulation models ignore mechanisms that control hydraulic fracture propagation in poorly consolidated formations. Principally, the assumption of linear elastic behavior and the normal displacement of the newly cracked surfaces are not always the dominant features observed in DEM simulations. Instead, minor adjustments of dislodged particles yield zones of high concentration of stresses and posterior extension of the fracture. Plots of injection vs. volumetric strain exhibit a multi-linear and sometimes non-linear shape. Moreover, particle readjustments occur in tangential directions (i.e. shear cracking) on a very regular basis. The importance

of shear cracking is commonly neglected in the better-known hydraulic fracturing models.

1 INTRODUCTION

Conventional hydraulic fracturing models are derived from the tenets of continuum fracture mechanics. By modeling the porous media as a continuum, the simulated behavior is uniform across all scales of the rock model. In other words, the selected constitutive deformation/fracturing mechanics determine the behavior of even the smallest unit of the body. Popular models rely on a constitutive linear elastic deformation equation, and a tensile failure criterion (Whittaker et al., 1992). Therefore, conventional hydraulic fracturing models neglect onset of macroscopic effects born from small scale mechanisms (due to the continuum assumption), the effect of shear cracking (due to the tensional fracturing-only criterion), and the possible non-linearities associated to shear. This approach works satisfactorily in well consolidated formations that exhibit high strength and high elastic modulus.

Micro-seismic evidence, however, suggests that shear and tensile cracking events become relevant in fracture propagation in weaker rock (Urbancic & Maxwell, 2002). It has been suggested that shear cracking in poorly consolidated formations may be rather significant (Chudnovsky et al., 1996).

This dissertation consisted of a numerical study aimed to determine the small scale mechanisms, including shear cracking, and the onset of non-linear behavior of hydraulic fractures in poorly consolidated rock. Numerical modeling was achieved by the Distinct Element Method (DEM). This method models the mechanical macroscopic response of materials as a direct result of the interaction of its constitutive elements. In other words,

DEM treats the material as a discontinuum, where the dimensions of its distinct particles are prescribed to match the size of the minimum scale necessary to accurately capture the macroscopic behavior observed. As a result, DEM is well suited to model situations where the response of the material is driven by micro- to meso- scale characteristics of the specimen under study, or when the interest is in phenomena occurring at those scales. For the above reasons, DEM was selected as the preferred method for the simulation of the interaction among the solid components of the rock.

The following sections of this introductory chapter contain the objectives, scope of work, and a description of the procedures followed to achieve the tasks laid out.

1.1 OBJECTIVES

The main goal of this work is to identify –via numerical modeling- the small scale mechanisms that govern hydraulic fracture tip propagation in poorly consolidated formations. The evaluated mechanisms refer to the type of displacements that bonded particles undergo after the concentration of stress at their contacts is sufficient to break them apart in either normal fashion (Mode I or tensile breakage), or by tangential sliding (Mode II or shear breakage). Hence, this study attempts to establish the regions where tensile and shear cracks (or their combination) are localized along the periphery of the main growing crack; and their importance on the overall macroscopic fracturing character of poorly consolidated rocks. Likewise, the pressure requirements to cause fracture propagation are assessed in relation to the ratio of shear-to-tensile features. Special attention is given to the interface between the tip of the crack and the region just ahead of

it, since it is believed that oversight of the phenomena occurring therein is what leads to reported discrepancies with respect to the fracture propagation pressure inferred from conventional simulation models and field-scale operations (Chudnovsky et al., 1996). These discrepancies are assessed in view of the results obtained by the numerical framework presented herein.

1.2 SCOPE OF WORK AND ASSUMPTIONS

The DEM technique was used in this dissertation to represent the solid skeleton of the rock. A pressure disturbance was forced upon the virtual sample until bonds between its elementary particles broke successively, as to represent a propagating fracture. The sample properties corresponded to a homogeneous, isotropic, porous interval, whose mechanical characteristics were those of 'weak' or 'soft' sandstone (see Chapter 2 for further details about strength/deformation characteristics of poorly consolidated formations). Fracture propagation was simulated until it reached any of the boundaries of the model. Nonetheless, analyses were based on partial saves in which the fracture was still away from the specimen limits, to avoid any boundary effects. The formation interval had the shape of a parallelepiped, upon which three mutually perpendicular stress components acted on its faces; the orthogonal stresses were named S_1 through S_3 , and by convention are assumed $S_1 = S_2 > S_3$. Each stress is uniform on the face on which it acts, and remained constant during fluid injection (i.e. constant stress boundary condition).

The solid rock was modeled as an assemblage of particles, joined by bonds that obey a linear force-displacement law. This technique is known as Discrete Element Method,

DEM. Models were built and simulations executed within the PFC3D[®] software environment, a DEM implementation generously provided by Itasca Consulting Group for this dissertation. The elemental particles used were spheres¹, and the bonds were modeled as linear springs (or contact) type; this seems as a good approximation to the fabric of typical low-strength rocks (see Mechanical Properties in Chapter 2). PFC3D[®] provides a built-in programming language denominated “Fish”. All essential tasks and custom procedures to execute and control the hydraulic fracture propagation simulations were written in “Fish”; the associated code is provided at the end of chapter 4.

Fluid flow is also provided as an optional feature in PFC3D[®], which incorporate a finite difference solver of the Navier-Stokes equations for a DEM ensemble. As above, setting of the fluid grid and configuration of the conditions of execution of the fluid-related parameters were implemented in “Fish” scripts. The corresponding files are attached at the end of Chapter 4.

1.3 PROCEDURE

The order of the chapters reflects the sequential steps followed throughout the realization of this study. The chapters are divided as follows:

- Chapter 1, “Introduction” describes the objectives and scope of work.
- Chapter 2, “Aspects of Poorly Consolidated Formations”, defines the classification of

¹ Overlapping of spheres is permitted and generates a proportional amount of stress that may be different for different directions. However, the sphere maintains its original shape at all times.

rocks according to its strength, and compiles mechanical behavior of this type of rock masses. This chapter is of relevance towards the development of the DEM model because a comprehensive set of input data is required for the genesis and calibration of the virtual specimen. This type of information is not easily attainable for a specific case; hence, one can only make indirect inferences from the small scale relations among sediments, and their impact on macro-mechanical properties. Thus, the review of the physical properties of unconsolidated porous media serves a dual purpose: (1) it provides an estimate of those properties required to set up the DEM model; and, (2) it verifies the behavior of the virtual DEM sample vis-à-vis the case histories reported in the literature.

- Chapter 3, “Conventional Hydraulic Fracturing Modeling”, presents the most commonly used modeling theories to simulate deformation and subsequent fracture propagation of the hydraulically stimulated formation.
- Chapter 4, “Numerical Simulation Setup”, describes the details about the numerical models used for this study, and the setup of the “base-case”. The geometry of the virtual specimen and the set-up of small-scale properties (based partially on the discussion in Chapter 2) are also included.
- Chapter 5, “Simulation Results”, documents the findings of the cases analyzed with the virtual specimen presented in Chapter 4.
- Conclusions and Recommendations are presented in Chapter 6.
- References are listed in Chapter 7.

2 ASPECTS OF POORLY CONSOLIDATED FORMATIONS

Because most of the small-scale properties of the components of the discrete element model (DEM) rock are not measurable with standard testing techniques, they need to be related to the real fabric of the rock. The sections in this chapter visit the aspects related to depositional environments that favor generation of poorly consolidated sedimentary formations, and their particular petrophysical and mechanical characteristics. This discussion is aimed to constrain the input properties for the discrete element model (DEM) described in detail in the next chapter.

2.1 SEDIMENTATION AND LITHIFICATION

Poorly consolidated sedimentaryⁱⁱ formations are usually associated to highly energetic depositional environments, in which large amounts of sediments may be transported, deposited, and buried, in a relatively short time span. Discharge from major rivers in the marine margin, and sediment gravity flows in deep water, are very efficient forms of sediment transport; both systems have the potential to move large masses of sediments for long distances (Boggs, 2006). Accordingly, many poorly consolidated reservoirs are traced back to either deltaic (Ostermeier et al., 2001) or turbiditic (e.g. Marlowe, 1968; Ostermeier, 1995) depositional settings.

Drainage systems (delta deposits) and turbidity currents (deep sea turbidites) can

ⁱⁱ For the purpose of this dissertation, only rocks of sedimentary origin are considered.

transport considerable amounts of material; such deposits may then be rapidly buried. Simultaneously, very fine sediments are easily transported by currents (both eolian and fluvial); hence, they are abundantly found in suspension in marine waters. These particles can settle from suspension in the marine margin, or flocculate and settle as somewhat larger clumps in deep water, creating a blanket on top of the sandstone deposits, which may generate impermeable layers after further burial (e.g. shales). Rapid burial, along with the presence of overlain fine sediments (i.e. low permeability layers), may effectively trap the fluid and particles into a ‘sealed’ deposit. As a result, fluid ejection is constrained during subsequent burial and compaction.

In a deposit of grains+fluid, the overlying load (i.e. overburden), is supported by both the fluid and the solid structure. This relation is expressed as:

$$S_v = \sigma_v + P_p$$

where the same set of “pressure” units may be used for all parameters (e.g. psi, Pa, etc), and:

S_v = overburden;

σ_v = effective stress; and,

P_p = pore pressure.

In the above relation, the effective stress (σ_v) can be interpreted as the fraction of the overburden transferred (or supported) by the solid structure, whereas P_p is the fraction

transferred to the fluid. Because in a ‘sealed’ deposit the fluid cannot escape upon burial, the overburden is mainly supported by the trapped fluid, and the effective load transferred to the particles is less than it would be in a normally compacted deposit. In other words, when compared to a normally compacted basin, the effective stress exerted in the sediments is reduced and the hydrocarbons are overpressured (Zoback, 2007). The lithification process slows down, due to the reduction of pressure at the contact points, which ultimately leads to formations that are capable to contain hydrocarbons, but that may be put in production when the cementation/lithification process is still incomplete. Because cementation is hindered, and the original sediments are not submitted to sufficiently high stresses to deform or fracture them during burial compaction, underconsolidated formations typically exhibit tangential contacts between the grainsⁱⁱⁱ. Davies and Davies (1999) documented the relation between tangential contacts and the permeability stress-dependency of the Gulf of Mexico (GOM) and Southern California poorly-consolidated reservoirs.

The described scenario is not the only one under which poorly consolidated rocks may form; i.e., neither all poorly consolidated reservoirs are associated to turbidite or delta deposition, nor all turbidite and/or delta systems turn out under-consolidated reservoirs. For example, in sediments buried at shallow depths, the overlying load is not sufficient to promote adequate lithification between grains. These type of deposits may present

ⁱⁱⁱ The contacts between rocks grains are generally classified as tangential, long, convex, and sutured. They are associated to increasing effective stress (higher geostatic column) during burial; these contacts are illustrated in **Figure 2-1**.

overpressures due to hydrocarbon content (migration from a nearby basin or source rock), rather than to undercompaction..

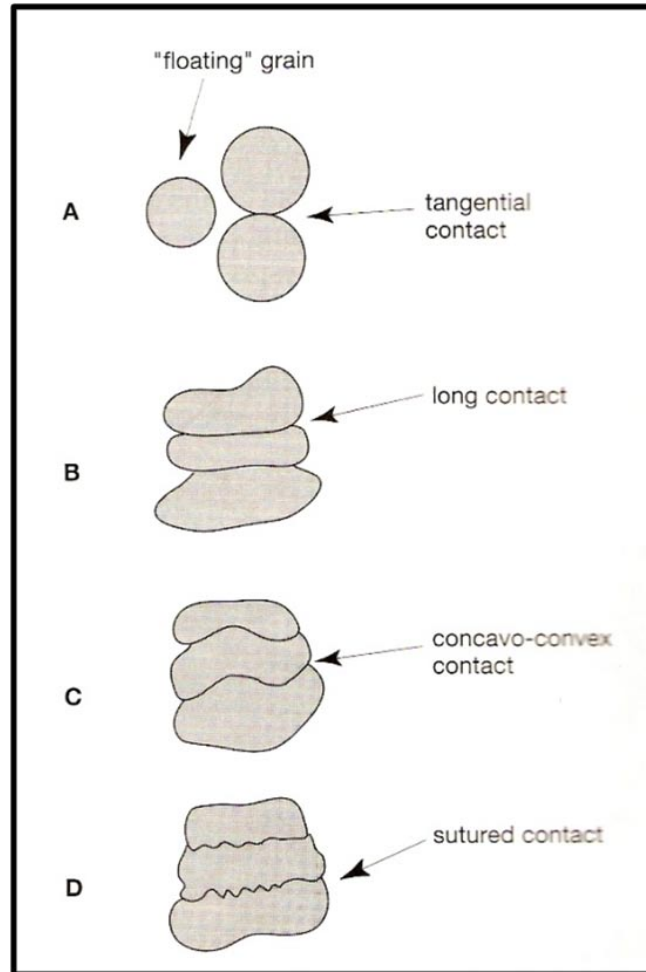


Figure 2-1. Basic types of grain contacts (Boggs, 2006)

2.2 PETROPHYSICS

Variability is usually observed in the properties of poorly consolidated rocks, even in reservoirs located at relatively short distances from each other. This is caused by the complex nature of these rocks' genesis, in addition to the countless parameters that are normally involved during transport, deposition and lithification of sediments. Moreover, the depositional environments described before (delta and turbidites) are responsible for

the generation of a variety of structures (sub-environments), all with distinct characteristics, depending on prevailing conditions. For instance, a deltaic environment is heavily affected by tides, waves, and strength of the main river currents, which results in the generation of different types of structures. Within the same structure, such as the distributary mouth bar of a river dominated delta, the sands deposited along the proximal margin would tend to be of better quality than those located toward distal margins (Slatt, 2006) because the coarser sediments are deposited at the proximal margin. Likewise, deep-water deposition (i.e. turbidites) may occur in a variety of dissimilar architectural elements such as sheets, channels, and levees (Slatt, 2006). This causes that sections within a single structure may exhibit very different characteristics.

Notwithstanding the effects of the conditions discussed above, it is common for poorly consolidated reservoirs to exhibit very good quality. Multiple published studies from disparate geographical locations report porosities in the range of 30%, and permeabilities in the range of fractions of Darcies to a few Darcies [e.g. Ostermeier (1995); Ostermeier (2001); Desroches and Woods (1998); Marzano (1988), etc.]

Ostermeier (1995) studied the high sensitivity to stress changes of poorly consolidated reservoirs in the Gulf of Mexico. Marzano (1988) corroborated this characteristic in the Gulf of Mexico unconsolidated sands, and also noted that these sands usually have low cement content, with an average of 4%, and are moderately to well-sorted. Even with the marked porosity and permeability decrease with the application of higher stresses, which

is of major importance for long term production aspects^{iv}, the final overall quality of the tested samples remained good. The distinct behavior observed for each sample sheds some light as to the mechanisms responsible for deformation of weak formations (deformation is a key player in the modeling of fracturing processes) and will be revisited later, in the section of mechanical properties.

Thus, the information from multiple sources evidences that unconsolidated reservoirs exhibit, in average, excellent quality, with porosity in the 30's and permeability in the Darcy order of magnitude, associated with sand size particles arranged in a moderate-sorted structure. These properties are a direct result of the processes responsible for the formation of the rock, whereby quick burial of the sediments prevented (or delayed) comprehensive compaction and lithification of the sediments. Thus, as compared to a normally consolidated rock, the fabric of the unconsolidated one preserves to some extent the original relations amongst the sediments, since mechanical compaction and cement generation still occur, but to a lesser degree. In addition, the structure of unconsolidated formations makes them really susceptible to ambient stresses changes caused by reservoir depletion. Naturally, these structures are responsible for the mechanical response of the rock to foreign loads, such as in fracturing operations.

2.3 MECHANICAL PROPERTIES

Deere and Miller (1966) reported the results of a comprehensive set of unconfined stress-

^{iv} Long term effects of stress changes in production are beyond the scope of this dissertation.

strain measurements (i.e. unconfined compressive tests) for an extensive range of rock types from various sources (Deere and Miller, 1966). They reported and classified the samples' strength according to two fundamental parameters of the curve obtained from the tests, namely the Uniaxial Compressive Strength (UCS) and the Young's Modulus (or elasticity modulus) at 50% of the peak stress (E). Deere and Miller's classification is depicted in Figure 2-2 (Roegiers, 2005a), including the ranges for different rock types. This classification is used throughout this dissertation to avoid ambiguity with other rock strength scales.

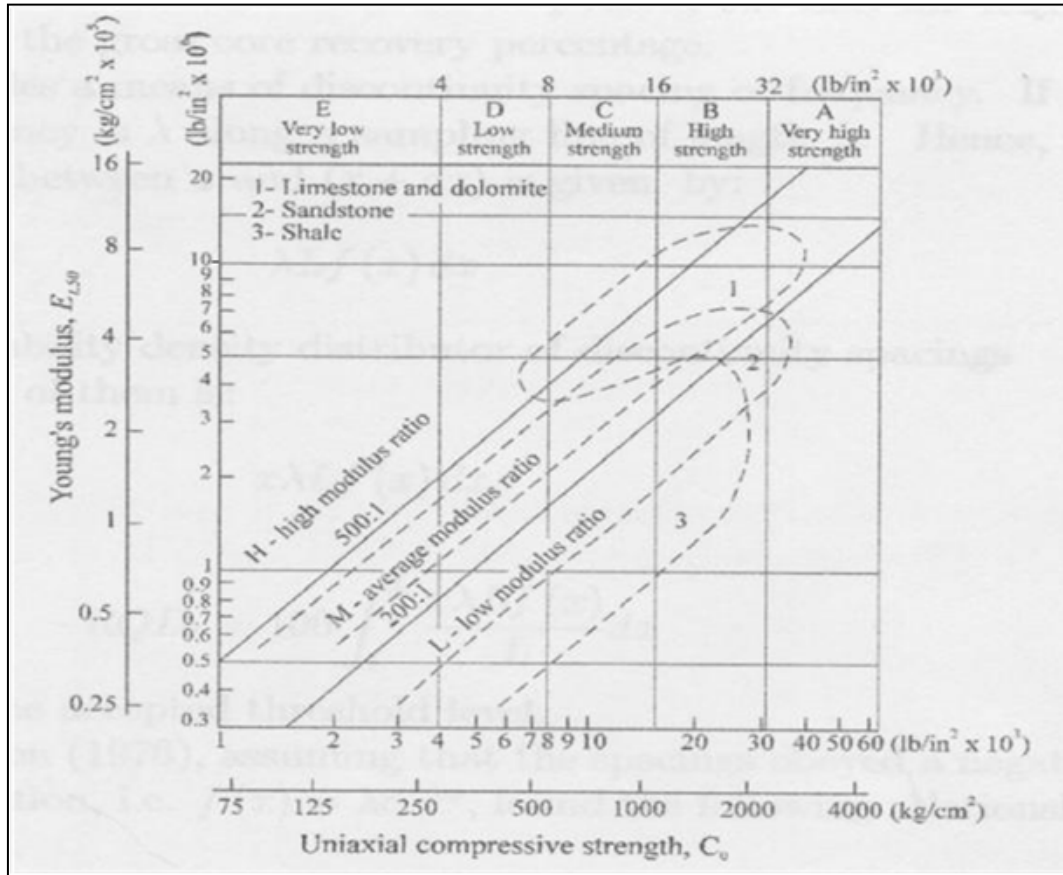


Figure 2-2. Deere and Miller's rock strength classification (Deere and Miller, 1966)

UCS and E are insufficient to capture completely the behavior of rock upon application of force fields, though. Observe the stress-strain curve represented in Figure 2-3, which

corresponds to the uniaxial compressive test of a consolidated rock. First, the deformation curve is rarely perfectly linear, and although sometimes the section that corresponds to the in-situ stresses may be approximated to a straight line, it may not occur at 50% of the peak stress (i.e. E_{50} may not represent in-situ conditions). Second, the unconfined tests provide a convenient way to qualify the general character of the rock, but in its natural environment, the sample is submitted to confining in-situ stresses. Thus, the parameters estimated from uniaxial stress tests are susceptible to changes in confinement conditions. Third, different combinations of applied vs. confinement stresses must be measured to devise some type of failure limit of the rock under various conditions (known as 'envelope' of failure) because the UCS and the ductile region are highly dependent on confinement changes. Finally, it is accepted that the most important failure mechanism during hydraulic fracturing is tension, and thus, in addition to compressive tests, tensional stress testing information must be collected.

One of the most common models to describe rock behavior assumes that deformation obeys a linear elastic relation, and that failure in shear (or compression in the macro-scale) is due to the contrast of the maximum and minimum stresses, without any intervention of the intermediate one (e.g. Mohr-Coulomb failure criterion). This approach is known as linear elastic - perfectly plastic rock model. This model is very popular because it fits reasonably well the behavior of well consolidated, strong rock, and also due to its simplicity, since it is based only on 4 parameters: 2 parameters for deformation (commonly Young's Modulus and Poisson's ratio), and 2 for shear failure (commonly UCS and internal friction angle) (Fjær et al., 1992). For tensile failure, it is typically assumed that it occurs when the minimum stress reaches the tensile strength of the rock,

because rocks are extremely weak in tension. These models, along with some others, are explained in detail in the next chapter entitled “Conventional Hydraulic Fracturing Modeling”.

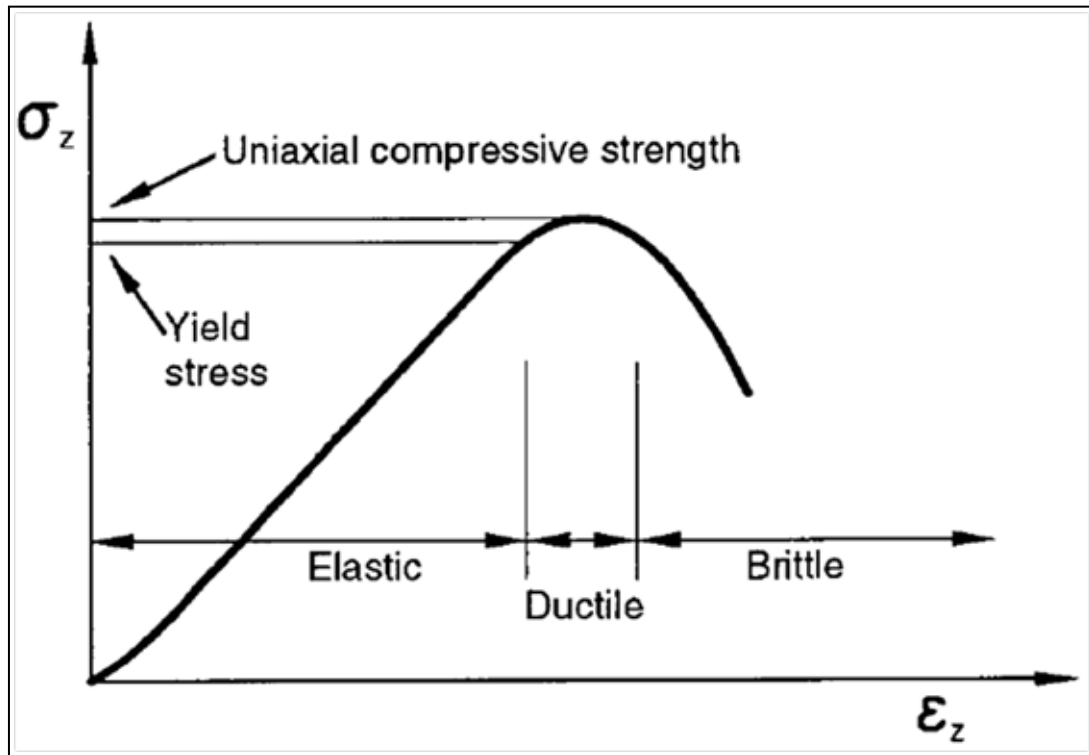


Figure 2-3. Stress-strain schematic of an uniaxial compression test (Fjaer et al. 1992)

It is important to remark that the physical characteristics of soft rock are highly variable (van den Hoek, 2000) and thus, the ranges reported correspond to most probable or average values, rather than to unique characteristics. Also, note that the degree of consolidation of the rock may be so low in some cases that its unconfined characteristics may fall below the range in Deere and Millers' classification (van den Hoek, 2000); as an example, Table 2-1 reports the properties of a synthetic rock built to represent typical - weakly consolidated, highly permeable- sand.

Table 2-1. Representative properties of a poorly consolidated synthetic rock (van den Hoek, 2000)

Unconfined compressive strength (MPa)	1.1 ± 0.3
Porosity (%)	34 to 37
Max. density variation (from CT scans)	38%
Young's modulus E (GPa)	0.4
Poisson's ratio, ν	~0.05
Friction angle, θ	37.5°
Cohesion C (MPa)	0.46
$2C \cos(\theta) / [1 - \sin(\theta)]$ (MPa)	1.9
Cohesion at yield	0.23
$\gamma^{p, peak}$	0.15
Air-mercury plateau capillary pressure (kPa)	14
Oil/water plateau capillary pressure (kPa)	1.4
Capillary cohesion = $1.4 \tan(\theta)$ (kPa)	1.1
$D_{10} / D_{50} / D_{90}$ (μm)	250/210/80
Permeability at 500 psi (3.45 MPa) conf. stress (D)	2 to 4
Connate water/residual oil (OMS) saturation	0.45/0.3
Water/oil (OMS) endpoint relative permeability	0.25/0.4

2.3.1 Stress-Strain Curve

Models for consolidated rock assume the deformation behavior to be dominantly elastic. Conversely, in softer rocks, the elastic region is shorter than usually assumed for more consolidated rocks (Ayoub et al., 1992).

The effects of isostatic loading on pore compressibility of unconsolidated rocks from the Gulf of Mexico are depicted in Figure 2-4 (Ostermeier, 1995); although such studies were aimed to evaluate porosity and permeability reduction with increasing stress, they directly reveal the volumetric stress-strain behavior of unconsolidated rocks. In this figure, Prospects A through D correspond to unconsolidated rock samples of different age and burial depth, with 'D' being representative of the oldest, deepest prospect. All tests underwent initial loading to in-situ stress, and were performed in drained samples. The

volumetric strain response to the applied isostatic stress is evidently non-linear. A plot of pore volume compressibility gives insight into the deformation nature of the rock, as illustrated in Figure 2-5; this plot is analogous to the slope of volumetric strain vs. applied isostatic stress, because the volumetric contraction comes mainly from porosity reduction. It is seen that compressibility is not constant, as would be predicted by assuming linear deformation. Indeed, the least consolidated prospect (prospect 'A') exhibits a highly variable compressibility: at the beginning it is constant, but after further loading it reaches a peak value, with a subsequent strain hardening profile^v. Strain hardening occurs when the internal structure has been compressed until a stable configuration is reached, and further compression will be harder to achieve than before. Conversely, at this scale the most consolidated sample (prospect D) does exhibit a constant compressibility throughout. It is observed that the different behavior between prospects A and D may be traced to the relative higher content of weaker load-supporting material (e.g. clay). Prospect 'A' has a higher content of weaker material and it is assumed that the initial part of the compressibility curve corresponds to loading and yielding of this material up to the point where it is "pushed" into the empty interstices of the harder grains; beyond this point the load is supported by the harder components of the rock, and strain hardening occurs. On the other hand, prospect 'D' is past the soft material yielding point, due to deeper burial (higher overburden) and more advanced age; in other words, prospect 'D' is at an advanced stage of mechanical compaction of the

^v A natural consequence of strain hardening is that a constant injection rate cannot be maintained with a constant pressure, because as the rock deforms it behaves as if it were stronger. Thus, fracture designs based on a single stress-strain will underestimate injection pressure.

grains, and then, they appear in close proximity to each other. It can be concluded then, that for poorly consolidated rocks the relation between volumetric strain and isostatic stress (i.e. compressibility, or the more common parameter -the bulk modulus- which is the reciprocal of compressibility) is very sensitive to stress changes, as compared to consolidated ones.

Compaction studies under uniaxial strain condition (i.e. the lateral strain is maintained constant) reveal similar tendencies as those under isostatic loading, introduced above (Dudley, 1998). Figure 2-6 depicts the compaction coefficient of different unconsolidated Gulf of Mexico samples as a function of applied axial stress. Observe that the plot, for the most part, does not conform to a linear relation.

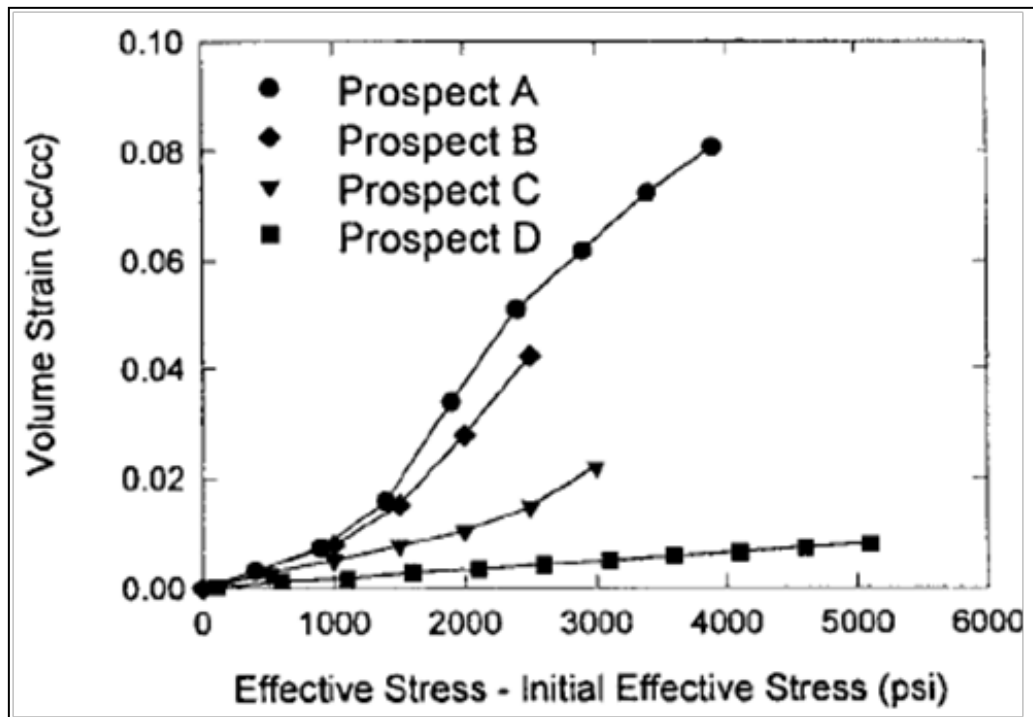


Figure 2-4. Isostatic compression of GOM unconsolidated samples (Ostermier, 1995)

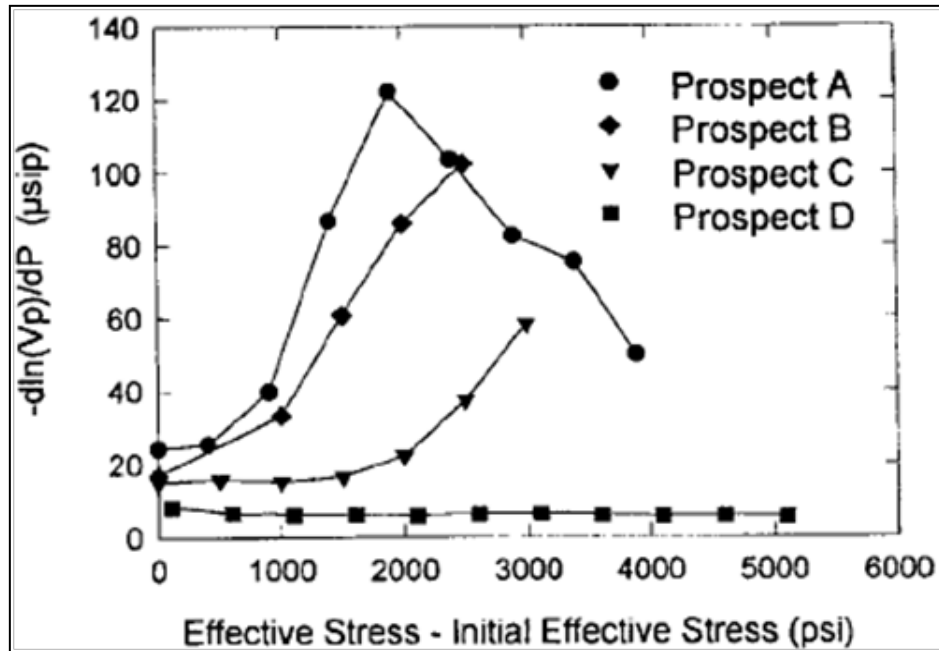


Figure 2-5. Pore volume compressibility^{vi} of GOM unconsolidated samples (Ostermier, 1995)

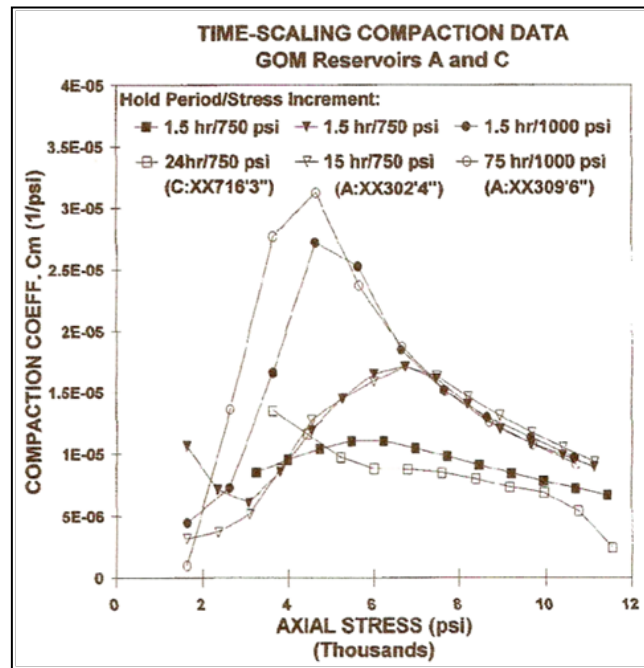


Figure 2-6. Compressibility of GOM unconsolidated reservoir samples (Dudley, 1998)

^{vi} Because the stress path during the test corresponds to isostatic compression, the volumetric strain results from pore compression. Therefore, the pore volume compressibility chart (Figure 2-5) is nothing more than a plot of the slope of the volumetric strain depicted in (Figure 2-4).

Apart from the reasons presented so far, studies have demonstrated that permeability susceptibility to stress changes is also due to the manner in which grains are packed in unconsolidated formations (Davies and Davies, 1999). Statistical modes derived from a grain distribution curve show that the more sensitive rocks correspond to well-sorted samples with little occurrence of fines, whereas grain size seems to have little to no effect. Soft rocks with the opposite characteristics -i.e. poor sorting and high percentage of fines- can resist loads better because there are more grain to grain contacts (incidentally, these type of rocks also exhibit lower quality characteristics). Meanwhile, consolidated rocks display the opposite behavior: the lower quality samples (less porous and permeable) are more sensitive to stress changes. Thin sections, Scanning Electron Microscope (SEM) and capillary measurements indicate that the pore throat shape is responsible for this behavior (Davies and Davies, 1999); the shape of the lower quality samples can be approximated to slots, whereas the higher quality samples feature a more pipe-like appearance. A slot-shaped pore is easier to collapse than a pipe-shaped one. Figure 2-7 display SEM images of slot pores of a well consolidated rock sample used in the mentioned study. The slot-pore configuration is due to compaction and diagenetic changes during the generation of the rock. Thus, the dominant pore shape in unconsolidated formations is that one of a pipe, because of lesser diagenesis effects.

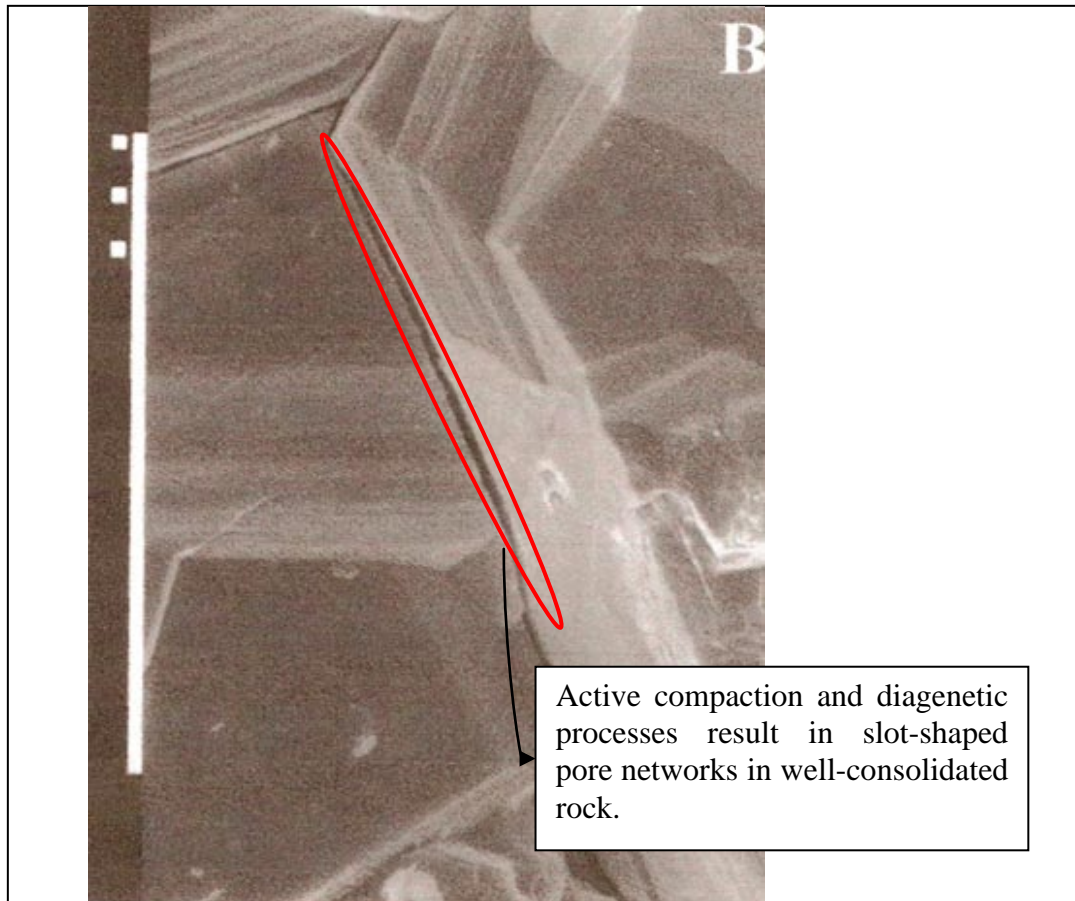


Figure 2-7. SEM picture of slot shaped pore network in a well consolidated rock (Bar = 10 microns) (Davies and Davies, 1999).

Uniaxial compressive stress testing is complicated to perform in poorly consolidated material, due to the effects of recovery, handling, and preparation of samples. Due to its low strength, the specimens structure may be affected by any changes in their ambient stress, especially one as dramatic as retrieval from deep underground location to surface; hence, the measured properties may not be representative of in-situ conditions (besides, unconfined testing is not a realistic representation of the underground environment and associated behavior). Results of this type of tests are depicted in Figure 2-8, for 2 samples exhibiting quite different behavior (Wu and Tan, 2000). Sandstone 4 appears as the more consolidated rock with properties of 1.5×10^6 psi elastic modulus, and 3190 psi UCS, whereas sandstone 5 exhibits an elastic modulus of 5.8×10^5 psi, and UCS of 1305 psi,

approximately. More importantly, observe that sandstone 5 features a more ductile behavior, as compared to sandstone 4.

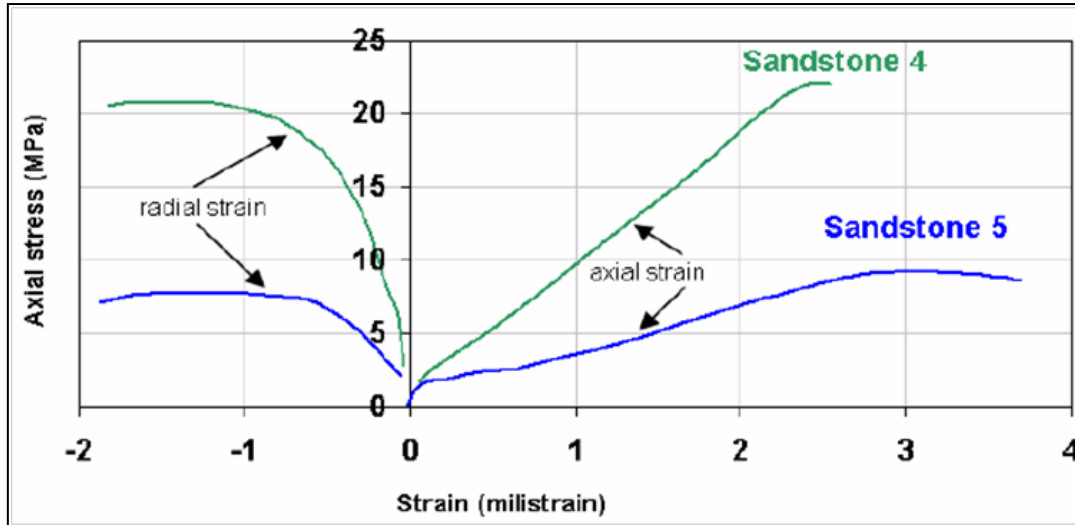


Figure 2-8. Uniaxial compressive testing of unconsolidated material (Wu and Tan, 2000)

Triaxial testing provides an insight into the failure character of the rock, while enabling a more realistic representation of the underground environment. A set of triaxial tests in unconsolidated rocks of the Adriatic Sea are depicted in Figure 2-9. Observe the trend of the sample toward more ductile behavior at larger confining stresses. In order to compare tests with different confining stresses, the parameter plotted corresponds to the difference between the applied and confining stress (deviatoric stress), since the sample is mostly affected by this difference (i.e. shear), and not only by the net applied stress. Notice the relative increase in strength and stiffness of the rock with increasing confining stress, as well as the enlarging of the ductile region^{vii}. Such effects –especially stiffening- are less severe in consolidated rocks. Similar findings for triaxial testing of unconsolidated

^{vii} Enhanced ductility is the result of sliding along microcracks, due to the increase in confining stress (Roegiers, 2005).

sandstones, have been reported by different authors [e.g. Wang et al. (1995) on Antler sandstone and Morita and Ross (1993) on North Sea samples].

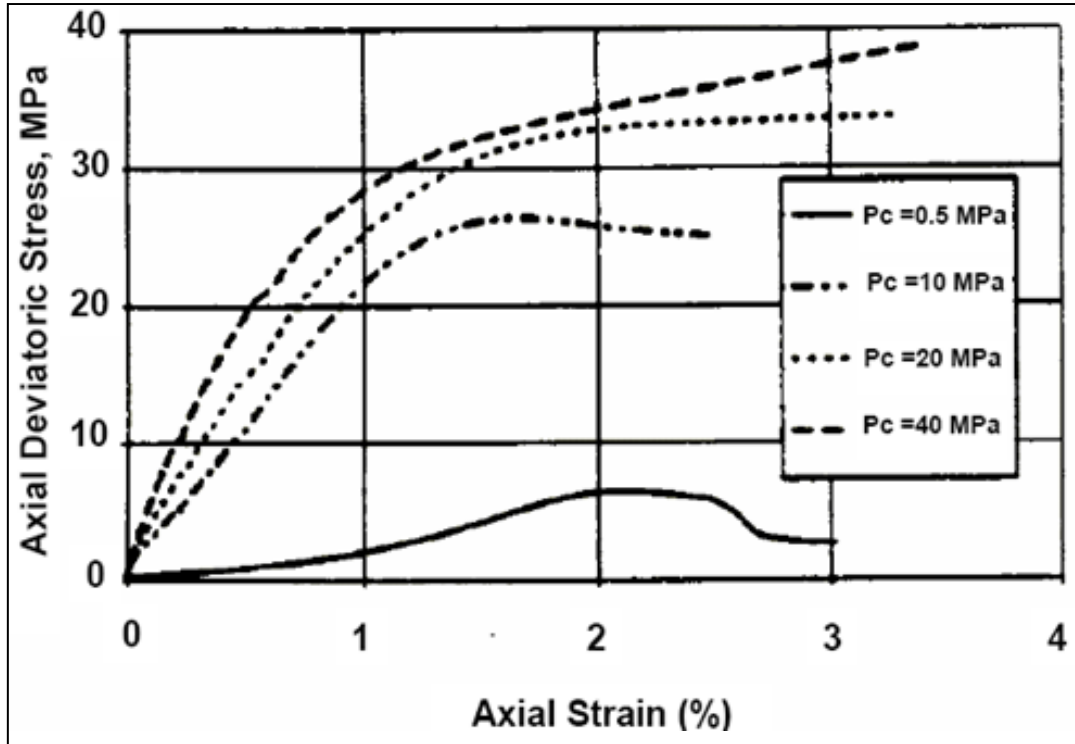


Figure 2-9. Triaxial compressive testing of unconsolidated material of the Adriatic Sea (Marsala, 1994)

2.3.2 Elastic Parameters

Reports for unconsolidated Gulf of Mexico sandstones put their Young's modulus in fractions of one million psi (Ayoub, 1992); compressibility is reported in the range $10-68 \times 10^{-6}$ psi as compared to 1-5 for consolidated formations (Ashford and Goniem, 1987).

The results of uniaxial compressive stress testing of a large collection of soft rock samples are presented in Table 2-2 (Nicholson, 1998). Nevertheless, the elastic modulus in this type of rocks is highly sensitive to confining stress, as discussed earlier. For instance, Wang et al. (1995) reported the increase of Young's modulus from 0.65×10^6 psi to 3×10^6 psi after confinement was raised from $1e3$ to $5e3$ psi.

Table 2-2. Results of triaxial testing data of various unconsolidated sandstones (Nicholson, 1998)

Sample	Condition	UCS, MPa (psi)	Young's modulus, GPa (psi)	Yield Strength, MPa (psi)
Jurassic 3-H2	Kerosene saturated	2.25 (326)	0.25 (50,750)	2.00 (290)
Jurassic 3-H5	16%vol. water	2.00 (290)	0.33 (47,850)	1.80 (261)
Jurassic 3-G2	Water saturated.	2.10 (304)	0.33 (47,850)	1.70 (246)
Jurassic 3-G4	Oven dried	6.10 (884)	0.71 (102,950)	4.70 (681)
Salt Wash South- N1-3	As received (16%vol. water)	3.40-6.00 (493-870)	0.80 – 1.40 (116,000-203,000)	3.30 – 5.60 (478-812)
Salt Wash South- N4-6	Kerosene	3.20-3.70 (464-1,116)	1.50-1.90 (27,500-275,500)	3.50-7.30 (507-1,058)
Salt Wash South- P7	16%vol. water	4.00 (580)	1.0 (145,000)	3.90 (565)
Red Wilmoor – RP1-3	As received (16%vol. water)	19.00-22.00 (2,755-3,190)	3.40 (493,000)	20.00 (2,900)
Red Wilmoor RP4-6	Kerosene saturated	20.40 (2,958)	3.50 (507,000)	18.50 (2,682)

It is usual that the stress-strain behavior does not follow a linear relation. Thus, during a single uniaxial test, Young's modulus decreases as the load is increased, as illustrated in Figure 2-10 (Fjær, 1999).

Some studies have examined the dependency between the stress-strain curve (i.e. elastic modulus) and the stress loading paths^{viii}. The susceptibility of the elastic modulus for various stress paths is depicted in Figure 2-11 for a confining pressure of 5,400 psi (Franquet and Economides, 1999). Notice the high degree of dependence for most of the

^{viii} The loading path –or stress path, K- is defined as the ratio of minimum to maximum stress increase rate [i.e. $(d\sigma_3/dt) / (d\sigma_1/dt)$]. For instance, for both uniaxial and triaxial compressive testing K is equal to zero, because only the maximum stress (σ_1) is increasing, whereas K equals unity in a compressibility (or volumetric) test, in which stress is maintained by means of hydrostatic pressure; hence, $K = 0$ also denotes the path of maximum shear, since the difference between stresses ($\sigma_3 - \sigma_1$) is maximized.

paths presented, and the variability of the general trend as K goes from unity to zero.

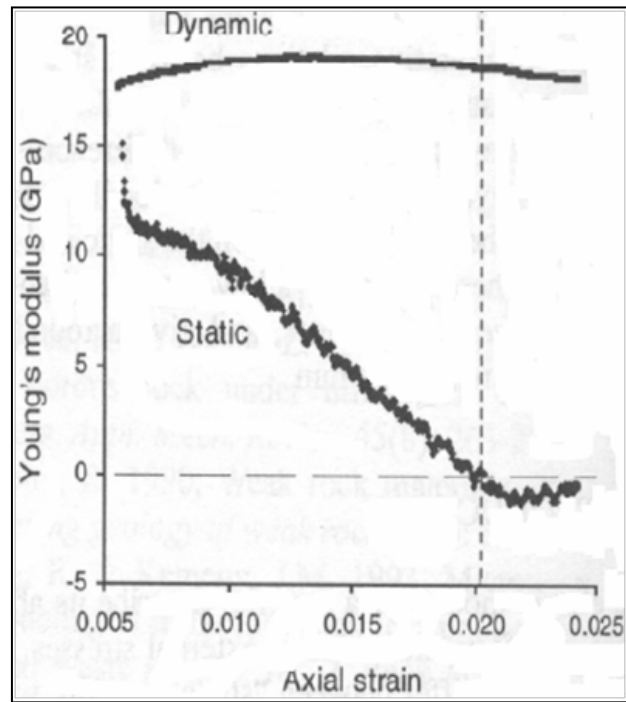


Figure 2-10. Triaxial compressive testing of weak North Sea samples (Fjaer, 1999)

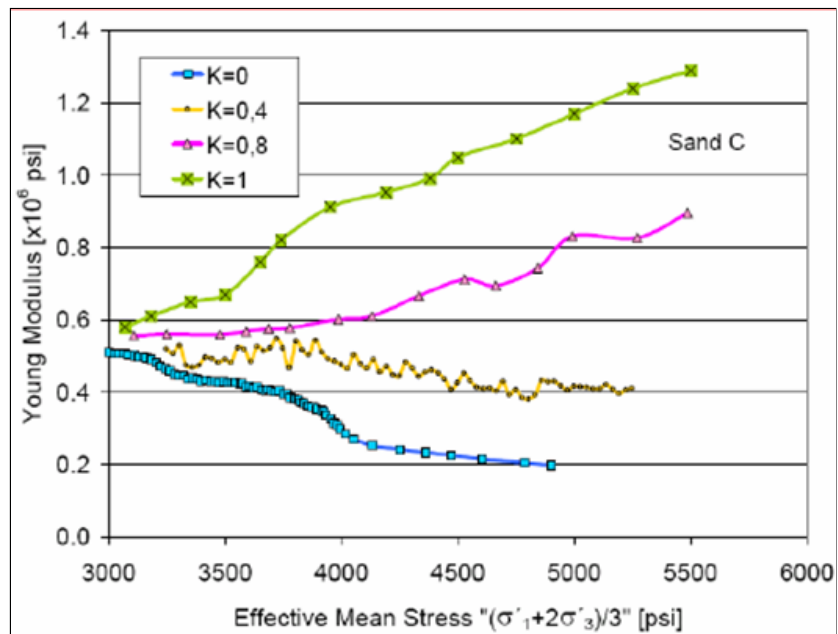


Figure 2-11. Dependence of elastic modulus on effective mean stress for different stress paths in unconsolidated sands (Franquet & Economides, 1999)

On the other hand, the Poisson's ratio (ν), which expresses the relation between radial to

axial strain, features as much or more variability with stress than the elastic modulus. During compression testing of sandstone (uniaxial/triaxial), ν has been reported to fall in the range from 0.1 to 0.2 at low shear stress (i.e. low difference between the applied and confining stresses), but increases as loading proceeds to higher levels (Larsen et al., 2000). Consolidated sandstone exhibits larger Poisson's ratios, in the range of 0.2 – 0.3 units, which remains almost constant until brittle collapse of the specimen. Thus, the variability of Poisson's ratio reflects the more ductile character of unconsolidated sandstones. A plot showing the increase of static Poisson's ratio with stress is depicted in Figure 2-12^{ix}. Also included in the plot is the behavior of the Poisson's ratio determined from dynamic methods. In addition to susceptibility to the change in shear stress, extreme variability is also observed with change of confining stress, as illustrated in Figure 2-13. At low confining pressures (e.g. 3,000 psi curve) Poisson's ratio exhibits the largest increment with applied differential stress. As confining pressure increases, the material appears more compressible, as reflected in lower Poisson's ratios, which are less susceptible to differential stress increase. Nevertheless, the positive relation Poisson's ratio-differential stress is still relevant, as suggested by the increase observed in the 5,000 psi confining pressure curve, from the 0.15 range to almost double that value with an increase of 3,000 psi differential stress increase.

^{ix} Notice that Poisson's ratio cannot exceed a value of 0.5. The static measurements of **Figure 2-12** show values in excess of 0.5 for applied shear stresses greater than 20 MPa, approximately. The reason is that at this stress level, breakage has occurred, and the rock cannot carry additional load. The dynamic measurements are still within normal range because the wave can still be transmitted along the crack faces.

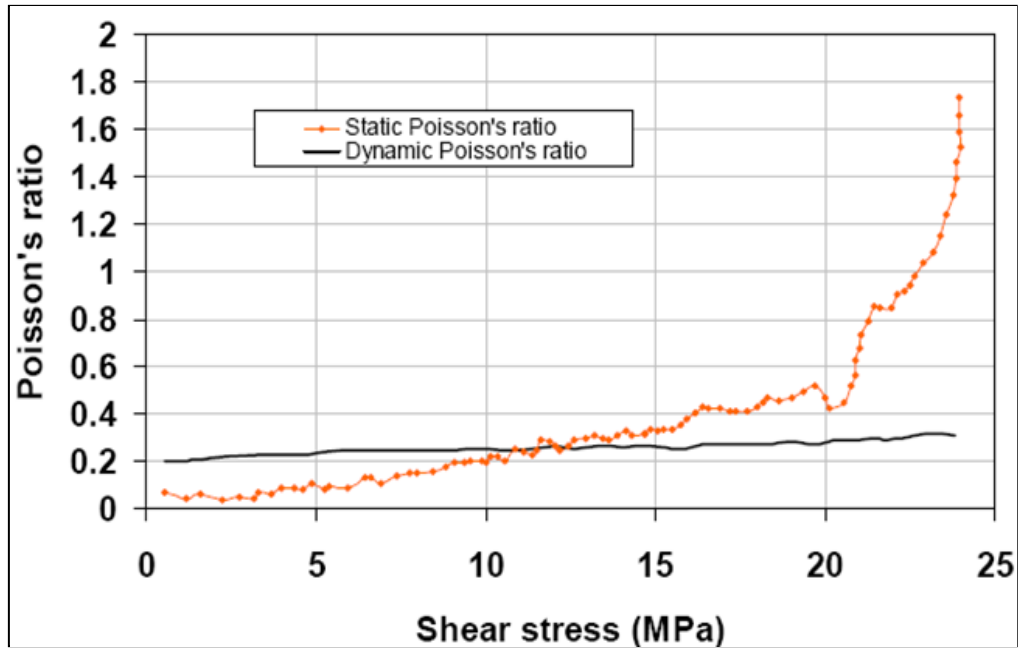


Figure 2-12. Dependence of Poisson's ratio on applied shear stress (Gil, 2005 with data from Larsen et al., 2000)

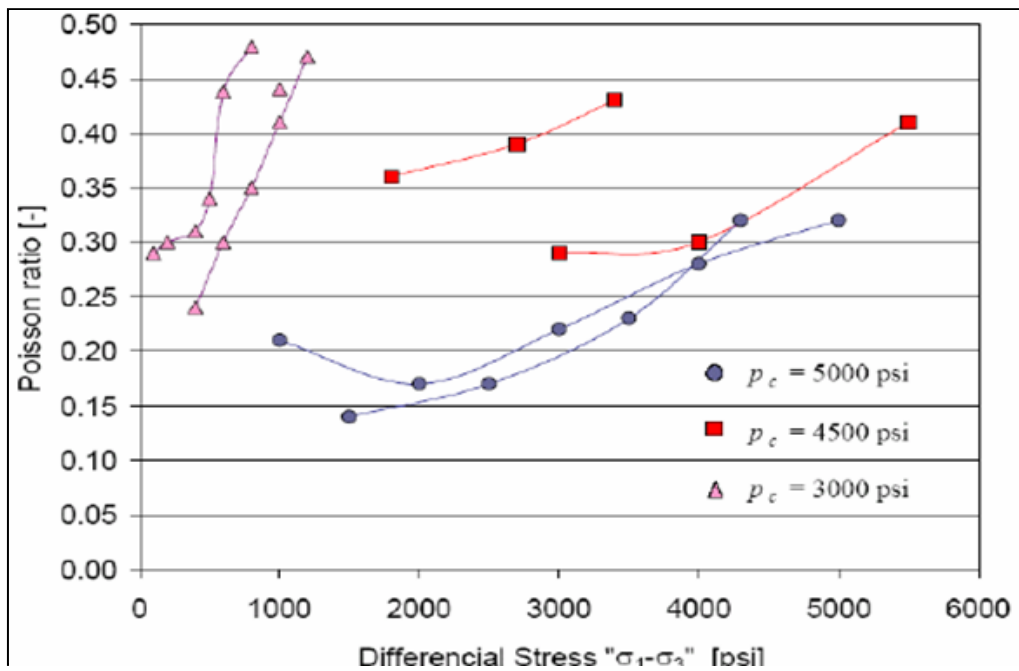


Figure 2-13. Dependence of Poisson's ratio on shear stress and confining pressure (Franquet and Economides, 1999)

Most hydraulic fracturing design models assume independence of the elastic parameters to the changing conditions during the ongoing treatment. This assumption breaks down for poorly consolidated formations, and the effect is more critical for weaker rocks, as

they are more susceptible to changes (Gil, 2005). An example of the impact of incorporating a varying elastic modulus in the calculation of fracture parameters is depicted in Figure 2-14 (Franquet and Economides, 1999). Notice the larger increase of average fracture width with half fracture length for a stress-dependent Young's modulus, as compared to a constant Young's modulus. For instance, the variable Young's modulus predicts an average fracture width for a length of 250 ft. that is approximately twice the prediction of the constant Young's modulus, by using the same mathematical model but calculating at different lengths for the variable modulus. The implications for production are important: the variable Young's modulus model predicts a much larger fracturing surface available for fluid flow than normally assumed under the typical constant Young's modulus condition.

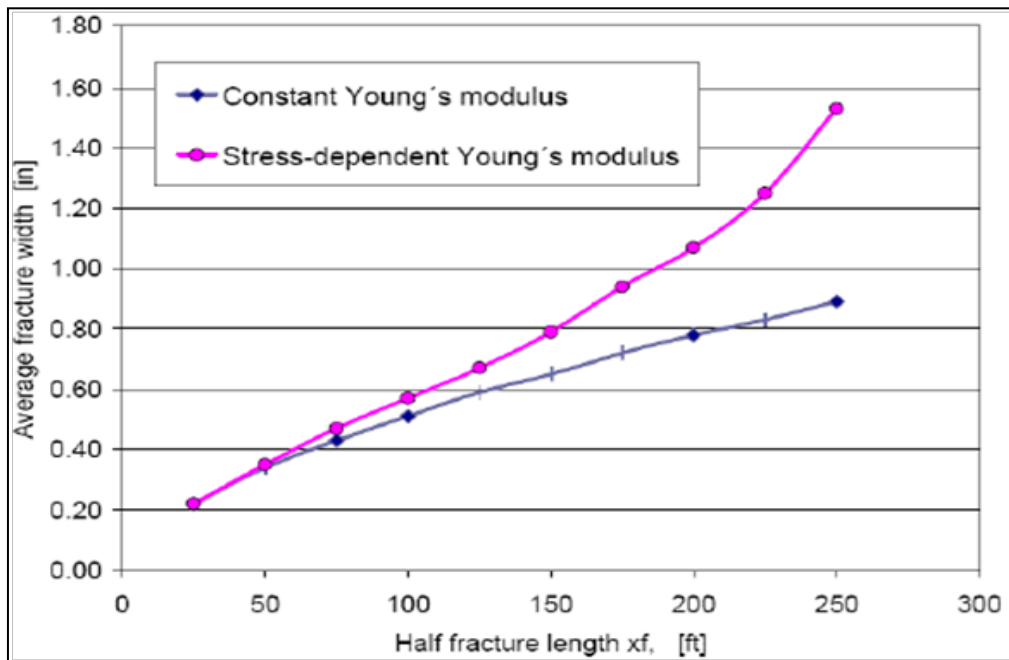


Figure 2-14. Effect of stress dependent Young's modulus on fracture properties (Franquet and Economides, 1999)

2.3.3 Failure Characteristics

UCS as low as 50 psi have been documented for unconsolidated sandstone (Huang et al., 2000). Other studies have reported 80 psi as the lowest UCS bound (Morita and Ross, 1993). More extensive testing indicates that UCS usually falls between hundreds to a few thousand psi (Wu and Tan, 2000). Because rock is tremendously weak in tension, as compared to compression, tensile testing is rarely documented. This is even worse for unconsolidated rock. Based on experimental results, it's been customary to assume tensile strength to be in the range of $1/6^{\text{th}}$ to $1/10^{\text{th}}$ of the UCS.

From triaxial testing it has been determined that the angle of internal friction of unconsolidated rocks is comparable to that of consolidated ones, with values ranging between 30-40 degrees (Huang et al., 2000). Since internal friction is a function of grain fabric, the correspondence of friction angles between consolidated and weak rock is somewhat expected. Conversely, the effective cohesion, being a function of UCS, is found to be extremely low, with reported ranges sometimes less than 100 psi (Huang et al., 2000). This characteristic is the result of the immaturity of the basin, which impairs the generation of cementitious material to support the grain structure.

It is apparent that, the more unconsolidated the formation, the more ductile its behavior becomes. This is reinforced by the absence of dilatancy behavior during stress-strain testing (Wu and Tan, 2000); (Morita and Ross, 1993).

2.3.4 Other Properties

Poorly consolidated rocks exhibit creep to some extent (Ostermeier, 1995).

Comprehensive testing has found the creep relaxation times to be in the range of decades (Dudley et al., 1998). Fluid content is another parameter that affects severely the elastic behavior of poorly consolidated rocks (Wu & Tan, 2001; Colback & Wiid, 1965). Because hydraulic fracturing is a short-lived disturbance in the rock, creep and water weakening are not relevant within the scope of this dissertation.

2.4 IMPLICATIONS FOR THE SIMULATION MODEL SETUP

Some common characteristics of poorly consolidated formations surveyed in this chapter revealed important implications for the definition of the Discrete Element Model that was used for simulations, as follows:

- Low cement content results in tangential contacts between particles: From the options available in DEM to join particles, “contact” bonds, defined as bonds over a vanishing area across the particles in contact, should represent better the mechanics of tangential contacts. The alternative, parallel bonds, seems to be more adequate for well cemented materials.
- High rock quality associated to good sorting: In addition, good sorted rocks seem to be more susceptible to mechanical structural changes upon the application of forces, as demonstrated by the dependency of compressibility and permeability to stress changes. Thus, it is appropriate to constrain the constitutive particles of the DEM specimen to a single size (i.e. with size standard deviation equal to zero), since this represents a critical configuration in regards to sensitivity to mechanical changes.

- The flow network (i.e. pore throats) exhibit a “pipe-like” appearance: This feature is well represented by the selection of spheres as the elemental particle in the DEM sample.
- Variation on macroscopic elastic properties upon application of forces, sometimes in a non-linear fashion: The macroscopic properties in DEM are not forced on the material. Instead, they result from the interaction between the particles through their bonds. Thus, non-linearities and macroscopic properties variation should result naturally during the DEM simulations.

3 CONVENTIONAL HYDRAULIC FRACTURING MODELING

The review of fundamental aspects of poorly consolidated formations in the last chapter revealed some interesting differences between the fabric of this type of rock and that of their well-consolidated counterparts. For instance, pores in low quality consolidated rock (i.e. low permeability/porosity) tend to conform to slot-like shapes. This feature makes them more sensitive to stress changes than rocks with high quality characteristics. The tendency is reversed in weak rock, for which stress sensitivity is greater for high quality samples. Thus, the reflection of the grain-structure on the mechanical properties of the rock clearly indicates that a predictive model based on the behavior of consolidated rock may not be adequately extrapolated to weaker specimens. However, the classical fracturing models for rock have usually been adapted from fracture mechanics theories for metals. These adaptations have been mostly successful for well-consolidated rock that responds in a markedly brittle fashion to stress changes. This chapter visits the fundamentals of the models that have been conventionally applied to hydraulic fracturing.

3.1 MODEL COMPONENTS

Fracturing models typically consist of the coupling of three basic components: 1) a fluid flow model; 2) a rock deformation model; and, 3) a fracture propagation criterion (Gidley et al., 1989).

The fluid flow model describes the pressure losses and pressure distribution along the fracture, and leak-off into the surrounding porous media. The rock deformation model

predicts the response of the fractured surface to hydraulic loading (i.e. pressure). The fracture propagation criterion establishes a combination of loading and deformation conditions that result in advance of the fracture into the intact rock volume. These models are combined by means of a usually iterative time-marching algorithm that determines critical deformation of the rock due to pressure loading, and calculates the resulting advance of the crack. Pioneering 2D models introduced simplifying assumptions from the aspect ratio of the fracture; longer fractures assume plane stress on the plane that is perpendicular to flow, whereas shorter fractures consider this plane to be on the direction of flow. Fully 3D models were later developed, as computational power improved over the years. Pseudo-3D models yield 3D fields, but out of solving equations for ‘2D slices’ of the fracture, based on plane stress assumptions.

Even for fully 3D models, the fracture is usually assumed planar. For instance the plane of the fracture depicted in Figure 3-1 lies onto the xy-plane. It is well documented that fracture propagation occurs perpendicular to the minimum principal stress (Hubbert and Willis, 1957); according to the figure, the minimum stress direction is assumed along the z-axis. Thus, it is reasonable to model fluid flow on the propagation plane (i.e. in two dimensions, only), since once the fracture starts growing, one dimension quickly becomes negligible as compared to the other two. As a result, only q_x and q_y appear on the fluid flow expressions.

The coordinate system depicted in Figure 3-1 is used in all subsequent discussion about the fracturing model. The major components of a conventional hydraulic fracture model are illustrated in Figure 3-2.

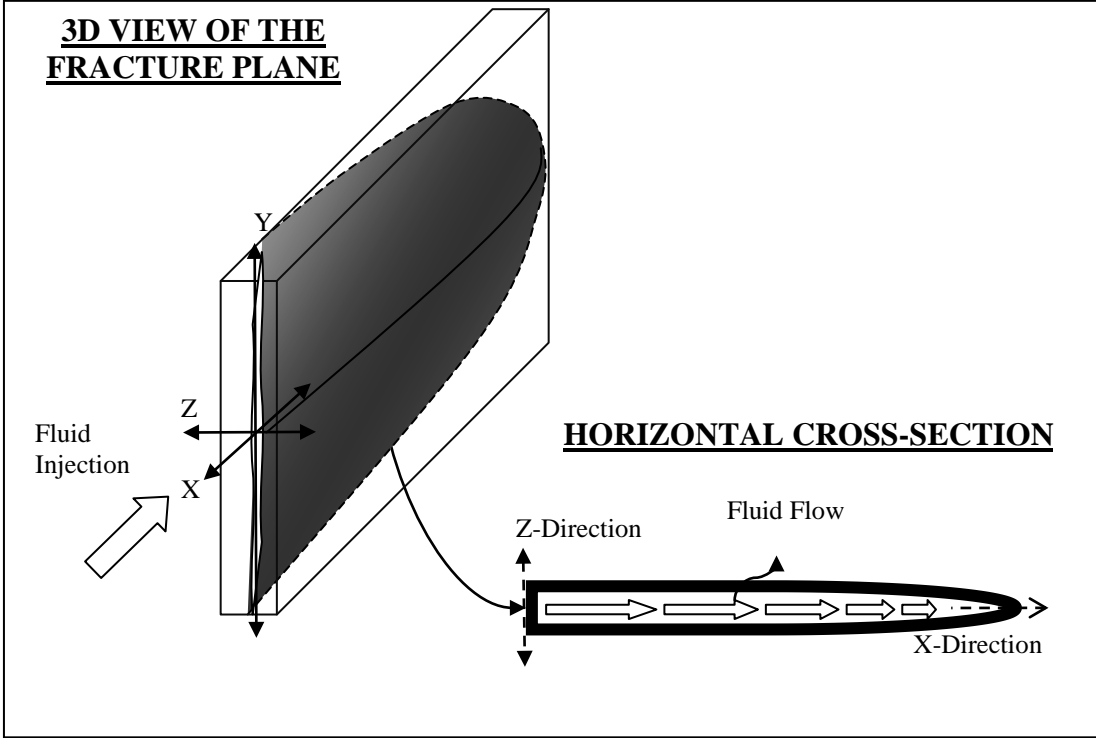


Figure 3-1. Schematic representation of a hydraulic fracture

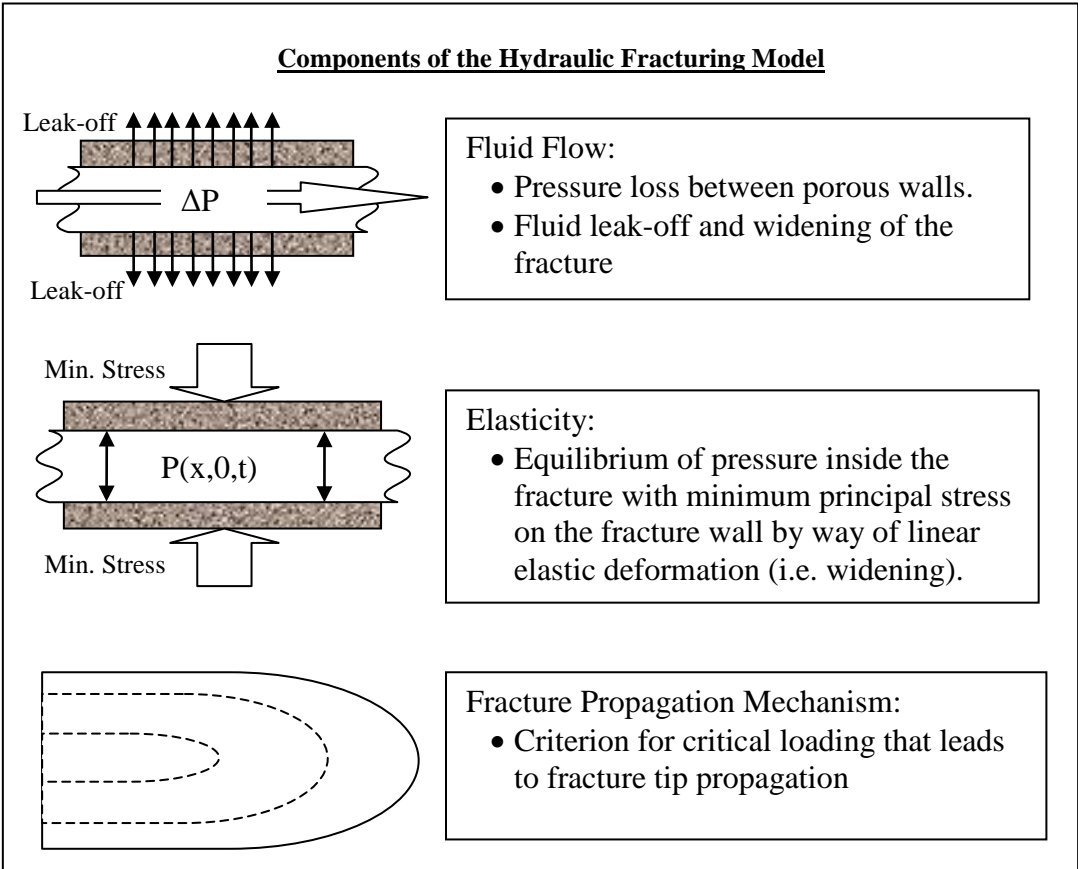


Figure 3-2. Components of a conventional hydraulic fracture model

The fracture tip propagation is usually identified as the main factor for the reported inconsistencies between simulation and field results (Chudnovsky et al. 1996). This chapter examines the theoretical background and the simplifying assumptions that make up the most popular hydraulic fracturing models.

3.2 FRACTURE MECHANICS FUNDAMENTALS

Most theories derive from the pioneering work by Griffith (1921), who proposed the existence of minute cracks that act as stress concentrators in the material; during propagation, part of the elastic energy concentrated in the body, especially around the crack tip, is released to create new surfaces. Posterior modifications of Griffith's theory to more general loading conditions in terms of measurable parameters led to the so-called "stress intensity factors" (Orowan, 1952; Irwin, 1957). These studies, along with many subsequent contributions, gave origin to the classic theory of fracture mechanics. In the case of fracture in rock, it is generally assumed that loading and deformation fall onto a linear relation, and that propagation of the crack occurs in brittle fashion before considerable non-linear features are discernible. The assumption of linear elasticity is combined with the principles of classic fracture mechanics in what is known as Linear Elastic Fracture Mechanics or LEFM, for short. By far, the most common rock fracture propagation models are based on LEFM concepts, with the fracture faces separating in a normal direction from each other or 'Mode I', as depicted in Figure 3-3. This has been proven to be a reasonable approach in well consolidated "hard" rock (Schmidt, 1976; Schmidt and Huddle, 1977).

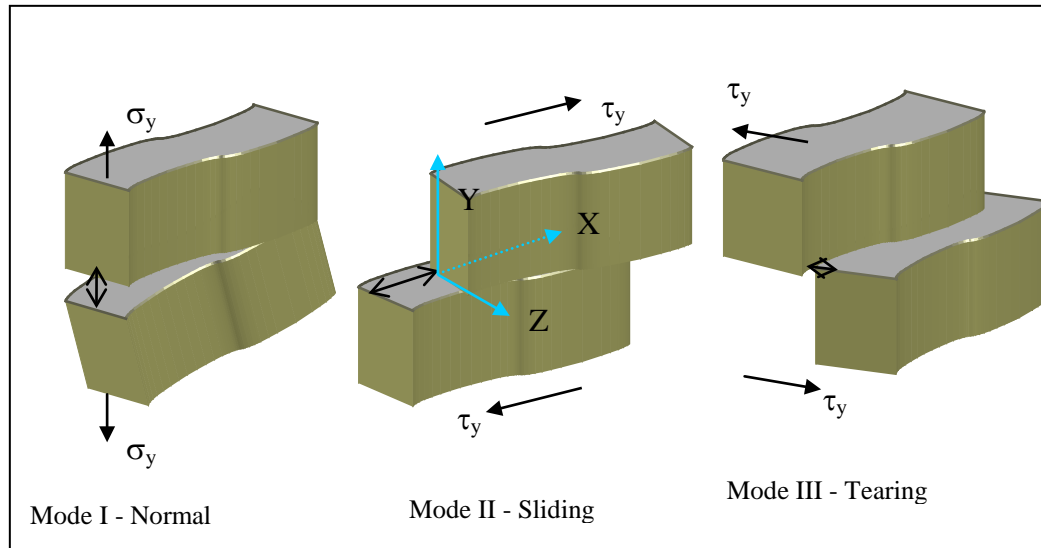


Figure 3-3. Fracture extension modes

3.2.1 Linear Elastic Fracture Mechanics (LEFM)

Ingraffea (1977) developed a scheme to model the propagation of an arbitrarily oriented elliptical cavity (i.e. a notch) inside a rock block, under the action of an external load, σ . The resulting model can be described as a combination between a Finite Element (FE) framework for deformation, and LEFM theory for fracture propagation.

In general, four steps are included in Ingraffea's scheme:

- Determination of the magnitude and location of maximum tangential stress around the surface of the notch. A failure criterion is used to resolve the necessary stress for initiation of a crack from the notch.
- Calculation of the length of the initial crack, by trial-and-error comparison of the energy available for rupture (strain energy release) to the energy 'consumed' by the newly created surfaces.
- Determination of the most likely location for further propagation, according to

fracture propagation criteria, in terms of fracture intensity factors.

- Calculation of the crack increment length, by the same trial-and-error scheme of step 2.

The process then continues by repeating the last two steps until a prescribed propagation length is reached, or until the crack reaches the boundary of the block. The theoretical bases of Ingraffea's algorithm are provided next.

3.2.1.1 Initiation of a crack from a notch

The magnitude and location of the maximum tangential stress are based on the analytical solution of the stress field around the surface of an arbitrarily oriented elliptical cavity (i.e. a notch), submitted to an external load, σ . The stress field is given by (Griffith, 1924):

$$\sigma_{\eta} = \frac{(P_1 + P_2) \sinh(2\xi_0) + (P_2 - P_1)[e^{2\xi_0} \cos 2(\beta - \eta) - \cos 2\beta]}{\cosh 2\xi_0 - \cos 2\eta} \quad (3-1)$$

where: η, ξ are elliptical coordinates;

ξ_0 is the coordinate of the ellipse that represents the initial notch;

P_1, P_2 are the principal stresses in 2D; and,

β is the angle between the notch's major axis and the principal stress.

From the above correlation, the point of fracture initiation from a notch is found at the

location of the maximum tangential stress. Assuming ξ_0 to be small as to represent a very flat ellipse (i.e. a crack), the largest tensile stress is given by:

$$\sigma_{\eta,m} = \frac{1}{\xi_0} \left[\sigma_y - (\tau_{xy}^2 + \sigma_y^2)^{1/2} \right] \quad (3-2)$$

and it is located at:

$$\frac{\eta}{\xi_0} = \left[\sigma_y + (\sigma_y^2 + \tau_{xy}^2)^{1/2} \right] / \tau_{xy} \quad (3-3)$$

where the stresses in rectangular coordinates are given in terms of the principal stresses P_1 and P_2 by:

$$\sigma_y = P_1 \sin^2 \beta + P_2 \cos^2 \beta \quad (3-4)$$

$$\tau_{xy} = \frac{1}{2} (P_1 - P_2) \sin 2\beta \quad (3-5)$$

The x-component of stress does not appear on the above correlations due to the assumption of a very flat ellipse lying along the x-axis. In other words, the crack is modeled as a flat slot, whose surfaces are pulled apart by tractions on the y-direction.

A failure criterion determines the fracturing load, and the propagation direction. Following, three of the better known criteria are presented.

3.2.1.2 Stress intensity factors

The presence of defects in the rock (e.g. minute cracks, vugs, soft inclusions, etc.), have

the effect of intensifying the magnitude of any applied load, according to the principles first set by Griffith (1921). The intensification effect is the result of a compromise between the surrounding loads, the geometry of the defect, and the mechanical properties of the medium. Ever since its inception by Irwin (1948) and Orowan (1949), such relations are defined in terms of stress intensity factors, which can be empirically determined.

For mode I fracture propagation, the stresses around the crack tip are defined by:

$$\begin{bmatrix} \sigma_x \\ \sigma_y \\ \sigma_{xy} \end{bmatrix} = \frac{K_I}{\sqrt{2\pi r}} \cos \frac{\theta}{2} \begin{bmatrix} 1 - \sin \frac{\theta}{2} \sin \frac{3\theta}{2} \\ 1 + \sin \frac{\theta}{2} \sin \frac{3\theta}{2} \\ \sin \frac{\theta}{2} \cos \frac{3\theta}{2} \end{bmatrix} \quad (3-6)$$

$$\begin{aligned} \sigma_z &= \nu(\sigma_x + \sigma_y) \quad \text{for plane strain} \\ \sigma_z = \sigma_{xz} = \sigma_{yz} &= 0 \quad \text{for plane stress} \end{aligned}$$

where K_I is the constant stress intensity factor for mode I, and groups the parameters related to load and fracture lengths; i.e. $K_I = \sigma\sqrt{\pi a}$.

With the help of Hooke's law, stress is correlated to displacements. Expressions for u and v , the displacements along the x and y – axes, respectively, are given by:

$$\begin{bmatrix} u \\ v \end{bmatrix} = \frac{K_I}{4\mu} \sqrt{\frac{r}{2\pi}} \begin{bmatrix} (2k-1) \cos \frac{\theta}{2} - \cos \frac{3\theta}{2} \\ (2k+1) \sin \frac{\theta}{2} - \sin \frac{3\theta}{2} \end{bmatrix}$$

for plane strain $k = 3 - 4\nu$ and $w = 0$; and

for plane stress $k = (3 - 4\nu)/(1 + \nu)$ and $w = -(\nu/E) \int (\sigma_x + \sigma_y) dz$

...(3-7)

Note: w is the displacement along the z -direction.

Analogous expressions for Mode II displacement are given by:

$$K_{II} = \tau_i \sqrt{\pi a} \quad (3-8)$$

The stress field is given by:

$$\begin{bmatrix} \sigma_x \\ \sigma_y \\ \sigma_{xy} \end{bmatrix} = \frac{K_{II}}{\sqrt{2\pi r}} \begin{bmatrix} -\sin \frac{\theta}{2} \left(2 + \cos \frac{\theta}{2} \cos \frac{3\theta}{2} \right) \\ \sin \frac{\theta}{2} \cos \frac{\theta}{2} \cos \frac{3\theta}{2} \\ \cos \frac{\theta}{2} \left(1 - \sin \frac{\theta}{2} \sin \frac{3\theta}{2} \right) \end{bmatrix} \quad (3-9)$$

for plane strain $\sigma_z = \nu(\sigma_x + \sigma_y)$

for plane stress $\sigma_z = \sigma_{xz} = \sigma_{yz} = 0$

The displacements are:

$$\begin{aligned} \begin{bmatrix} u \\ v \end{bmatrix} &= \frac{K_{II}}{4\mu} \sqrt{\frac{r}{2\pi}} \begin{bmatrix} (2k+3) \sin \frac{\theta}{2} + \sin \frac{3\theta}{2} \\ -(2k-3) \cos \frac{\theta}{2} - \cos \frac{3\theta}{2} \end{bmatrix} \\ \text{for plane strain } w &= 0 \\ \text{for plane stress } w &= -\left(\frac{\nu}{E}\right) \int (\sigma_x + \sigma_y) dz \end{aligned} \quad (3-10)$$

Similar expressions for Mode III can be found elsewhere (e.g. Whittaker et al., 1992).

Nevertheless, implementation of the above correlations to a FE model is impractical for various reasons. For instance, the correlations are continuous and would need to be adapted to the discretized geometry of the grid. Additionally, FE models have been extensively used to calculate the displacements of a given elastic geometry. So, the natural extension of this capability is to compute the stress intensity factor from the FE-derived displacements, rather than to force the above correlations into the FE elements.

The technique used to compute the stress intensity factor, based on the FE-displacement calculations is referred to as displacement correlation method. The corresponding correlations involve the displacements around the crack tip, and are given by:

$$K_I^* = \left(\frac{2\pi}{r_{AB}}\right)^{\frac{1}{2}} \frac{G(1+\nu)}{4} (v_B - v_C) \quad (3-11)$$

$$K_{II}^* = \left(\frac{2\pi}{r_{AB}}\right)^{\frac{1}{2}} \frac{G(1+\nu)}{4} (u_B - u_C) \quad (3-12)$$

where $K_{I,II}^*$ are stress intensity factors for displacement modes I and II;

A is the node at the crack tip;

B, C are nodes immediately behind the crack tip;

r_{AB} is the distance from A to B ; and,

u, v are the horizontal and vertical displacements of the nodes, according to the FE numerical solution.

An illustration of the FE grid showing the location of the nodes in the vicinity of the tip is depicted in Figure 3-4.

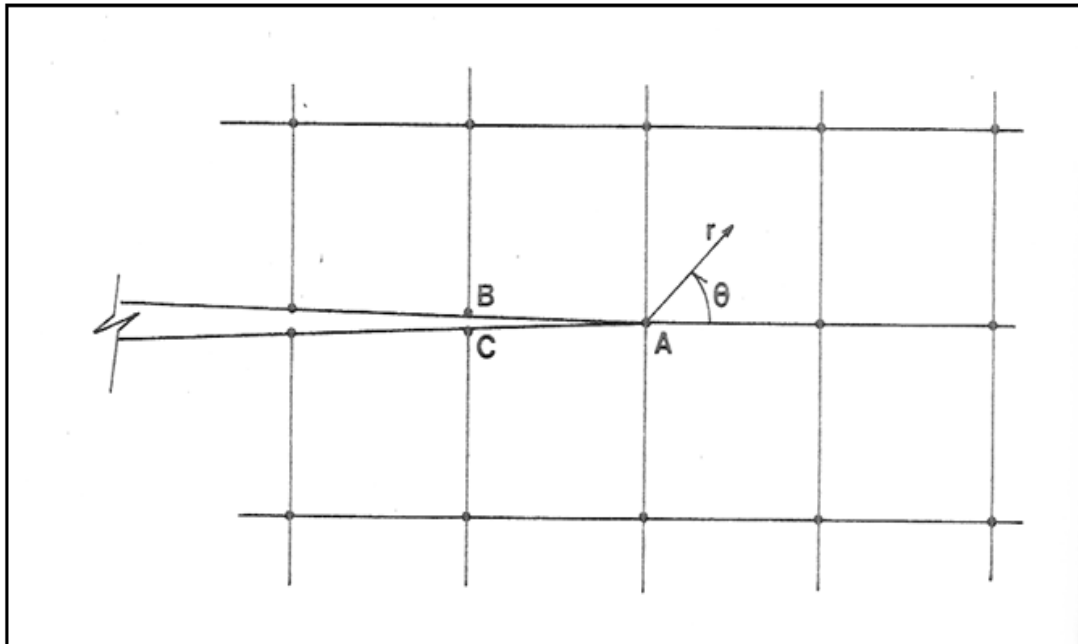


Figure 3-4. Finite element grid of a propagating fracture (Ingraffea, 1977)

3.2.1.3 Crack propagation criteria

Three models commonly used for fracture propagation are the maximum tangential stress, the maximum rate of energy release, and the minimum strain energy density

intensity. These models predict points of initiation and angle of propagation. Usually, the solution is valid beyond a distance r_0 from the crack tip, because of the tip singularity generated by stress intensification from the crack's presence. The models assume mixed mode propagation, involving some combination of Mode I and Mode II displacement of the just created new cracked surfaces.

Maximum tangential stress model ($\sigma_{\theta, \max}$):

The main assumptions of this theory are that crack extends from the tip, in a plane normal to the direction of largest tension (i.e. at an angle such that shear stress vanishes), and that propagation initiates when $\sigma_{\theta, \max}$ reaches a critical material constant.

The critical material constant is given by:

$$\sigma_{\theta} \sqrt{2\pi r} = \text{const.} = K_{I,cr} = \cos \frac{\theta_0}{2} \left[K_I \cos^2 \frac{\theta_0}{2} - \frac{3}{2} K_{II} \sin \theta_0 \right] \quad (3-13)$$

where σ_{θ} is the tensile circumferential stress;

r is the distance from the tip to some point inside the rock;

$K_{I,cr}$ is fracture toughness;

θ_0 is the propagation angle; and,

$K_{I,II}$ are the stress intensity factors for fracturing modes I and II, respectively.

The propagation angle can be found from:

$$K_I \sin \theta_0 + K_{II} (3 \cos \theta_0 - 1) = 0 \quad (3-14)$$

Maximum rate of energy release $(G(\theta))_{\max}$:

This theory states that a crack propagates in the direction of maximum energy release rate, provided that the maximum reaches a critical material value.

The rate of energy release is given by (Hussain et al., 1974):

$$G(\theta) = \frac{4}{E} \left(\frac{1}{3 + \cos^2 \theta} \right)^2 \left(\frac{1 - \theta/\pi}{1 + \theta/\pi} \right)^{\theta/\pi} [(1 + 3 \cos^2 \theta) K_I^2 + 8 \sin \theta \cos \theta K_I K_{II} + (9 - 5 \cos^2 \theta) K_{II}^2] \quad (3-15)$$

where all the parameters have been previously defined.

Thus, the angle of propagation can be found from maximization of the above equation:

$$\frac{\partial G(\theta)}{\partial \theta} = 0 \quad (3-16)$$

Eq. (3-15) was derived for the energy release rate of the extension of a branch-crack of infinitesimal length (i.e. the crack branches from the tip of the principal crack), in an infinite plate. Consequently, the stress intensity factors “K” do not correspond to those defined for the main crack tip. K is a function of the angle, and is given by:

$$K_I(\theta) = \left(\frac{4}{3 + \cos^2 \theta} \right) \left(\frac{1 - \theta/\pi}{1 + \theta/\pi} \right)^{\theta/2\pi} \left[K_I \cos \theta + \frac{3}{2} K_{II} \sin \theta \right] \quad (3-17)$$

$$K_{II}(\theta) = \left(\frac{4}{3 + \cos^2 \theta} \right) \left(\frac{1 - \theta/\pi}{1 + \theta/\pi} \right)^{\theta/2\pi} \left[K_{II} \cos \theta + \frac{1}{2} K_I \sin \theta \right] \quad (3-18)$$

where,

$$K_I = \sigma_y^\infty \sqrt{\pi a} \quad (3-19)$$

$$K_{II} = \tau_{xy}^\infty \sqrt{\pi a} \quad (3-20)$$

and,

$$\sigma_y^\infty = P^\infty \sin^2 \beta \quad (3-21)$$

$$\tau_{xy}^\infty = P^\infty \sin \beta \cos \beta \quad (3-22)$$

Minimum strain energy density intensity $S(\theta)_{\min}$:

This theory states that crack propagation occurs along the direction of minimum strain energy density ($\partial U / \partial V$), provided that a critical strain energy density intensity value ($S(\theta)$) is reached. $S(\theta)$ is evaluated along a contour $r = r_0$, where r_0 is a material constant.

Strain energy density is given by:

$$\frac{\partial U}{\partial V} = \frac{S}{r_0} \quad (3-23)$$

where “S” is referred to as strain energy density, and is defined as:

$$S = \frac{a_{11}K_I^2 + 2a_{12}K_I K_{II} + a_{22}K_{II}^2}{\pi} \quad (3-24)$$

and the “a” coefficients are found from:

$$a_{11} = \frac{1}{16G} [(1 + \cos\theta)(k - \cos\theta)] \quad (3-25)$$

$$a_{12} = \frac{\sin\theta}{16G} [2\cos\theta - (k - 1)] \quad (3-26)$$

$$a_{22} = \frac{1}{16G} [(k + 1)(1 - \cos\theta) + (1 + \cos\theta)(3\cos\theta - 1)] \quad (3-27)$$

where k and G correspond to bulk and shear modulus, respectively.

The critical failure condition is given by:

$$S_c = \frac{(k - 1)K_{I,cr}^2}{8\pi G} \quad (3-28)$$

Remarks on the crack propagation models:

The models described above seemingly constitute a most natural evolution from the basic “maximum tangential stress”, to the more complex “minimum strain energy density” one. Although their chronological development supports this idea, limited available experimental data is inconclusive as to the universal applicability of any one of them (e.g. Shetty et al., 1987; Ingraffea et al., 1981). Indeed, different authors have proposed many more models, mostly based on those just presented (Richard, 1984).

The fundamental differences amongst the models are based on the degree of complexity of the physics behind each one of them. The straightforward maximum tangential stress criterion simply states that propagation will occur upon generation of tensile stress beyond a critical point, which is a material property, and in a direction perpendicular to such stress. The maximum strain energy criterion states that fracture will occur once a critical amount of energy is stored in the material and in the direction towards which this energy is a maximum. The minimum strain energy density criterion looks at the volumetric distribution of strain energy, and proposes that fracture propagation occurs towards the direction that shows the larger volumetric scatter of stored strain energy.

A main characteristic of the latter criterion is that, from the models discussed, it is the only one that provides a direct estimation of propagation length, because it involves a volume in the material that “supports” fracture growth when critical conditions are reached. Nonetheless, it is the most complicated model to apply because it is given in terms of many material properties that are usually not available. For this same reason, the maximum stress criterion is arguably the most popular, since it involves fewer parameters and it is easier to apply.

Note that these models provide the means to estimate propagation from an initial fracture that is oriented arbitrarily with respect to the stress field. However, hydraulic fractures are started from perforations that are, for the most part, oriented in the same direction as the expected fracture propagation. The three models reduce to a common criterion in such case, which predicts that propagation occurs in the same direction as the initial fracture (i.e. the perforation direction). Fracture turning, when perforations are oriented oblique to

the stress field, is beyond the scope of study of this dissertation. The discussed models are not presented for their relevance in the propagation of the main hydraulic fracture, but to illustrate the rather large effects caused by generation of secondary cracks, and most importantly, the current limitations on the accurate prediction of the pressure that is deviated towards the generation of such features.

3.2.1.4 Crack increment calculation

The crack length is based on an energy balance between the available energy (rate of strain energy release, G) and the required energy for propagation (a material property, R) at the moment of rupture.

The crack increment Δa is the value for which:

$$\int_a^{a+\Delta a} G(\theta_0, \Delta a) da = \int_a^{a+\Delta a} R da \quad (3-29)$$

Thus, the procedure consists on assuming a few trial values of Δa , and its corresponding stress intensity factors, from the FE model. In this way a few points of the G -function (Eq. (3-15)) are traced, so that a polynomial fit can be obtained. The function G is then compared to R through Eq. (3-29), and the correct crack increment is determined. The concept is illustrated graphically in Figure 3-5.

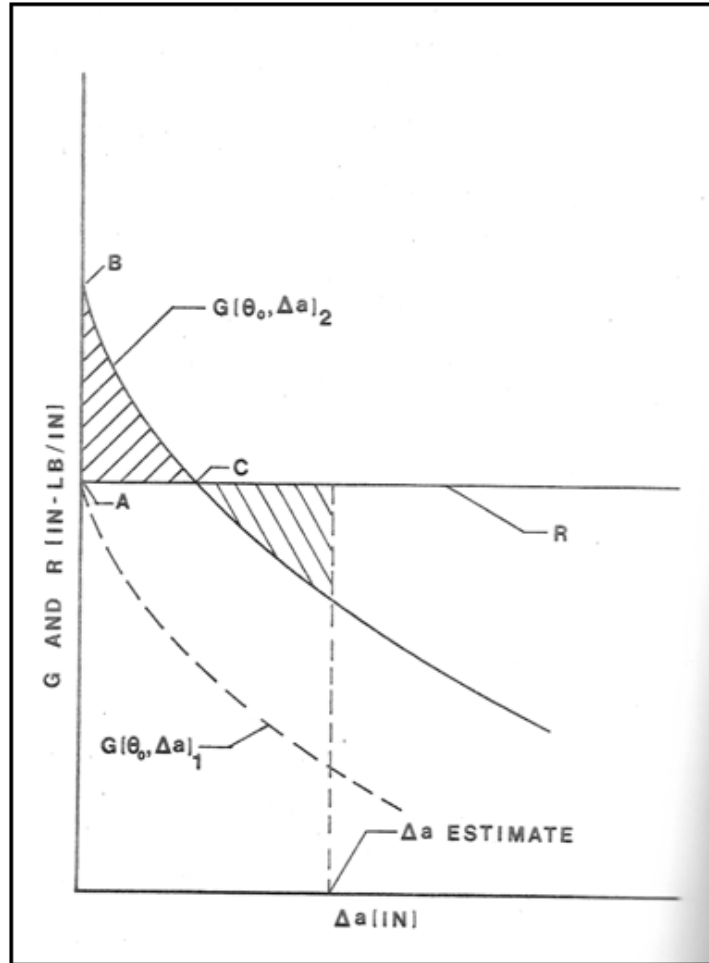


Figure 3-5. Energy balance used for fracture increment calculation (After Whittaker, 1992).

3.2.2 Non-Linear Elastic Fracture Mechanics (NEFM)

NEFM hypotheses aim to determine the extent and effect of the non-linear area in front of the crack tip. Typically, theories for NEFM are developed from the assumption of a fundamental shape wherein the non-linear behavior concentrates; equations to calculate the length of this region are then derived.

The basic postulate of NEFM proposes that outside of the NEFM section –sometimes referred to as the ‘K-dominant’ section-, LEFM takes over and the respective equations for linear elasticity are applicable. This assertion neglects the stress redistribution caused

by the fracturing process zone; in other words, some of the stress is released from the plastic section and transferred onto the neighboring elastic section. The models proposed by Irwin and Dugdale [(Irwin (1957); Dugdale (1960))] account for stress redistribution due to the plastic region, and are very popular in fracture mechanics applications for metals. Both models assume the plastic region to be concentrated in front of the crack tip, but they differ from each other in the shape of the region; the former assumes it to be concentrated into a circular region of diameter $2r_y$, whereas the latter assumes it to be concentrated onto a strip of length r_y . These theories originated the concept of a ‘notional crack’, which states that while the ‘true’ crack is still of length ‘a’, the LEFM calculations should proceed by replacing the crack length by an ‘effective’ crack length of $a + r_y$. Or, put another way, the effect of the plastic region is equivalent to assume LEFM behavior, but as if the length of the crack have been increased by an amount equal to the length of that plastic section. In practice, there is only a slight difference between the calculations carried by either method.

Whereas in metals the plastic behavior near the crack tip is due to excessive shear, in rock is due to a region where micro-cracks are formed ahead of the propagating crack, and known as the Fracturing Process Zone (FPZ). Consequently, NEFM theories for rock are basically derived from the analyses made for metals (especially Irwin’s and Dugdale’s models), but modified to match the behavior of the Fracturing Process Zone (FPZ) in rocks. The most representative models for fracture propagation in rock, according to NEFM, are the “maximum normal stress criterion” and the “cohesive crack model”. Their basic tenets are presented next.

3.2.2.1 Maximum normal stress criterion (Schmidt, 1980)

According to this criterion, a FPZ takes place when the maximum principal stress reaches the ultimate uniaxial tensile strength of the rock, i.e. $\sigma_1 = \sigma_t$. If this relationship is replaced into the expression for σ_1 (Eq. (3-30)), an equation for the shape of the FPZ, $r(\theta)$, can be calculated as follows (Eq. (3-31)):

$$\sigma_t = \sigma_1 = \frac{K_I}{\sqrt{2\pi r}} \cos \frac{\theta}{2} \left(1 + \left| \sin \frac{\theta}{2} \right| \right) \quad (3-30)$$

$$r(\theta) = \frac{1}{2\pi} \left(\frac{K_I}{\sigma_t} \right)^2 \cos^2 \frac{\theta}{2} \left(1 + \left| \sin \frac{\theta}{2} \right| \right)^2 \quad (3-31)$$

In the plane of the crack, $\theta = 0$, the above expression reduces to:

$$r_y = r(0^\circ) = \frac{1}{2\pi} \left(\frac{K_I}{\sigma_t} \right)^2 \quad (3-32)$$

It is usual to represent schematically the FPZ as a normalized length, defined as $r(\theta)/r_y$.

The conceptual schematic of the maximum normal stress criterion can be observed in Figure 3-6.

The condition for fracture propagation is established when the FPZ is fully developed and its length reaches a critical value r_{yc} , defined as:

$$r_{yc} = r_c(0^\circ) = \frac{1}{2\pi} \left(\frac{K_{IC}}{\sigma_t} \right)^2 \quad (3-33)$$

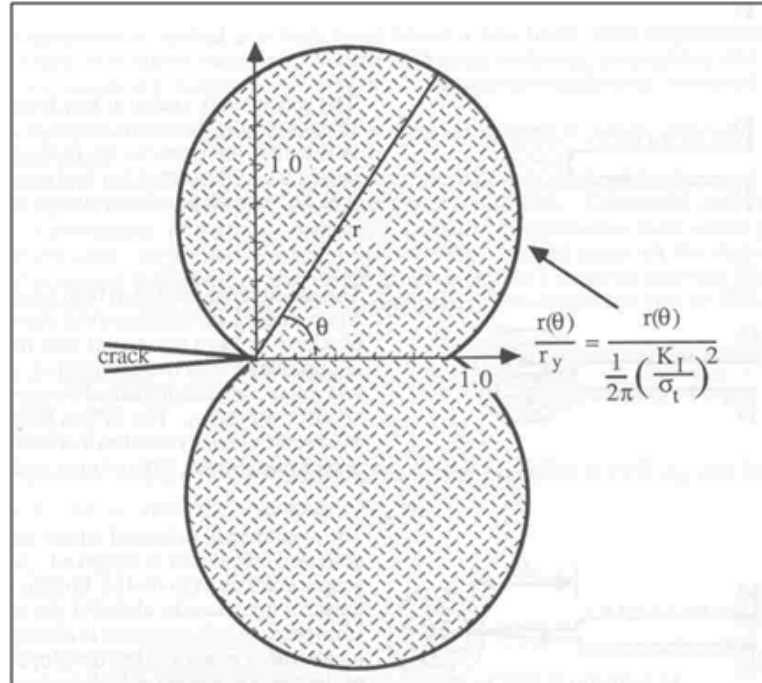


Figure 3-6. FPZ for the maximum normal stress criterion (Schmidt, 1980)

3.2.2.2 Cohesive crack model

This is arguably the most used model for FPZ characterization, because it incorporates stress redistribution, given that it is an adaptation of Dugdale's model for metals. The basic premise of this theory is that the FPZ consists of a strip region in front of the crack tip that -although damaged- can still carry some stress, which tends to close the crack. Central to this model is the concept of the notional or effective crack: it consists of the 'true' crack, which is the section where the crack faces are traction free, plus the FPZ length. This crack model is also known as fictitious crack, and is illustrated in Figure 3-7.

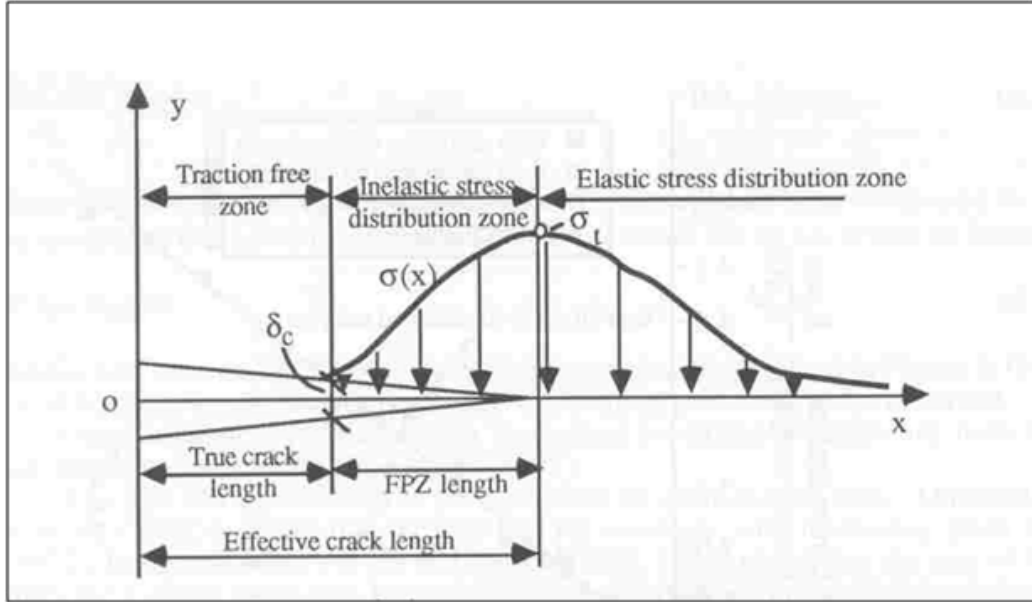


Figure 3-7. FPZ cohesive crack model (After Whittaker, 1992)

The FPZ stress distribution is approximated with the following linear relation (Labuz et al., 1983):

$$\sigma(x) = \frac{x-a}{r_y} \sigma_t \quad (3-34)$$

In the FPZ region, $K_{\sigma(x)}$ is given by:

$$K_{\sigma(x)} = -2 \int_a^{a+r_y} \sqrt{\frac{a+r_y}{\pi[(a+r_y)^2 - x^2]}} \left[\frac{x-a}{r_y} \sigma_t \right] dx \quad (3-35)$$

Whereas in the elastic region K_I is:

$$K_I = \sigma \sqrt{\pi a} \quad (3-36)$$

Considering that the stress singularity, as calculated from LEFM, disappears at the

notional crack tip, and applying the superposition principle for the overall stress intensity factor:

$$K = K_{\sigma(x)} + K_I = 0 \quad (3-37)$$

Combining the above equations and solving for the FPZ size along the crack plane r_y results in:

$$r_y = \frac{9\pi}{32} \left(\frac{K_I}{\sigma_t} \right)^2 \quad (3-38)$$

And the critical stress intensity factor for fracture propagation is calculated from:

$$K_{IC} = \sqrt{E \int_0^{\delta_c} \sigma(\delta_t) d\delta_t} \quad (3-39)$$

3.2.3 Statistical Fracture Mechanics

This theory is based on the assumption that strength of a material is a stochastic quantity, due to the random distribution of minute defects in the medium (Weibull, 1981). The strength, then, must be characterized by a probabilistic model, based on the results of a representative amount of sample tests. Most of the advances in this discipline are due to the pioneering work of Weibull (1939).

Statistical fracture mechanics is based on similar principles as those due to Griffith, i.e., multiple defects are responsible for intensification of applied loads. The main difference

is that the defects are not idealized as Griffith's cracks, but rather, they are of arbitrary shape and include softer inclusions in rock.

The statistical description requires a criterion for failure behavior of individual defects (local criterion) and another for total collapse of the sample (global criterion).

Ratigan (1981) applied statistical fracture mechanics to determine the probability distribution of brittle rock. The following sections are based on his work.

3.2.3.1 Global failure criterion

Two main categories are recognized:

- Single defect: Also known as weakest link criterion. Failure is due to collapse of the weakest component of the rock.
- Multiple defect: Total collapse occurs when multiple components fail.

The single defect criterion is the most popular, because failure of multiple components is extremely difficult to track (although microseismicity advances may soon make this criterion more feasible to be applied).

The global single defect criterion is stated as the probability of survival (P_s) of all the links of the material, as given by:

$$P_s = e^{[\sum_{i=1}^n \ln(1-f_i)]} \quad (3-40)$$

where f_i is the probability of failure of the i -th link.

The failure probability is replaced by a material function that accounts for flaws per unit region (volumetric or areal). This function is the local failure criteria, described next.

3.2.3.2 Local failure criterion

The local criterion is a function of stress, but it considers only the components that are normal to the defect (pure Mode I fracturing). This correlation is also known as the risk of rupture “B”, and is given by (Weibull, 1939):

$$B = \int_v \left[\frac{\sigma - \sigma_u}{\sigma_0} \right]^m dV \quad (3-41)$$

where: σ is a stress variable;

σ_u is the stress value below which rupture does not occur;

σ_0 is a scaling constant; and,

m is the Weibull modulus.

Since the model can be extended to 3D, the equation of the local failure criterion must be integrated along two angular directions and a volumetric region, as expressed by:

$$B = \int_V \left[\int_{-\pi/2}^{\pi/2} \int_{-\pi/2}^{\pi/2} \frac{F \cos(\phi) d\phi d\psi}{2\pi} \right] dV \quad (3-42)$$

Because the theory yields a probability of survival, a mean tensile strength formulation is devised by integration of the probability, and added to the minimum value below which

no rupture is observed:

$$\bar{T}_a = \sigma_u + \int_{\sigma_u}^{\infty} e^{-B} dT_a \quad (3-43)$$

The above equation is recognized as Weibull's three parameter model. Ratigan (1981) found this model to be appropriate for brittle rock. The three parameters referred to are σ_u , σ_0 and m . They can be derived experimentally; the larger the number of samples tested, the more representative the statistical distribution will be.

Notice that the σ is not a value, but rather a function that depends on the geometry of the problem. A typical replacement utilizes strain energy release, instead of a function based on stress distribution.

Whereas the parameters of Weibull can be derived from any configuration of tensile test, they can be extended to a different type of test, by replacing for the correct σ -function (and hence, risk of rupture) for that new configuration. Risk of rupture function for some of the most popular tensile tests can be found in Ratigan (1981).

The obvious advantage of the statistical description of rock strength is that scaling is made possible due to the generality of the distribution, which has to be integrated along the dimensions of the sample. Moreover, results of one series of tests can be extrapolated to a totally different configuration.

3.3 HYDRAULIC FRACTURE PROPAGATION MODELS

Clifton (1989) laid out the components of the most commonly utilized model for hydraulic fracture propagation. The hydraulic fracturing model assumes the propagation of a unique planar fracture, whose faces undergo tensional separation only.

This model commonly separates the crack surface into a major inner region dominated by deformation and a minor outer region dominated by the effects of stress intensity and crack propagation. The latter is referred to as near-crack-tip region, and its length is a function of the fracture perimeter 's'.

The criteria for crack advance in fracture mechanics is that once the stress intensity reaches a critical value at the tip, propagation will occur. Nevertheless, in the classical hydraulic fracturing model, this criterion is applied as critical width in the near-crack-tip region, instead. This is achieved by maintaining the stress intensity at its critical value, and finding the critical width from:

$$w_c = \frac{2(1 - \nu)K_{Ic}}{G} \left[\frac{2a(s)}{\pi} \right]^{1/2} \quad (3-44)$$

where w_c is the critical width at the near-crack-tip region;

ν is Poisson's ratio;

K_{Ic} is the critical stress intensity factor in Mode I.

G is the elastic shear modulus; and,

$a(s)$ is the length of the near-crack-tip region.

Thus, fracture propagates when the width at the near-crack-tip region is greater than the critical aperture:

$$w_a(s) > w_c \quad (3-45)$$

where $w_a(s)$ is the fracture width at the near-crack-tip region.

The critical stress intensity is taken as a material property that is determined in the lab, although numerous authors have proven it to be strongly scale-dependent (Valkó and Economides, 1997). The stress intensity factor is fixed at critical state by determining a propagation velocity that will produce this effect. In principle, this should be a trial-correction process to calculate the appropriate velocity. Nevertheless, since the dimensions of the problem are known, a volume balance for the next crack-size increment allows the derivation of the following expression to estimate velocity propagation (Gidley et al., 1989):

$$v = \frac{[\bar{q}_n - 2C_L d(\bar{p} - \bar{p}_f)] \Delta s - dV/dt}{(\bar{w}_d + 2C_S) \Delta s} \quad (3-46)$$

where the overbar sign indicates average values, dV/dt refers to the change in volume, and $C_{l,s}$ are the normalized and instantaneous leak-off coefficients, respectively.

In the form presented above, the equation is used as an “estimator” of the velocity required for the fracture surfaces at time t_0 , to increase the fracture width to the critical

condition of failure w_c . Thus, it indicates whether the crack velocity should increase or decrease during the next timestep to maintain critical width.

Hydraulic fracturing models from classic fracture mechanics theory –specifically from stress intensity approach- have not had major acceptance as compared to the classical hydraulic fracture theory. Predictions from fracture mechanics, such as increase of net treatment pressure with lower injection rates, have not been corroborated either in experimental or field procedures (Valko and Economides, 1997). This might be due in part that K_I characterization is difficult because it should reflect all the geometrical, loading, and fluid-solid interactions of the system (Whittaker, 1992), whereas interpretation of pressuring history tests, as carried out in hydraulic fracture calibration tests, is relatively straightforward.

Abou-Sayed et al. (1978) found solutions based on stress intensity theory, for a model consisting of a pressurized borehole in an infinite medium, with stresses σ_H and σ_h applied at the boundaries (Figure 3-8).

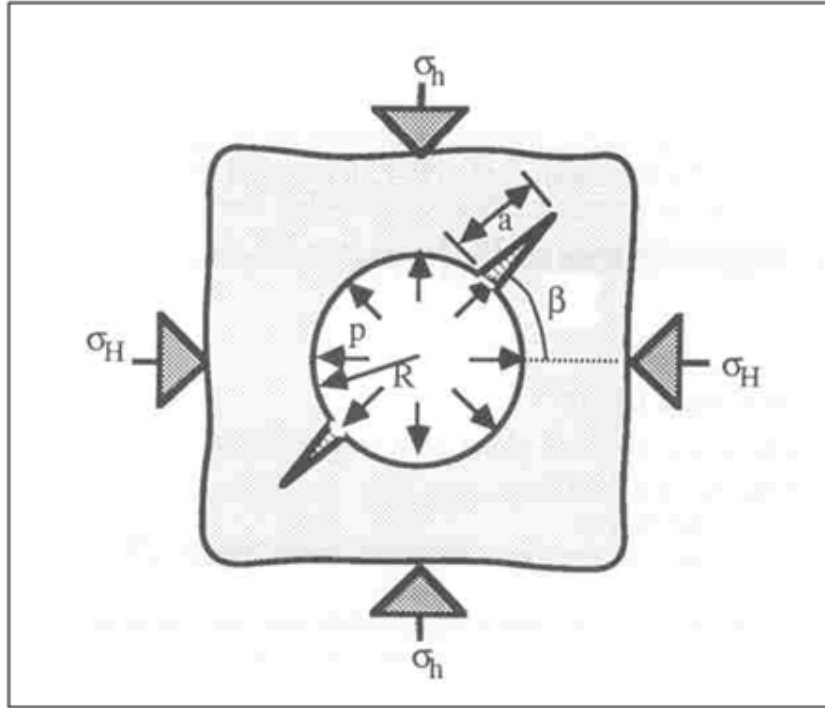


Figure 3-8. Abou-Sayed's model

The results of Abou Sayed's model, in comparison with Clifton's model, yield the following equivalence between fracture toughness and in situ tensile strength:

$$\sigma_T = \frac{K_{IC}}{f(a/R)\sqrt{\pi a}} \quad (3-47)$$

Thus, σ_T , as derived from stress intensity procedures, includes the effects of crack size and fracture toughness, whereas in Clifton's theory it depends on the nominal stress only.

Meanwhile, Rummel and Winter (1982) proposed the model depicted in Figure 3-9.

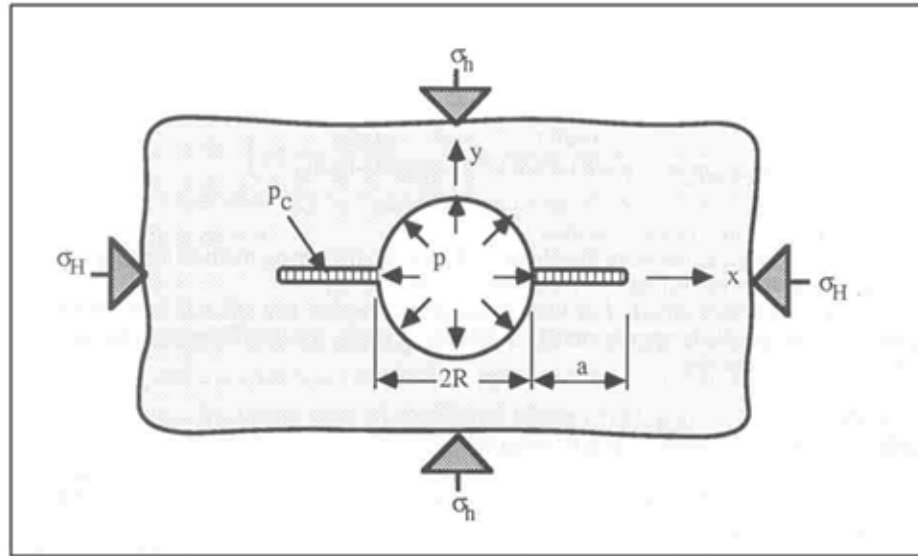


Figure 3-9. Rummel and Winter model

The methodology used followed the principle of superposition; the total stress intensity factors are equal to the addition of the individual stress intensity factors derived from each loading or pressure condition. As a result, the relation between Rummel and Winter model and Clifton's is given by:

$$\sigma_T = \frac{K_{IC}}{\sqrt{R[h(\beta) + h_c(\beta)]}} \quad (3-48)$$

Thus, unlike Clifton's, Rummel & Winter model predicts the influence not only of fracture size, but also the pressure distribution along the fracture, which is represented by the functions $h(\beta)$ and $h_c(\beta)$.

3.4 COMPARISON OF FRACTURE PROPAGATION MODELS

The theory of fracture mechanics describes the stress re-distribution due to the presence of a fracture in a body, the response of said fracture to stress changes, and the conditions

for its propagation once initiation has been achieved. Some relevant aspects of the fracture mechanics theory are as follows:

- Displacements related to fracture propagation can be envisioned as the combination of three fundamental fracture modes, namely, Mode I, Mode II and Mode III, as illustrated in Figure 3-3;
- The governing stress-strain relation can be linear, with varying degrees of influence of non-linearities due to plastic deformation ahead of the crack tip;
- The markedly different mechanisms of linear and non-linear behavior gives origin to the distinct theories of Linear Elastic Fracture Mechanics (LEFM), and Non-linear Elastic Fracture Mechanics (NEFM);
- LEFM assumes the plastic zone around the tip zone to be negligible for any practical effects, and fracture propagation is said to occur in a completely brittle fashion;
- In NEFM, the shape and effects of the plastic region immediately ahead of the crack tip are determined; beyond this boundary, LEFM applies.

The classical hydraulic fracturing model takes elements of the fracture mechanics theory, and couples them with the fundamentals of fluid flow inside the fracture and the mechanisms of leak-off towards the formation. Specifically, these models assume a main fracture that propagates in a Mode I fashion (pure tension), on a plane that is perpendicular to the minimum in situ stress, and it is governed by a linear stress-strain relation (i.e. brittle failure described by LEFM). Thus, hydraulic fracturing theory inherits one limitation from fracture mechanics as is the dominance of a single propagating fracture, and adds two more of its own on neglecting other possible modes of failure and

denying the influence of shear deformation around the fracture tip. Nonetheless, this theory has been proved time and again as an invaluable predicting tool in the design of hydraulic stimulation jobs in brittle rocks, for treatments initiated in the direction of the expected propagating plane. Recent development in microseismic monitoring has revealed, however, large cracking activity in the vicinity of the main propagating fracture, but not necessarily connected hydraulically with it. This seems to indicate that some of the energy provided by the injected fluid is spent in such events, and suggest the possibility that for some rock characteristics the extra-energy requirements become important, and the hydraulic fracture model would underpredict the treatment parameters and/or overpredict the fracture dimensions.

Statistical fracture mechanics does consider the probable effects of some other material defects in the rock. However, the sample size to characterize the parameters required for this type of models is unrealistically high.

4 NUMERICAL SIMULATION SETUP

A discontinuum technique (the Discrete Element Model, or DEM for short) was selected to model the solid part, because it allows evaluating the influence of minor scale features on the overall hydraulic fracturing behavior. Specifically, it allows tracking the different modes of fracturing (i.e. by shear or tension) that drive onset and extension of the macroscopic fracture, without making à-priori assumptions about the dominant mode. Although the small-scale mechanical properties of the modeled material may follow a linear elastic behavior, the combination of cracking modes yields a macroscopic fracture that is not necessarily linear-elastic.

In contrast, most conventional hydraulic fracturing models envisage the rock as a continuum, whose behavior conforms to the precepts of Linear Elastic Fracture Mechanics (LEFM). LEFM is usually applied under the assumption that the rock breaks in tension, which neglects the effect of shear fracturing. In addition, the continuum approach overlooks the effects of discrete, small-scale features, which may be especially important at the tip of the advancing fracture.

The continuum LEFM approach has been continuously and successfully applied in well consolidated, brittle rock; nevertheless, it is suggested that its inherent assumptions -with respect to the effects of shear cracking and minor scale features- are responsible for the discrepancies between predictive simulations and actual field observations, when applied to soft rock (Chudnovsky et al., 1996).

4.1 DEM OVERVIEW

As mentioned before, DEM was used to model the solid part. Indeed, DEM provides the means to model the behavior of solids, only. A complementary technique must be used alongside DEM, to provide for simulation of fluid flow. The Navier-Stokes (NS) version of the balance equations is used for this purpose. A discretized version of NS equations for porous media is solved in a regular grid, by means of Finite Differences (FD) techniques^x. Notice that the combination of NS with FD assumes the material as being continuous, whereas DEM conceptualizes it as being composed of discrete elementary particles. Nonetheless, fluid flow does not merit a comprehensive discontinuum formulation in this particular study; in the creation and propagation of a hydraulic fracture, there are no large-scale processes derived from minor scale properties of the fluid, nor is there any interest in any small-scale phenomena that may develop within the fluid. In other words, for the purposes of this dissertation, it was assumed that there are no small-scale features that are distinct of those of the fluid as a whole. Thus, the fluid behavior expected in hydraulic fracturing should fit nicely within the assumptions of continuum mechanics.

The code PFC3D^{®xi}-was used to build the numerical models of this dissertation. This program provides an implementation of DEM, as well as an optional fluid coupling algorithm based on the NS equations for porous media (Itasca Consulting Group, 2005a).

^x Alternative methods to couple fluid flow and DEM are summarized in Appendix A

^{xi} PFC3D[®] is proprietary software, generously provided by Itasca Consulting Group.

Currently, PFC3D[®] is a command-driven program. For this reason, simulations are performed by execution of scripts (i.e. text files) written in Itasca's proprietary programming language "Fish", which are invoked from within the software's user interface. The scripts developed to build the specimens, set-up the fluid/solid grids, and control execution of hydraulic fracturing simulations during this study, are included at the end of this chapter. The corresponding references to those routines are made throughout the text, where appropriate.

4.2 DEM THEORETICAL BACKGROUND (Itasca Consulting Group, 2005c)

Proposed by Cundall and Strack (1979), the Distinct Element Method (DEM) consists of generating a virtual specimen composed of particles^{xii} that interact with one another by means of a general contact law that is applied at the bonds of the contacting elements (Itasca Consulting Group, 2005b). Mechanical properties are specified for the particles and their bonds at the micro-level. The resulting assembly must mimic the response of the rock to force fields at the macro-scale, which is achieved by a calibration process. The specifics of the physical model and the numerical solution are presented next.

Thus, the DEM specimen in PFC3D[®] consists of a tri-dimensional assortment of spheres joined together by contact bonds, and contained within a set of enclosing walls. The physics of the ensemble is developed by interaction amongst the particles through the contacts. Thus, the physical model utilizes only two fundamental equations: (i) particles'

^{xii} The implementation of DEM in PFC3D[®] uses spheres as the elemental particles.

kinematics modeled by Newton's law of motion; and, (ii) their interactions at the contacts obeying the force-displacement law (soft contact approach).

Newton's laws of motion (at particles), are given by:

$$\mathbf{M}_i = I\dot{\omega}_i = \left(\frac{2}{5}mR^2\right)\dot{\omega}_i \text{ (rotation)} \quad (4-1)$$

$$\mathbf{F}_i = m(\ddot{\mathbf{x}}_i - \mathbf{g}_i) \text{ (translation)} \quad (4-2)$$

where: M is the torque, $[ML^2/T^2]$ ^{xiii};

I is the moment of inertia $[ML^2]$;

ω is the angular velocity $[1/T^2]$;

m is the particle's mass $[M]$; and,

R is the particle's radius $[L]$;

Subscript "i" is a free index that denotes the direction (x, y, z); and,

Dot(s) "·" on top of variables denote derivative(s) with respect to time.

^{xiii} Terms in square brackets refer to the dimensions of the parameter; as usual, M=Mass, L=Length, T=Time.

The force-displacement law (at contacts) has the general form:

$$F_i = -kU_i \quad (4-3)$$

where: F is the force [ML/T²];

k is the contact bond stiffness [units of force/L]; and,

U is the displacement [L]

If the boundary condition is a displacement value, the application of the equation reverses, i.e. the force-displacement law is applied first, and Newton's law follow. Time marching occurs through an explicit finite difference (FD) scheme. The procedure is illustrated schematically in Figure 4-1.

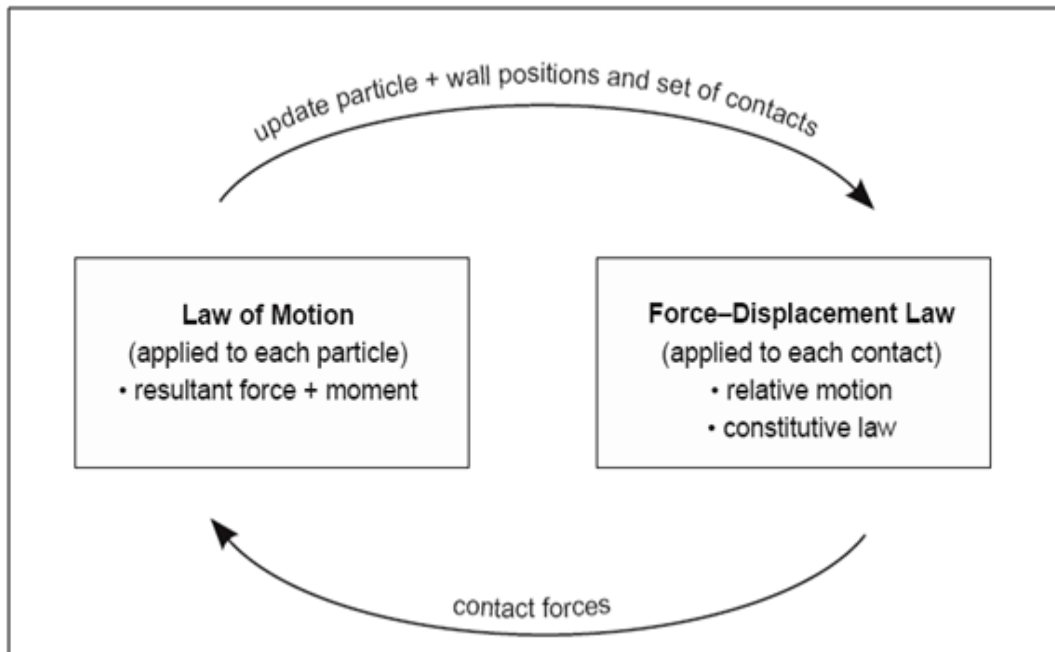


Figure 4-1. PFC3D® calculation process (Itasca Consulting Group 2005c).

4.3 DEM SPECIMEN DEFINITION

In a DEM specimen the macroscopic properties cannot be prescribed; they must develop naturally out of the interactions among the constituent particles. These interactions depend on the micro-properties assigned to particles and to contacts. After a finalized DEM-specimen was produced, the fluid grid was overlain on it, and the fluid cell properties specified.

The procedure to generate a mechanically calibrated DEM sample was outlined by Potyondy and Cundall (2004). A set of scripts within the PFC3D framework (Itasca Consulting Group, 2005d) implement their main ideas.

The complete suite of data required for the definition of a bonded DEM assembly is listed in Table 4-1.

The necessary steps towards creating a stable ensemble are (Itasca Consulting Group, 2005d): 1) generation and compaction of the spheres' arrangement; 2) installation of the isotropic stress throughout the sample; 3) modification of particle sizes to achieve at least three contacts with neighboring particles; and, 4) finalization of the ensemble.

Table 4-1. Input Parameters for the creation of a contact bonded material

	PARAMETER, UNITS
GEOMETRY	Sample Length, m
	Sample Width, m
	Sample Height, m
	Minimum Ball Radius, m
	Ball Size Ratio, dimensionless
BALL	Ball density, kg/m ³
	Ball-Ball Contact Modulus, Pa
	Ball Stiffness Ratio (k_n/k_s), dimensionless
	Ball Friction Coefficient, dimensionless
CONTACT	Contact-Bond Normal Strength (mean), Pa
	Contact-Bond Normal Strength (std.dev.), Pa
	Contact-Bond Shear Strength (mean), Pa
	Contact-Bond Shear Strength (std.dev.), Pa
OTHER	Wall Normal Stiffness Multiplier, dimensionless
	Isotropic Stress, Pa
	Number of Contacts for non-floater

It is important to remark that an individual sphere represents the smallest entity that can be deformed^{xiv}, but that would not be broken in the simulated experiment; hence, a sphere does not need to conform to the rock's grain size, and neither does their distribution in the virtual specimen, because the hydraulic fracture dimensions are much larger than the individual grains. Although each particle size can be selected from a Gaussian distribution, for example the real grain distribution, it was estimated that an appropriate configuration for the simulations of this dissertation was that with a uniform distribution of particles, with a radius of 0.5 cm. This size is small enough as to not to dominate the

^{xiv} Deformability is included by way of differing directional stiffness for each sphere, but the original spherical shape is maintained throughout the simulations.

path of fracture extension. In other words, in the unlikely event that a small deviation from the “real” propagation direction occurs around one particle due to its size, it will reach only 0.5 cm of error. This deviation is expected to self-correct after more simulation timesteps have gone by, due to the uniform application of forces in the boundaries. A drawback of the specimen with same-size particles is that it is not optimized for convergence speed because the size selection is based on the smallest particle that will not introduce errors in the calculation. In an analog continuum-model grid, this would be equivalent to reducing the size of all cells to the minimum size required, instead of doing local refinements. Probably, a single sizing scheme would not have been the optimum for the many simulations planned in this study; for this reason, the uniform, small spheres distribution was used.

Note that a prescribed porosity can be achieved either (i) by specification of a size distribution that results in such porosity, or; (ii) by forcing overlapping of elementary spheres until the prescribed porosity is reached. Both procedures are somewhat impractical to model low porosities^{xv}. The former calls for size distributions featuring considerable skewness towards very small particles. The timestep is greatly reduced if there is a considerable spread of particles’ sizes, because it will be governed by the size of the smallest particles. Thus, high standard deviation and markedly skewed distributions result in an unreasonable high number of simulation cycles. Meanwhile, the former approach generates repulsive forces due to the overlapping of the particles. The

^{xv} The porosity of a uniform packing of spheres hovers around 35%. The hydraulic effect of porosities under 30% were assessed by the alternative method proposed in section 4.6 of this dissertation.

larger the overlapping needed to reach small porosities, the larger the induced repulsive forces between particles. These force distribution affect the numerical results and, in critical cases, compromise the integrity of the initial specimen.

For the above reasons, the created specimens' porosity was neither matched nor prescribed. Instead, the net hydraulic effects of the desired porosity were matched by scaling of the flow properties density and viscosity. The scaling rules are described in section 4.6, later in this chapter.

4.4 MECHANICAL TESTING AND CALIBRATION^{xvi}

Shear and normal stiffness values are found from the ball-ball contact modulus and ball stiffness ratio (Itasca Consulting Group, 2005d), according to the following relations:

$$k_n = 2E_c(2\tilde{R}) \quad (4-4)$$

$$k_s = \frac{k_n}{(k_s/k_n)} \quad (4-5)$$

where k_s , k_n are shear and normal stiffness, (k_s/k_n) is their ratio, and E_c is the ball-ball contact modulus.

^{xvi} Mechanical testing and calibration was achieved through the use of scripts provided within the “Augmented Fishtank” (Itasca Consulting Group, 2005d).

E_c is linearly related to –and usually larger than- the overall elastic modulus. Hence, the real sample modulus can be used as an initial E_c guess and, upon testing of the virtual sample, an accurate estimate of E_c can be found by establishing a simple linear relation between the initial E_c guess, E obtained from virtual testing, and the target E .

Figure 4-2 compares the stress-strain curve of unconfined testing of virtual against real samples. For this dissertation, matching of properties is focused in deformability and strength before peak loading is reached. Theoretically, post-peak behavior could also be matched. However, a formal procedure has not yet been outlined, due to the complicated interaction between the many micro-properties, and because data for this section of the test is not usually provided.

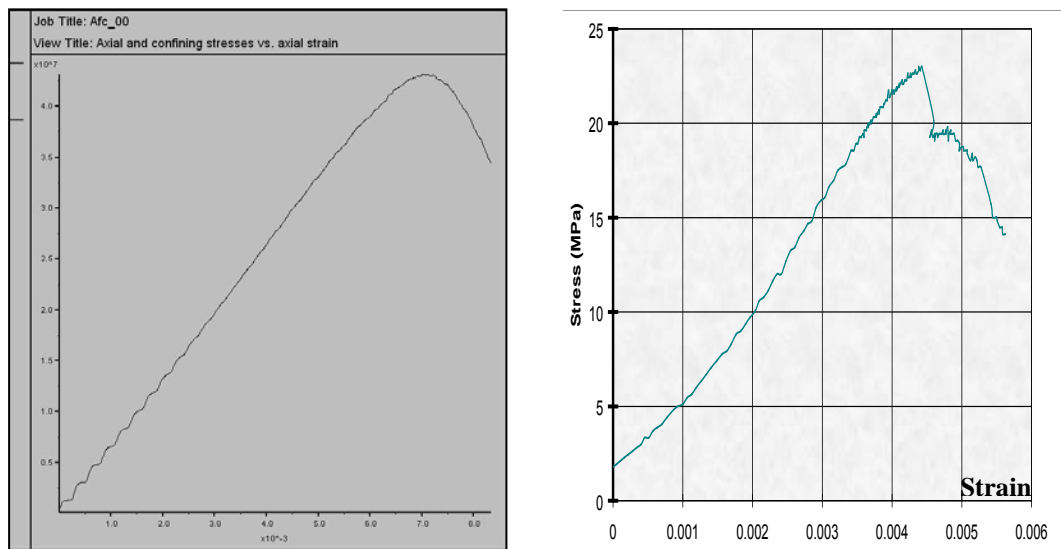


Figure 4-2. Unconfined testing of the virtual (left side) and real (right side) samples

4.5 FLUID COUPLING^{xvii}

The fluid coupling scheme in PFC3D[®] solves the continuity and Navier-Stokes correlations for each cell of the fluid grid that is superimposed onto the DEM specimen (Kawaguchi et al., 1992). The resulting driving forces are then applied to the particles as body forces.

The coupling implementation is schematically illustrated by the algorithms of Figure 4-3.

^{xvii} The fluid coupling scheme, provided as an optional feature in PFC3D, was used to assess the mechanical response of the specimen to fluid flow (Itasca Consulting Group, 2005a).

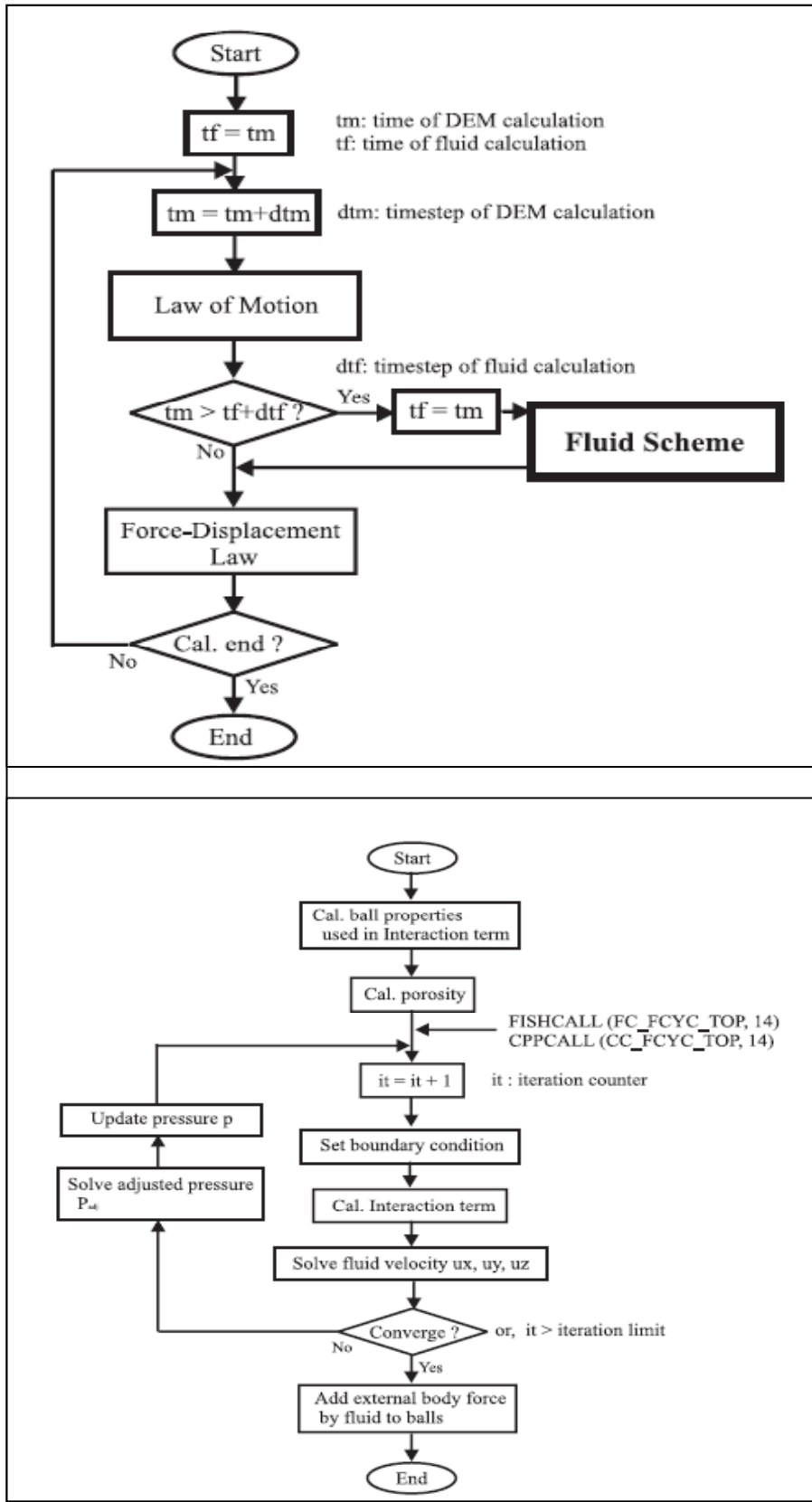


Figure 4-3. Fluid flow implementation in PFC3D (Itasca Consulting Group 2005a).

The pressure and velocity vector of fluid in each cell are calculated by applying the Semi-Implicit Method for Pressure Linked Equations (SIMPLE) algorithm (Patanker, 1980).

4.6 FLUID PROPERTIES CALIBRATION

The distinct element is prescribed to be the minimum size that captures correctly the interactions that are being investigated. Thus, the size distribution of the virtual specimen elements does not have to reflect the rock's real grain size distribution. Indeed, trying to replicate low values of porosity may result in impractical simulation times, because as porosity goes towards smaller values, the grain size distribution must exhibit larger standard deviation over the average particle diameter (assuming a clean rock, without an important content of material that impairs porosity); highly disparate sizes causes the timestep to decrease, given that the DEM implementation used here consists of a first order, explicit solution of Newton's second law.

As a result of the DEM specimen exhibiting an element size distribution that is different of the rock's grain size distribution, the relation between pressure drop and fluid relative velocity does not match the rock's hydraulics: for the virtual specimen, higher porosity values imply lesser pressure drops, as compared to the real rock. In this work, this mismatch in hydraulics was overcome by calibration factors that modify the fluid flow parameters of the specimen, according to Ergun's Law:

$$\frac{\partial p}{\partial x} = - \left(150 \frac{(1 - \varphi)^2}{\varphi^3 d_p^2} \mu u_{x0} + 1.75 \frac{(1 - \varphi)}{\varphi^3 d_p} \rho_f u_{x0}^2 \right) \quad (4-6)$$

$$= -(C_1 \mu u_{x0} + C_2 \rho_f u_{x0}^2)$$

where, $\frac{\partial p}{\partial x}$ = pressure change in specific direction;

μ = fluid viscosity;

ρ_f = fluid density;

u_{x0} = apparent relative velocity between fluid and particles;

φ = specimen porosity; and,

d_p = particle diameter.

In the above equation, C_1 corresponds to the inverse of permeability (i.e. $1/k$) for the virtual specimen, according to Carman-Kozeny correlation, with a coefficient of proportionality $1/c = 150$, as follows:

$$C_1 = 150 \frac{(1 - \varphi)^2}{\varphi^3 d_p^2} = \frac{1}{k} \quad (4-7)$$

Observe that permeability depends on the virtual specimen parameters, which are likely different of those of the real rock, as discussed before. Thus, in order to obtain the same net effect of the hydraulic properties of the rock, the above relation is multiplied by a

calibration factor and equated to the rock permeability:

$$\left[\frac{150(1-\varphi)^2}{\varphi^3 \bar{d}_p^2} \right]_S * F_K = \left[\frac{1}{k} \right]_R \quad (4-8)$$

where F_K is the calibration factor, and sub-indices S, R indicate whether the variables inside the brackets correspond to the virtual specimen or the real rock, respectively.

Because rock permeability is a known parameter, the calibration factor F_K is obtained from the above relation, and results in:

$$\rightarrow F_k = \left[\frac{\varphi^3 \bar{d}_p^2 d}{150(1-\varphi)^2} \right]_S * \left[\frac{1}{k} \right]_R \quad (4-9)$$

This concludes the calibration of the first term C_1 , of Ergun's correlation [Eq. (4-6)]. Now, the contribution of the second term C_2 , as given for the specimen, must match the contribution of the properties of the real reservoir rock. Thus, a multiplying factor F_t must be derived, according to the relationship:

$$\left[1.75 * \frac{(1-\varphi)}{\varphi^3 \bar{d}_p} \right]_S * F_t = \left[1.75 * \frac{(1-\varphi)}{\varphi^3 \bar{d}_p} \right]_R \quad (4-10)$$

Using again Carman-Kozeny correlation for the real rock, the permeability is expressed as a function of porosity and particles' size, as follows:

$$\left[\frac{150(1 - \varphi)^2}{\varphi^3 \bar{d}_p^2} \right]_R = \frac{1}{k} \quad (4-11)$$

Equating for d_p and replacing in Eq. (4-10), results in:

$$\left[\frac{(1 - \varphi)}{\varphi^3 \bar{d}_p} \right]_s * F_t = \left[\frac{(1 - \varphi) * \varphi^{3/2}}{\varphi^3 \sqrt{150 * k} (1 - \varphi)} \right]_R$$

$$\rightarrow F_t = \frac{\varphi_s^3 \bar{d}_{p_s}}{\varphi_R^{3/2} \sqrt{150 * k}} \quad (4-12)$$

In practice, these terms were included by multiplying the viscosity times F_k and the density times F_t , which can be thought of as a scaling of viscosity and density to match the hydraulic properties of the porous media being simulated. The reason for this can be deduced from Eq. (4-6): The first term of Ergun's equation is multiplied by viscosity, and the second one by density. So, by introducing the calibration factors at these places, the pressure drop of the specimen should match those of the rock.

Finally, notice that permeability and porosity of the rock must be supplied as input data.

4.7 FLOW GRID DEFINITION

The script file “Fl_Inject.DVR” was developed to control the installation of the flow grid onto the DEM specimen, to set all fluid-related variables and boundary/initial conditions, and to initiate the simulations. This script starts by calling a confinement procedure “Confine.DVR”, which installs prescribed stresses at the boundaries, and initializes

simulation monitoring utilities for all parameters NOT related to the fluid. Then, the flow injection configuration file “InjThruPerf.DVR” is invoked; the flow grid, fluid properties, and fluid-related monitoring utilities are defined and installed from within this file.

Therefore, in order to run a fluid injection simulation, the variables in the Fl_inject.DVR and InjThruPerf.DVR are set, and the Fl_inject.DVR is invoked from PFC3D’s command prompt.

Table 4-2 lists the properties and facilities that are installed by each script file^{xviii}.

Table 4-2. List of variables within the driver

Fl_Inject.DVR	_Confine.DVR	InjThruPerf.DVR
et3_kn[x,y,z]fac: Wall stiffness variables.	et3_wallstiff: Function that sets the wall stiffness	All variables related to the fluid scheme are set here.
et3_ws[x,y,z] variables: Stress at the boundary	et3_seattriax: Applies initial stresses at the wall boundaries	
p_vel variable: Max. velocity in the boundary walls	crk_init: The crack tracking package is installed	
et3_servo_1 = 1: Activates servocontrol using only one wall.	History log for: cracks, wall derived stresses/strains, specimen derived stresses/strains, and energies are initialized.	
_Confine.DVR and InjThruPerf.DVR are invoked		

The fluid flow discretization grid is superimposed onto the DEM specimen. The grid dimensions, fluid characteristics and boundary conditions (given as pressure or velocity) constitute the components of the fluid flow framework; the specific required input

^{xviii} The script files are presented at the end of this chapter.

properties are listed in Table 4-3.

Table 4-3. Fluid flow input information

Geometry	Fluid	Boundary Condition
Depth	Density	Velocity, pressure, stresses at the boundary, etc.
Height	Viscosity	
Width		
No. of cells in X-direction		
No. of cells in Y-direction		
No. of cells in Z-direction		

4.8 SIMULATION MONITORING^{xix}

A list of monitoring variables and their description is provided in Table 4-4.

Table 4-4. Parameter tracking list

PARAMETER	VARIABLE NAME	DESCRIPTION
Cracks	crk_num, crk_num_cnf, crk_num_csf,	Total number of cracks, and total cracks by contact type broken (normal contact bond, shear contact bond)
Strains	et3_wexx, et3_weyy, et3_wezz, et3_wevol.	Strains in all directions, and volumetric strain
Stress	et3_wsxx, et3_wsyy, et3_wszz,	Stress in all directions
Energy	Boundary energy, friction energy, kinetic energy, strain energy	Energy on the specimen by the walls (boundary), energy dissipated by sliding (friction), kinetic energy of all particles (kinetic), strain energy at all contacts (strain).
Fluid	frate, ftime, et3_fl_InjRate, et3_fl_InjPress	Flow rate, elapsed time, injection rate, injection pressure

^{xix} All variables' histories are defined during the flow grid definition, which was discussed in the last section.

4.9 SIMULATION SETUP

The simulations consisted in the injection of a fluid until pressure built-up is enough to create and propagate a fracture into the virtual rock. Fracture propagation was tracked in terms of broken bonds under the action of the fluid. Bond breakage (i.e. cracks) was logged according to their fracturing mode as either shear or tensile cracks. The experiments were designed as to assess the virtual rock fracturing response to changing mechanical parameters and stress boundary conditions of the overall system.

4.9.1 Model Genesis

A “base-case” sample was created. This sample was used to do a control run that was compared to the results of other simulations which featured specimens with a wide range of mechanical parameters and/or boundary conditions.

As discussed earlier, the creation of a DEM assembly consists of four stages: 1) generation and compaction; 2) installation of the isotropic stress; 3) elimination of floaters; and, 4) finalization of the specimen. The creation of the base-case specimen is defined by the variables listed in Table 4-5.

The ‘Ball Size Ratio’ parameter being equal to 1 indicates that all spheres have the same dimension. An optimized size distribution could be envisioned, in which smaller particles would be located in areas where the major changes are expected (i.e. similar to refinement in a conventional continuum grid). Nevertheless, since different mechanical properties and stress configurations were evaluated through various simulations, the optimal distribution might have been different for each case run. Consequently, the

approach in this dissertation was to create uniform same size particles that are small enough to capture the fracturing mechanisms. In this way, the results are not compromised by the size of the particles, although execution time is not optimized; in other words, a distribution with coarser sizes in the regions where no fracturing and lesser stress changes are expected would result in shorter execution times. However, due to the multiple conditions that were evaluated in different simulations, the optimal size distribution would have been most likely different between cases

Table 4-5 . Input information for the base-case specimen

PARAMETER, Units	Value
Sample Length, cm	10
Sample Width, cm	10
Sample Height, cm	10
Minimum Ball Radius, cm	0.25
Ball Size Ratio ^{xx} , dimensionless	1
Isotropic stress, Pa	3×10^5
Min. number of contacts per sphere	3
Type of bonds	Contact bond

4.9.2 Mechanical Calibration

The base-case sample was designed as to exhibit a macroscopic mechanical behavior characterized by a linear elastic stress-strain relation, with elastic modulus of 6 GPa. (or 8.7×10^5 psi, approximately), and uniaxial compressive strength (UCS) of 25 MPa. (or 3.6×10^3 psi, approximately). According to Deere and Miller's classification, these

^{xx} Ball size ratio = R_{\max}/R_{\min} , maximum to minimum radii permissible for the spheres.

properties fall onto the range of very low-strength rock, as depicted in Figure 4-4.

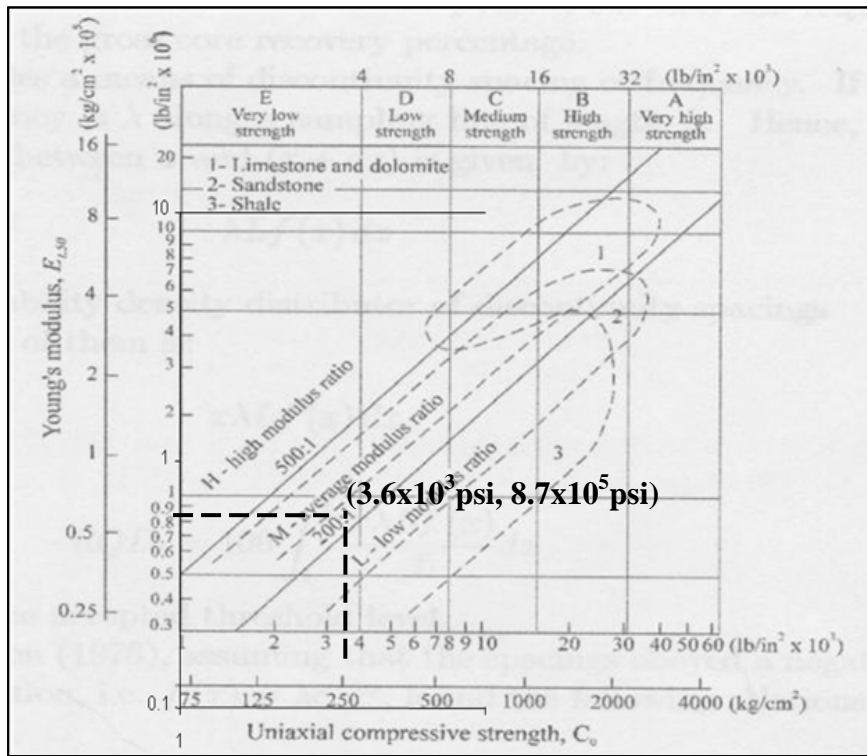


Figure 4-4. Deere and Miller's classification of base-case rock specimen.

The micro-properties derived from virtual testing of the DEM sample are listed in Table 4-6.

Table 4-6. Micro-properties derived from virtual mechanical testing.

PARAMETER, UNITS	VALUE
Ball density, kg/m ³	2,630
Ball-Ball Contact Modulus, Pa	7x10 ⁹
Ball Stiffness Ratio (k _n /k _s), dimensionless	1
Ball Friction Coefficient, dimensionless	0.5
Contact-Bond Normal Strength (mean), Pa	1.0x10 ⁷
Contact-Bond Normal Strength (std.dev.), Pa	0
Contact-Bond Shear Strength (mean), Pa	2.0x10 ⁷
Contact-Bond Shear Strength (std.dev.), Pa	0

Virtual testing of the DEM sample with the properties reported above yield the plot depicted in Figure 4-5.

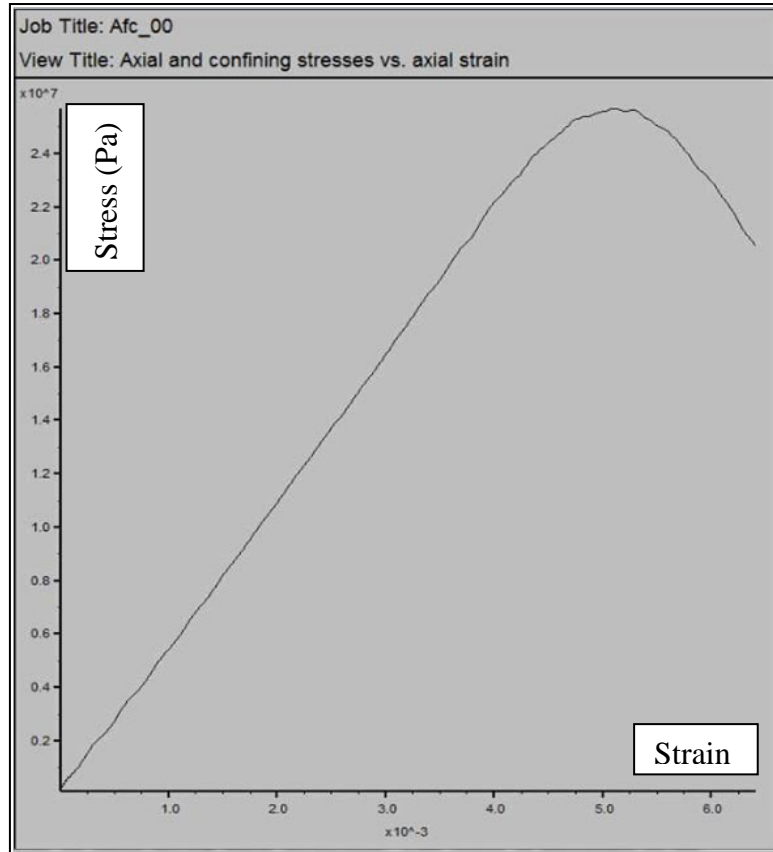


Figure 4-5. Unconfined testing of the virtual sample.

4.9.3 Boundary Layer

The simulation consisted in the injection of a steady flow into one end of the DEM sample in order to create cracks and propagate a fracture away from the injection point. The injection velocity was increased in short intervals to accelerate the process of crack propagation (preliminary tests showed that 3000 mechanical cycles were enough for the pressure disturbance to be transmitted throughout the sample). The criterion for test termination was the rupture of 1000 inter-granular bonds (cracks); it was determined that with this number of cracks the fracture was still sufficiently far from the boundaries, to be

unaffected by them (i.e. no boundary effects have been felt, yet). Preliminary simulations showed that if the enclosing walls were used as outer boundaries, sliding of the entire ensemble occurred, because at the time of this study bonding between the walls and the spheres was not allowed in PFC3D[®]. Thus, routines to replicate the original DEM sample were built, but with the inclusion of an extra boundary layer around it^{xxi}, as illustrated in Figure 4-6; the boundary conditions can be readily prescribed on these new boundary elements.

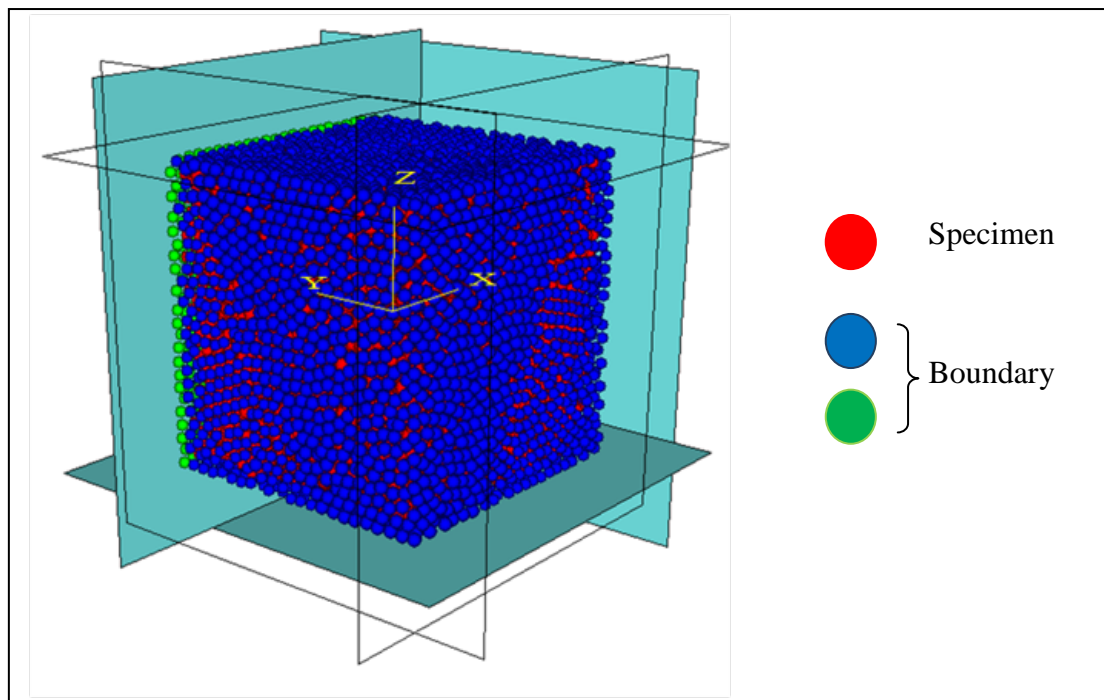


Figure 4-6. Group of particles acting as boundary layer.

^{xxi} The routines that control installation of the boundary layer were included in the file “HandleBdry.FIS”. The modified specimen generation file was named “AfcWithBL.DVR”. Both files are presented at the end of this chapter.

The color convention in the above figure is as follows:

Red encompasses the main ensemble particles, representing the formation being simulated; blue and green correspond to the boundary layer group of particles.

4.9.4 Flow Grid

The flow grid was superimposed on the DEM-sample. The parameters that define it are its dimensions, and number of cells along each direction. The fluid is assumed to be Newtonian (water, in the base-case), and its properties are density and viscosity. The boundary conditions consist of the injection velocity, and the stresses applied at the boundary. Description of the fluid set-up is summarized in Table 4-7. A graphical depiction is given in Figure 4-7.

Table 4-7. Fluid set-up information.

Geometry	Fluid (water)	Boundary Conditions
Length: 10 cm	Density: 1,000 Kg/m ³	Injection rate: 7.5e-6 m ³ /s + 1e-6 m ³ /s
Height: 10 cm	Viscosity: 1 cp	Constant stress X-dir., Sxx = 500 psi
Width: 10 cm		Constant stress Y-dir., Syy = 1,000
Cells X-direction:		Constant stress Z-dir., Szz = 1,000 psi
Cells Y-direction:		
Cells Z-direction:		

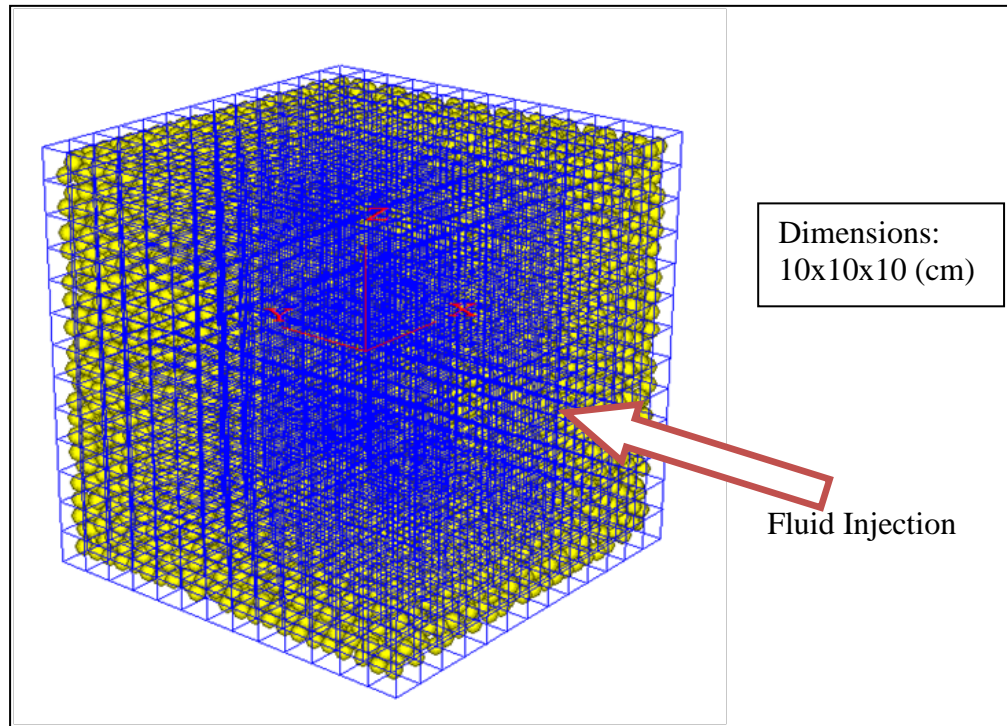


Figure 4-7. Fluid grid depiction

4.9.5 Supporting Algorithms

Table 4-8 summarizes the main function of the various programming scripts that were written to generate the framework for the simulations of this dissertation, and to guide their execution.

Table 4-8 Brief description of scripts used to set-up and execute the simulations

SCRIPT FILENAME	MAJOR FUNCTION
AfcWithBL_Run#.DVR	Solid specimen definition
Fl_Inject_Run#.DVR	Fluid definition (simulation execution is launched from this driver)
Confine.DVR	Confining stress installation
HandleBdry.FIS	Extra-layer functions
InjThruPerf.FIS	Injection control functions

In the table, the suffix “.DVR” refers to driver files, whilst those with the extension “.FIS” are fish function files. The driver files contain commands that make part of the set of keywords that can be interpreted by PFC3D. These drivers are mostly used to call sequentially the functions created in FISH that control simulation execution, and to supply input parameters. The FISH files are the actual programming routines that initialize, execute and monitor the simulation, while carrying out all related mathematical calculations (e.g. monitoring of parameters’ histories during a specific simulation).

The algorithms implemented in the FISH scripts are presented in the Appendix B, at the end of this document.

5 DISCRETE ELEMENT HYDRAULIC FRACTURING SIMULATION

RESULTS

The discrete element specimen described in the last chapter underwent a series of simulations to assess the influence of varying material properties and boundary conditions on the fracturing behavior of the specimen. The results were evaluated in terms of eight parameters, namely: injection pressure vs. rate; fraction of shear cracks vs. pressure; pressure vs. volumetric strain; shape of the induced cracks ‘cloud’; location and magnitude of compressive, tensional, and shear contact forces; and particles’ displacements. Note that, except for the pressure plots, all parameters correspond to discrete measurements, which are consistent with the discontinuum modeling technique that was used in this study. These amounts permit to discern any mechanisms that have been overlooked by conventional continuum approaches, in which properties are averaged over larger sectors encompassing groups of particles. Conversely, pressure vs. volumetric strain was used as the only macroscopic measure allowing comparisons with the linear constitutive model that is commonly used to study hydraulic fracturing.

The examined mechanical properties were made up of combinations of uniaxial compressive strength (UCS) and Young’s modulus (E). Because these properties are macroscopic, they cannot be prescribed directly in a discrete model. Instead, the microscopic parameters were set so that upon virtual uniaxial testing of the specimen, proper values were obtained.

As described in the previous chapter, the fluid is modeled by a conventional continuum

grid. The fluid properties evaluated were density and viscosity, which were prescribed directly at the definition stage of the simulations.

Evaluation of boundary conditions concerned the state of stress at the boundaries^{xxii}. Evaluation of the stress field effects was performed by changing the net stresses and the net difference between the maximum and minimum stresses, in two sets of simulations: the first set assessed the effect of horizontal and vertical stress anisotropy by varying the intermediate stress from being equal to the maximum to being equal to the minimum stress^{xxiii}; the second set of simulations evaluated the effect of the deviatoric stress by changing the difference between the minimum stress and the maximum one (stresses orthogonal to the minimum stress were maintained equal).

The effects of different mechanical properties and stress conditions on the simulated hydraulic fracture are presented next.

5.1 METHODOLOGY

A base-case was built to be used as a yardstick for subsequent simulations. General characteristics of the base-case were:

^{xxii} The stress direction convention used defined one principal direction in the same orientation as injection (y-direction), the minimum stress in the x-direction, and the vertical stress in the z-direction.

^{xxiii} Horizontal stress anisotropy was evaluated by varying the y-stress from a maximum value equal to z-stress, to a minimum value equal to x-stress; whereas vertical stress anisotropy was evaluated by varying z-stress from a maximum equal to y-stress, to a minimum value equal to x-stress.

- The mechanical properties corresponded to a very low strength rock, according to the Deere and Miller classification;
- The in situ stress was defined by a biaxial stress condition, in which stresses in the y- and z-directions were equal and greater than the stress in the x-direction^{xxiv};
- Constant boundary stress conditions were maintained during the simulation; and,
- Fluid injection was along the y-direction.

Specific and complete details of the base-case were given in last chapter.

A set of simulations was aimed to assess the effects of changing an individual property or boundary condition, on the fracturing behavior of the virtual specimen. When a mechanical property was evaluated, the other properties and stress conditions of the base-case were used; conversely, when the evaluation corresponded to a change of a stress condition, the rest of the base-case parameters were used. The simulation results were then compared against the results of the base-case simulation. In a few cases, it was necessary to modify slightly some additional property or boundary conditions of the base-case to make the comparisons viable. Any such modifications are reported in the text, where appropriate.

The cracks formed a cloud around the propagating fracture. It was observed that cracks at the beginning of the simulations were created by detachment of particles from the fixed injection boundary. At one thousand cracks, the cloud had progressed deep into the rock

^{xxiv} i.e. y and z correspond to the maximum and intermediate stresses, whilst x correspond to the minimum stress.

and was free of this boundary effect. Thus, the creation of one thousand cracks was the criterion to terminate the simulation.

Some simulations became unstable, causing the specimen to disintegrate; for these cases, the extent of the fracture analyzed consisted of a lower value of cracks formed, sometimes considerably less than one thousand.

The cause of simulation instability is related to the selection of an inappropriately short timestep for the fluid as compared to the timestep for the solid mechanical calculation. This caused large fluid pressure buildup before proceeding with a solid computation, which resulted in excessive forces applied to the particles at once and the subsequent specimen disintegration.

Figuring out adequate timesteps for each unstable simulation was considered impractical due to the vast number of conditions that were tested. In addition, the used constant timesteps worked fine for a number of simulations that were sufficient to establish valuable comparisons.

The results are presented in terms of the following parameters: i) curves of injection pressure vs. rates; ii) curves of crack number and type vs. injection rates; iii) curves of injection pressure vs. volumetric strain; iv) location and type of cracks induced by the injection; v) contact forces in the specimen, including compressive, shear, and tensional types, and; vi) displacement of particles in the vicinity of the injection point. The last three parameters require some explanation:

- Location and type of cracks: the agglomeration of cracks around the propagating fracture is depicted for selected cases. A crack is represented by a circle that is tangential to the contact broken by the crack; i.e. the crack is perpendicular to an imaginary line through the centroids of the previous conjoined particles. Normal cracks are represented by blue circles and shear ones by red circles. An illustration of the cracks location and the conventions used is presented in Figure 5-1.

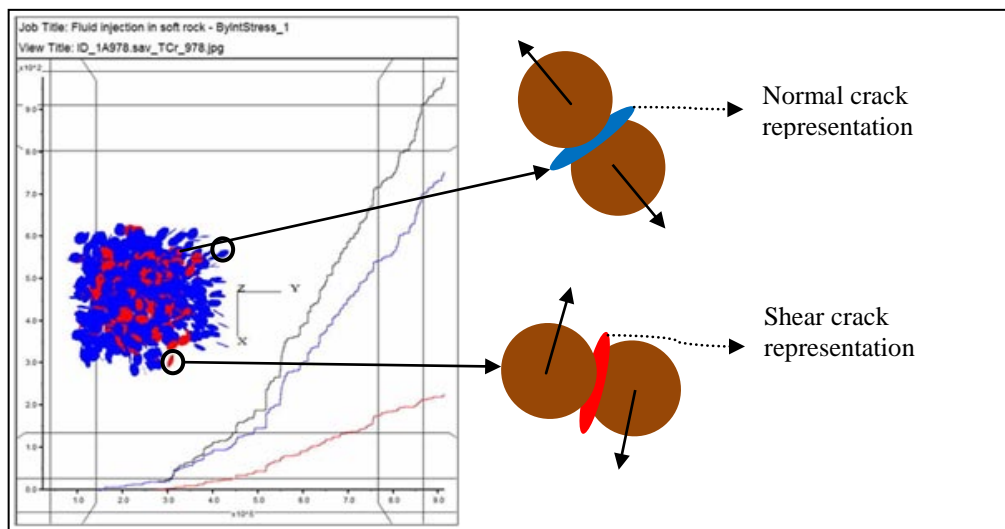


Figure 5-1 Cracks representation

- Contact forces: The force between two particles is represented by a rectangular bar across them, with their thickness being proportional to the force magnitude. Naturally, force chains can form between more than two consecutive spheres, and the bars appear as a continuous line composed of segments of varying thickness. Compressive forces were graphed in green color, shear forces in red, and tension forces in blue. An example of the compressive forces in a specimen is depicted in Figure 5-2.

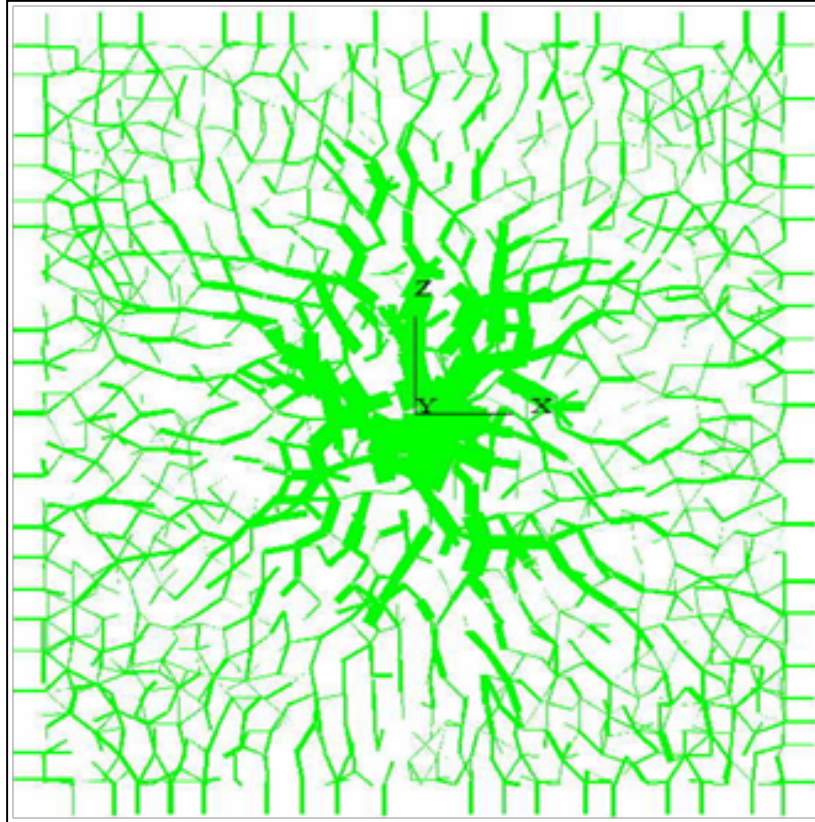


Figure 5-2 Representation of compressive forces chains

- Displacements: Relative particle displacements are represented by vectors.

The above parameters –cracks, forces, and displacements- are presented on three orthogonal planes, or views, namely, back, top, and side. All plots have been normalized, i.e. all plots are in the same scale to facilitate comparisons.

5.2 MECHANICAL PROPERTIES EFFECTS

Specimens with different uniaxial compressive strengths (UCS) or Young's modulus (E) values were generated to evaluate the effect of their varying properties on the hydraulic fracturing character. Runs 1 to 5 corresponded to numerical hydraulic fracturing testing of specimens with monotonically increasing UCS values (Run 1 is the base-case). Runs 6

to 9 correspond to specimens with varying E values; runs 6 and 7 had increasing E values, whereas runs 8 and 9 were for decreasing E values. The exact values of mechanical properties are reported in Table 5-1. The suffix letter ‘A’ identifies the stress boundary condition equivalent to that of the base-case (see previous chapter).

Table 5-1 Mechanical properties of the specimens constructed for the simulations

Run ID	UCS, ($\times 10^3$) psi	E, ($\times 10^6$) psi
Base-case (Run1A)	3.8	0.83
Run2A	5.0	0.83
Run3A	7.0	0.83
Run4A	10.0	0.83
Run5A	13.0	0.83
Run6A	3.8	1.20
Run7A	3.8	1.80
Run8A	3.8	0.60
Run9A	3.8	0.40

5.2.1 Uniaxial Compressive Strength (UCS) (Runs 2A to 5A)

Plots of pressure vs. flowrate show that all UCS runs fall onto the same line. However, in order to generate a fixed number of total cracks (~1000), the higher UCS specimens require a larger pressure buildup. For instance, the difference between Run2A and the base-case (Run 1A) is about 13%, as depicted in .

Probably due to the excessive pressure increase, the corresponding elastic energy stored, and the sudden energy release when the bonds broke (cases 3A through 5A) failed catastrophically when much less than one thousand cracks had been created. Nonetheless, the pressure and rate for these cases had already exceeded those for the creation of one thousand cracks in the lower UCS cases. This tendency is expected: UCS is defined by

the specification of tensile and shear strengths of the contact bonds^{xxv}; thus, these micro-parameters determine the amount of tensile/shear load that can be sustained by an individual bond; and, hence, stronger samples require larger pressures before a crack is formed. The effect of increasing UCS is that initially bonded particles can be separated further before bonds are broken (albeit considerable additional pressure is required). The extra-separation provokes larger concentration of stresses, since the deformability parameters, Poisson's ratio and Young's modulus, were maintained constant for all these specimens. Once rupture conditions are reached, the release of stored energy is enough to send particles moving beyond the boundaries of the specimen, and instability occurs.

A plot of number of cracks vs. flowrate showed that at the same rate, more total cracks have been created in the lower UCS specimen. In addition, the relation of shear to normal cracks is greater in the low UCS specimens (see). The significance of the higher fraction of shear cracks is that, even though lesser pressure is required to reach a number of total cracks, the shear ones are isolated from the main fracture; and, hence are expected to be hydraulically disconnected from it. Thus, the higher UCS specimens may require a higher pressure input to create a specific number of cracks, but they are more efficient at generating hydraulic connectivity. These and some additional observations are included in .

^{xxv} In order to achieve higher UCS specimens, both micro-strength parameters (shear and tensile strengths) were increased in similar proportions, but always maintaining shear strength greater than normal strength by a factor of 2. A change on this factor, or on the shear/normal strength relation, may obscure the UCS effects being analyzed in this section.

At the same pressure, the specimens with higher UCS exhibit less volumetric strain. This is observed in plots of pressure vs. strain as the slope increases for higher UCS specimens (see). In other words, it appears as if the higher UCS specimens were stiffer (as evidenced by the slope increase with UCS), even though the Young's modulus was constant for all the samples. A possible explanation of this effect is that, at a fixed pressure, fewer cracks have been created in the higher UCS samples, and there remain more intact bonds supporting the injection pressure. Additionally, the graph shows a bi-linear or sometimes multi-linear behavior. This is a reflection of the creation of cracks either in "jumps", as discussed earlier, since the multi-linear behavior is more noticeable in the higher UCS specimens. Finally, it is noted that the pressure/strain lines depart at higher pressure levels as UCS increases. This indicates that for high UCS samples, the apparent stiffness increase becomes less severe.

The high UCS specimens show more uniform and orderly creation of cracks, which results in a more compact grouping of cracks. For the low UCS specimens crack creation occurs gradually, as discussed earlier, but isolated crack groups can be identified. Illustration of these characteristics is presented in Figure 5-6 for runs 1A (lower UCS, on the top) and 2A (higher UCS, on the bottom). The samples with higher UCS values (i.e. 3A through 5A) became unstable after approximately 500 cracks; for this reason, the comparison of crack locations was made for runs 1A and 2A only, even though their UCS difference is not as large as that for some of the other specimens.

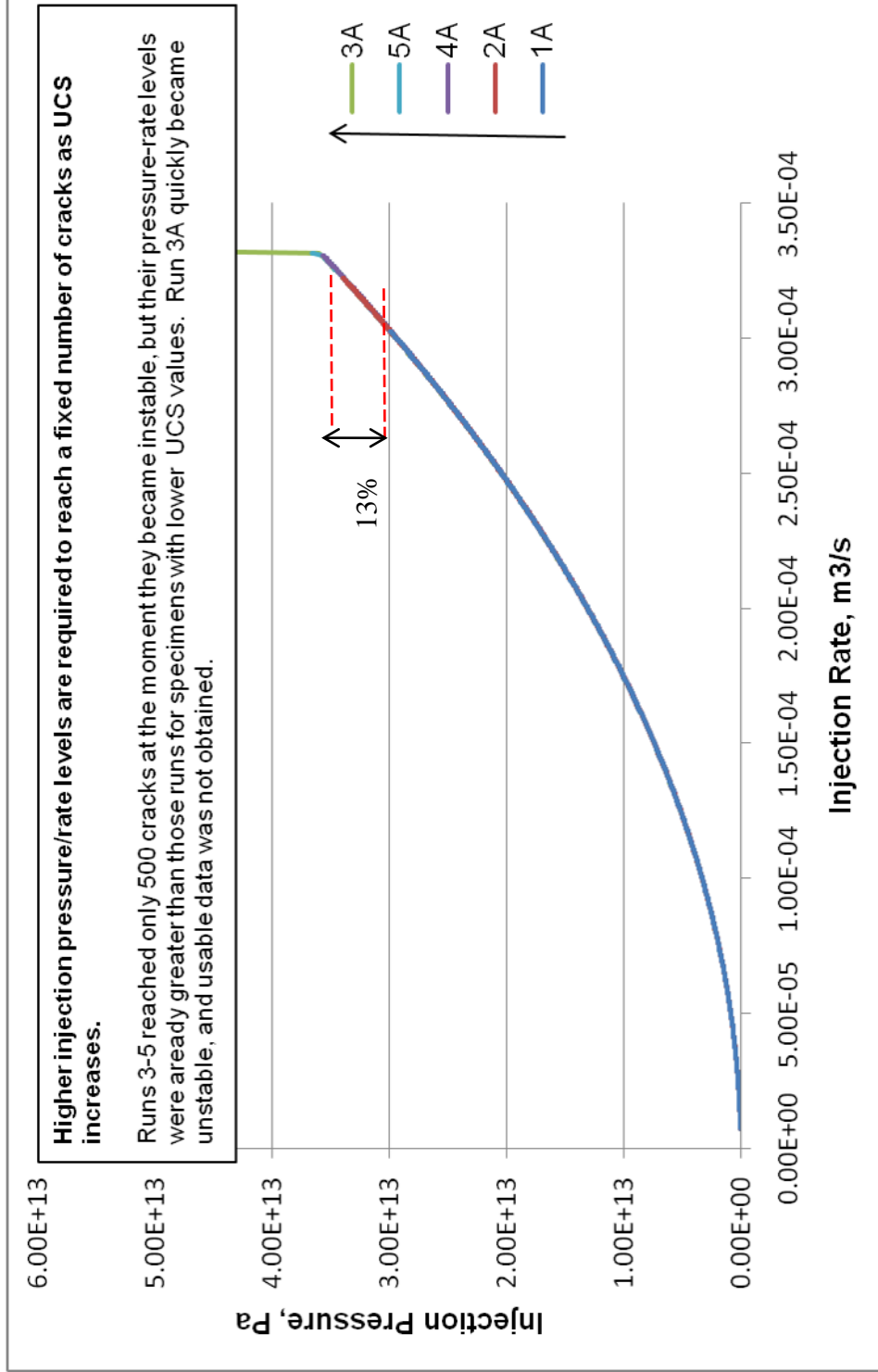


Figure 5-3 Curves of injection pressure vs. flowrate for various UCS runs

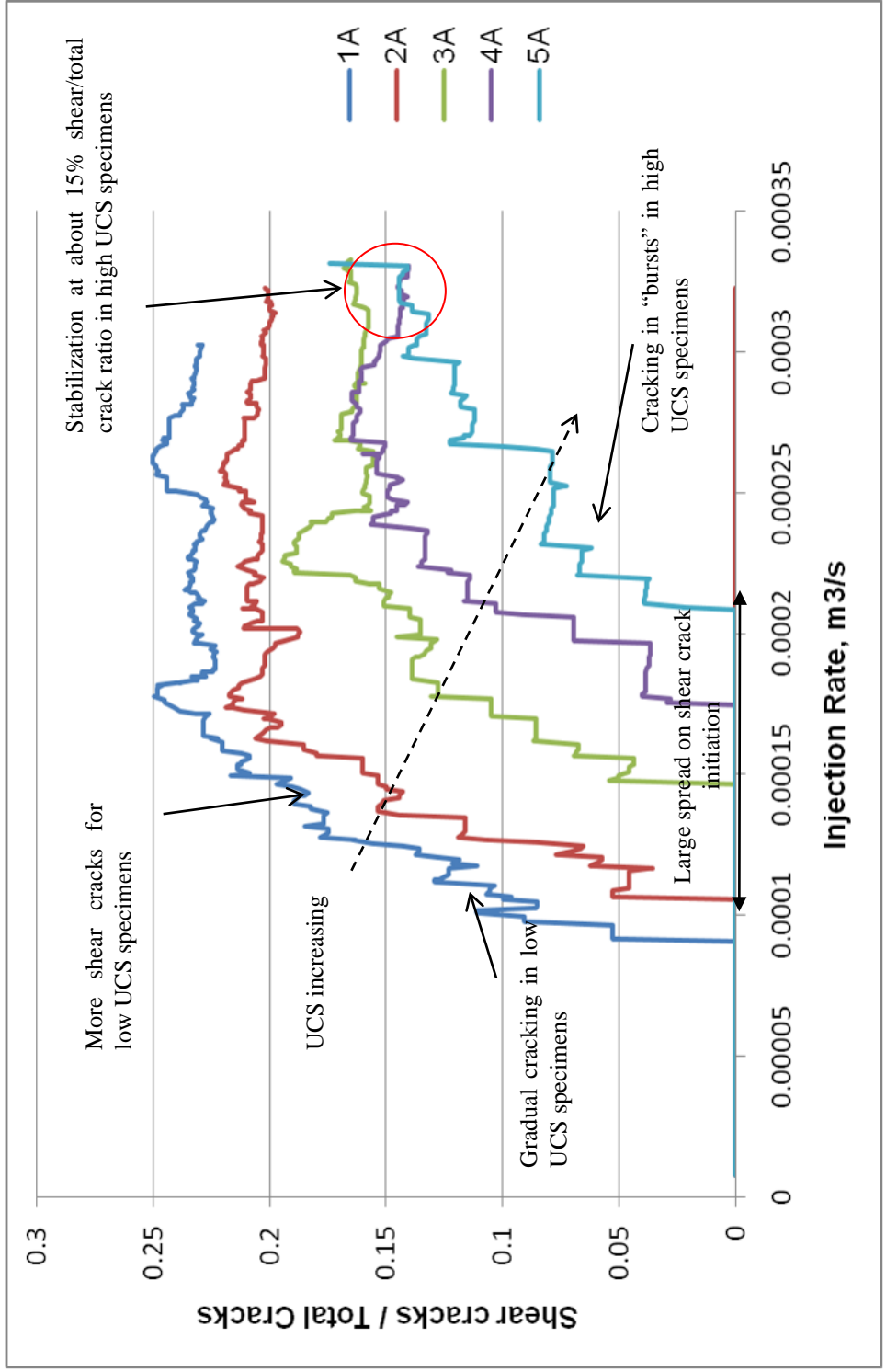


Figure 5-4 Shear to total cracks vs. injection flowrate for various UCS runs

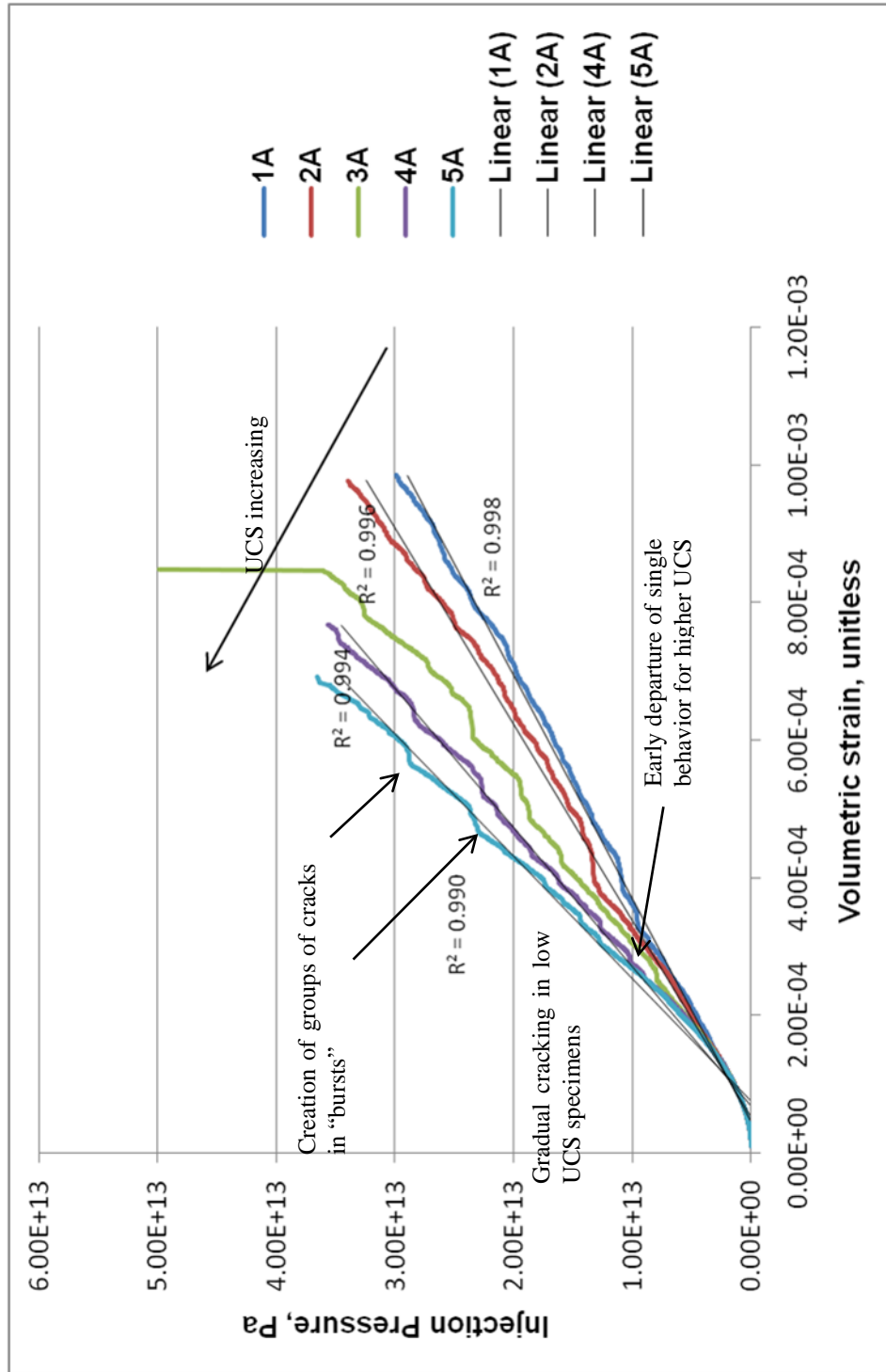


Figure 5-5 Curves of injection pressure vs. volumetric strain for various UCS runs

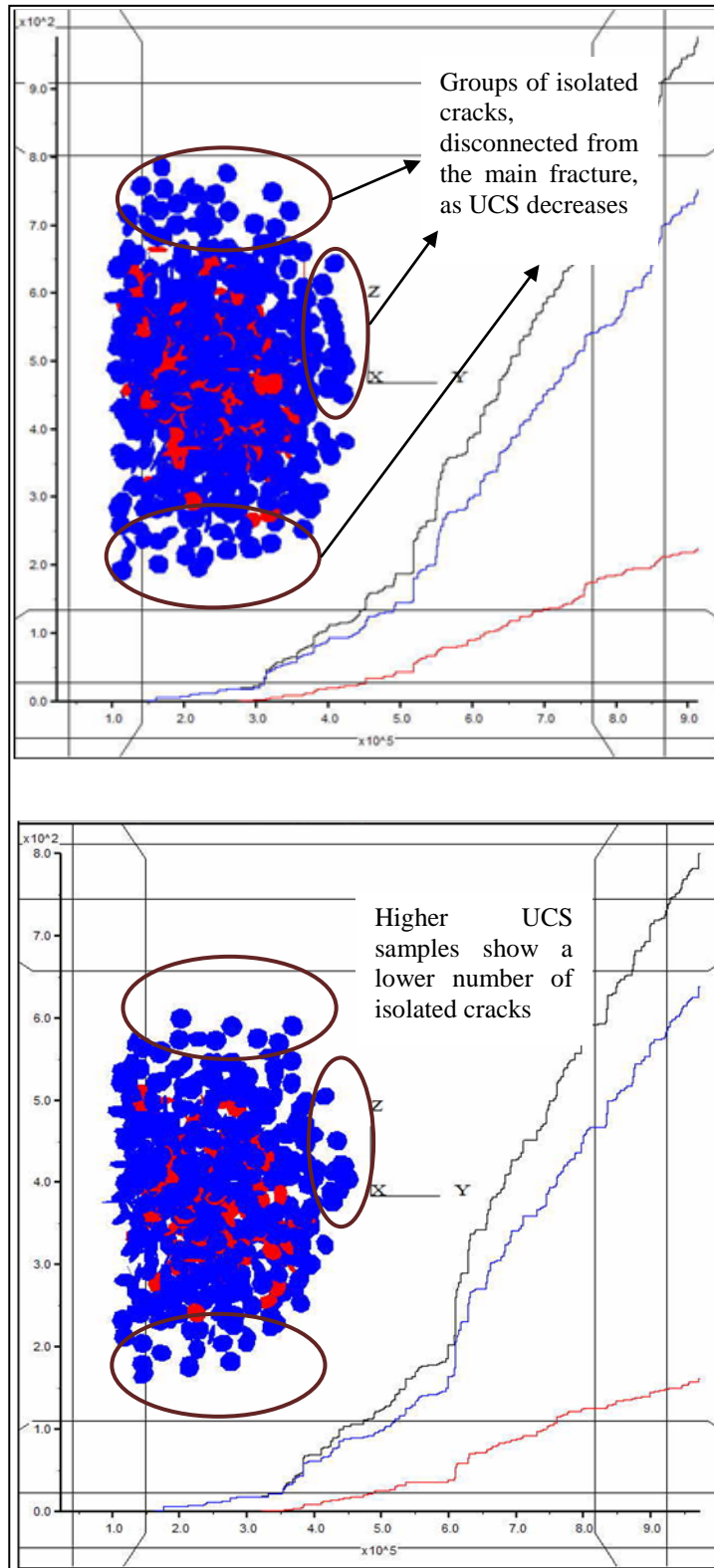


Figure 5-6 Crack agglomeration for Run1A (lower UCS specimen, Top) and 2A (higher UCS specimen, Bottom)

The cracks in stronger rocks are distributed within a narrower region; thus, it is probable that a zone of good connectivity is being created by the injection. Conversely, some of the cracks in the weaker rock are spread out, and seem to be ‘disconnected’ from the main agglomeration. This sector is possibly the so-called “Fracture Process Zone or Damaged Zone”, and is created ahead of the more continuous propagating fracture due to concentration of stresses that break contact bonds that are not in direct contact with the injection fluid.

Compression force patterns look similar for all specimens; if anything, the weaker rocks show slightly less compression.

For the stronger specimens, shear forces concentrate somewhat more towards the interior of the crack agglomeration, whereas in the base-case (weaker rock) the shear distributes more towards the periphery.

Regarding forces, the more notorious differences are observed in the onset of tension. In the stronger rock of Run2A, there is a large drop-off in the tensional force along the contacts on the periphery of the main fracture, and the particles in deeper layers of the specimen (see Figure 5-7, top). Conversely, the tension forces decrease much more gradually in the weaker rock of run2A (Figure 5-7, bottom). This pattern explains the reason for which cracks are generated further away from the immediate fracture tip in the lower UCS specimen or Run1A, as compared to its stronger counterpart of Run2A.

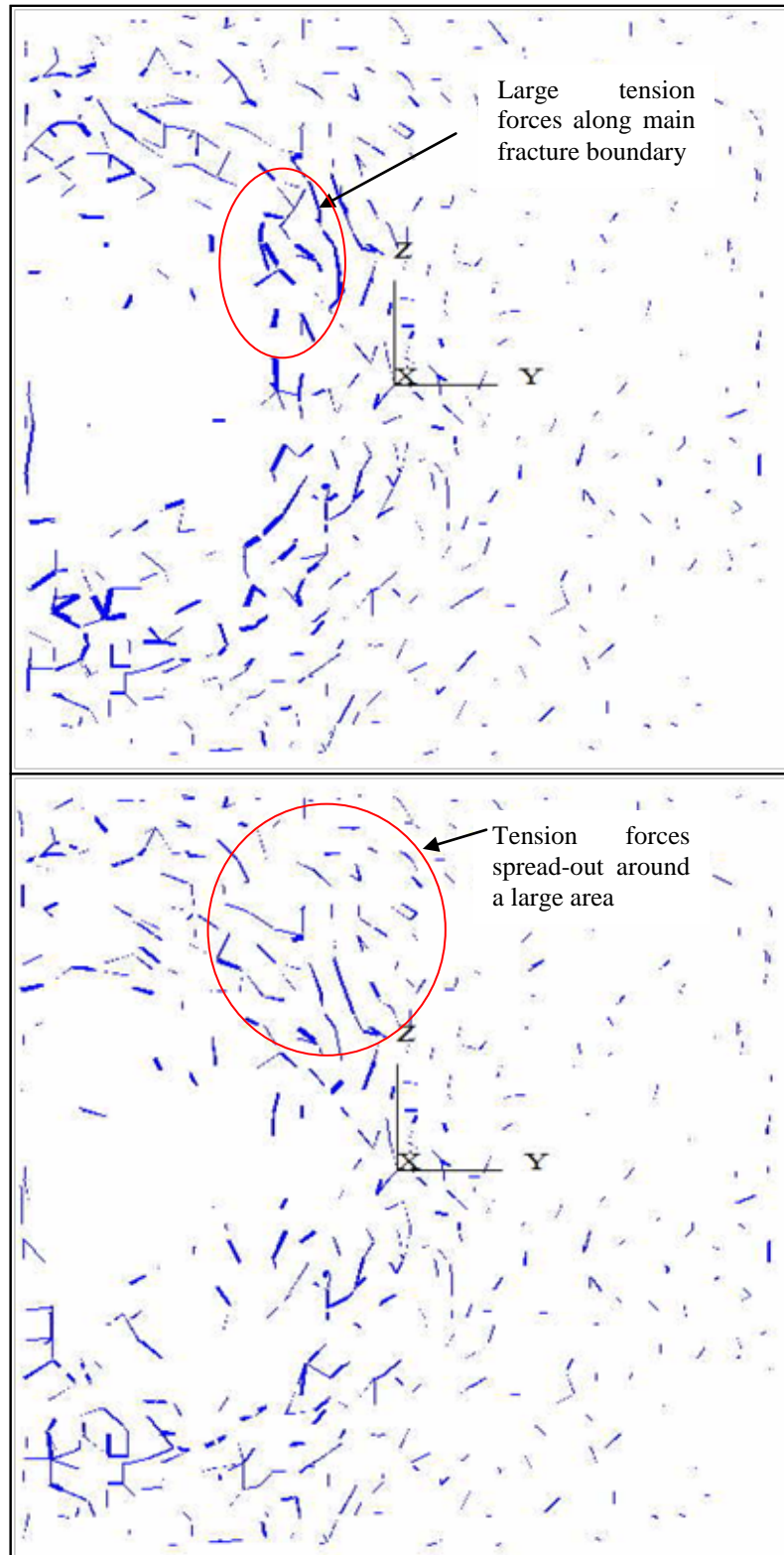


Figure 5-7 Compressive forces for Run1A (lower UCS specimen, bottom) and 2A (higher UCS specimen, top)

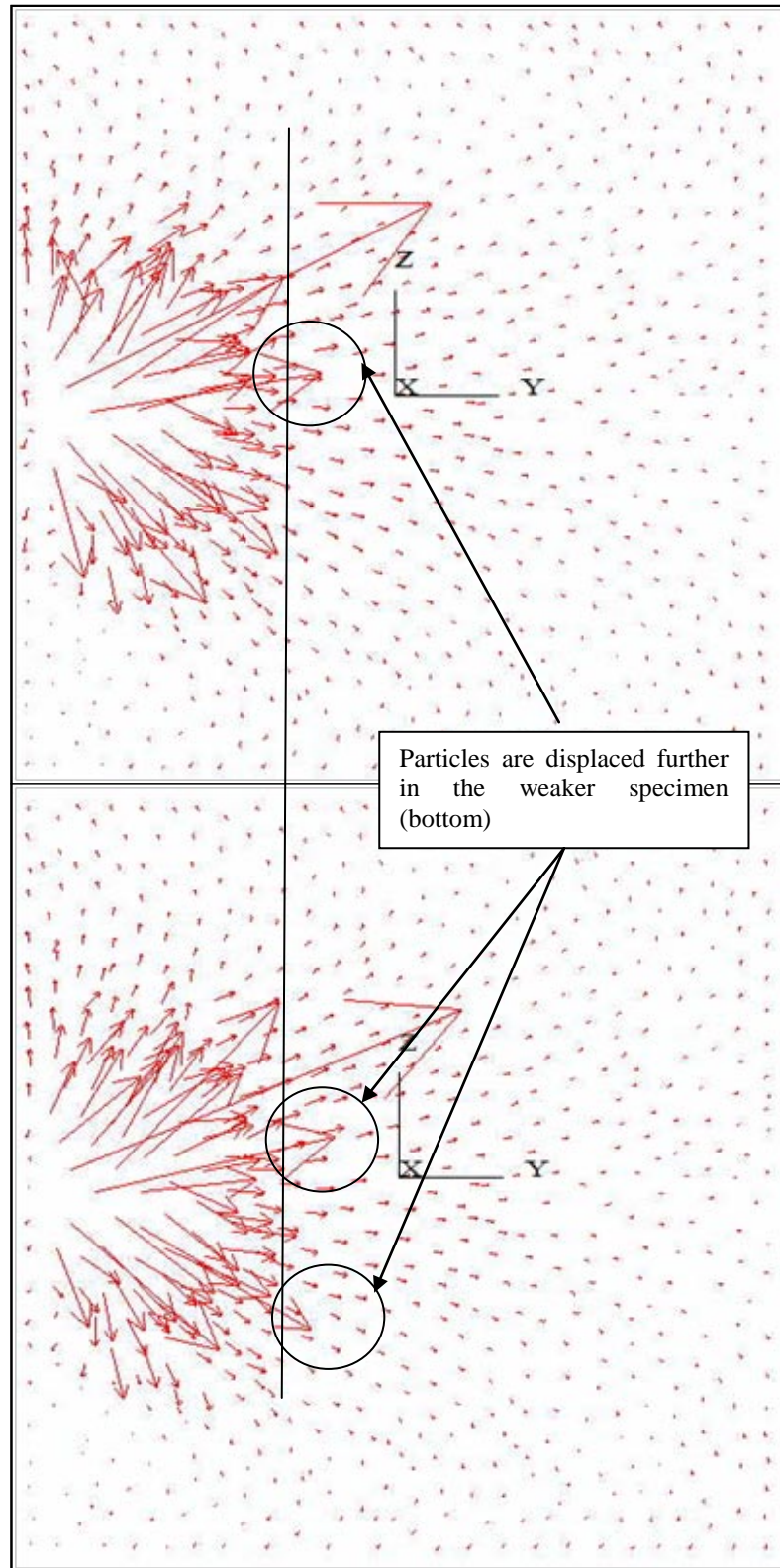


Figure 5-8 Displacements for Runs 1A (lower UCS specimen, bottom) and 2A (higher UCS specimen, top)

A displacement vector mapping shows that particles in the weaker specimen or Run 1A

moved more than in the corresponding stronger case of Run2A (see Figure 5-8^{xxvii}). This is due to a greater number of bonds still intact in the stronger rock, which hinders particle displacements.

5.2.2 Young's Modulus, E (Runs6A to 9A)

Runs 6 and 7 correspond to stiffer samples, as compared to the base-case, whereas runs 8 and 9 correspond to more compliant ones.

Plots of pressure vs. flowrate () show that, in general, stiffer samples developed higher pressures at a fixed rate. This observation is expected since larger forces are required to displace a fixed distance the particles of a higher Young's modulus specimen. An exception to the trend occurs for the lowest Young's modulus specimen (Run8A): at an earlier time the curve for this run starts climbing at a faster rate than those for the stiffer specimens 1A and 6A, such that a fixed rate produces a higher rate for the least stiff Run8A. Another interesting observation is that rupture of 1000 bonds occurs at lower levels of flowrate and pressure as stiffness increase, even though the higher E specimens develop higher pressures with rate. The only exception corresponds to the stiffest specimen of Run7A, which reaches 1000 cracks at considerable higher pressure. A possible theory to reconcile all these observations is that for low E runs, the pressure is transmitted deeper into the body of the specimen. Pressure distributed over a larger volume permit the lower E specimens to support higher pressurization before 1000 cracks

^{xxvii} The vectors in the figure were scaled to an appropriate size for visualization; they do not correspond to real displacements.

are generated. In other words, low E permits specimens to “consolidate” at some degree, until they become so compact that breakage of bond accelerates. It is probable that the re-accommodation, or “compaction”, of the lowest E specimen of Run8A is so extended throughout the ensemble, that the rock develops an apparent higher E. Conversely, consolidation is so limited in the highest E specimen of Run7A that higher pressures are generated at low rates, and 1000 cracks are readily generated.

Plots of shear/total cracks vs. injection flowrate (see) show that as injection proceeds, shear becomes more important in the stiffer rocks or Runs 6A and 7A. The generation of groups of shear cracks in these two cases occurs in “jumps” rather than gradually, as does happen in the more compliant specimens. The stiffest sample (Run 7A) exhibits also a stabilized fraction of shear to total cracks after some injection time. The behavior exhibited by the stiffer specimens is consistent with the tenets of classical hydraulic fracturing modeling, in the sense that fracture propagation occurs in instable rather than in gradual fashion, when enough stress has concentrated on the fracture tip. In addition, the stabilization towards a fraction of shear to tensile cracking fits the description of continuum mechanics, since averaging of parameters would be independent of fracture propagation. A final observation is that shear cracking delay is observed in the lowest E specimen of Run8A. This seems to be consistent with the theory proposed earlier with regards to rock “consolidation” by way of larger displacements of particles allowed in this specimen (8A), before onset of rapid cracking.

Plots of injection pressure vs. volumetric strain () show markedly different slopes, as expected for samples with various Young’s modulus; the largest slope corresponds to the

stiffest specimen of Run 7A, meaning that large pressures generate small strains. Run7A also shows the best linear fit between pressure and strain, as the correlation coefficient equals 0.99. The lower E runs are still somewhat linear, but the correlation coefficient is less. There is a clear tendency towards “stiffness degradation”, i.e., it seems as if E decreases, with injection times. Interestingly, the lowest E specimen (Run 8A) shows a complex behavior: at earlier times it seems more compliant than the other cases, as characterized by a softer slope; then, it shows what appears as a strain-hardening effect (steeper slope), probably indicating ‘consolidation’ of some of the material, and; finally, the rock becomes compliant again, probably due to onset and continuation of damage.

Graphs of crack location show a more orderly generation around the injection point for the stiffest specimen of Run 7A (see Figure 5-12, bottom); conversely, the lowest E specimen of Run 8A exhibits multiple spots of crack generation, which result in isolated crack groups (see Figure 5-12, top). This observation supports the assumption that, at low stiffness, stress concentration may occur away from the injection point, due to relatively large displacements of the specimen’s particles, i.e. the specimen goes somewhat through a consolidation process. The net effect of this behavior is that fractures in low E rocks must be shorter and smaller, since a lot of the energy produces stress concentration away of the main fracture.

The contact forces pattern is consistent with earlier observations. For the stiffest specimen of run 7A, the compression forces were concentrated around the injection point (see Figure 5-13, bottom). Conversely, the lowest E case of run 8A shows long stress concentration chains and large stresses away of the injection point (see Figure 5-13, top).

The displacement vector field clearly shows that, in average, the particles move less as E increases (Figure 5-14).

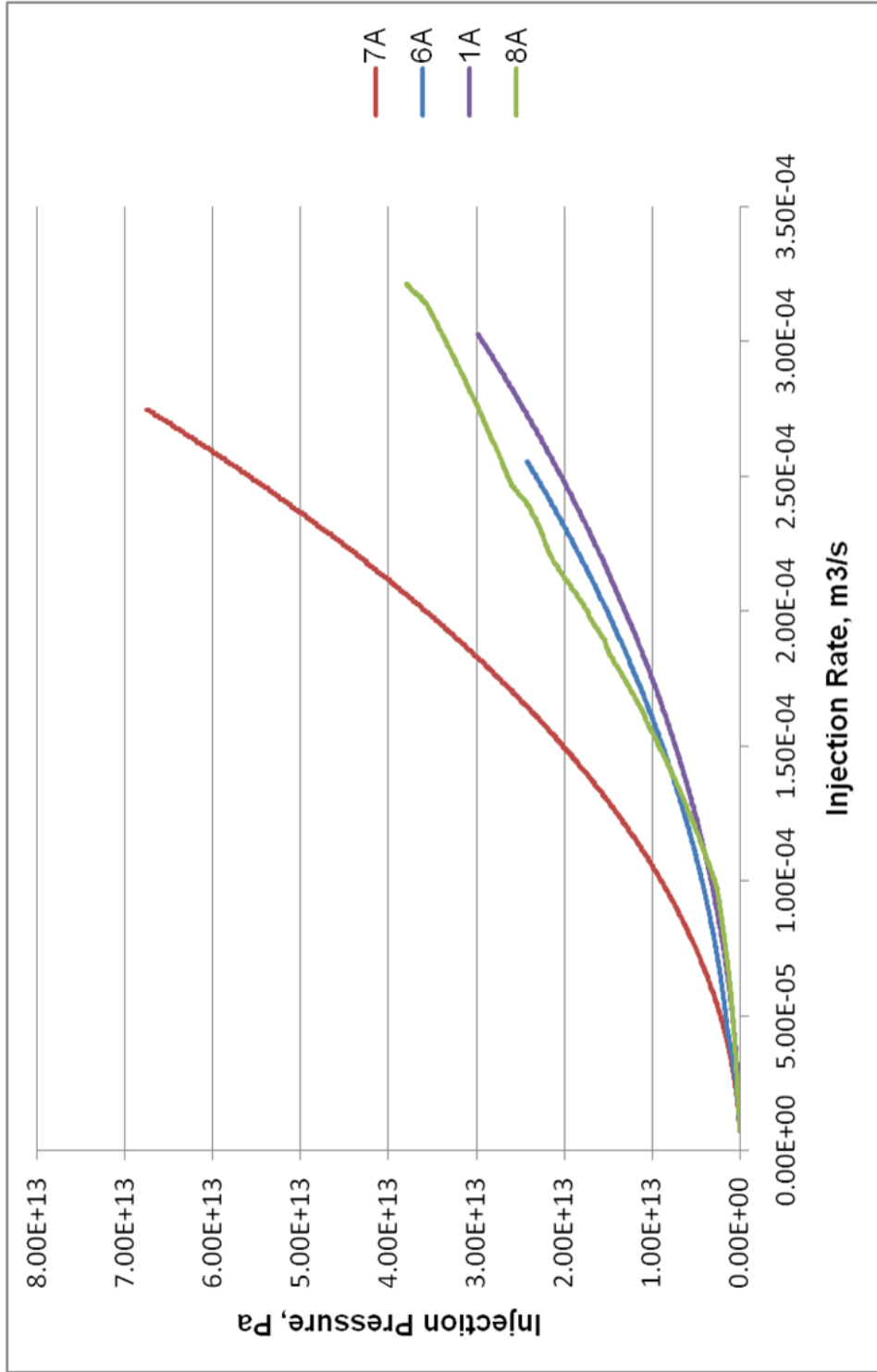


Figure 5-9 Curves of injection pressure vs. flowrate for various Young's modulus runs

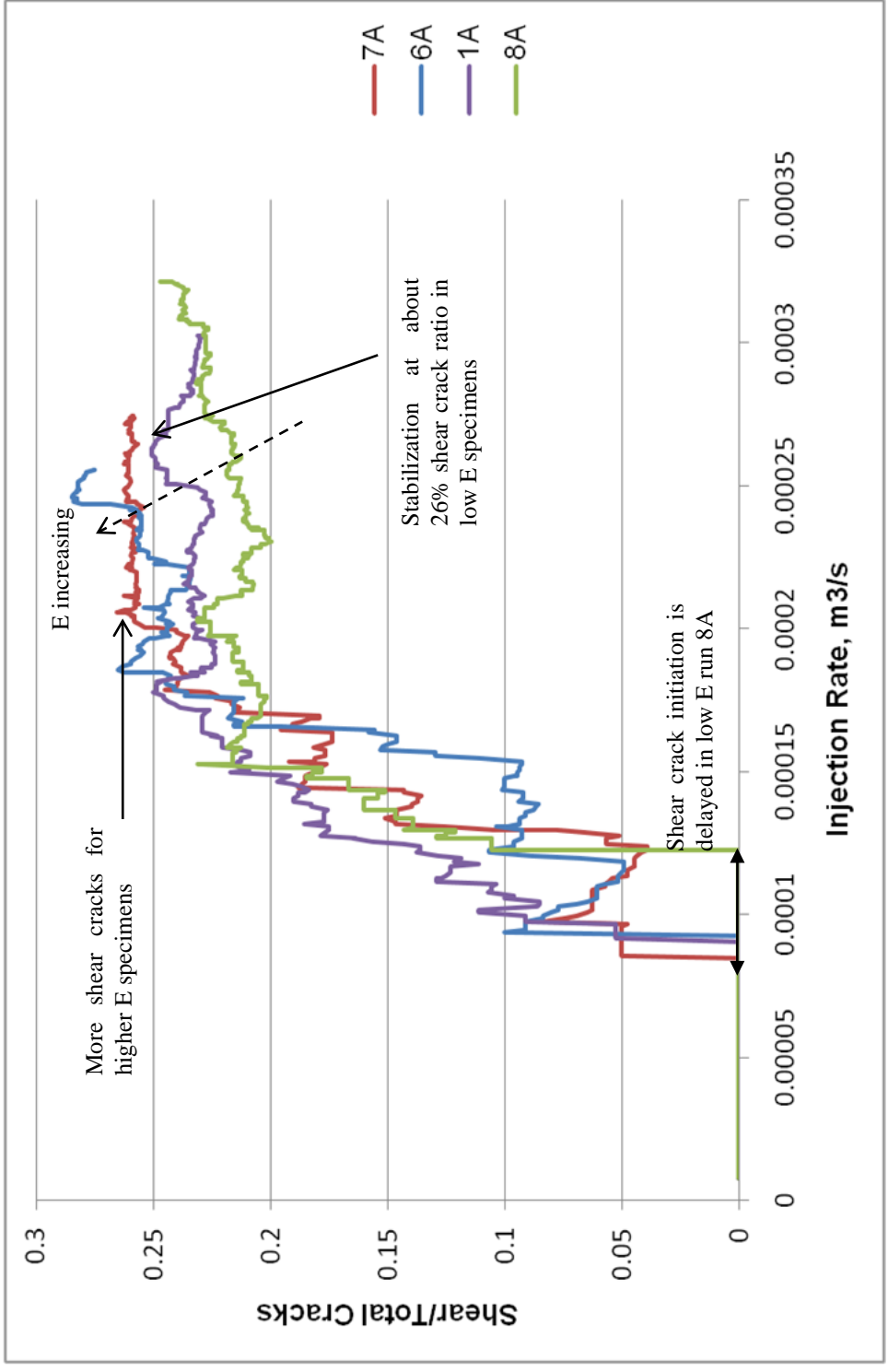


Figure 5-10 Shear to total cracks vs. injection flowrate for various E runs

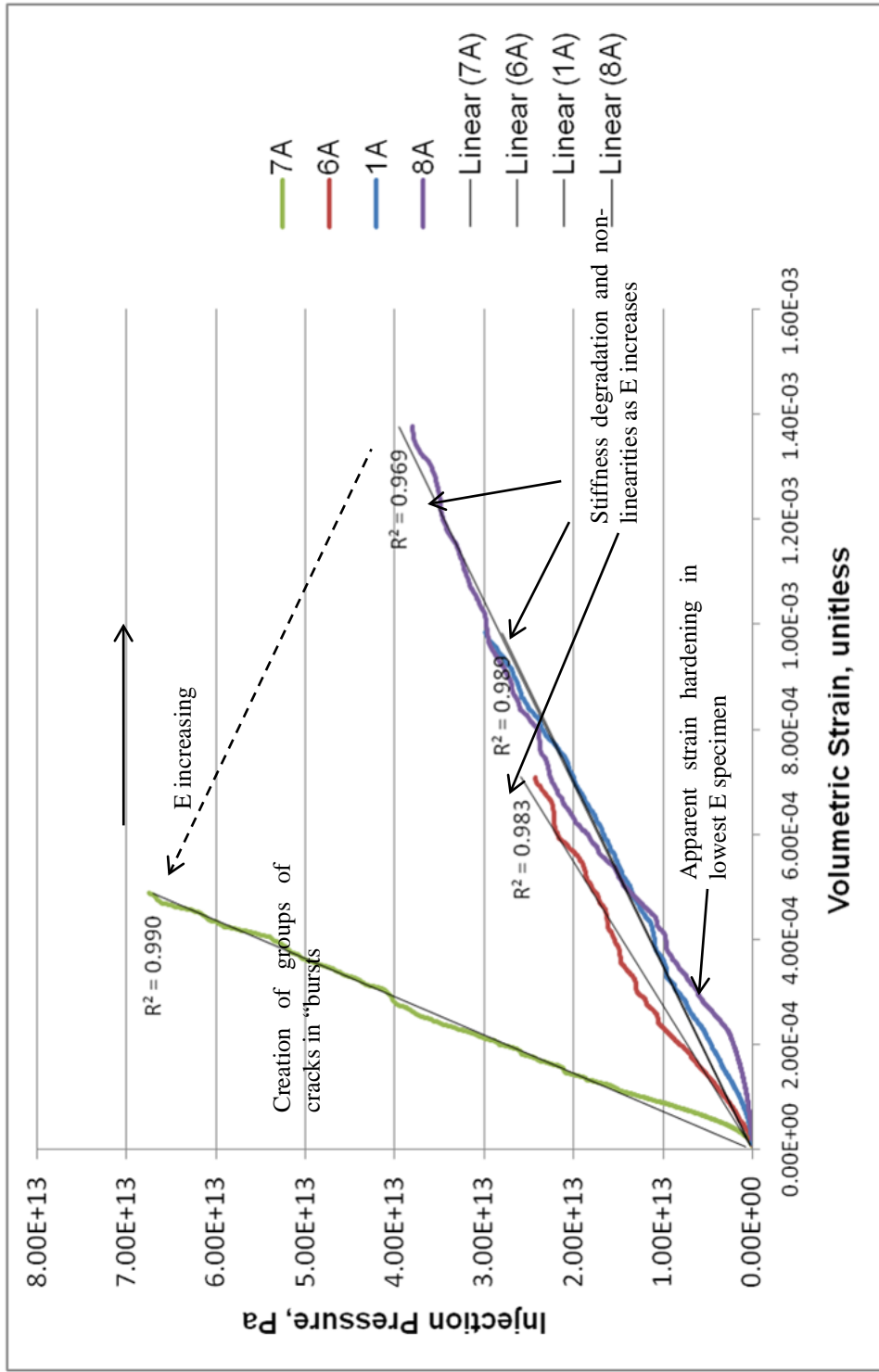


Figure 5-11 Curves of injection pressure vs. volumetric strain for various E runs

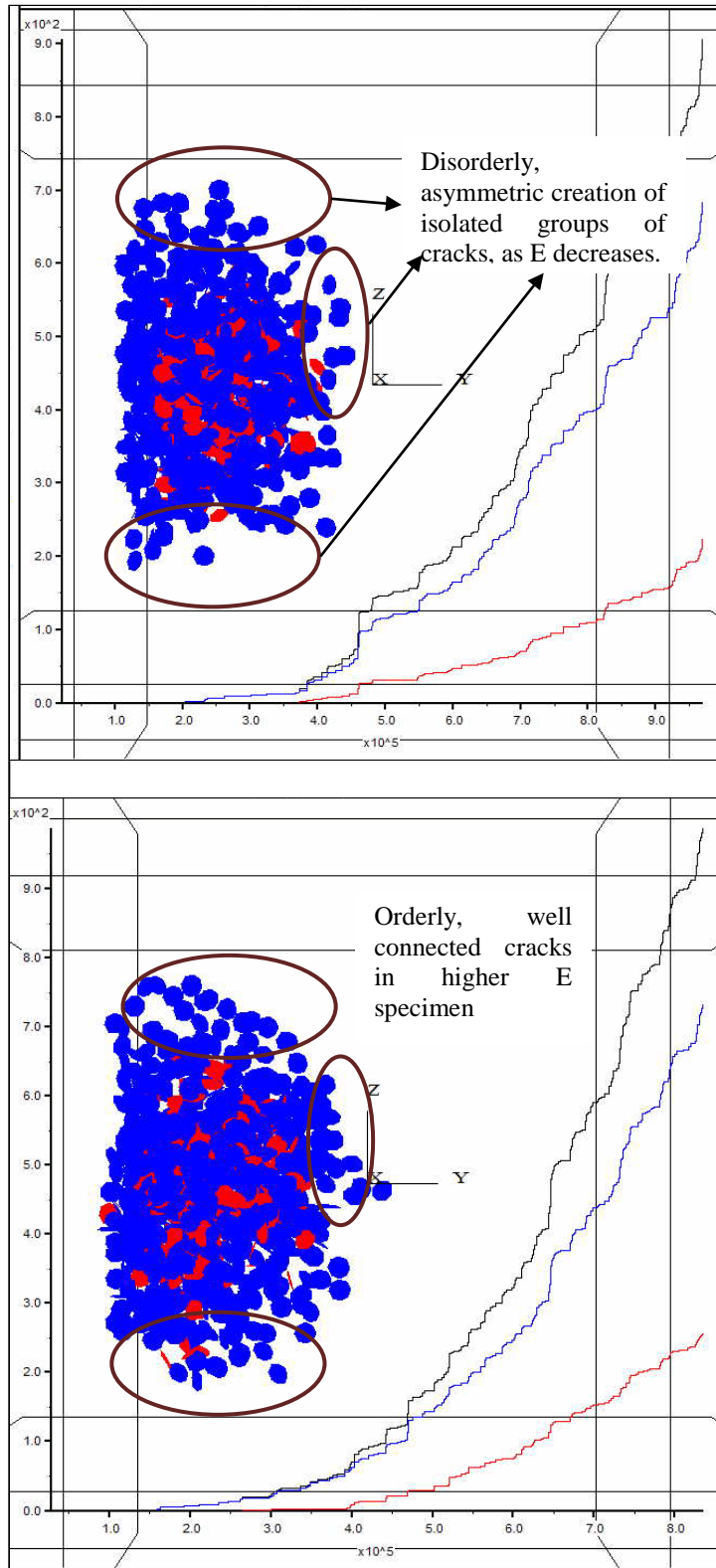


Figure 5-12 Crack agglomeration for Runs 8A (lowest E specimen, top) and 7A (highest E specimen, bottom)

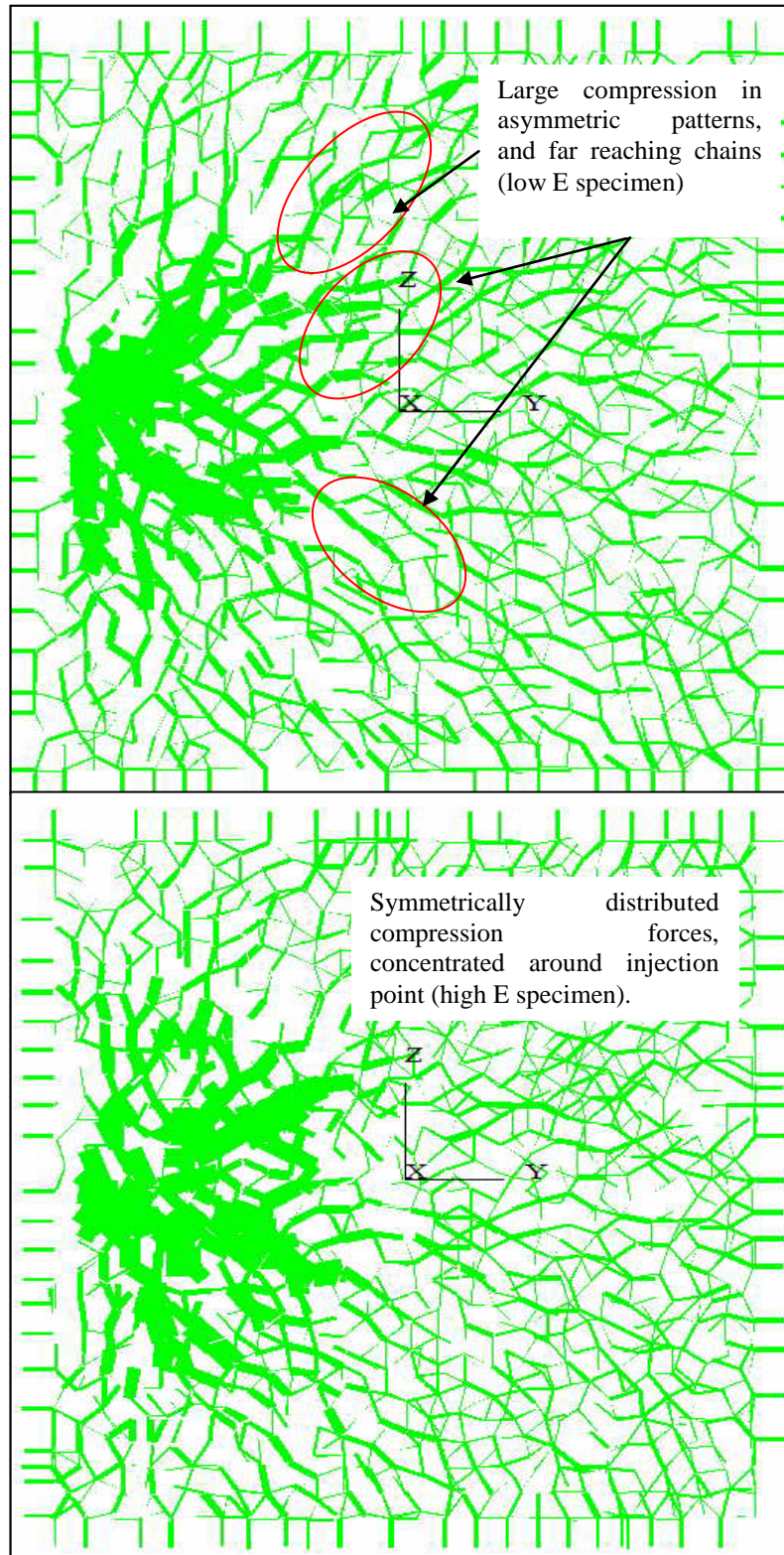


Figure 5-13 Compressive forces for Runs 8A (lowest E specimen, top) and 7A (highest E specimen, bottom)

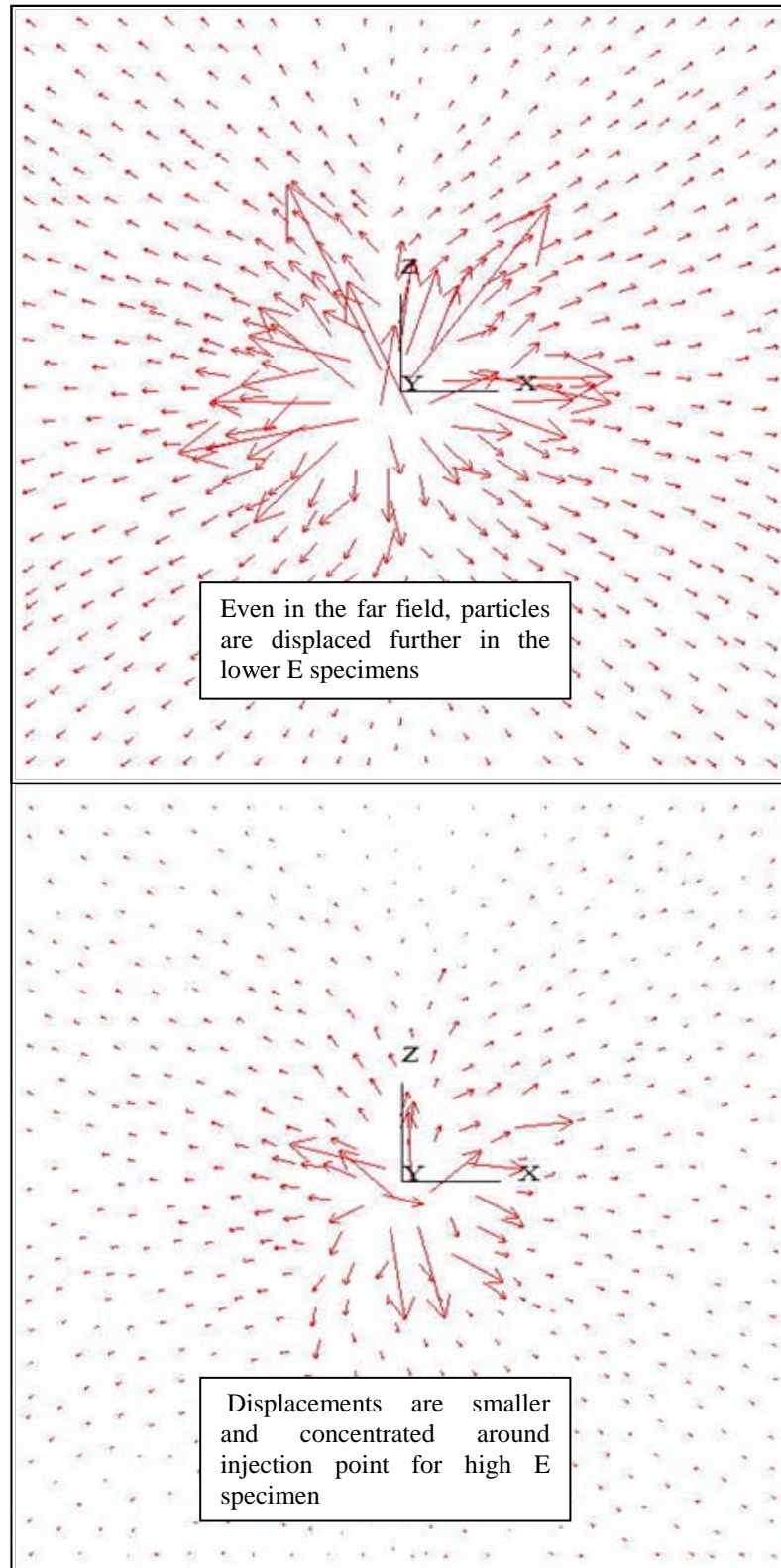


Figure 5-14 Displacements for Runs 8A (lowest E specimen, top) and 7A (highest E specimen, bottom)

5.2.3 Poisson's Ratio Effects

Four specimens with different Poisson's ratio values (ν) were created. The hydraulic fracturing simulations runs were named "Run1_PR1" through "Run1_PR4". The prefix "Run1" was used because with the exception of the Young's modulus, the properties were based on those of the "base-case", or Run1. E had to be increased because the simulations with higher ν became unstable, and the specimen disintegrated at the moment that fluid injection was activated. E was increased from 8.3×10^5 psi to values around 2.9×10^6 psi. The reason for specimen disintegrations at high ν and low E, was that even low forces caused excessive displacements, the simulation boundaries were quickly reached, and the particles escaped across the boundaries, effectively destroying the specimen.

Because ν is a macroscopic property, it can't be directly prescribed in the discrete element specimen. The main discrete parameter controlling ν is the ratio of normal to shear particle stiffness, K_n/K_s . Nonetheless, this ratio also affects E (albeit the effect is much less than it is on ν); an increase in K_n/K_s causes an increase in ν and decreases E, for this set of simulations.

Table 5-2 summarizes the properties of the 4 runs of this section.

Table 5-2. Parameters of the specimens used to investigate the Poisson's ratio effect

Run ID	K_n/K_s	E, ($\times 10^6$) psi	ν
Run1_PR1	1.5	2.7	0.15
Run1_PR2	2.0	2.3	0.17
Run1_PR3	3.0	2.1	0.23
Run1_PR4	4.0	2.0	0.27

Plots of injection pressure vs. flowrate show that for higher ν specimens, the pressure

generated at a given flowrate decreases (see). A fixed number of ~1000 cracks are reached at similar levels of flowrate. However, as v increases lower levels of injection pressure are required to reach the 1000 cracks. A possible reason for this behavior is that a higher v means that a larger fraction of an applied force will be transmitted in the transversal direction, as compared to a lower v material. By distributing the force disturbance throughout the sample, cracking becomes widespread, and the number of total cracks is readily reached. In addition, more broken bonds allow larger displacements of the specimen particles. Because more displacement is allowed, high v materials generate lower pressure upon fluid injection.

Comparative plots of cracks vs. injection rate for runs PR1 through PR4 show that shear cracking increases as v decreases (see). In other words, as v increases, shear cracking becomes less important. There seems to be an exception with Run PR2, in which the start of shear cracking is visibly delayed. Nonetheless, once this run has caught up with the rest of simulations, the same trend is observed. The reason for shear cracking delay and overall less importance with increasing v can be explained as follows: higher v causes larger displacements in the transversal direction, with respect to the direction of the applied forces; this scenario favors a tensional setting.

The plots of pressure vs. volumetric strain conform to the behavior expected from variations in v (). Higher v specimens show larger volumetric strains at a given pressure, as particles re-accommodate easier due to increased displacements and cracking.

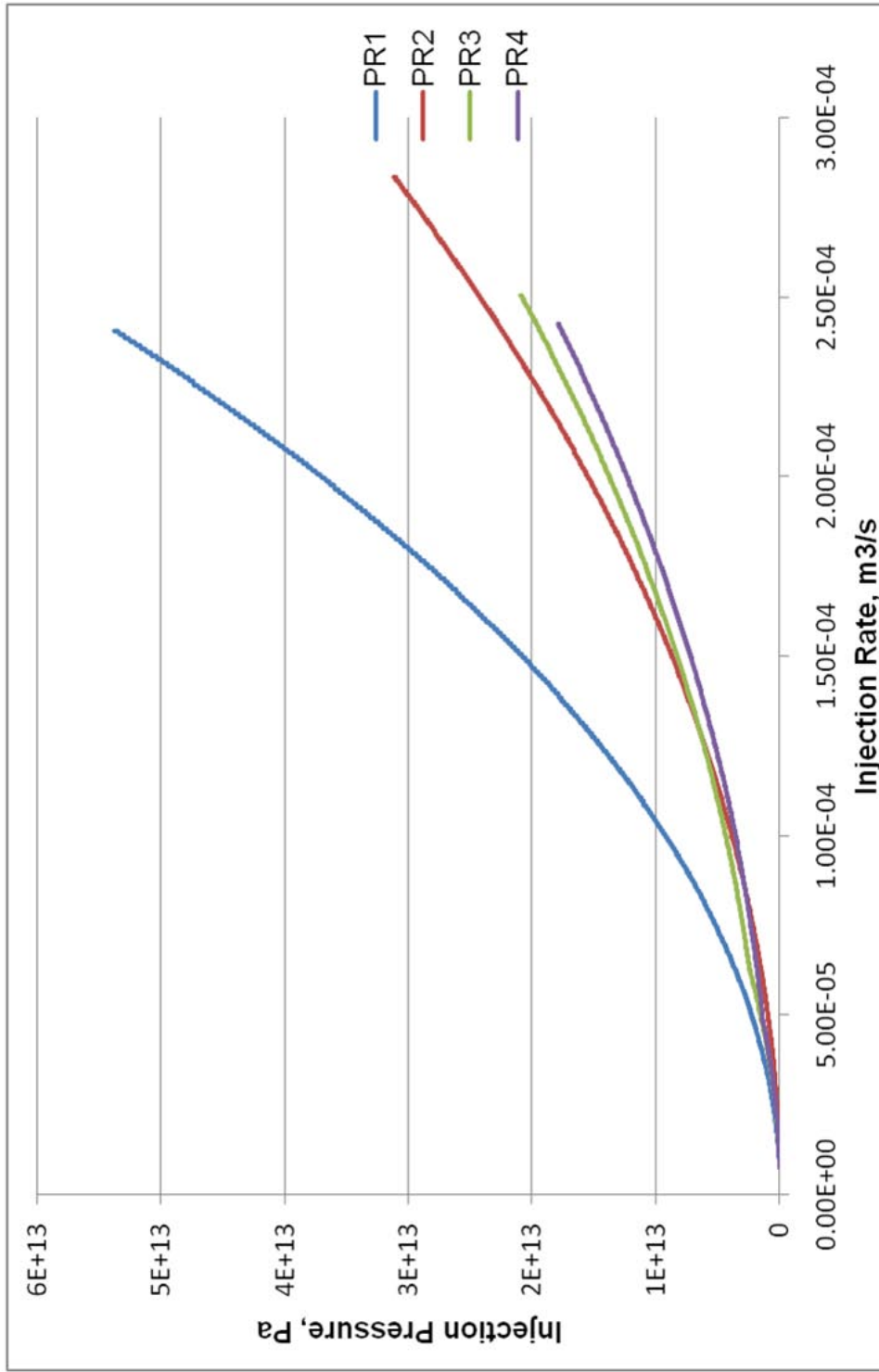


Figure 5-15 Curves of injection pressure vs. flowrate for various Poisson's ratio runs

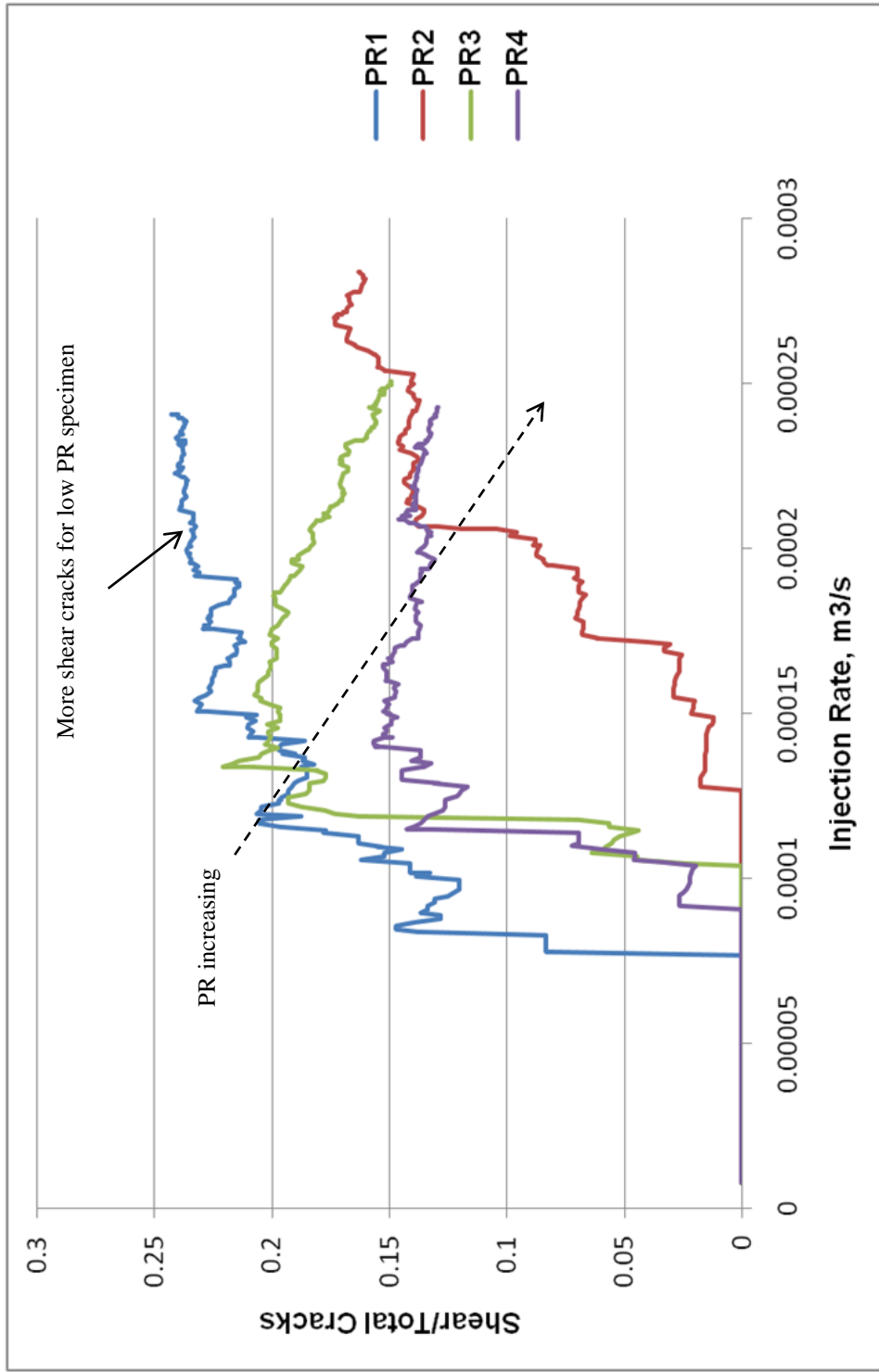


Figure 5-16 Shear to total cracks vs. injection flowrate for various PR runs

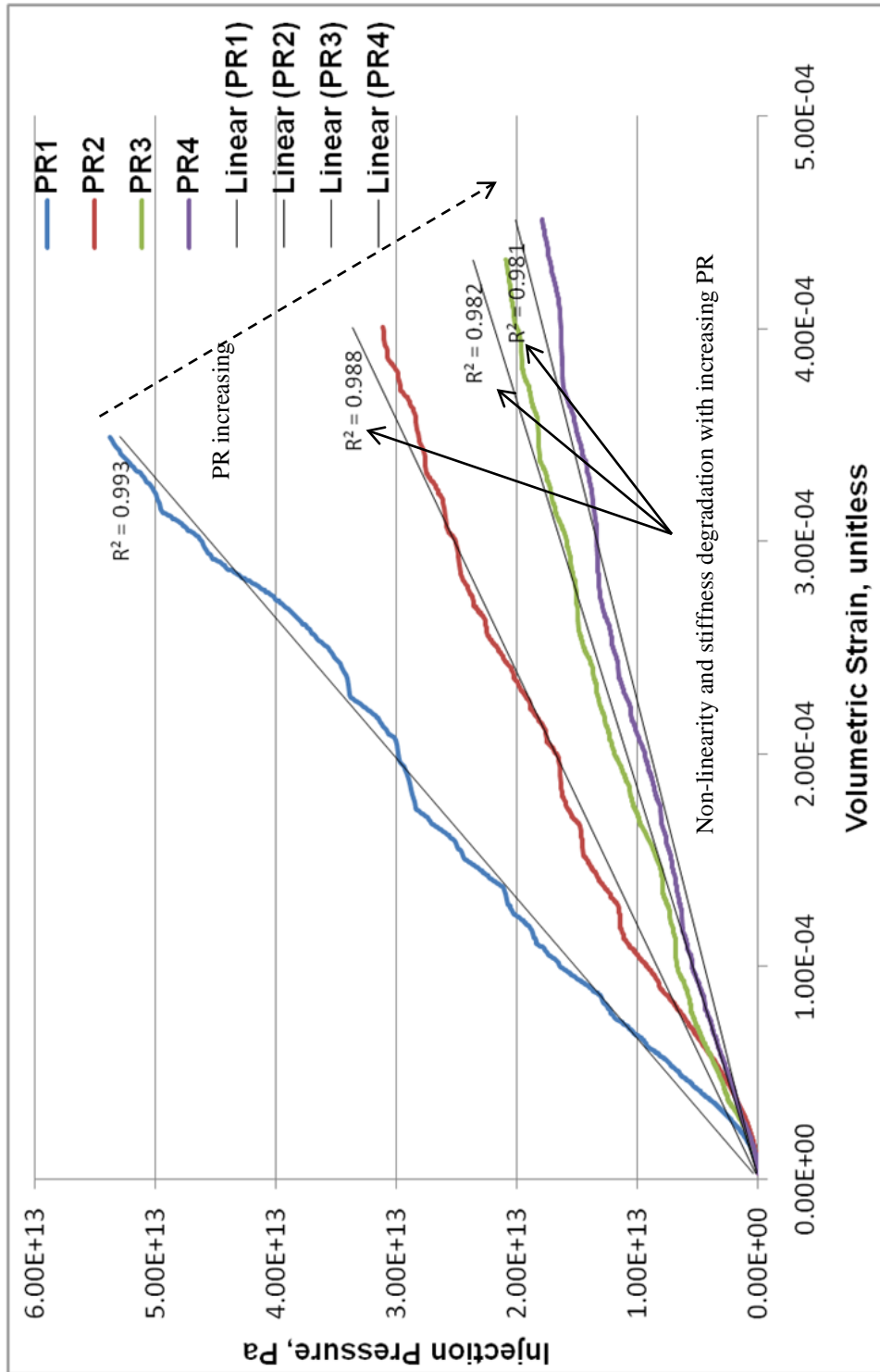


Figure 5-17 Curves of injection pressure vs. volumetric strain for various PR runs

Figure 5-18 shows the spatial distribution of generated cracks with v variation. At high v (Run PR4), the formed cracks are more widely distributed (Figure 5-18, bottom). In contrast, low v specimens (Run PR1) show cracks to be more tightly distributed around a central group (Figure 5-18, top). As discussed earlier, tensional cracking is more important with higher v ; the wider crack distribution is composed by these additional tensional cracks. The location of the extra-tensional cracks is clearly observed within a “corridor” ahead of the main crack agglomeration. This corridor fits the description of the so-called “Fracture Process Zone or FPZ”. The FPZ is usually thought of as a shear zone caused by compressive stresses ahead of the main fracture tip. Nonetheless, compressive shear failure is the result of coalescence of small-scale tensile cracks along a shear plane. Therefore, the observations on this set of simulations must correspond to such tensile cracks.

Figure 5-19 depicts concentration of compressive forces away of the injection point (and hence, main crack agglomeration) for the higher. The localization of these forces explains the generation of the isolated group of cracks, assumed to be the region usually known as FPZ.

The displacement vector field shows a large increase in the movement of particles in the high v specimen of Run PR4 (see Figure 5-20).

Figure 5-18 through Figure 5-20 are presented in the next pages.

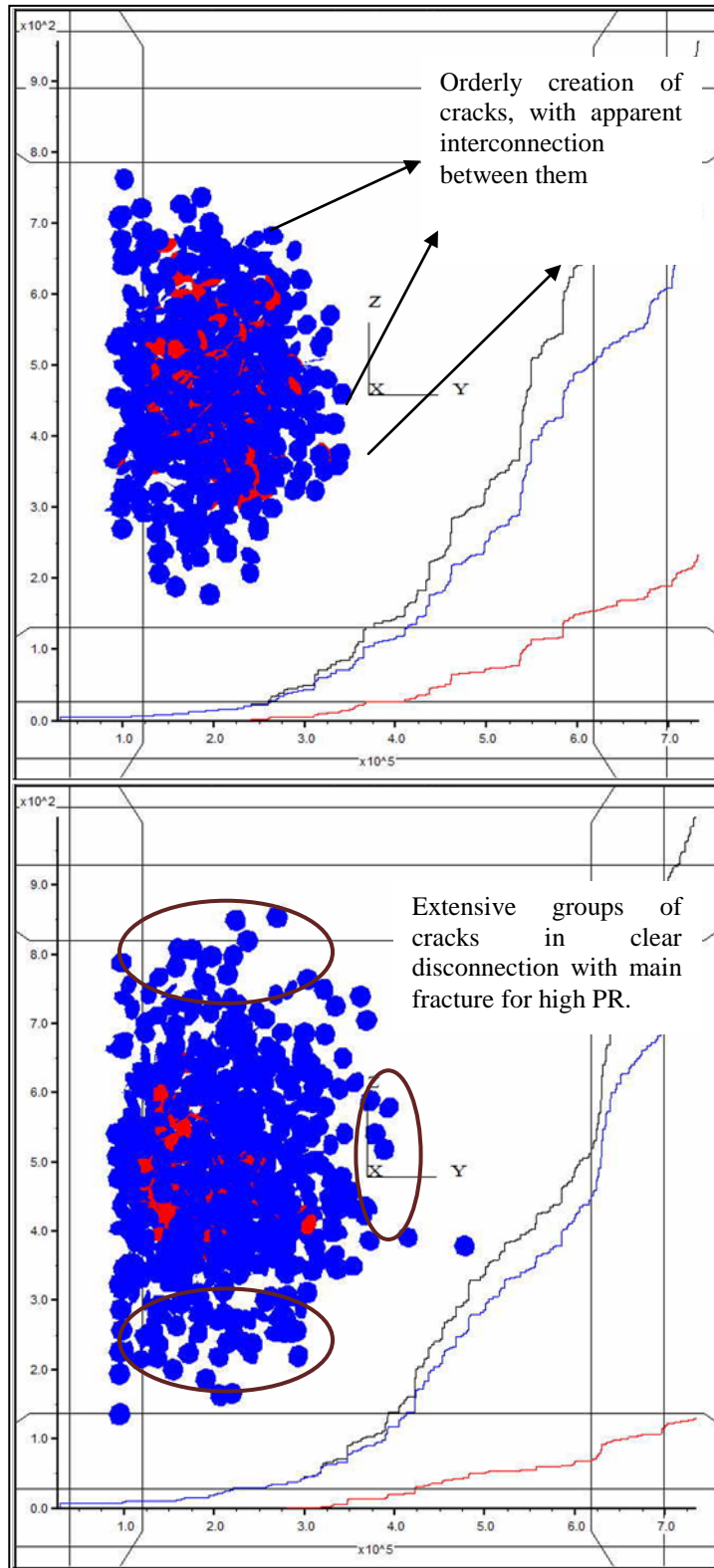


Figure 5-18 Crack agglomeration for Runs 1A-PR1 (lower v specimen, top) and 1A-PR4 (higher v specimen, bottom)

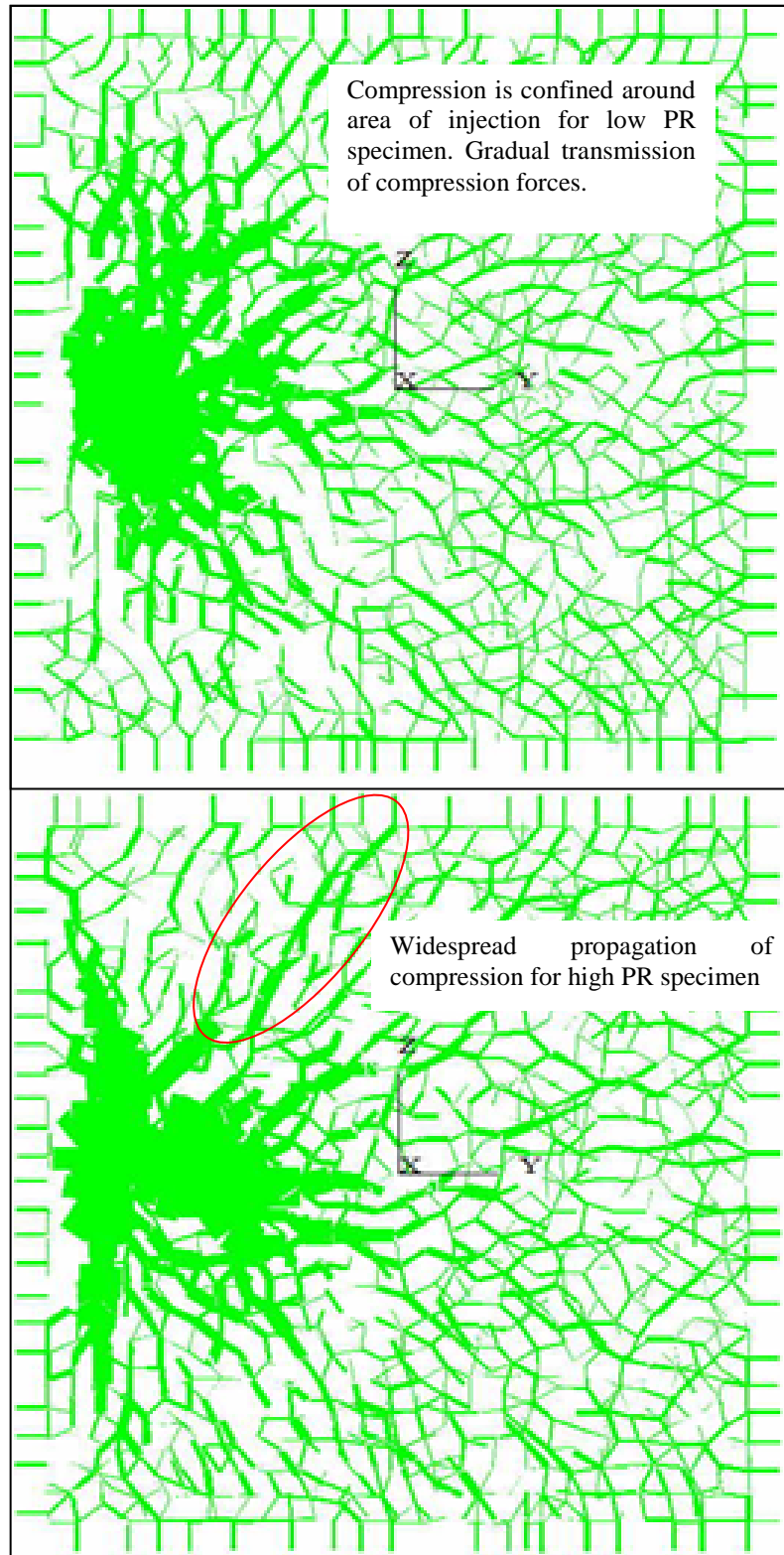


Figure 5-19 Compressive forces for Runs 1A-PR1 (lower v specimen, top) and 1A-PR4 (higher v specimen, bottom)

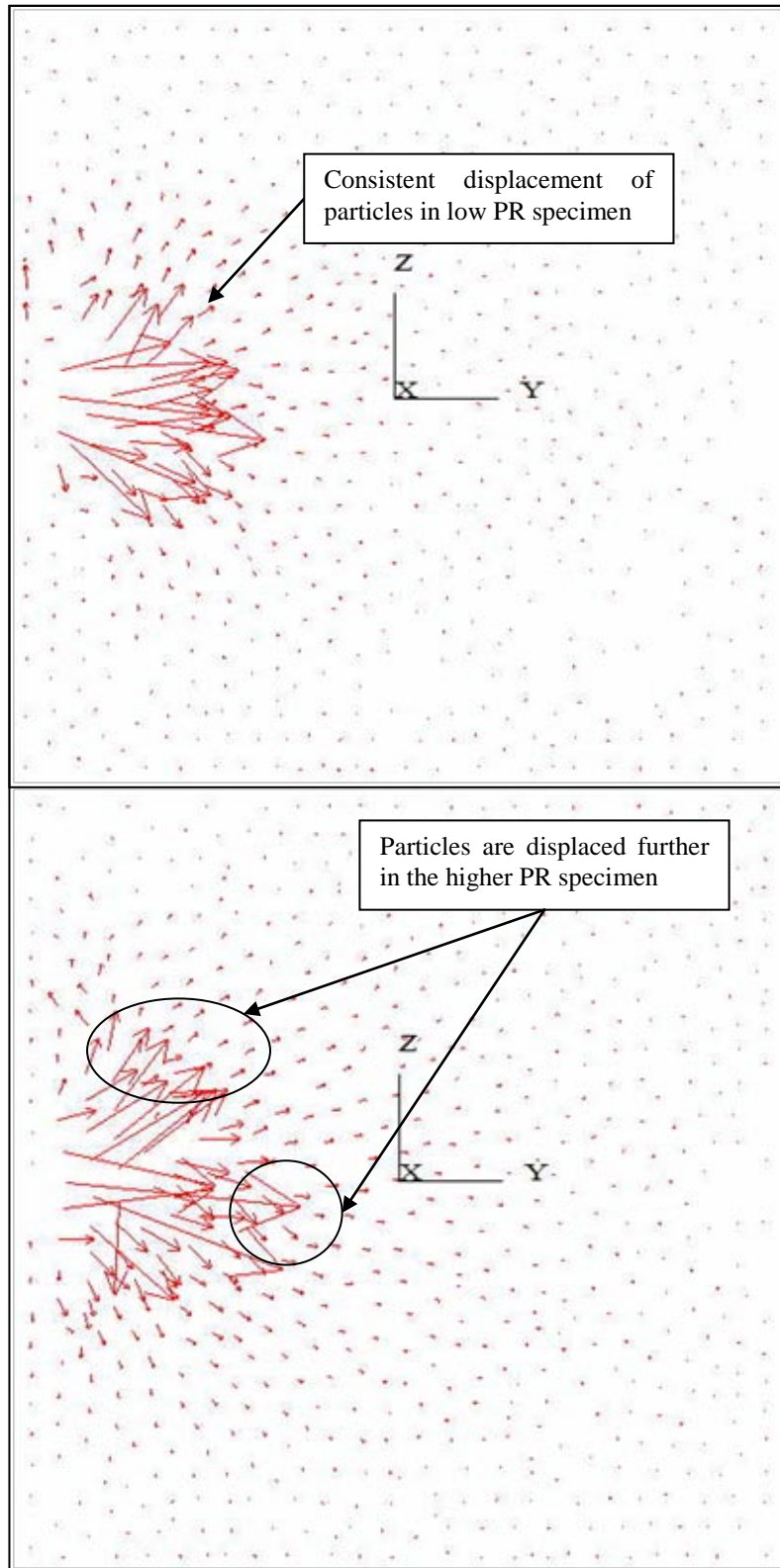


Figure 5-20 Shear forces for Runs 1A-PR1 (lower v specimen, top) and 1A-PR4 (higher v specimen, bottom)

5.2.4 Ductility Effects

In a discrete element specimen, the controls on ductility come from the relationship existing between normal and shear strengths and stiffness, respectively. Specimens with different strength and stiffness ratios were used to evaluate the effect of ductility in fracturing behavior. These specimens were identified by the suffix “Duc1” through “Duc4”. The Run1_PR4 specimen from the previous section was used as the control simulation. In addition, Run1A, which exhibits a lower Poisson’s ratio (~ 0.15), was used for comparison. Table 5-3 lists the different runs, along with the strengths of the specimens used.

Table 5-3 Properties of specimens used to determine ductility effects

Run ID	Sn, MPa	Ss, MPa
Run1A (PR ~ 0.15)	10	20
Run1_PR4 (Base-Case)	10	20
Run1_PR4_Duc1	13	20
Run1_PR4_Duc2	16	20
Run1_PR4_Duc3	20	20
Run1_PR4_Duc4	20	10

Stress-strain curves of these specimens are depicted in . There are a few interesting observations regarding the stress strain curves:

- The specimen that exhibits highest ductility, according to the definition of area under the stress-strain curve, is that of Run Duc3, which corresponds to Sn equal to Ss, and with the strengths being the highest for this set of runs.
- When one strength is twice the other, i.e. $S_n = 2S_s$, or $S_s = 2 S_n$, the pre-peak behavior is very similar; however, the post-peak behavior exhibits larger ductility for the case in which Ss is less than Sn.

- The pre-peak behavior of all the specimens is approximately linear, with the Run Duc4 specimen being the most brittle, and the rest of them showing a somewhat more ductile behavior.
- The curve of Run 1A was included to illustrate the common denomination of a material as ductile when it exhibits a lower E.

Plots of injection pressure vs. flowrate () show that specimens with similar E and ν follow the same line (i.e. Runs with the prefix PR4 in Table 5-3), although the required pressures and rates to cause a fixed number of apparently 1000 cracks, increases for run Duc3. Surprisingly, Duc4 and PR4 show similar pressure/rate requirements, despite the strength ratios being inverted from one specimen to the other^{xxviii}. So, it is apparent that the absolute magnitude of the lesser strength is responsible for the injection pressure/rate fracturing requirements, whereas the ratio of the strengths is not relevant. In other words, the needed injection pressure/flowrate to create a fixed number of cracks is unaltered as long as the lesser strength, either the shear or normal one, is unchanged. Interestingly, the pressure/rate requirements for Run1A are similar to those of Duc2, even though 1A has lower E (but also less ν). In view of these results, ductility, regardless if defined as a lower E material, or the larger area under the stress-strain curve, seems to increase the required pressure-flowrate to reach a fixed number of cracks.

^{xxviii} The base case PR4 strength ratio is $S_n/S_s = 0.5$. This ratio was inverted for the specimen Duc4, i.e. $S_s/S_n = 0.5$.

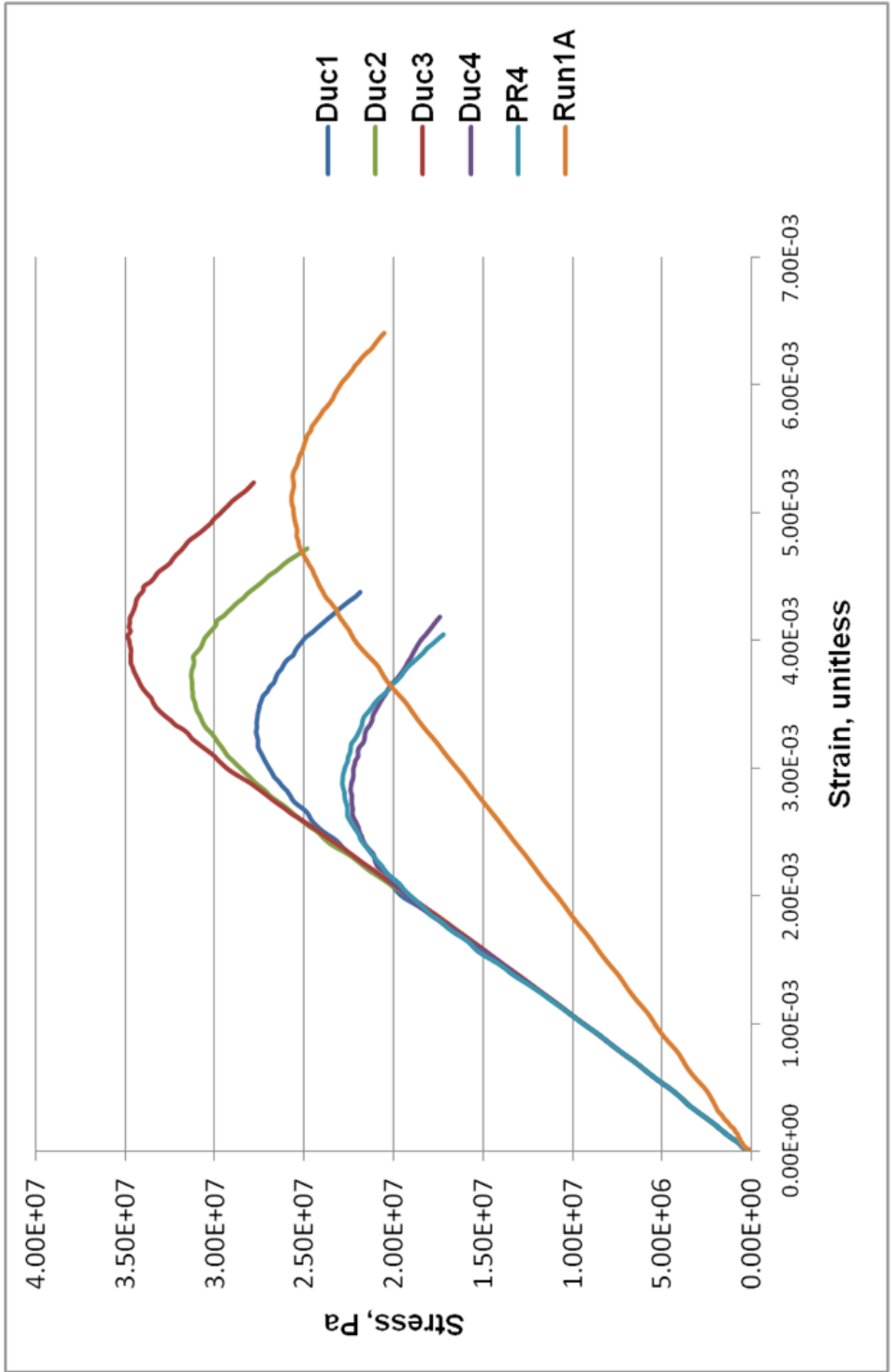


Figure 5-21 Stress-strain curves of specimens used to determine ductility effects

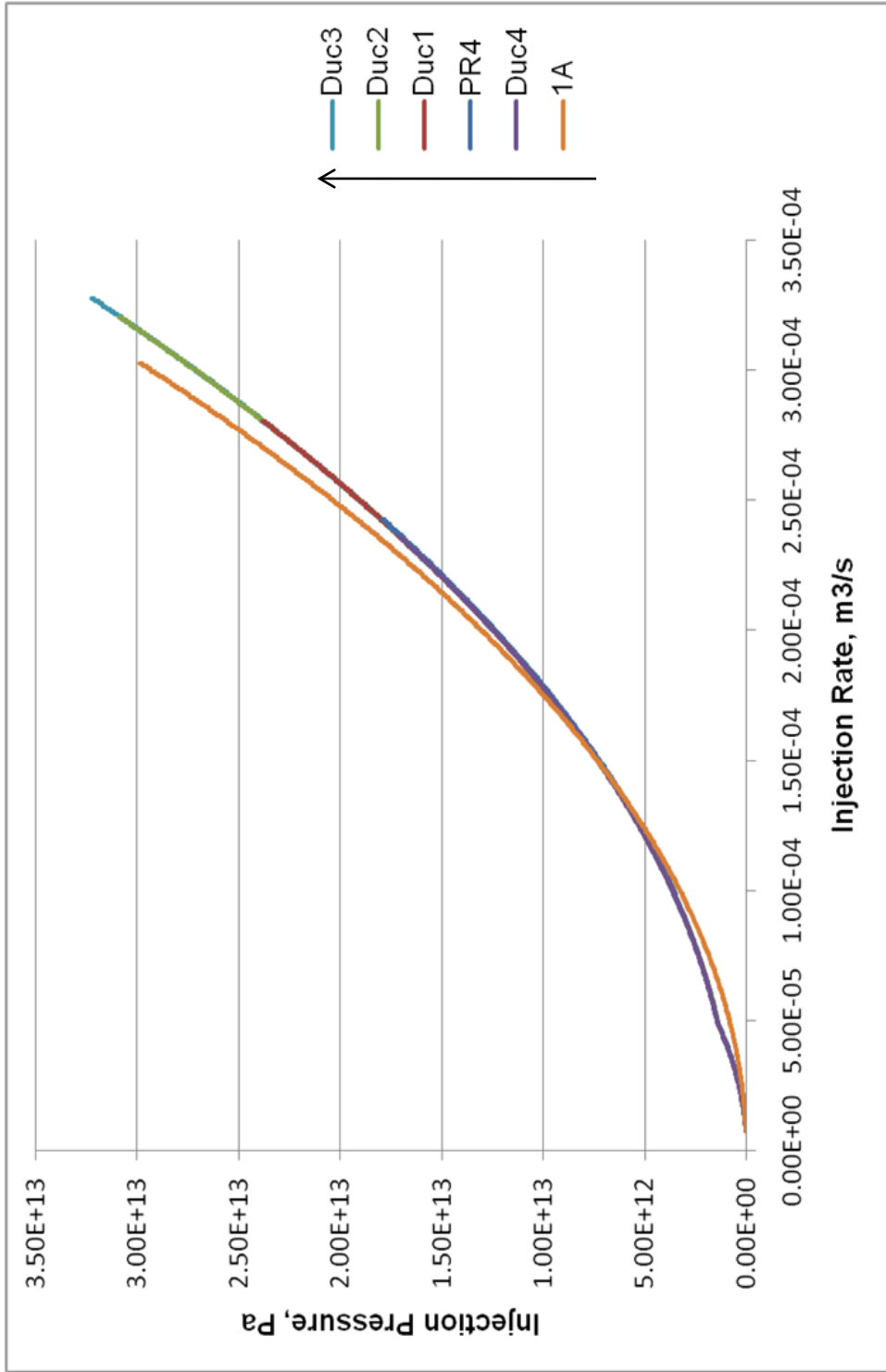


Figure 5-22 Curves of injection pressure vs. flowrate for various ductility runs

Plots of shear/total cracks vs. flowrate () show that the crack types are almost equally distributed in the specimen of Run Duc3, which features a split of approximately 60% for tensile cracks and 40% for shear cracks (recall that for this specimen $S_n = S_s$). The higher shear strength specimen of Run Duc4 shows a higher percentage of tensile cracks (~87%). Meanwhile, the higher normal strength specimen of Run PR4 exhibits approximately 83% of shear cracks. Thus, any deviation from unity for the ratio of shear-to-tensile strength causes a large disparity between the fractions of shear and normal cracks; tensile cracks are more favorably created, though. Considering that PR4 and Duc4 showed similar stress-strain areas under the curve and pressure-flowrate requirements to reach 1000 cracks, it is revealing to find that their cracking behavior is completely opposite. These results suggest that both specimens show equivalent pressure fracturing signatures, but the high percentage of shear cracking for Duc4 hinders the generation of effective hydraulic connectivity. Furthermore, inspection of the stress-strain curves for these 2 specimens shows that the only marked difference occurs in the post-peak behavior. This feature, which is rarely used, may have more relation with ductility than the rather loose descriptions about area under the curve or E comparisons.

On the other hand, the shear/total crack behavior of Run 1A is similar to that of Run Duc1 and not far from Duc2, either. This shows that E alone is a bad predictor of type of cracks to be created, since Run1A has a lower E.

Although UCS increases somewhat with ductility for these samples, the net effect observed in the cracks ratio is opposed to that of the UCS analysis presented earlier; i.e. shear cracking increases with UCS, but the increase in UCS is an effect of the

microproperties modifications needed to increase ductility. On the contrary, in the analysis of UCS, it was observed that shear cracking decreased with UCS. In increasing ductility, the ratio of shear to normal strength was changed by increasing normal strength. As a result, less tensile cracking is observed, and the overall resistance of the specimen increases, which results in a UCS increase. In contrast, the UCS increase in an earlier section was achieved by increasing both shear and normal strength, but keeping the ratio constant. This caused an increase in UCS and in the fraction of tensile cracking. The significance of this result is that tensional settings are induced easier in stronger rocks than in weaker ones.

The behavior of the pressure vs. volumetric strain can be described as linear for all ductility runs (i.e. Duc1 through 4, and PR4), as illustrated in . Nonetheless, the apparently stiffer curves correspond to specimens that were supposed to be more ductile, such as Duc2 and Duc3. This seems to be an effect of the collateral increase in UCS, since it follows the same pattern that was described in UCS runs; i.e. the specimens appear stiffer with UCS increase. However, the comparison with Run1A, which is decidedly more ductile, reveals the correspondence of ductility and stiffness, as the slope of this run is lower. Thus, it appears as if ductility matches the corresponding decrease in stiffness, but does not seem to affect much the linearity of the pressure-volumetric strain relation.

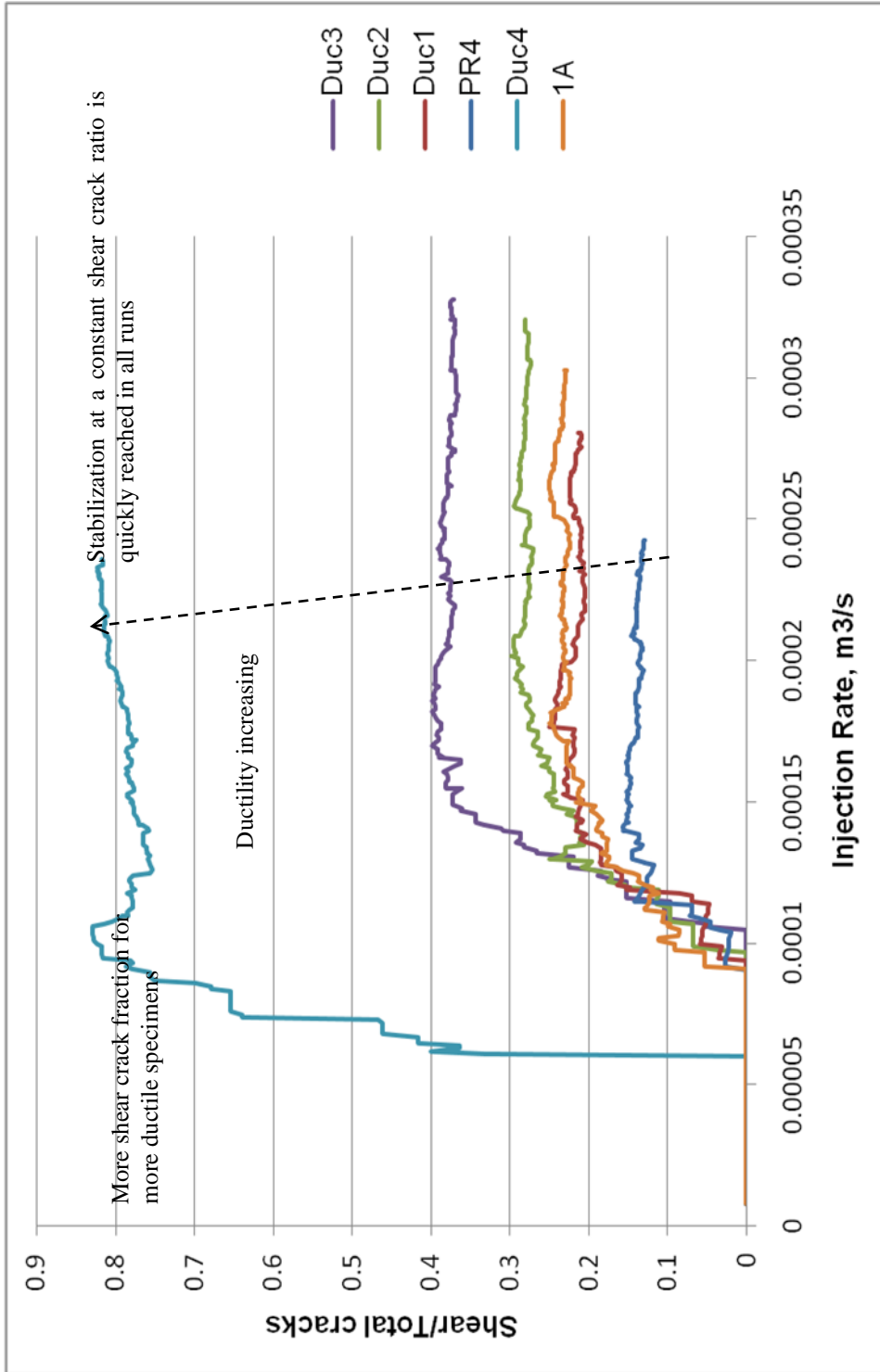


Figure 5-23 Curves of cracks formed vs. injection flowrate for various ductility runs

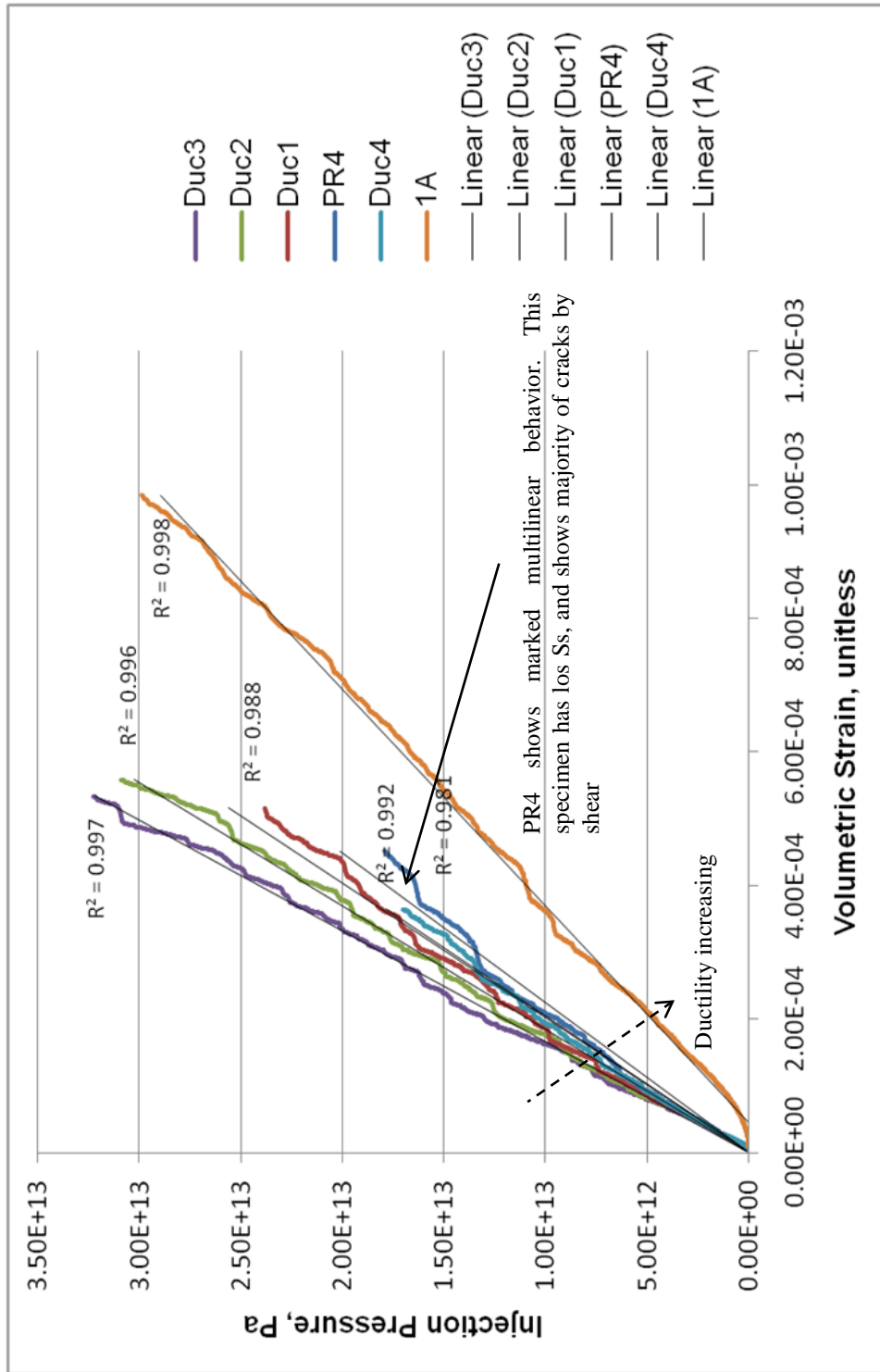


Figure 5-24 Curves of injection pressure vs. volumetric strain for various ductility runs

A narrow crack distribution pattern, stretched in the vertical direction, is observed for the base-case run PR4 (Figure 5-25, top). In comparison, the more ductile Run Duc3 exhibits a flatter pattern (Figure 5-25, bottom). This behavior is associated to the higher brittleness of PR4.

Figure 5-26 shows large compression forces with a wider spread for Duc3, which reinforces the observation about crack distribution. In addition, particles' displacements are larger in the simulation for Duc3, whereas in PR4 the movements are less and more orderly, as depicted in Figure 5-27.

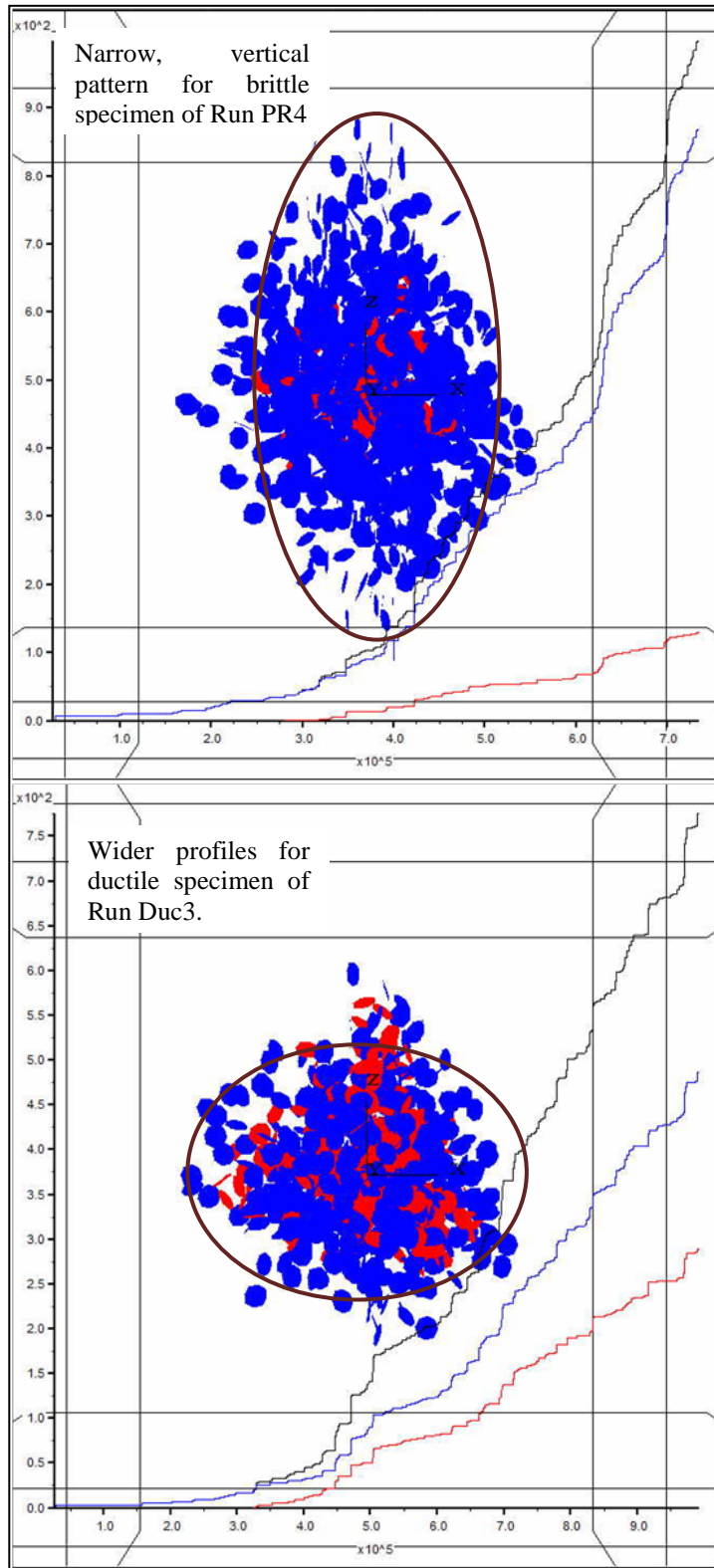


Figure 5-25 Crack agglomeration for Runs 1A-PR4 (top) and Duc3 (bottom)

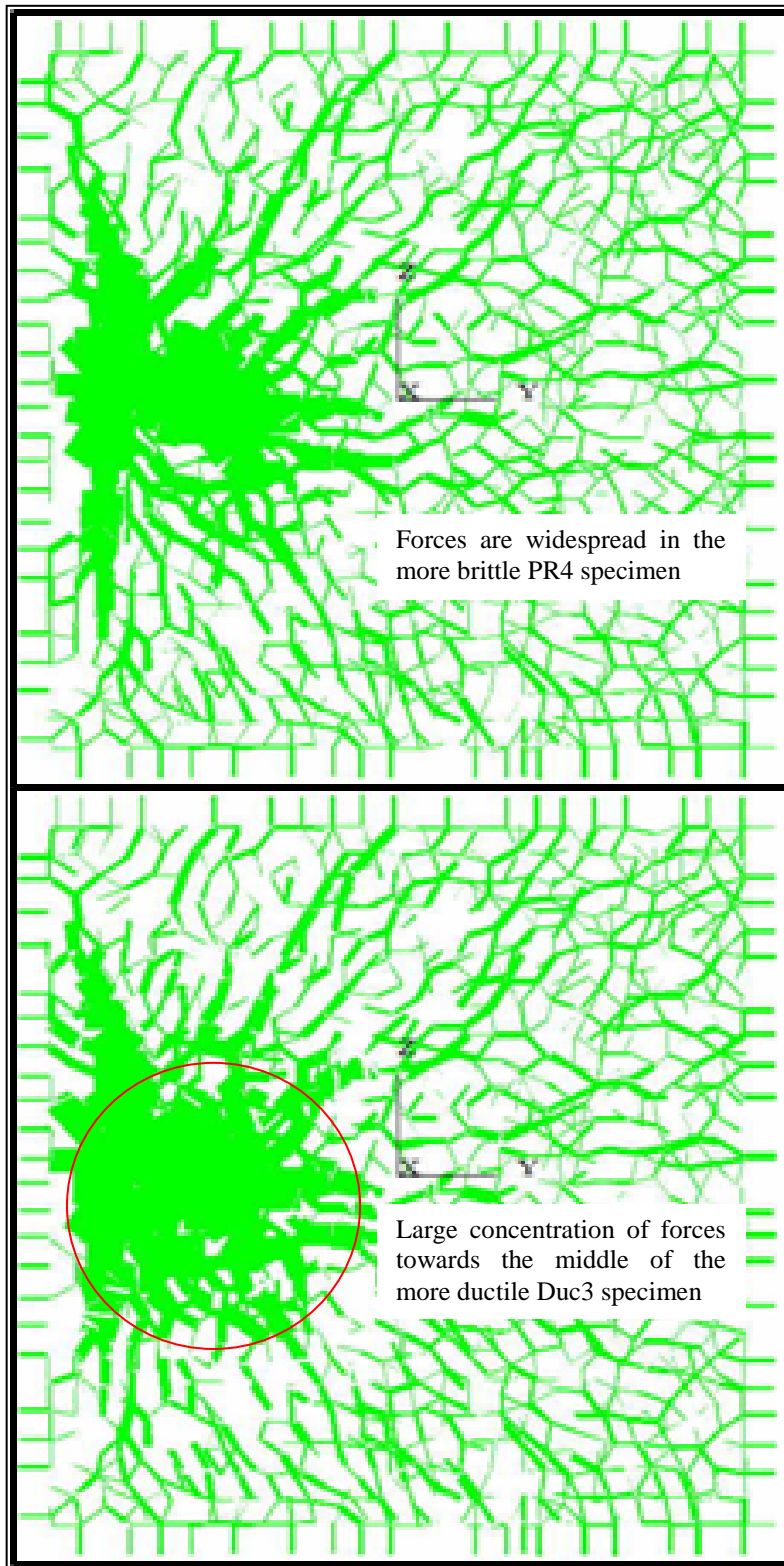


Figure 5-26 Compressive forces for Runs 1A-PR4 (top) and Duc3 (bottom)

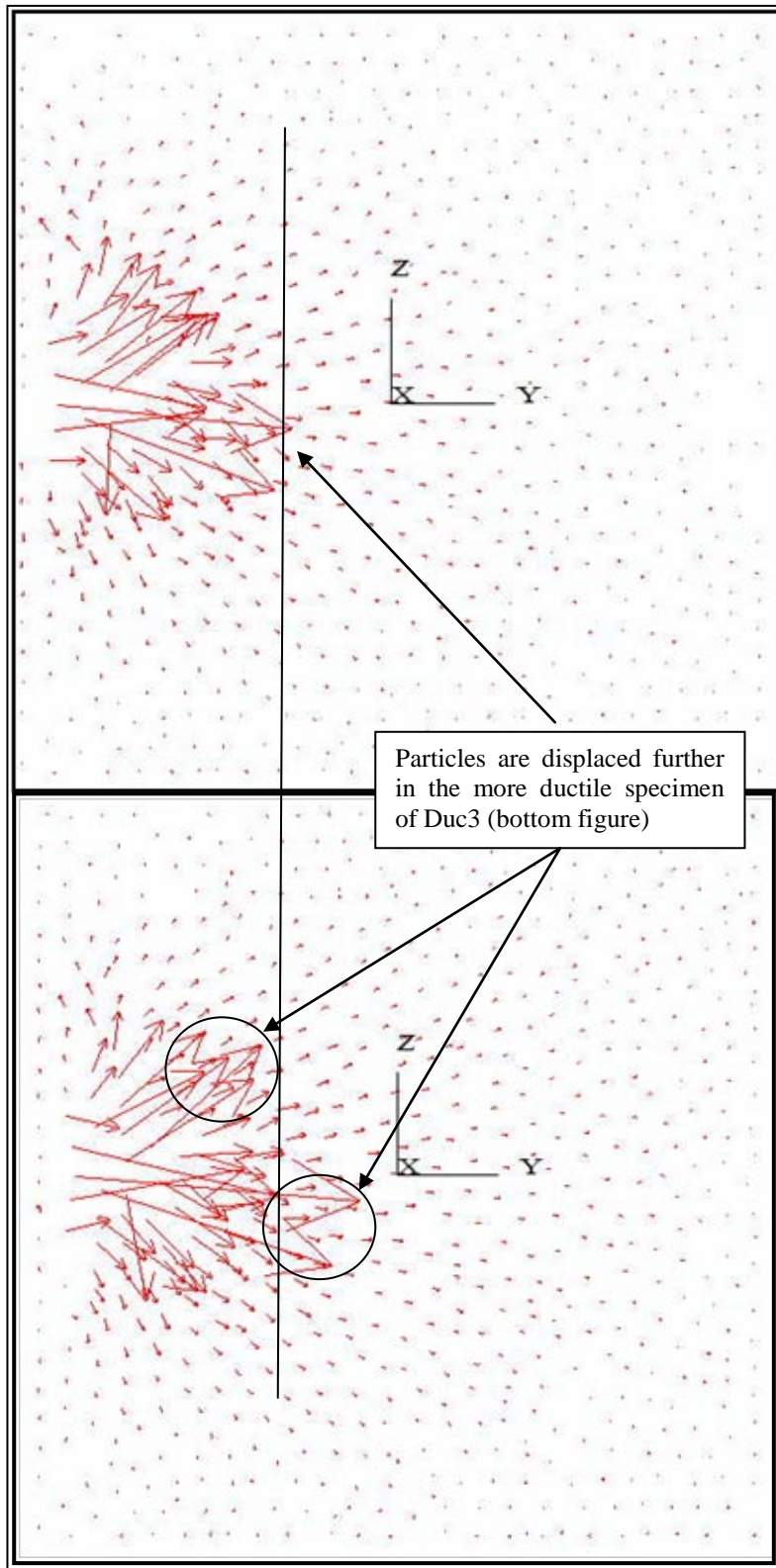


Figure 5-27 Shear forces for Runs 1A-PR4 (top) and Duc3 (bottom)

5.2.5 Strength Heterogeneity Effects

So far, all installed bond strengths were fixed to have the same value. Runs with different values of strength standard deviation were examined, as reported in Table 5-4.

Table 5-4 Strength heterogeneity runs

Run ID	Strength Standard Deviation
Run1_PR4 (Base-Case)	0
Run1_PR4_SD11	5%
Run1_PR4_SD22	10%
Run1_PR4_SD33	20%
Run1_PR4_SD44	30%

It was observed that an increase in standard deviation “weakened” the specimens, i.e. UCS decreased. This is somewhat expected, since the larger standard deviation implies the existence of a greater number of “weaker” links throughout the rock, which are the first to break. Upon further pressurization the remaining bonds, although stronger, are less in number and the overall resistance of the sample diminishes.

Thus, the effects of increasing the strength stress deviation are similar to reducing UCS. One difference is that some stiffness “degradation” process is observed as the fracture propagates. The degradation is more severe for the more heterogeneous samples, as observed in . Another significant difference with respect to the UCS cases is that the cracks are much more scattered for higher strength standard deviations, as observed in Figure 5-29 for the 30% standard deviation-case (top) and the base-case (bottom). The natural reason for this behavior is that stresses generated away from the injection point are high enough to break the weaker bonds existing at those locations.

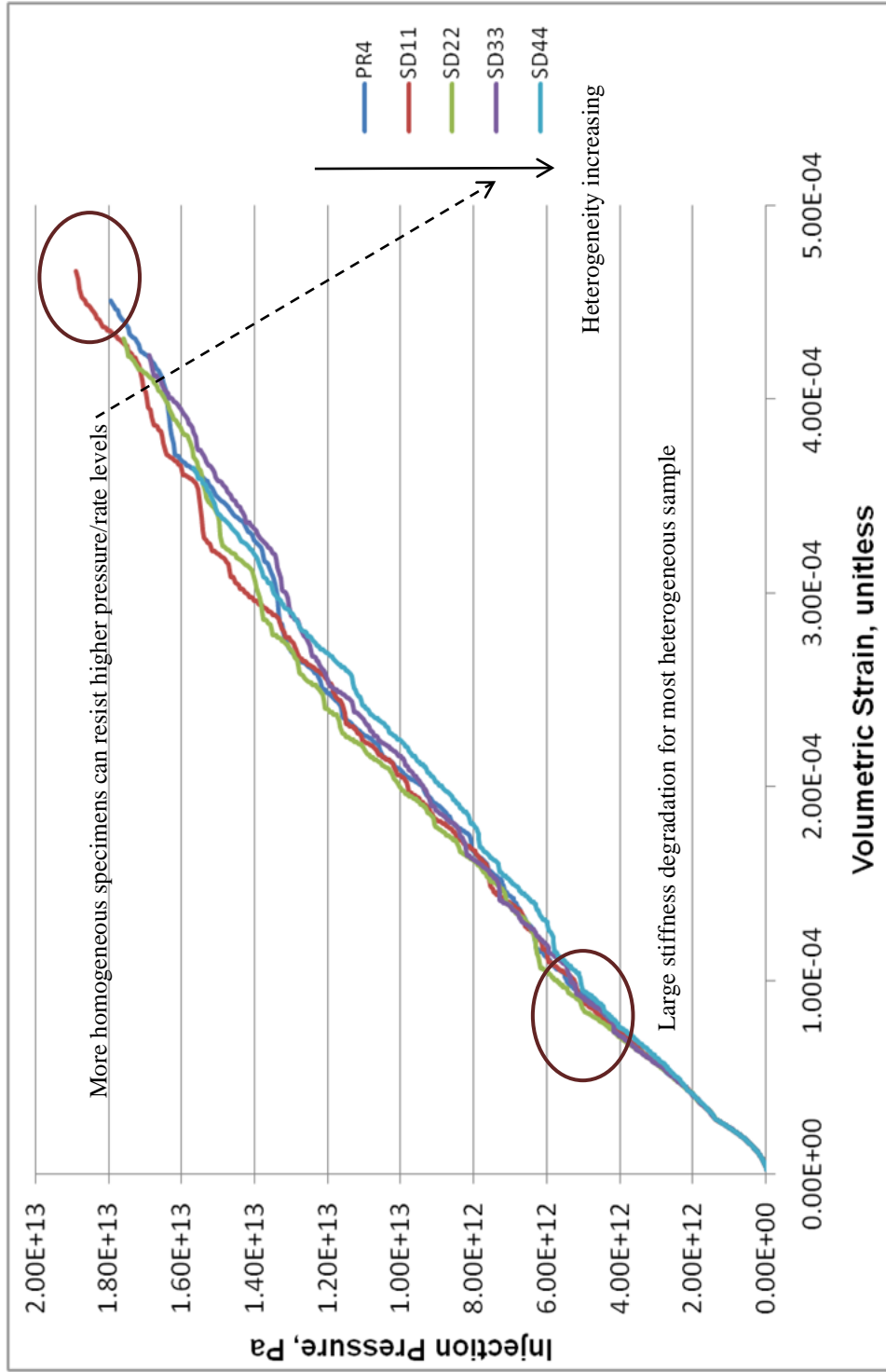


Figure 5-28 Curves of injection pressure vs. volumetric strain for various heterogeneity levels

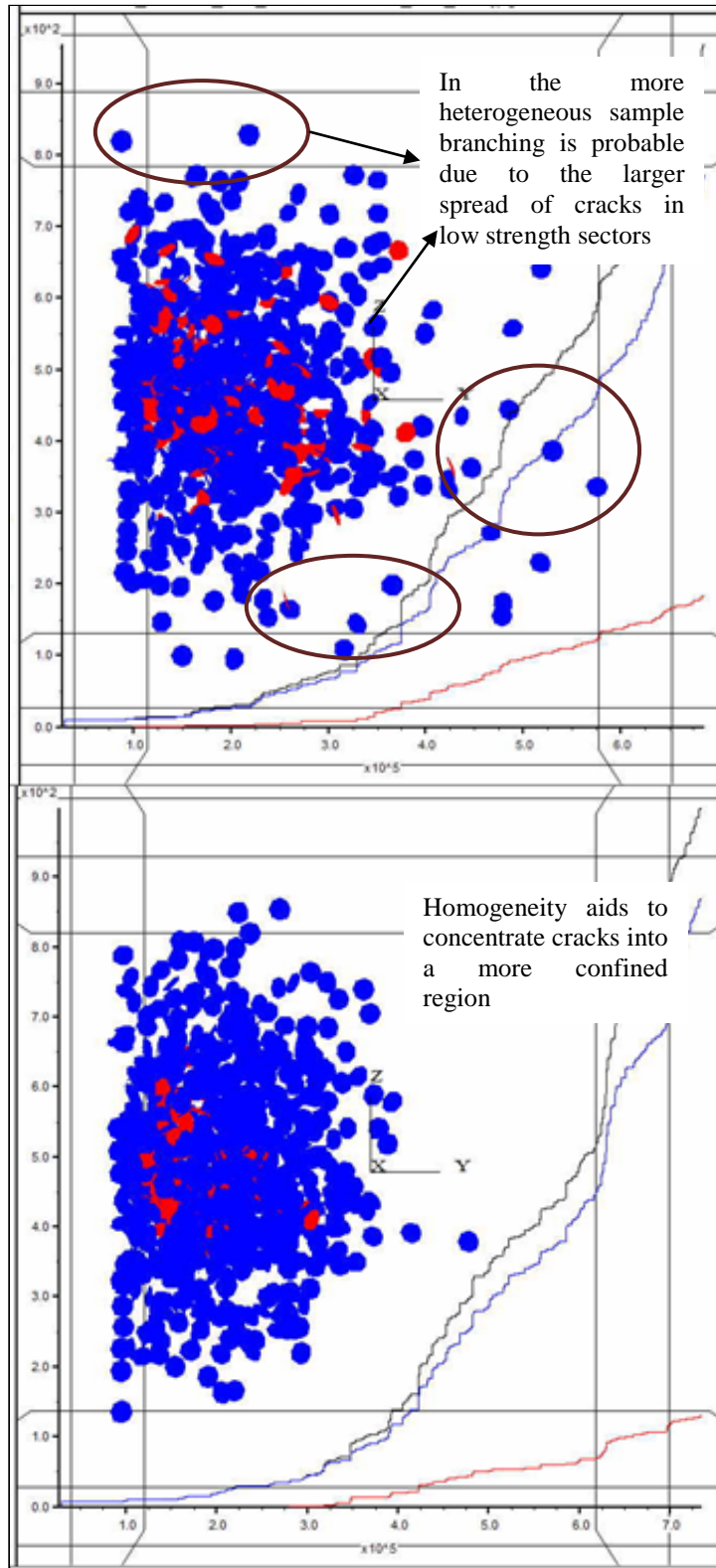


Figure 5-29 Crack agglomeration for Run SD44 (top) and base-case PR4 (bottom)

5.3 STRESS BOUNDARY CONDITIONS EFFECTS

The stress configuration for the base-case consisted of a minimum horizontal stress (S_x), orthogonal to the injection direction, a maximum horizontal stress along the injection direction (S_y), and a vertical stress (S_z) whose magnitude was equal to that of the maximum horizontal stress. This configuration was modified as to evaluate the effects of stress anisotropy, and net deviatoric stress.

5.3.1 Anisotropy

4 runs of decreasing S_y values were carried out, in addition to the base-case, to test horizontal anisotropy; these runs were named 1B through 1E. Similarly, vertical anisotropy was tested by 4 runs of decreasing S_z values, in addition to the base-case; these runs were named 1F through 1I. Table 5-5 lists the stress values used (S_x was maintained at 500 psi).

Table 5-5 Stress values used to evaluate stress anisotropy effect (recall that S_x is 500 psi)

Run ID	S_y , psi	S_z , psi
Base-case (Run1A)	1,000	1,000
Run1B	875	1,000
Run1C	750	1,000
Run1D	625	1,000
Run1E	500	1,000
Run1F	1,000	875
Run1G	1,000	750
Run1H	1,000	625
Run1I	1,000	500

Plots of pressure vs. rate for the horizontal anisotropy cases follow the same line (see).

The run corresponding to the intermediate stress being equal to the minimum stress, i.e.

horizontal stress isotropy, Run 1E, generated 1000 cracks at about 10% lower flowrates and pressures as compared to the base-case, Run1A. A similar trend is observed for the vertical isotropy case, Run 1I. These results indicate that the intermediate stress seems to play a minor role in the fracturing character of the specimen; as this stress reduces, so does the required flowrate and injection rate required to generate cracks. An explanation for this observation is that stress isotropy in an arbitrary plane eliminates shear in that plane, while the stress component perpendicular to the plane creates additional tension via the Poisson's ratio effect (recall that isotropy was achieved by reducing the intermediate stress). Nonetheless, this trend is not absolute across all runs. For instance, Run1C shows the highest pressure-flowrate values to reach 1000 cracks. This Run corresponds to the intermediate (horizontal) stress being halfway between the maximum (vertical) and minimum (horizontal) stress. In contrast, when the intermediate (vertical) stress is halfway between the other stresses, the necessary pressures and rates were very low. A combination of effects is suggested to explain these observations: in the former case, the decrease in the intermediate stress in the horizontal direction induces some rotation of the preferential orientation of cracks, because of onset of vertical anisotropy that did not exist in the base-case; in the latter, a similar scenario develops, but with the vertical boundary being closer to the injection point, new crack directions are added to the existing ones.

Overall, graphs of shear-to-total cracks vs. flowrate (see) show that runs with low intermediate stresses tend to favor tensional cracking, especially for those simulations where the intermediate stress is horizontal. For instance, runs 1F, 1A, and 1G are at the top of shear crack fraction, whereas 1C, 1D, and 1E are at the bottom. These observations

agree with those about pressure-rate curves.

The analysis of pressure vs. volumetric strain shows multi-linearity (see). The results for lower horizontal intermediate stress appear as if those specimens were stiffer. For example, Runs 1D and 1E seem as if they were stiffer than the rest.

The above results suggest that horizontal isotropy facilitates fracture creation and propagation. However, inspection of crack locations paints a different picture. As the intermediate horizontal stress decreases, the preferential horizontal direction propagation is blurred due to the onset of a bi-axial stress situation (Figure 5-33). As a result, as stress isotropy develops on the horizontal plane, the cracks' agglomeration becomes shorter and wider. Hence, the expected fractures would be much less efficient in penetrating deep into the formation. Although a short and wide fracture may be beneficial in many cases, the crack location graphs reveal the importance of considering the magnitude of the intermediate stress. A similar situation is observed with variation of the intermediate vertical stress, (Figure 5-34) but in those cases the "flattening" of the fracture profile occurs on the horizontal plane.

Graphs of compressional contact forces for 1A (Figure 5-35, top) and 1E (Figure 5-35, bottom) confirm the trend observed in cracks' location. Likewise, the displacement vector field of these two runs show that movement occurs more preferably along Shmin direction in Run1A (Figure 5-36).

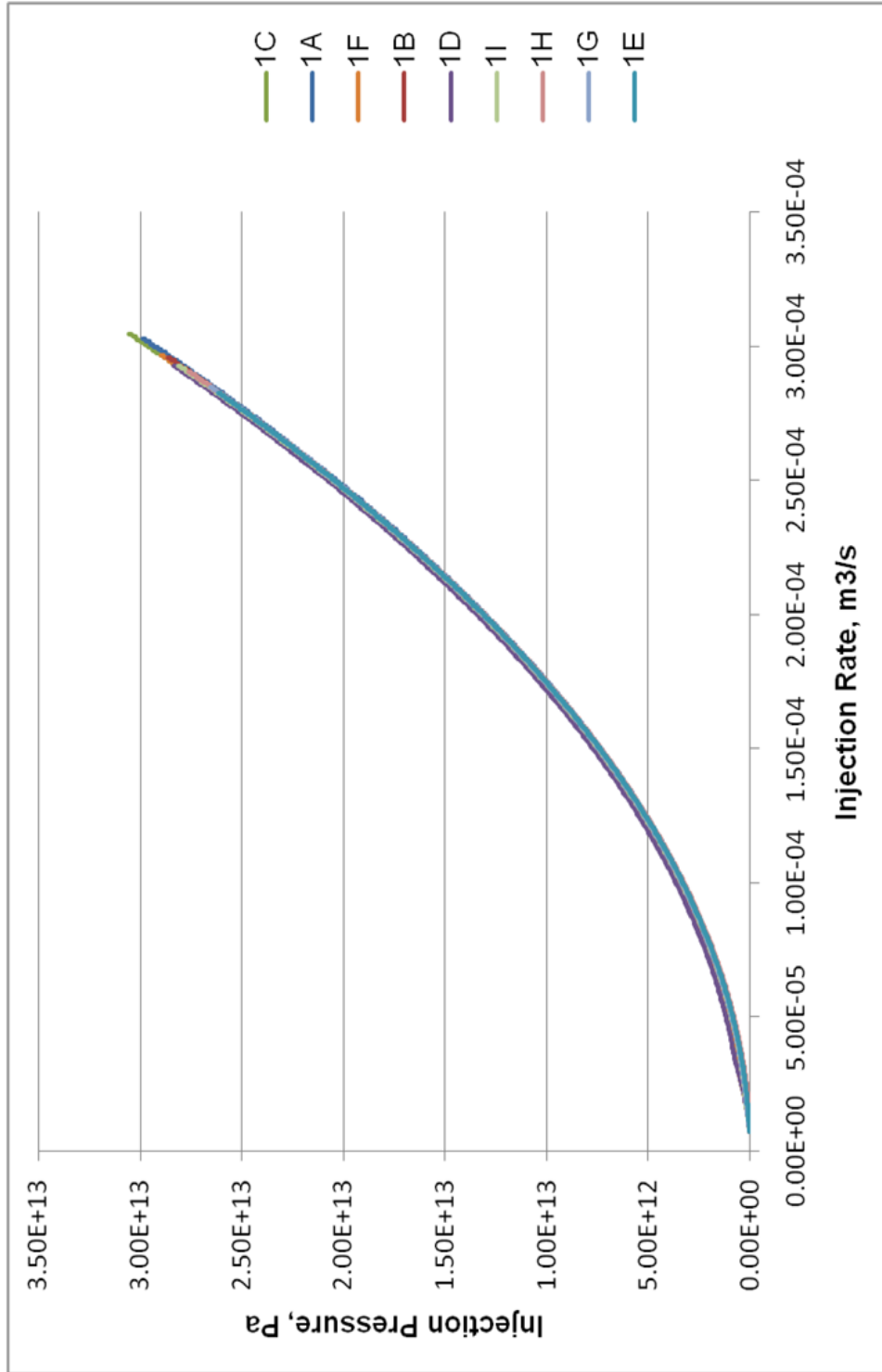


Figure 5-30 Curves of injection pressure vs. flowrate for various stress anisotropy runs

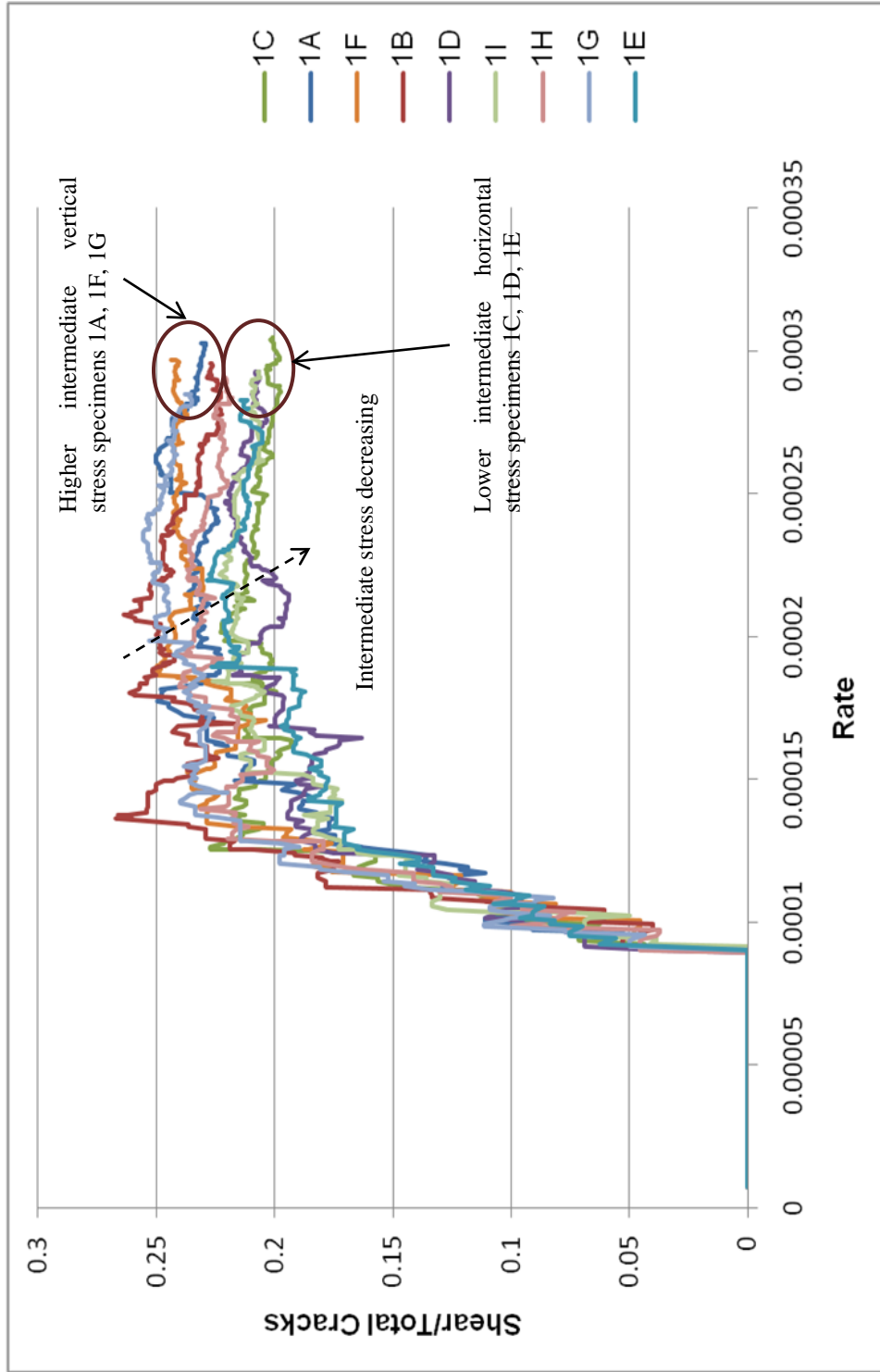


Figure 5-31 Curves of shear to total cracks vs. injection flowrate for various stress anisotropy runs

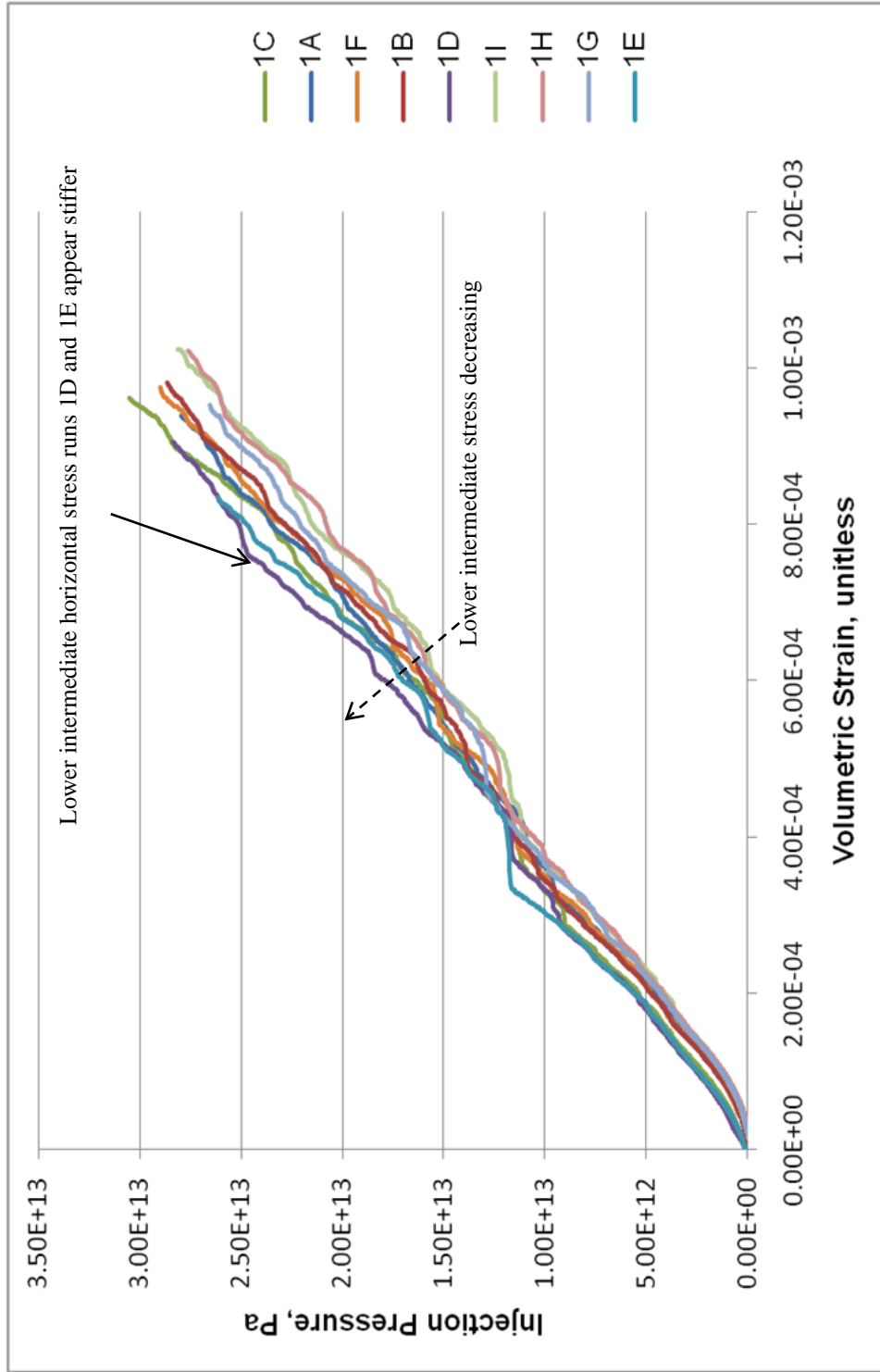


Figure 5-32 Curves of injection pressure vs. volumetric strain for various stress anisotropy runs

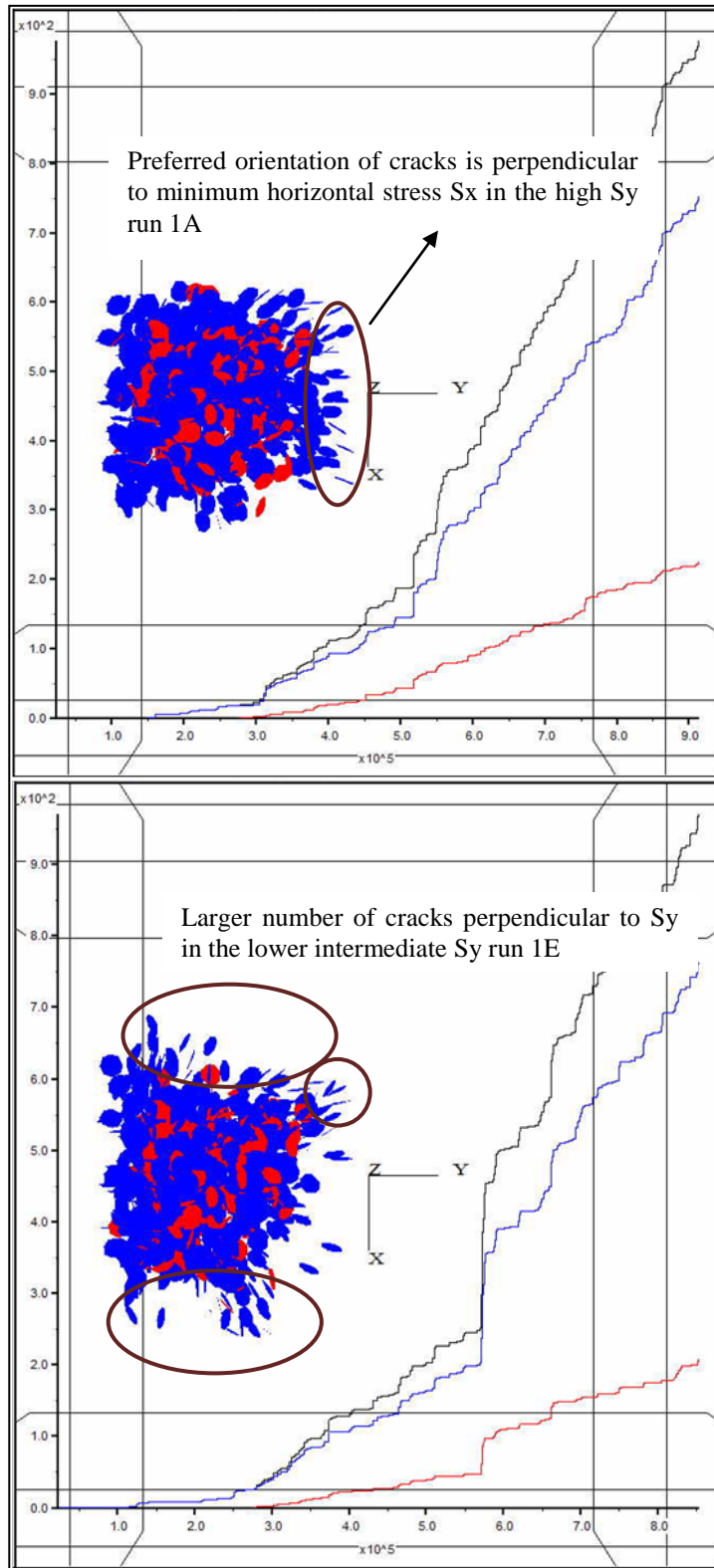


Figure 5-33 Top view of crack agglomeration for Runs 1A (high intermediate horizontal stress S_y , on top), and 1E (low intermediate horizontal stress S_y , on bottom)

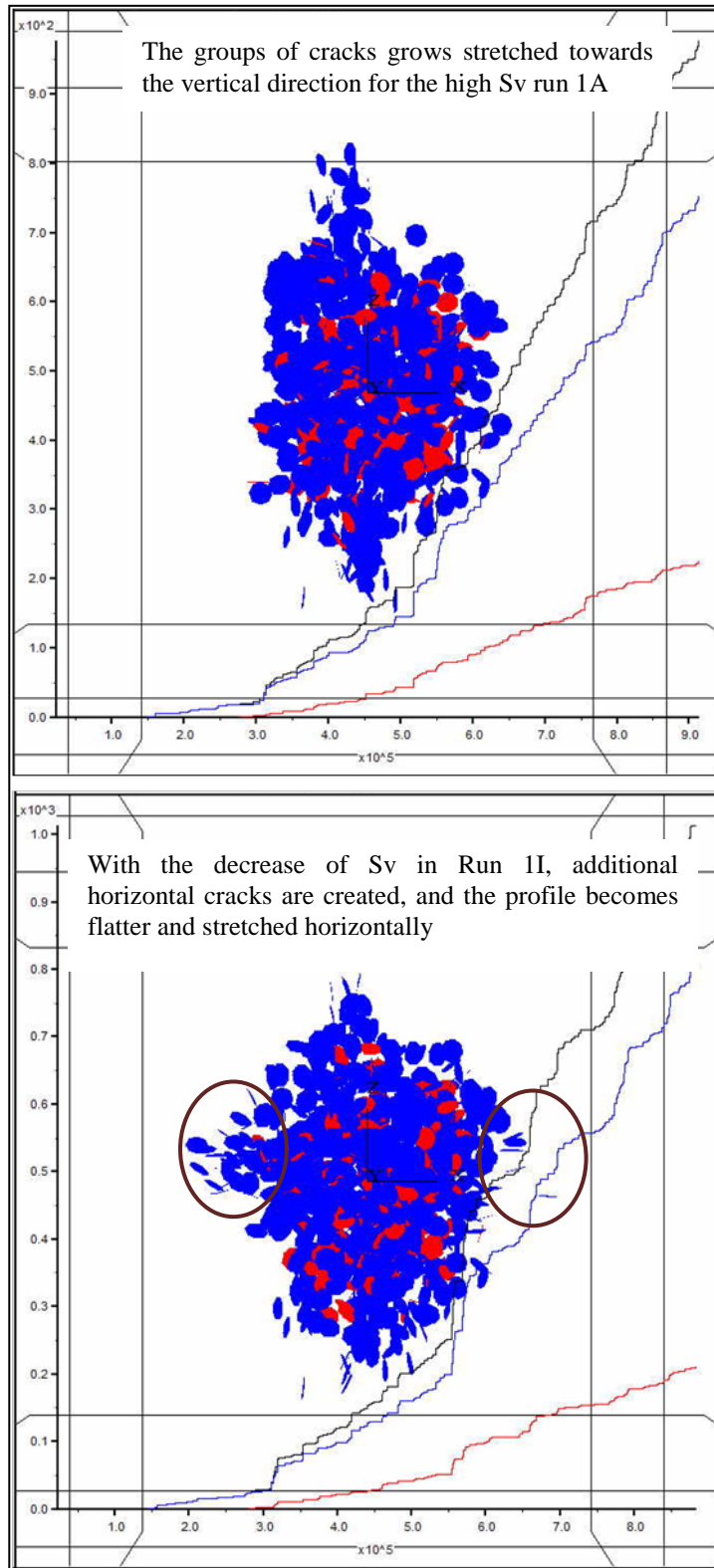


Figure 5-34 Back view of crack agglomeration for Runs 1A (high intermediate vertical stress S_v , on top), and 1E (low intermediate vertical stress S_v , on bottom)

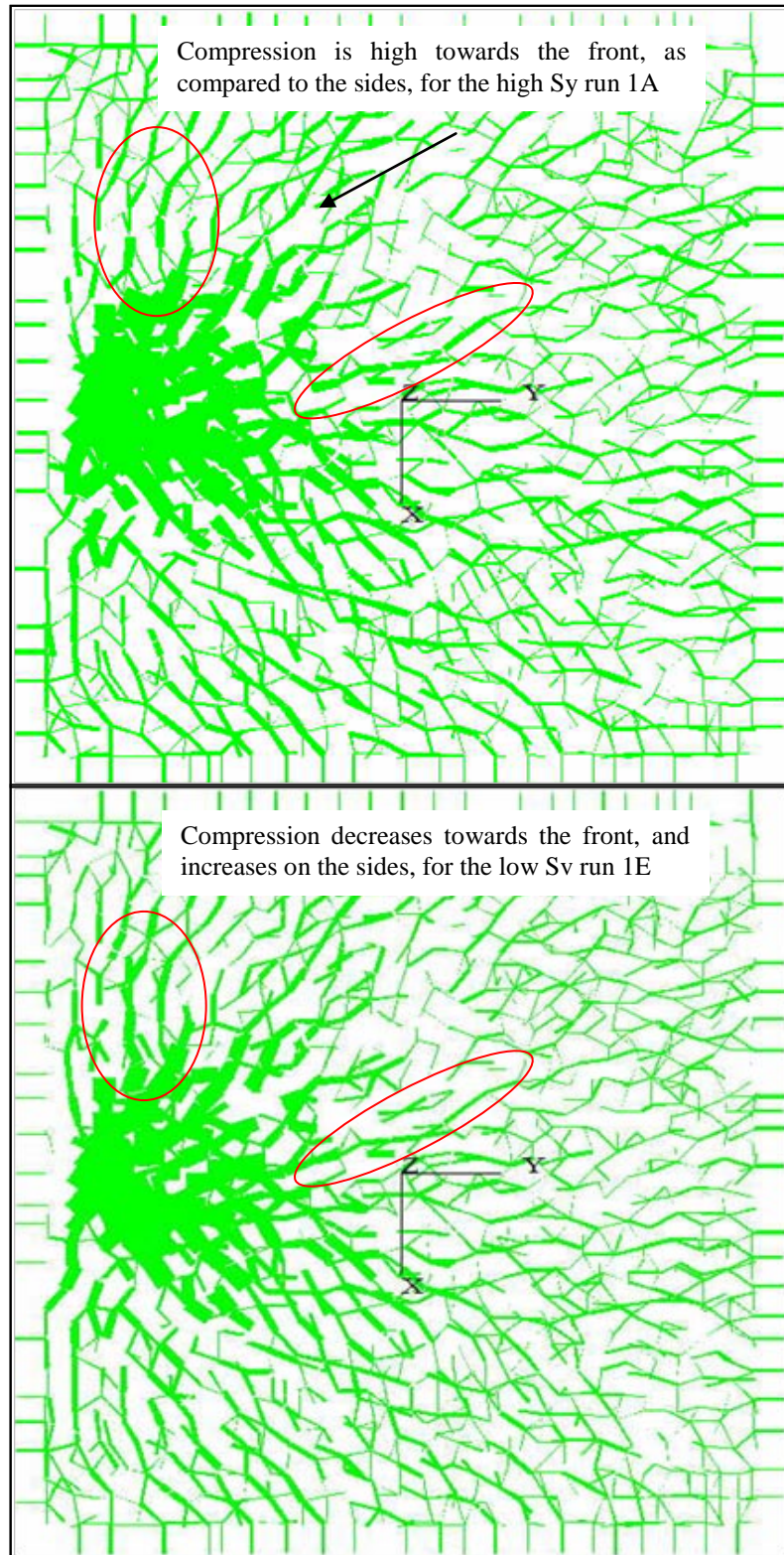


Figure 5-35 Top view of compressive forces for Runs 1A (high intermediate horizontal stress S_y on top), and 1E (low intermediate horizontal stress S_y , on bottom)

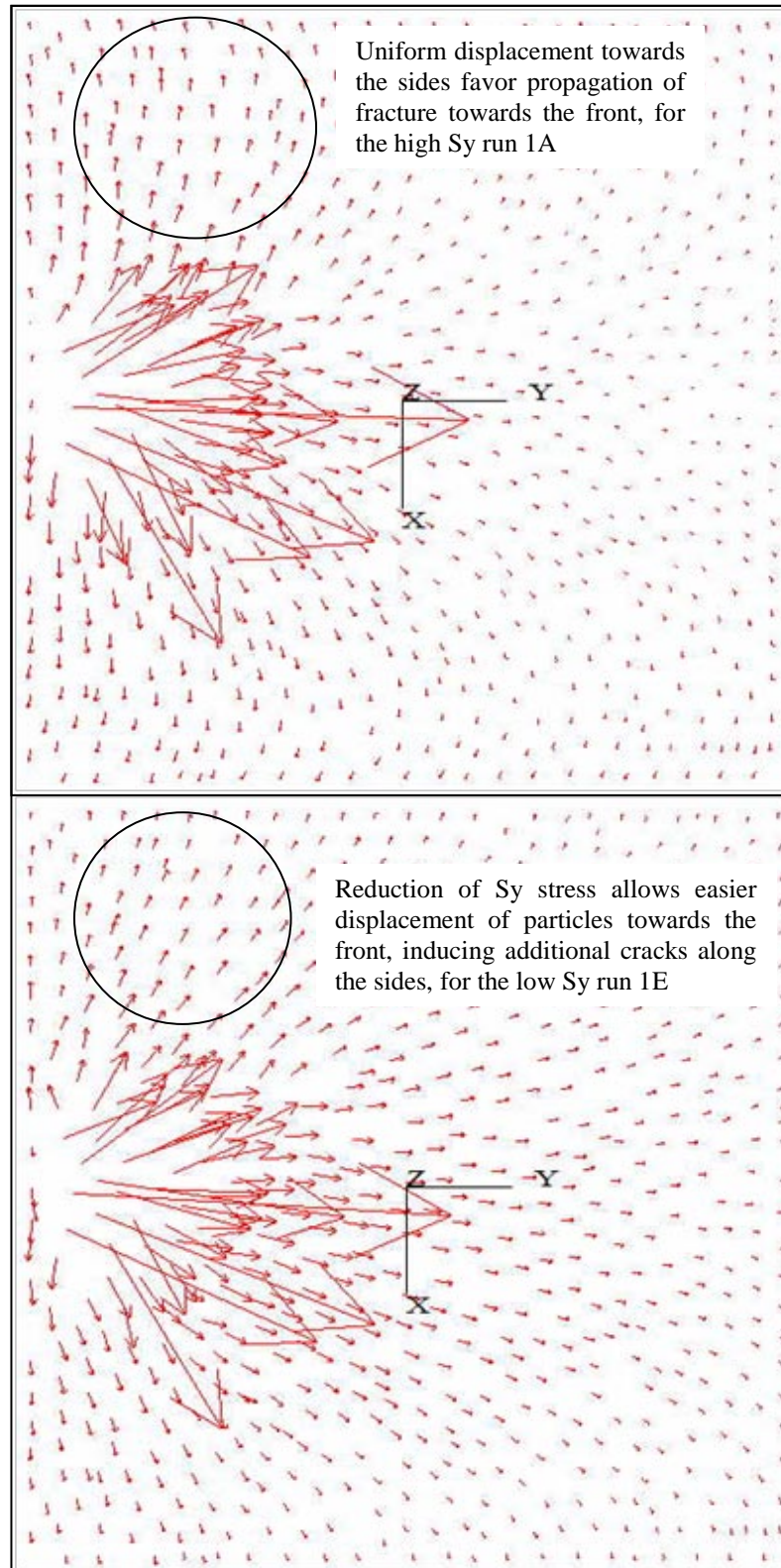


Figure 5-36 Top view of displacements for Runs 1A (high intermediate horizontal stress S_y on top), and 1E (low intermediate horizontal stress S_y , on bottom)

5.3.2 Deviatoric Stress

To test the influence of deviatoric stresses, the difference between the maximum and minimum stresses was decreased in regular 100 psi intervals. Two series of 3 runs were executed, named 1A1 to 1A6; the first series consisted of reducing S_y and S_z in equal 100 psi steps, while maintaining S_x constant at 500 psi; the second series consisted of increasing S_x in 100 psi steps, while maintaining S_y and S_z constant at 1000 psi. The list of the values used and the run names are reported in Table 5-6.

Table 5-6 Stress values used to evaluate deviatoric stress effect

Run ID	$S_y = S_z$, psi	S_x , psi
Base-case (Run1A)	1,000	500
Run1A1	900	500
Run1A2	800	500
Run1A3	700	500
Run1A4	1,000	600
Run1A5	1,000	700
Run1A6	1,000	800

Plots of injection pressure vs. rate () show that the pressure to create a fixed number of cracks increases for higher S_{hmin} cases, even if the deviatoric remains constant. For instance, the deviatoric stress given by the difference between 1,500-1,900 psi and between 1,600-2,000 psi is the same (400 psi), but the latter case requires higher pressure, which may be attributable to S_{hmin} being greater. Also, it seems as if the pressure increases as stress approximates isotropy as demonstrated by the pressure-rate increase from between 1A1 and 1A2, and between 1A4 and 1A6. Nonetheless, 1A5 and 1A do not conform to this trend.

Plots of shear to total cracks vs. flowrate showed that isotropy and larger minimum

stresses favor shear cracking (). In other words, the shear cracking response depends both on the net deviatoric, but also on the magnitude of the minimum stress. Once again, Run 1A does not fit the trend perfectly, but it seems that the reason may be that fluctuations of shear to total cracking are more severe on this run than in the others. Run 1A5 is starting to show some stabilization and seems to conform to the shear cracking trend.

Analyses of pressure vs. strain show a similar multilinear tendency for all cases (). The largest apparent stiffness “shift” from one line to the next occurs for Run 1A. The apparent stiffness increases successively as deviatoric stress is reduced (Runs 1A1, 1A2, in order), and then as the minimum stress increases (Runs 1A4, 1A5, 1A6, in order). Thus, increasing stress isotropy and minimum stress favors apparent stiffness.

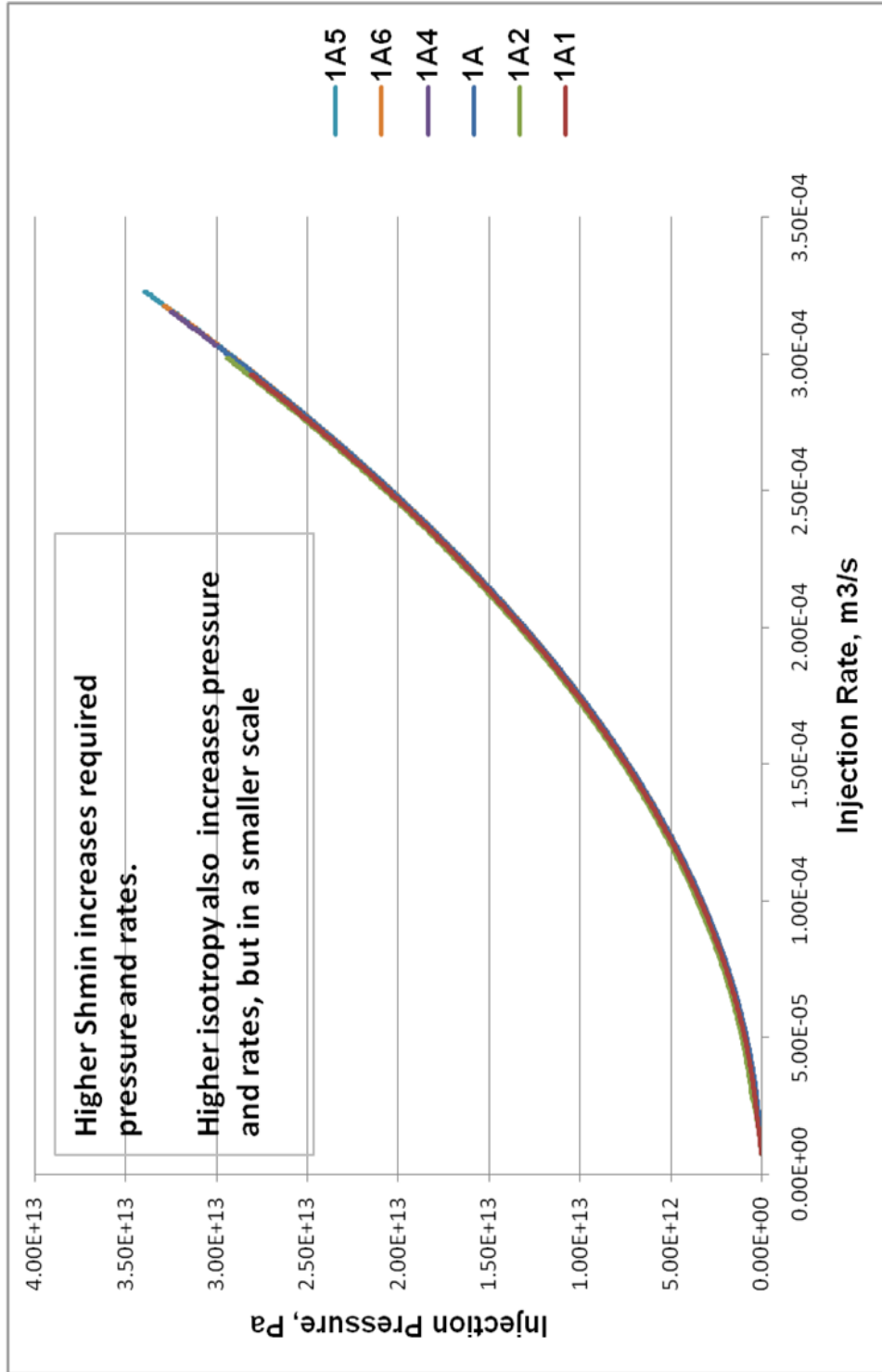


Figure 5-37 Curves of injection pressure vs. flowrate for various deviatoric stresses

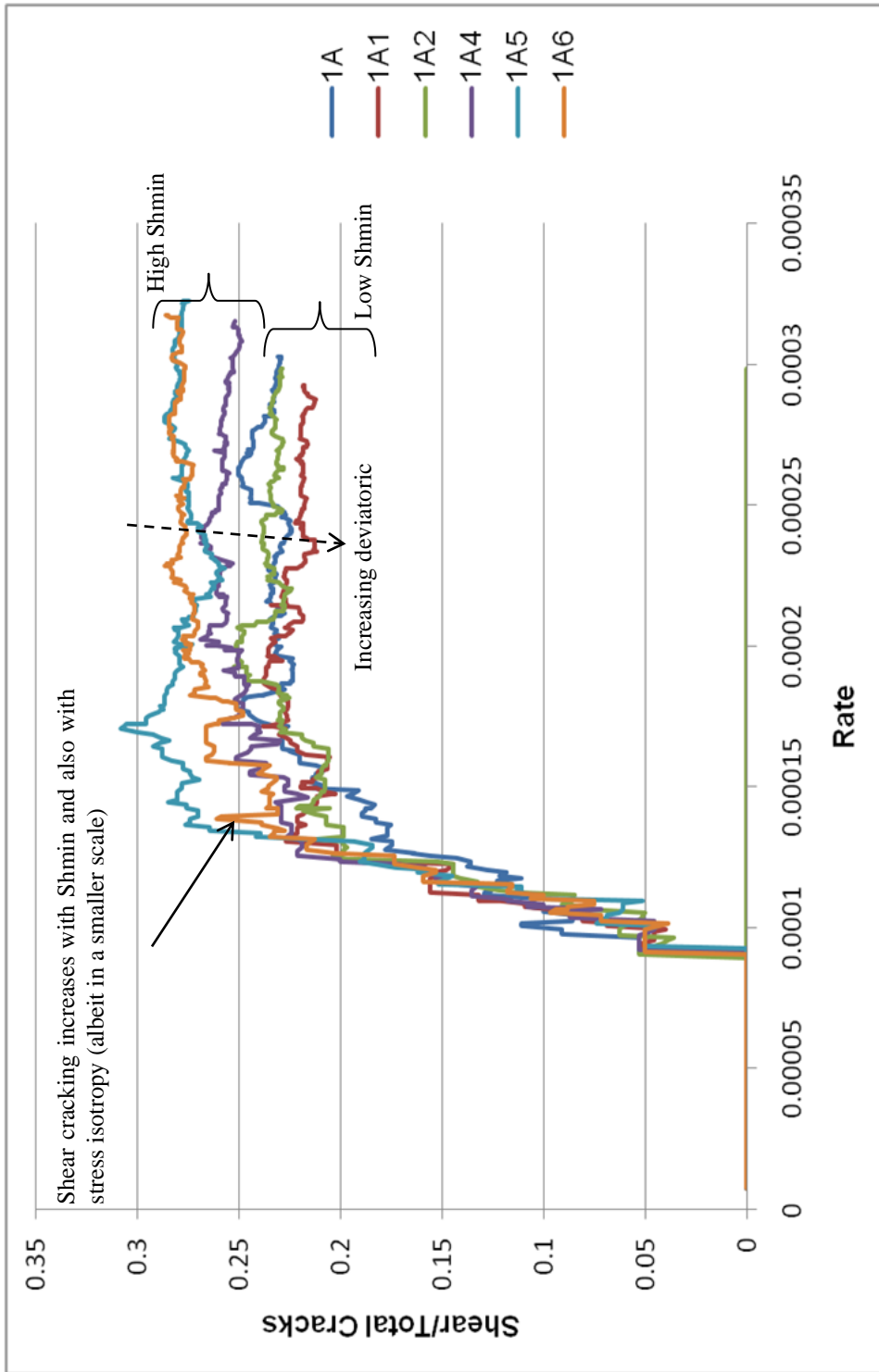


Figure 5-38 Curves of shear to total cracks vs. flowrate for various deviatoric stresses

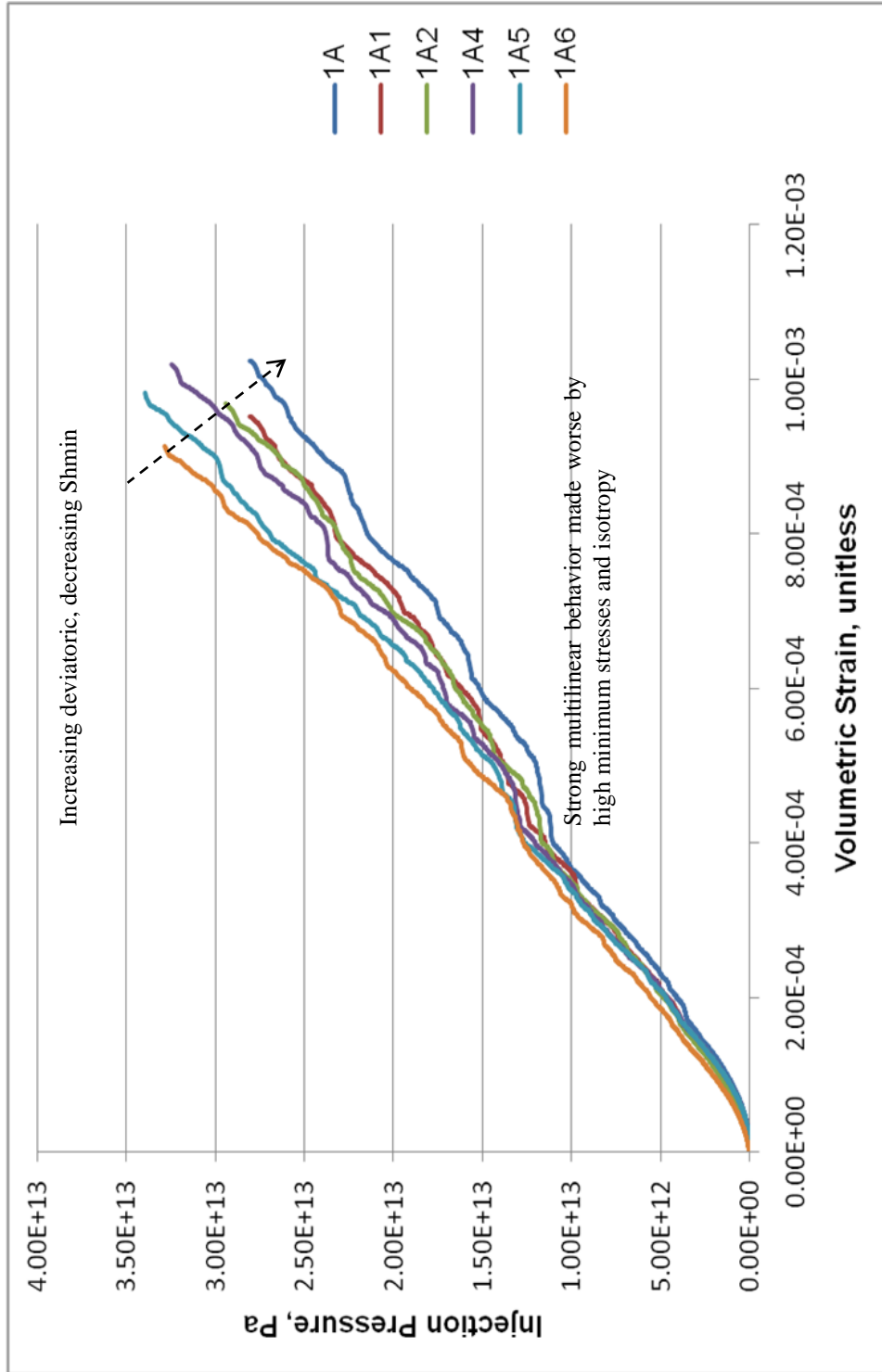


Figure 5-39 Curves of injection pressure vs. volumetric strain for various deviatoric stresses

With respect to crack locations, comparison of Run 1A (Figure 5-40, top) with 1A2 (Figure 5-40, bottom) show that the fracture shape becomes more rounded and compact as the deviatoric stress decreases by reduction of the maximum stresses. This is an expected consequence, since a lower differential stress distorts the preferential fracture growth tendency onto the higher stresses plane, by permitting generation of cracks in oblique directions to such plane. These oblique cracks can't be created under a high deviatoric stress ambient. The effect is much more pronounced when the deviatoric is reduced by successive increments of the minimum stress, as observed in Figure 5-41 for Runs 1A (top) and 1A6 (bottom). The reason can be traced to the higher minimum stress, which enables a higher increment in pressure before a group of cracks can be formed. Due to the extra pressure (and hence, stresses), a greater amount of energy is released during cracking of bonds, and the fracture is propagated to the immediate neighboring locations.

The compressive contact force analyses reinforce the observations from the crack locations; i.e., in the more isotropic configurations, the forces are more concentrated toward the center. For example, see the contact forces of Runs 1A and 1A2 in Figure 5-42 top and bottom, respectively. The response on the minimum stress increasing runs is similar to those in the maximum stress decreasing; i.e. as isotropy increases, the crack agglomeration tends towards a more concentrated elliptical (almost circular) shape. The difference at similar anisotropy configurations between the two series of runs is that compression forces seem higher in the case of increasing minimum stresses. This makes sense because higher stresses require higher pressures to counteract it.

The displacements between runs show very subtle rotation in displacements of the particles in the center of the sample as deviatoric increases, as illustrated by Runs 1A (Figure 5-43, top) and 1A6 (Figure 5-43, bottom).

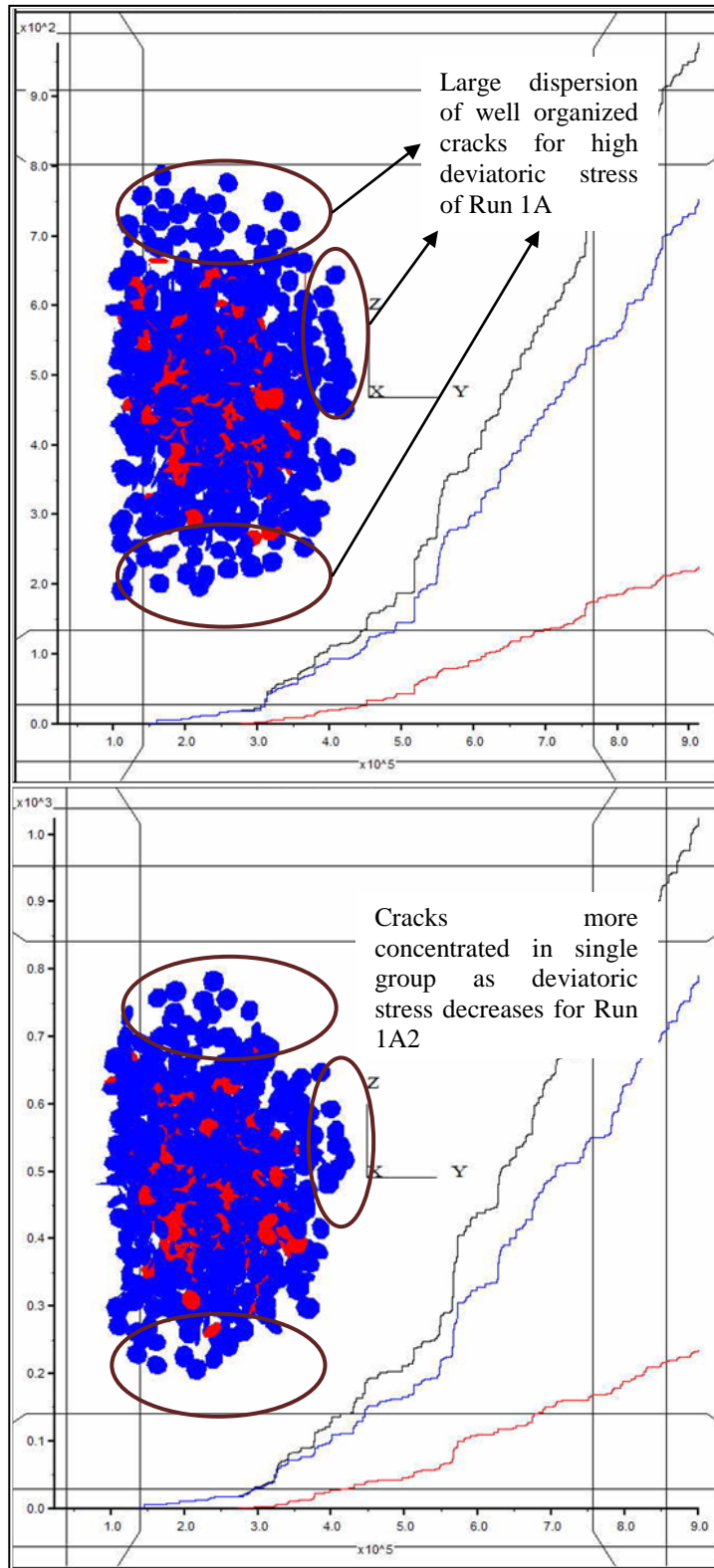


Figure 5-40 Crack agglomeration for Runs 1A (top), and 1A2 (bottom)

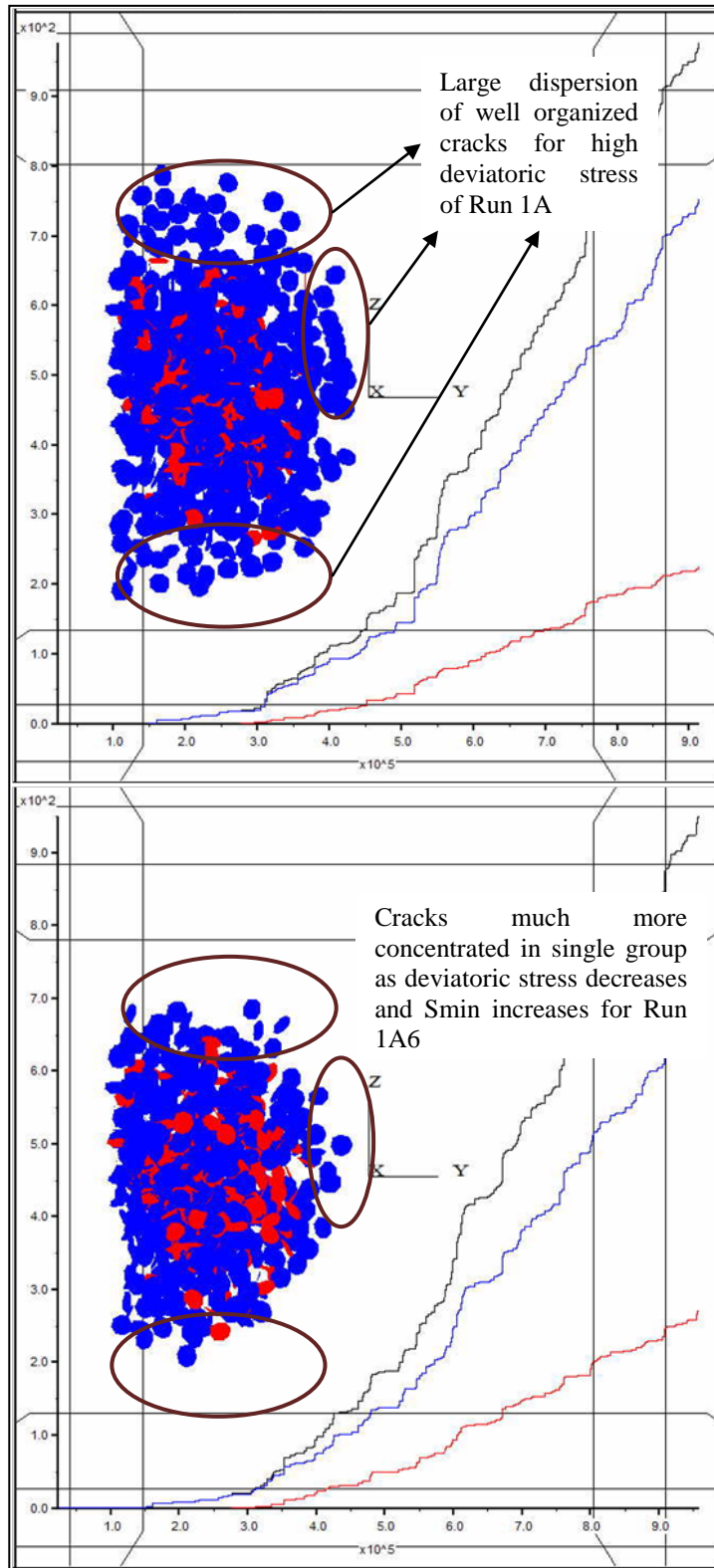


Figure 5-41 Crack agglomeration for Runs 1A (top), and 1A6 (bottom)

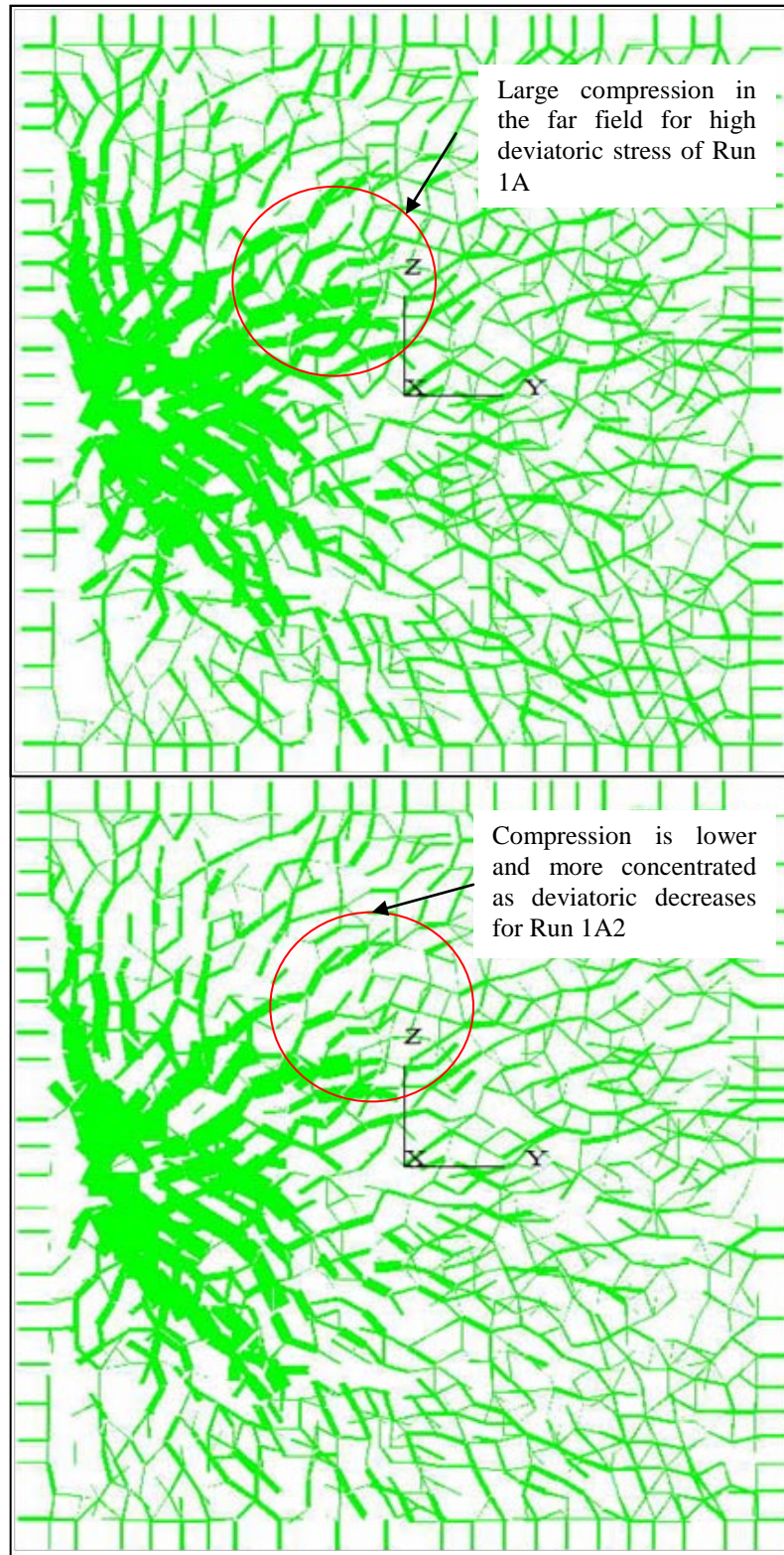


Figure 5-42 Compressive forces for Runs 1A (top), and 1A2 (bottom)

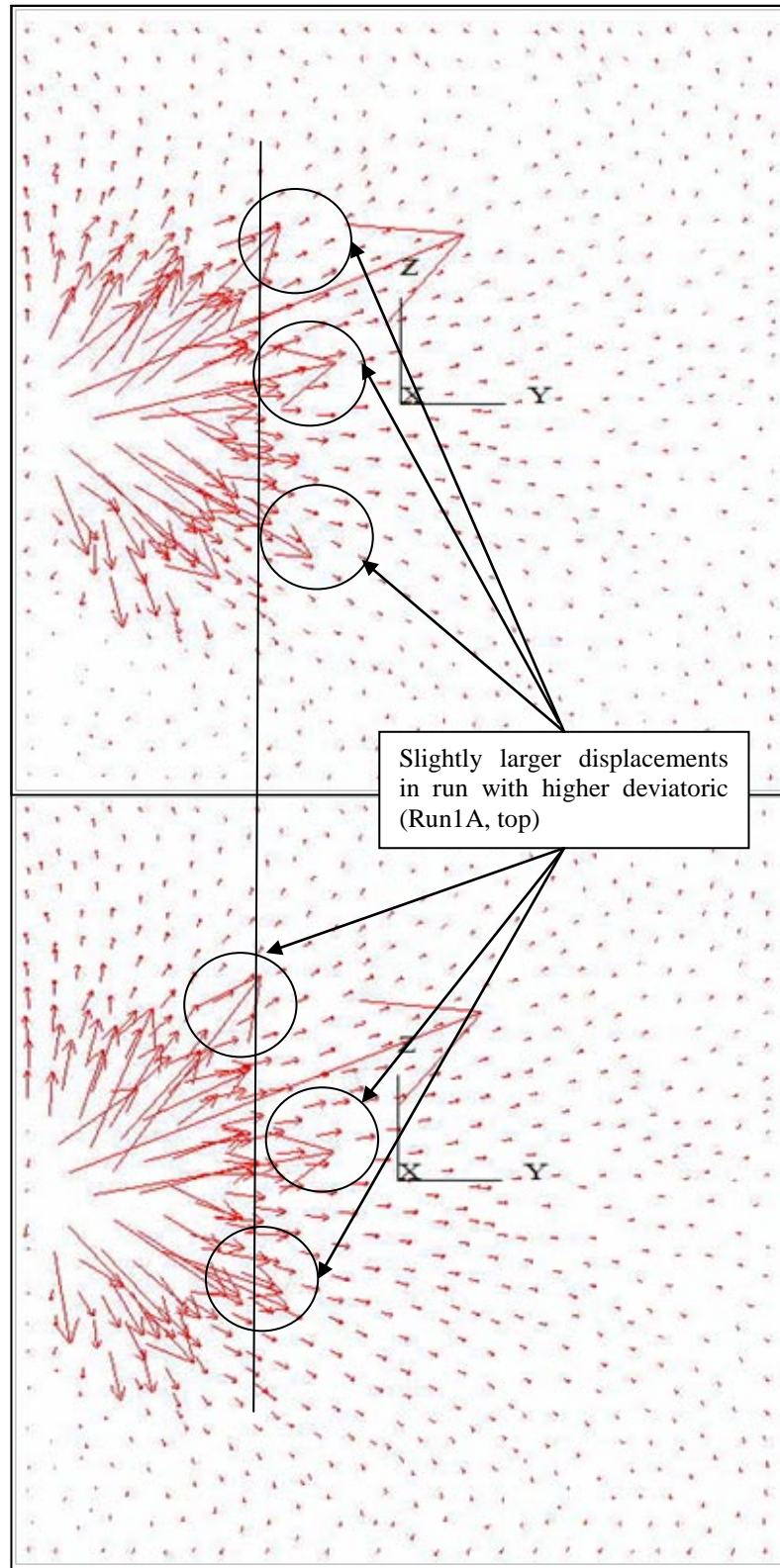


Figure 5-43 Displacements for Runs 1A (top), and 1A6 (bottom)

5.4 MOHR DIAGRAM ANALYSIS

The Mohr diagram is a plot of shear (τ) vs. normal stresses (σ), as illustrated in Figure 5-44. For a bi-axial stress configuration (i.e. two of the three principal stresses are equal in magnitude), a circle drawn through the stress values represent the stress exerted on all and any surfaces oriented arbitrarily with respect to the stress field direction, at that particular location (Roegiers, 2005b). In the same plot, failure criteria can be represented as straight lines that define the combination of stresses that will cause damage to the rock, in either shear or tensional fashion.

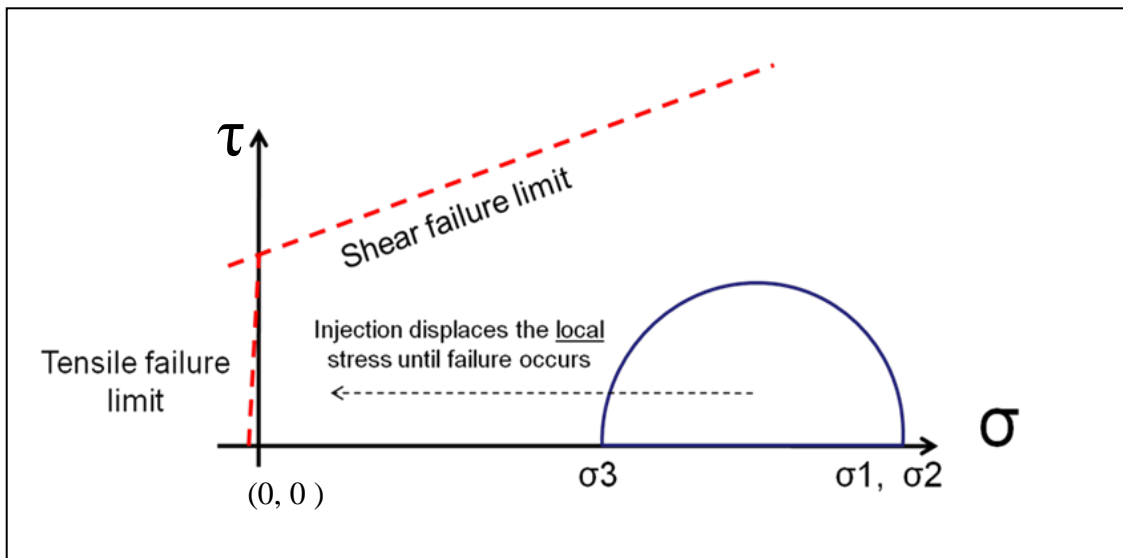


Figure 5-44 Representation of stress, failure criteria, and pressure injection effect on the Mohr diagram

As illustrated in the figure, the effect of increasing injection pressure is to reduce the stress effectively carried by the rock, which is represented in the diagram by displacement of the circle towards the failure limit lines (left direction in this case). Therefore, the Mohr diagram enables macroscopic analysis of the behavior observed in the simulations, in which cracking resulted from small-scale interactions.

The effect of lowering UCS is readily illustrated in the Mohr diagram: a rock that has been brought to conditions close to failure, will show a higher number of shear cracks for lower UCS values, since the shear failure limit would drop, and a larger intersection with the Mohr circle is obtained, as observed in Figure 5-45 .

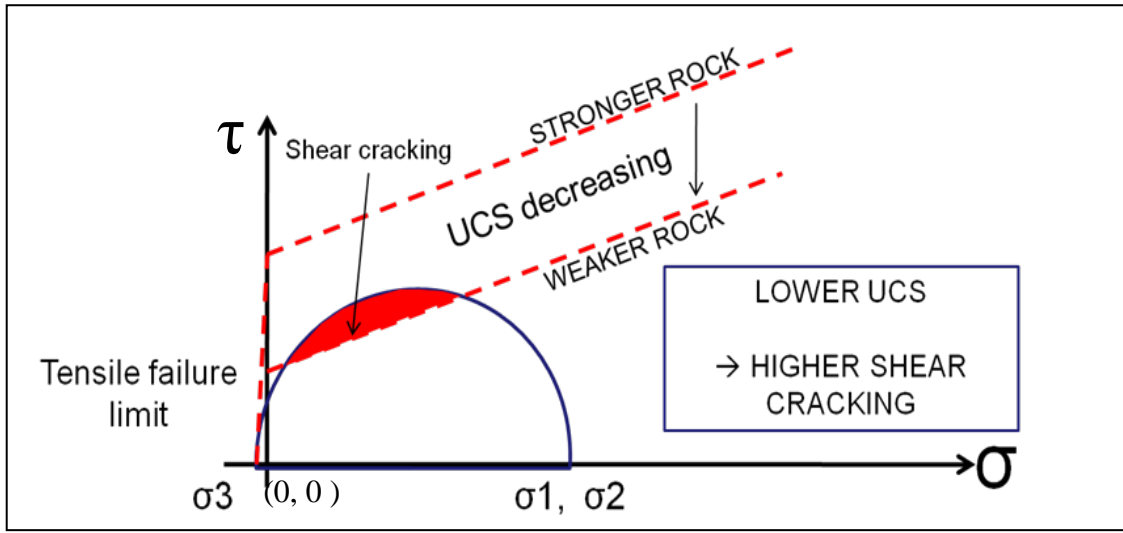


Figure 5-45 Mohr diagram representation of the effect of decreasing UCS on shear cracking

Increasing Young's modulus has a different effect on the diagram; in a rock mass, any displacement generates stress in the direction of the displacement in proportion to the magnitude of Young's modulus, but only a fraction of this value will be transmitted in the transversal direction. Thus, the difference between the maximum and minimum stresses increases as Young's modulus increase. In the Mohr diagram, this is reflected as a larger circle, which naturally exhibits a larger intersection area with the shear failure limit line, and enhanced shear cracking is expected (see Figure 5-46). The fraction of stress transmitted from the displacement direction towards the transversal direction is proportional to Poisson's ratio; thus, decreasing Poisson's ratio has a similar effect to increasing Young's modulus.

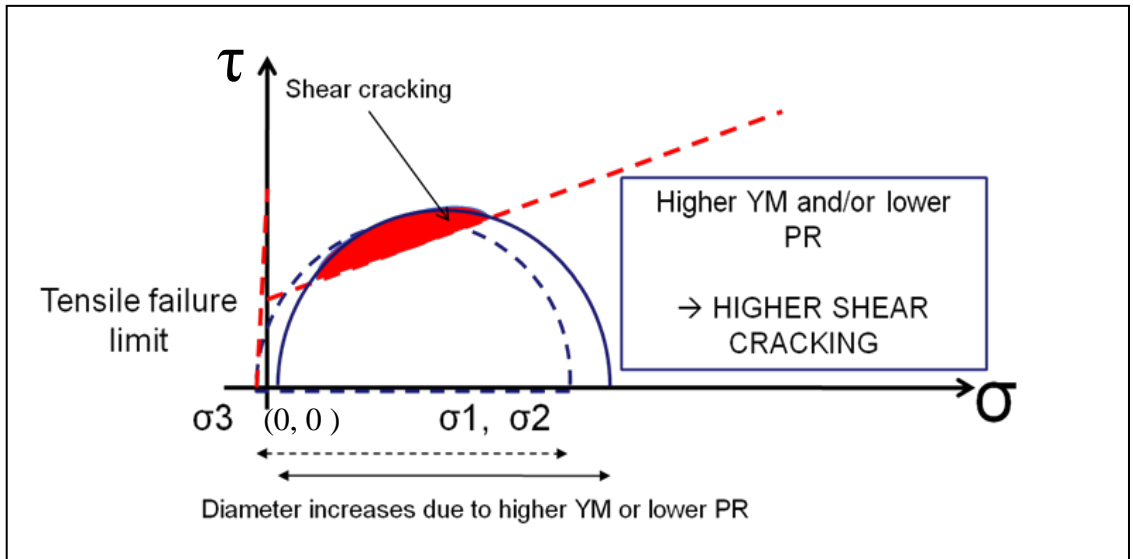


Figure 5-46 Mohr diagram representation of the effect of Young's modulus (YM) and Poisson's ratio (PR) on shear cracking

Naturally, stress differential increase associated to any reason (e.g. faulting, folding, etc.) will have the same representation in the Mohr diagram, i.e. the higher the difference between the minimum and maximum principal stresses, the larger the circle, and the higher the induction of shear cracking.

When the intermediate principal stress is different of the other two stresses, the area between the big and small circles represents the stresses exerted on any and all possible surface orientations at that particular location. Thus, as the intermediate stress approximates the maximum stress, most of the possible orientations get "pushed" toward the periphery of the circle, and close to the failure limit, increasing the chances for shear cracking (see).

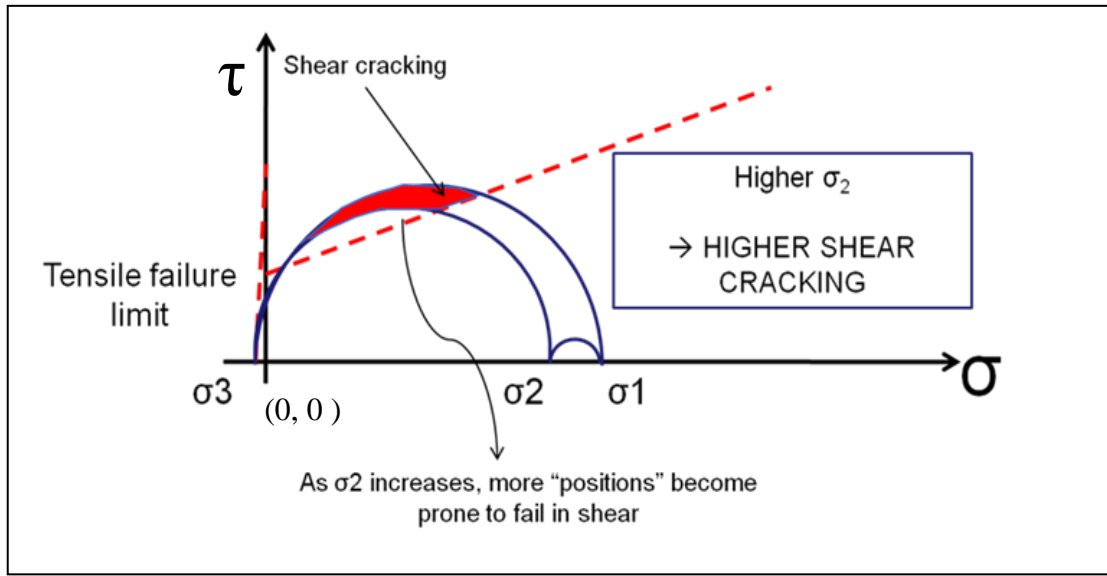


Figure 5-47 Mohr diagram representation of the effect of stress anisotropy on shear cracking

Therefore, the results obtained in the simulations fit the well-established macroscopic relations described by the Mohr diagram. Note, however, that the Mohr diagram analysis only confirms the possibility of shear cracking generation due to fluid injection, but does not describe in detail the evolution of the cracks after the onset of damage.

5.5 SOME PRACTICAL IMPLICATIONS

In view of these results, it can be said that there are many parameters that cause seemingly negligible mechanisms to become important during hydraulic fracturing.

The simulations with low UCS suggest a rapid degradation of the rock resistance to deformations ahead of the crack tip, even at high elastic modulus values. In other words, due to the constant breakage of the initial contact bonds, the rock seems weaker as the cracks form around the propagating fracture. Thus, a large increase in the amount of cracks is observed with increasing pressure, as UCS decreases. Low-clay siltstones,

sometimes classified erroneously as shales, are often characterized as high E and relatively low UCS. Thus, active increase in cracking away of the main hydraulic fracture is induced by the fluid being injected. Likewise, existing fractures with planes oriented favorably may become re-activated. An important implication of this chain of events is that micro-seismic monitoring may be reflecting re-activation of fractures, rather than pinpointing fracture propagation.

Even in high UCS formations, if an additional tensional-inducing mechanism is present, such as a sudden temperature change due to a cooled fluid in geothermal applications, it would be expected that tensional cracks could be formed in various directions, creating multiple branches.

As was expected, higher ductility specimens seem to exhibit important signs of stress and correspondingly crack concentration ahead of the fracture tip. The implications for hydraulic fracturing modeling is that conventional LEFM models would underpredict the required pressure, since the additional crack activity is not in direct communication with the main fracture. Rocks that fit this description are high-clay shales, and the implication is that fractures may be relatively shorter and wider, with respect to less ductile formations, if all other conditions are the same.

Stress heterogeneity, such as that associated to highly energetic depositional environments like turbidites, exhibit the highest level of crack induction activity away of the main fracture.

6 CONCLUSIONS AND RECOMMENDATIONS

The following conclusions can be drawn from this study:

1. The Discrete Element framework captures properly the macroscopic mechanisms described by well established analytical tools for failure onset during hydraulic fracturing; however, more robust fluid coupling algorithms are needed to model adequately fluid leak-off, and hence, generate realistic predictions.
2. These results suggest that the effective volume generated by hydraulic fracture in poorly consolidated rock is much less than in an equivalent strong rock, because shear cracking does not generate fracture width.
3. Likewise, the treating pressures are expected to be higher in poorly consolidated rock, because some part of the supplied energy is diverted by shear cracking.
4. An additional mechanism affecting pressure requirements is the stiffness degradation observed as the fracture propagates, and that causes the rock to become apparently less brittle.
5. The low strength of poorly consolidated formations is the main cause for this type of rocks to go partly into shear cracking mode during hydraulic fracturing.
6. Tensile cracking still appears to be the dominant cracking mode, but shearing represents a sizable fraction of the total number of cracks, with values reaching up to 30-35%.
7. High Young's modulus, low Poisson's ratio, and bi-axial loading (i.e. two principal stresses are equal in magnitude) enhance shear cracking modes during propagation of the hydraulic fracture, but in a lesser degree than low UCS values.

8. For rocks with low Young's modulus, high Poisson's ratio, or both, there is a compaction-like process before a significant number of shear cracks can be formed.
9. The characteristics of isolated groups of cracks ahead of the main group seem to correspond to the usual description of a Fracture Process Zone (FPZ). However, these groups were composed exclusively of tensional cracks. Thus, onset of the FPZ is characterized by generation of tensile microcracks, just like the failure shear plane in compressional testing is preceded by the formation of multiple tensile microcracks.
10. As compared to modeling of stronger rocks, the cracks and contact forces are more widely distributed in the fracturing of poorly consolidated formation. Thus, the expected induce fractures will tend to be shorter and wider.
11. Because one of the three boundaries was located at a greater distance from the injection point, its effect on the simulations could not be properly evaluated.
12. There is a high degree of uncertainty about the controls of the shape of the stress-strain curve, and the resulting strength parameters. The ductility runs are thus deemed inconclusive, because each stress-strain relation tested had uncertain consequences in the deformability and strength parameters.
13. Comprehensive characterization of shear failure must be integrated into conventional hydraulic fracture models in order to achieve more accurate predictions.
14. Because current rock mechanic testing does not include microproperties characterization, it is invaluable the integration with sedimentary information to

validate the specific set of microproperties selected for a given simulation.

The following recommendations are derived from the present study:

1. DEM has proven an invaluable tool to model the mechanisms of fracturing in poorly consolidated formations. The fluid/solid coupling described in this dissertation was sufficient to determine the fundamental mechanisms of fracture propagation, but in order to obtain realistic design values, it is recommended the continuation of research on a more flexible fluid scheme that can adapt to the structural changes brought about by the propagating fracture.
2. Additionally, a methodology to calibrate tensional strength of the ensemble must be developed, since the current workflow is calibrated for compressive strength only.
3. The results suggest that in order for continuum models to be adapted for poorly consolidated formations, they would need to include the effects of post-peak behavior, and incorporate the dependency of Young's modulus and Poisson's ratio to fracture propagation.
4. DEM can be used complementarily to validate any new continuum models, but also as a stand-alone alternative to conventional modeling methods.
5. The results obtained for the simulations with varying degree of strength heterogeneity throughout the sample inadvertently revealed that DEM may be used to analyze even more complex patterns of hydraulic fracture propagations, such as those in highly fractures reservoirs.

7 REFERENCES

- Abou-Sayed, A. (1978): "An Experimental Technique for Measuring the Fracture Toughness of Rock under Downhole Stress Conditions". VDI-Berichte, No.313, pp.819-824.
- Ashford, F.E.; Ghoniem, Y. (1987): "Preliminary Evaluations Applicable to Predicting the Probability of Occurrence for Compaction and Subsidence Resulting From Fluid withdrawal in Unconsolidated Shallow Sands". Proceedings AAPG: Exploration for Heavy Crude Oil and Natural Bitumen Research Conference, pp 607-613. Santa Maria, California (USA).
- Ayoub, J.A.; Kirksy, J.M. (1992); Malone, B.P.; Norman, W.D.: "Hydraulic Fracturing of Soft Formations in the Gulf Coast". SPE Formation Damage Control Symposium, February 26-27, 1992. Lafayette, Louisiana (USA).
- Boggs, S. (2006): Principles of sedimentology and stratigraphy. 4th ed. Upper Saddle River, N.J. Pearson Prentice Hall.
- Chudnovsky, A.; Fan, J.; Dudley, J.; Shlyapobersky, J.; and Schraufnagel, R. (1996): "A new hydraulic fracture tip mechanism in a statistically homogeneous medium". SPE Paper No. 36442 presented at the 71st Annual Technical Conference and Exhibition. Denver, Colorado (USA).
- Clifton, R. J. (1989): "Three-Dimensional Fracture Propagation Models". Chapter 5 in Recent Advances in Hydraulic Fracturing (Gidley et al., 1989), pp. 95-108.
- Colback, P.S.B., and Wiid, B.L., (1965): "The Influence of Moisture Content on the Compressive Strength of Rocks". Proceedings of the 3rd Canadian symposium on rock mechanics, pp. 65-83. Toronto (CANADA).
- Cundall, P., & Strack, O. (1979). A Discrete Numerical Model for Granular Assemblies. Geotechnique, 29 , pp. 47-65.
- Davies, J.P.; Davies, D.K. (1999): "Stress-Dependent Permeability: Characterization and Modeling". SPE Paper No. 56813 presented at the SPE Annual technical Conference and Exhibition, October 3-6, 1999. Houston, Texas (USA).
- Deere, D.U.; Miller, R.P. (1966): "Engineering Classification and Index Properties for Intact Rock". Tech. Report Air Force Weapons Lab., New Mexico, pp 65-116. [In Roegiers (2005a)].

Desroches, J.; Woods, T.E. (1998): "Stress Measurements for Sand Control". SPE Paper No. 47247 presented at the SPE/ISRM Rock Mechanics in Petroleum Engineering, 8-10 July, 1998. Trondheim, Norway.

Dudley, J.W., Myers, M.T., Shew, R.D., and Arasteh, M.M., (1998): "Measuring Compaction and Compressibilities in Unconsolidated Reservoir Materials by Time-Scaling Creep". SPE Reservoir Evaluation & Engineering, October, 1999, pp. 430- 437.

Dungdale, D. (1960): "Yielding of Steel Sheets Containing Slits". Journal of the Mechanics and Physics of Solids, v.8, pp. 100-104.

Fjær, E., (1999): "Static and Dynamic Moduli of Weak Sandstones", Rock Mechanics for Industry; Amadei, Kranz, Scott & Smeallie (eds.), proceedings of the 37th U.S. Rock Mechanics Symposium, Vail, Colorado, vol. 2, pp. 675-681.

Fjær, E.; Holt, R.E.; Horsrud, P.; Raaen, A.M. (1992): "Petroleum Related Rock Mechanics". Elsevier Science Publishers. Amsterdam, the Netherlands.

Franquet, J., and Economides, M.J., (1999): "Effect of Stress and Stress Path on Young's Modulus and Poisson Ratio of Unconsolidated Rocks: A New Idea for Hydraulic Fracturing", SPE paper No. 54012, presented at the 1999 SPE Latin American and Caribbean Petroleum Engineering Conference. Caracas, Venezuela.

Gidley, J.; Holditch, S.; Nierode, D.; Veatch, R. (1989): "Recent advances in hydraulic fracturing". SPE Monograph Volume Series. Richardson. Texas (USA).

Gil, I. PhD. Dissertation (2005): "Hydraulic Fracturing of Poorly Consolidated Formations: Considerations on Rock Properties and Failure Mechanisms". Un. Of Oklahoma, Norman, OK (USA).

Griffith, A. (1921): "The phenomenon of rupture and flow in solids". Phil. Trans. R. Soc. London, Series A, No. 221, pp. 163-198.

Griffith, A. (1924): "The theory of rupture". Proceedings of the 1st International Congress of Applied Mechanics, pp. 56-63.

Huang, A.B., Liao, J.J., Pan, Y.W., Cheng, M.H., Hsieh, S.Y., and Peng, J.K., (2000): "Characterization of Soft Rocks in Taiwan". Pacific Rocks 2000, Rock around the Rim; Girard, Liebman, Breeds & Doe (eds.), pp. 83-90. Seattle, WA (USA).

Hubber, M.K. & Willis, D.G. (1957): "Mechanics of Hydraulic Fracturing". Trans. AIME, 210, 153-163.

Hussain, M. A.; Pu, S. L.; Underwood, J. (1974): "Strain Energy Release Rate for a Crack under Combined Mode I and Mode II". Fracture Analysis, ASTM STP 560, pp. 2-28.

Ingraffea, A. R. (1981): "Mixed Model Fracture Initiation in Indiana Limestone and Westerly Granite". Proc. 22nd US Symposium on Rock Mechanics, pp. 186-191. Cambridge, MA. (USA).

Ingraffea, A. R. PhD Dissertation (1977): "Discrete Fracture Propagation in Rock: Laboratory Tests and Finite Element Analysis". Un. of Colorado. Denver, Colorado (USA).

Irwin, G. (1948): "Fracture Dynamics: Fracture of Metals". American Society of Metals, pp. 147-166.

Irwin, G. (1957): "Analysis of Stresses and Strains near the End of a Crack". Journal of Applied Mechanics, 24, pp. 361.

Itasca Consulting Group. (2005a): "Section 2: Fixed Coarse-Grid Fluid Scheme. In PFC3D MANUAL: Optional Features". Minneapolis, MN. (USA).

Itasca Consulting Group. (2005b): "Section 1: Introduction. In PFC3D MANUAL: User's Guide". Minneapolis, MN. (USA).

Itasca Consulting Group. (2005c): "Section 1: General Formulation. In PFC3D MANUAL: Theory and Background". Minneapolis, MN. (USA).

Itasca Consulting Group. (2005d): "Section 3: Augmented FishTank. In PFC3D MANUAL: Fish in PFC3D". Minneapolis, MN. (USA).

Kawaguchi, T., Tanata, T., & Tsuji, Y. (1992): "Numerical Simulation of Fluidized Bed Using the Discrete Element Method (the Case of Spouting Bed)". Japan Society of Mechanical Engineering (B), Vol. 58, No. 551, pp. 79-85.

Klosek, J. M. Sc. Thesis (1997): "The Integration of Fluid Dynamics with a Discrete Element Modelling System: Algorithms, Implementation, and Applications". Massachusetts Institute of Technology. Cambridge, MA (USA).

Labuz, J., Shah, S., and Dowding, C. (1983): "Post-Peak Tensile Load-Displacement Response and the Fracture Process Zone in Rock". Proceeding of the 24th US Symposium on Rock Mechanics, Mathewson, C., (Ed.), Texas, A & M University, pp. 421-428. College Station, TX (USA).

Larsen, I.; Fjær, E.; and Renlie, L. (2000): "Static and Dynamic Poisson's Ratio of Weak Sandstones". Pacific Rocks 2000, Rocks around the Rim; Girard, Liebman, Breeds & Doe (eds.), pp. 77-82. Seattle, WA (USA).

Marlowe, J. (1968): "Unconsolidated Marine Sediments in Baffin Bay". J. of Sedimentary Petrology, Vol. 38, No. 4, pp 1065-108.

Marsala, A.F.; Ragazzini, G.; Meazza, O.; Brignoli, M.; and Santarelli, F.J. (1994): "Basin scale rock mechanics; logs and core measurements", Eurock 94 (also in SPE paper 28034), SPE/ISRM Rock Mechanics in Petroleum Engineering Conference, pp. 105-112. Delft, the Netherlands.

Marzano, M.S. (1988): "Controls on Permeability for Unconsolidated Sands from Conventional Core Data Offshore Gulf of Mexico". Transactions Gulf Coast Association of Geological Societies, Vol. XXXVIII, pp. 113-120.

Morita, N., and Ross, C.K., (1993): "Core-Based Horizontal or Highly-Inclined Well Stability Analysis for Unconsolidated formations", SPE paper No. 26332, presented at the 68th Annual Technical Conference and Exhibition. Houston, TX (USA).

Nicholson, E.D., Goldsmith, G., and Cook, J.M., (1998): "Direct Observation and Modeling of Sand Production Processes in Weak Sandstone". SPE/ISRM paper No. 47328, presented at the SPE/ISRM Eurock 98, pp. 97-106. Trondheim, Norway.

Orowan, E. (1949): "Fracture and Strength of Solids". Rep. Prog. Phys, 12, p. 185.

Orowan, E. (1952): "Fundamentals of Brittle Behavior in Metals". W.M. Murray, Editor, Fatigue and Fracture of Metals, pp. 139-154. John Wiley, New York, NY(USA).

Ostermeier, R.M., (1995): "Stressed Oil Permeability of Deepwater Gulf of Mexico Turbidite Sands: Measurements and Theory". SPE paper No. 30606, presented at the 1995 SPE Annual Technical Conference and Exhibition. Dallas, TX (USA).

Ostermeier, R.M., Pelletier, J.H., Winker, C.D., and Nicholson, J.W. (2001): "Trends in Shallow Sediment Pore Pressure – Deepwater Gulf of Mexico". SPE/IADC paper No. 67772, presented at the SPE/IADC Drilling Conference. Amsterdam (The Netherlands).

Patanker, S. (1980): "Numerical Heat Transfer and Fluid Flow". Hemisphere Publishing.

Potyondy, D. O.; Cundall, P. A. (1996): "Modeling of Shock and Gas Driven Fractures Induced by a Blast Using Bonded Assemblies of Spherical Particles". Rock Fragmentation by Blasting (Proceedings 5th Int. Symp., Montreal, August 1996): 55-62, B . Mohanty (Ed.), Rotterdam. Balkema, 1996.

Potyondy, D.O; Cundall, P.A. (2004): "A Bonded-Particle Model for Rock". International Journal of Rock Mechanics and Mining Science, 41, pp. 1329-1364.

Ratigan, J.L. PhD. Dissertation (1981): "A Statistical Fracture Mechanics Approach to the Strength of Brittle Rock". Un. Of California. Berkely, CA (USA).

Richard, H. A. (1984): "Examination of Brittle Fracture Criteria for Overlapping Mode I and Mode II Loading applied to Cracks". Application of Fracture Mechanics to Material and Structures, G.C. Sih et al., (Eds.), Martinus Nijhoff Pub. The Hague (The Netherlands).

Roegiers, J-C. (2005a): "Introduction to Rock Mechanics Handouts". Unpublished Material, pp. 180-245. University of Oklahoma at Norman (USA).

Roegiers, J-C. (2005b): "Introduction to Rock Mechanics Handouts". Unpublished Material, pp. 40-50. University of Oklahoma at Norman (USA).

Rummel, F., and Winter, R. (1982): "Application of Laboratory Fracture Mechanics Data to Hydraulic Fracturing Field Tests". Proc. 1st Japan-USA Symp. on Fracture Mechanics Approach, Hydraulic Fracture and Geothermal Energy, pp. 495-501. Sendai, (Japan).

Schmidt, R. A. (1976): "Fracture Toughness Testing of Limestone". Expl. Mech., Vol. 16, pp. 161-167.

Schmidt, R.A. and Huddle, C.W. (1977): "Effect of Confining Pressure on Fracture Toughness of Indiana Limestone". International Journal of Rock Mechanics and Mining Science and Geomechanics Abstracts, v. 14, pp. 289-293.

Schmidt, R.A. (1980): "A Microcrack Model and its Significance to Hydraulic Fracturing and Fracture Toughness Testing". Proceedings of 21st US Symposium on Rock Mechanics, pp. 581-590. Rolla, MO (USA).

Shetty, D.K.; Rosenfield, A. R.; Duckworth, W.H. (1987): "Mixed-mode Fracture in Biaxial Stress State: Application of the Diametral-Compression (Brazilian disk) Test". J. Am. Ceram. Soc. Vol. 26, No. 6, pp. 825-840.

Slatt, R. (2006): "Stratigraphic reservoir characterization for petroleum geologists, geophysicists, and engineers. 1st ed". Amsterdam; Boston: Elsevier, 2006.

Succi, S (2001).: "The Lattice Boltzmann Equation for Fluid Dynamics and Beyond". Oxford University Press, NY (USA).

Sukop, M., Thorne Jr., D (2006): "Lattice Boltzmann Modeling: An Introduction for Geoscientists and Engineers". Springer-Verlag Berlin Heidelberg. Berlin, NY (USA).

Urbancic, T.I.; Maxwell, S.C. (2002): "Source Parameters of Hydraulic Fracture Induced Microseismicity". SPE paper No. 77439, presented at the SPE Annual Technical Conference and Exhibition, September 29 – October 2, 2002. San Antonio, TX (USA).

Valko, P., and Economides, M. (1997): "Hydraulic Fracture Mechanics". John Wiley and Sons, England.

Van den Hoek, P.J.; Kooijman, A.P.; de Bree, P.; Kenter, C.J.; Zheng, Z; Khodaverdian, M. (2000): "Horizontal Wellbore Stability and Sand Production in Weakly consolidated Sandstones". SPE Paper No. 65755. SPE Drilling and Completion, Vol. 15, No. 4, pp 274-283.

Wang, H.; Khrishnan, G.R.; Zaman, M.; and Roegiers, J.C., (1995): "Behavior of Natural and remolded Antler Sandstone: Sample Preparation and Grain Crushing Aspects". Proceedings of the 35th U.S. Rock Mechanics Symposium, pp. 127-133. Daemen & Schultz (eds.). Reno, NV (USA).

Weibull, G. W. (1981): "This Week's Citation Classic: Weibull, W. A Statistical Distribution Function of Wide Applicability". Citation Classic, No. 10, March 9, 1981.

Weibull, W. (1939): "A statistical theory of the strength of materials". Ingeniorsvetenskap Akademiens Handlingar, Nr. 151. [in Ratigan, 1981]

Weimer, P; Slatt, R.M. (2006): "Introduction to the petroleum geology of deepwater settings". AAPG Studies in Geology Series (CD book), 816p.

Whittaker, B., Singh, R., Sun, G. (1992): "Rock Fracture Mechanics: Principles, Design and Applications". Elsevier Science Publishers. Amsterdam, the Netherlands.

Wolf-Gladrow, D.(2000): "Lecture Notes in Mathematics: Lattice Gas Cellular Automata and Lattice Boltzmann Models; An Introduction". Springer-Verlag, Berlin Heidelberg, Berlin, NY (USA).

Wu, B. and Tan, C.P., (2000): "Relationship Between Thick-Walled Cylinder and Unconfined Compressive Strength for Application in Sand Prediction", Pacific Rocks 2000, Rock Around the Rim; Girard, Liebman, Breeds & Doe (eds.), pp. 287-294. Seattle, WA (USA).

Zoback, M. (2007): "Reservoir Geomechanics: Earth Stress and Rock Mechanics Applied to Exploration, Production and Wellbore Stability". Cambridge University Press. New

York, NY (USA).

APPENDIX A: ALTERNATIVE METHODS FOR FLUID FLOW COUPLING IN DISCRETE ELEMENT SPECIMENS

Fluid flow coupling by finite-difference (FD) discretization of the Navier-Stokes equations were discussed in Chapter 4. This section summarizes alternative methods that have been used to integrate fluid flow within porous media modeled by Discrete Elements (DEM).

Finite Element Method (FEM) – DEM coupling

This approach was implemented by Klosek (1997). For the fluid part, the author used FEM to solve the equation of continuity as applied to Darcy's law:

$$\mathbf{K}_x \frac{\partial^2 \Psi}{\partial x^2} + \mathbf{K}_y \frac{\partial^2 \Psi}{\partial y^2} = \mathbf{0} \quad (\text{A.1})$$

where \mathbf{K} is the permeability in the x- and y-directions, and Ψ is a potential function (a common potential is pressure difference) that constitutes the only degree of freedom (DOF) of the problem. The elements used were bi-linear triangular elements.

After all the steps involved in FEM, the resulting element matrices $\mathbf{A}^{(e)}$, are given by:

$$\mathbf{A}^{(e)} = \frac{K_x}{4A} \begin{bmatrix} b_i^2 & b_i b_j & b_i b_k \\ b_i b_j & b_j^2 & b_j b_k \\ b_i b_k & b_j b_k & b_k^2 \end{bmatrix} + \frac{K_y}{4A} \begin{bmatrix} c_i^2 & c_i c_j & c_i c_k \\ c_i c_j & c_j^2 & c_j c_k \\ c_i c_k & c_j c_k & c_k^2 \end{bmatrix} \quad (\text{A.2})$$

where A is area of the element, $[i,j,k]$ are the nodes of each triangle, and the coefficients b and c are given by:

$$b_i = Y_j - Y_k$$

$$b_j = Y_k - Y_i$$

$$b_k = Y_i - Y_j$$

$$c_i = X_k - X_j$$

$$c_j = X_i - X_k$$

$$c_k = X_j - X_i \quad \dots(A.3)$$

The system of equations to solve can be expressed as:

$$[A]\{\Phi\}=[q] \quad (A.4)$$

These equations are completely determined by the introduction of the boundary conditions of the problem. Since the unknown of the problem is the potential function Ψ , the solution reduces to:

$$\{\Phi\}=[A]^{-1}[q] \quad (A.5)$$

The above discussion is limited to steady flow. For transient state the governing equation is:

$$K_x \frac{\partial^2 \Psi}{\partial x^2} + K_y \frac{\partial^2 \Psi}{\partial y^2} = \rho c \frac{\partial \Psi}{\partial t} \quad (A.6)$$

where ρ is fluid density and c is a storativity coefficient. The derivative in time is approximated with a time marching scheme (e.g. central difference finite difference).

Coupling with DEM is carried via the permeability term, which is estimated from a Carman-Kozeny type correlation.

In summary the overall process of FEM-DEM integration is:

- Construction of the DEM specimen and application of initial boundary conditions to the ensemble.
- The FEM grid is superposed on the DEM assembly and meshed into triangular elements.
- From the particles' displacements, the porosity in each cell of the FEM grid is calculated, and the permeability is estimated and transmitted to the FEM procedure.
- FEM element matrices are calculated and the global matrices are assembled and solved. Updated values of pressure are then transmitted to the DEM particles.
- The values of pressure are converted into body forces that are applied to the particles, and the process starts again.

As compared with the finite-difference coupling used in the dissertation, this method can be applied to more arbitrary geometries, because each element formulation includes information about its dimensions, i.e. the solution matrix is first evaluated for each individual element, and a global matrix is assembled with the information of each element and its nodal neighbors.

For both numerical approaches (FD and FEM), the use of the constitutive laws (Darcy's,

Ergun's, etc.) for porous media precludes refining of the discretization grid to cells whose size is comparable to that of a few particles, because the definitions of porosity and permeability break down at such scale. Thus, by definition, the grids must be coarse. A direct consequence of this constrain is that discretization models can be applied only when no refining might be necessary, i.e., for small pressure or velocity variations across the domain. If coarse grids are applied to a domain across which the pressure differential is large, the truncation error shoots up to unacceptable values or stability problems might arise.

Pipe network approximation

Proposed by Potyondy and Cundall (1996), this methodology consists of detecting the interconnected gaps throughout the assembly, and approaching this system to a 'pipe network'. Then, fluid will be transferred from one void to the next via their interconnecting 'pipe'.

Notice that a single particle in DEM does not necessarily represent an individual grain, but can be thought of as a discretization of some solid section of the rock. Consequently, a void between particles represents an abstraction of some pore volume, and not necessarily an individual pore. Hence, the voids within the DEM sample are referred to as 'domains', and by definition corresponds to the volume enclosed within the tetrahedron formed by 4 neighboring particles that are in contact.

Flow through a pipe joining two domains 1 and 2, and positive flow from 2 to 1, is given by:

$$q = k a^3 \frac{(P_2 - P_1)}{L} \quad (\text{A.7})$$

where ‘a’ is a nominal aperture allowing the transfer of fluids from one domain to the next, k is a conductivity factor, P is pressure, and L is the distance between the centers of the domains.

When a compressive force acts on the particles that make up the pipe, in a direction normal to the plane tangential to both particles at the contact, a reduction in the aperture ‘a’ is expected, since the particles involved are pushed closer together. The heuristic expression correlating these parameters is:

$$a = \frac{a_0 F_0}{F + F_0} \quad (\text{A.8})$$

where F_0 represents the force F that would cause a reduction in the aperture ‘a’ to half its initial or residual size a_0 . The residual aperture is the nominal aperture when no load is being applied.

For tensile forces, the nominal aperture ‘a’ is thought to increase linearly with the separation between the particles in contact:

$$a = a_0 + m g \quad (\text{A.9})$$

where g is the separation of the particles from the initial position, and m is a calibration factor.

The bulk modulus of the fluid (K_f) is defined as the pressure necessary to compress the

fluid a fraction of its initial volume. The fluid volume fraction change is given by total volume increase divided by the initial domain volume (V_d); the total volume in the domain increases in one timestep (Δt) by the amount of fluid that enters the domain (Σq , contribution of all pipes connected to the domain), minus the volume change of the domain enclosing boundaries (the solid DEM part). Thus, the pressure change is given by:

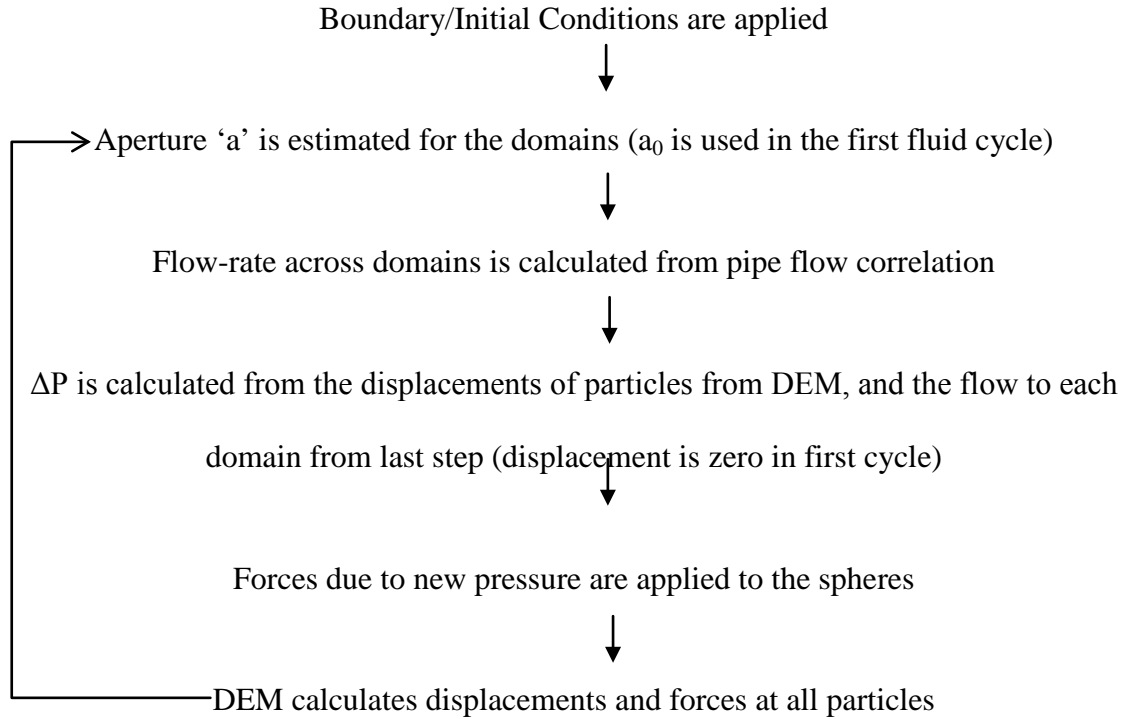
$$\Delta P = \frac{K_F}{V_d} (\Sigma q \Delta t - \Delta V) \quad (\text{A.10})$$

Finally, the pressure ‘P’ inside the domain, acts on the enclosing spheres by means of a traction force ‘ F_i ’ on a section S of the surface that is ‘exposed’ to the inner side of the domain , according to:

$$\mathbf{F}_i = P \mathbf{n}_i S \quad (\text{A.11})$$

where the sub-index ‘i’ represents the orientation of the force, which is parallel to the centers of the domain, and the sphere; n represents the unitary vector in ‘i’ direction.

Summarizing, coupling of the pipe network fluid flow approximation to the DEM calculations proceeds as follows:



Lattice-Boltzmann Models (LBM)

According to the kinetic theory of gases, the mechanics of a system of particles could be described by distribution functions of each particle; every distribution function is dependent on the interactions between all the particles contained within the domain of the problem (Wolf-Gladrow, 2000). Obviously, such a description would be extraordinarily complicated, since a single mole of a substance contains $\sim 10^{23}$ particles. Nevertheless, the main postulate in statistical mechanics affirms that any micro-system has exactly the same probability to represent the overall system (the macro system is assumed to be in equilibrium), i.e., a system can be thought of as a combination of many copies (Sukop, 2007). Hence, the distribution function of a single particle ($f^{(1)}$) suffices to represent the mechanical state of the entire system:

$$f^{(1)} = f^{(1)}(\vec{x}, \vec{p}, t) \quad (\text{A.12})$$

where \vec{x} refers to the position vector, \vec{p} is the momentum vector, and t is time.

Moreover, the probability that particle 1 is found at a particular position interval (dx), with a particular momentum variation (dp) at a specific time t , is given by $f^{(1)}(\vec{x}, \vec{p}, t) d\vec{x} d\vec{p}$. The latter expression might also be interpreted as the probable number of molecules enclosed within the interval $dx dp$, in (x,p) phase space. If flow advance is due only to an external force field on the system, the following relation is established:

$$f^{(1)}(\vec{x} + \Delta\vec{x}, \vec{p} + \Delta\vec{p}, t) d\vec{x} d\vec{p} = f^{(1)}(\vec{x}, \vec{p}, t) d\vec{x} d\vec{p} \quad (\text{A.13})$$

which indicates that the same number of particles are just moving from one point to the next along their flow path; this is called the streaming factor of the Boltzmann equation. However, collisions occur during the time dt , and some particles will be lost whereas other will end up in the new coordinates $\vec{x} + \Delta\vec{x}, \vec{p} + \Delta\vec{p}$:

$$\underbrace{f^{(1)}(\vec{x} + \Delta\vec{x}, \vec{p} + \Delta\vec{p}, t) d\vec{x} d\vec{p}}_{\text{Streaming Phase}} = \underbrace{f^{(1)}(\vec{x}, \vec{p}, t) d\vec{x} d\vec{p}}_{\text{Streaming Phase}} + \left. \frac{\partial f^{(1)}(\vec{x}, \vec{p}, t)}{\partial t} \right|_{\text{coll}} d\vec{x} d\vec{p} dt \quad \dots(\text{A.14})$$

Note: The complete Boltzmann equation is formally obtained by expanding the left hand side of the above equation into Taylor series, and grouping similar terms; however, the equation presented above is used in some approximate form to model fluid flow.

The last term of the equation represents the collision factor. This factor is a non-linear

differential integral term, and it results extremely difficult to find a closed form solution for it. Instead, it has been customary to divide the continuous medium into a discrete lattice, and apply a solution scheme that proceeds in two steps: the first step corresponds to the streaming part of the above equation, and the second one applies some type of collision logic to the system.

The discrete medium for the approximation of the Boltzmann equation is referred to as a 'lattice' and is made up of 'nodes', in which the particles reside in 'bins' called cells (see Figure A.1). During the streaming phase, the particles 'jump' from their initial cells in their specific nodes, to their neighboring ones. Then, rules are applied to the particles inside a node that end up moving towards each other (i.e. colliding particles), and their position is updated accordingly. The collision rules must conserve momentum; mass is usually conserved by assigning a single mass value to all particles.

This technique, in association with Cellular Automata (CA), has been applied successfully to the modeling of diluted gas flows, in a methodology that is commonly known as Lattice Gas Cellular Automata (LGCA). CA consists on an entity known as the automaton, which is composed of cells whose status is updated via a set of rules that depend on the current statuses of the cell being updated, as well as its neighbors'. In the case of LGCA the automaton corresponds to the nodes; the cells are those 'bins' around the node and their status might vary only between occupied or not occupied by a particle, as illustrated in Figure A.1; the set of updating rules corresponding to collision probabilities that conserve momentum.

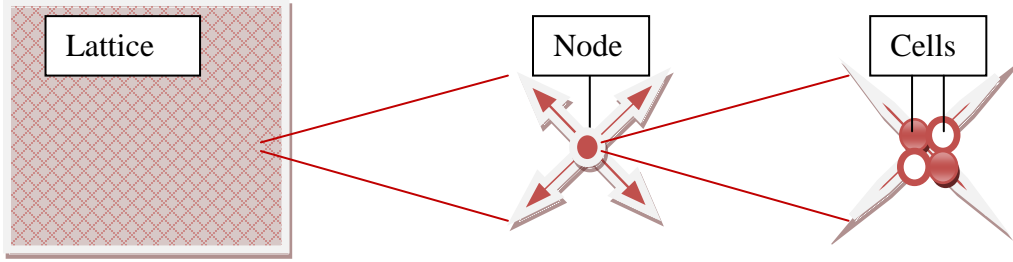


Figure A.1 Boltzmann Lattice Components. Solid red cells are occupied cells; white-filled cells are not occupied.

The above lattice is meant to be an illustrative example; many different configurations have been proposed, and they are selected according to the situation under study.

In order to model flows of fluids other than gas, the collision factor is replaced by a linearized version, known as BGK approximation (from their authors Bhatnagar-Gross-Krook). More models exist, but BGK is one of the most popular, due to its simplicity. Also, the boolean logic is replaced by a continuous distribution based to some extent on Maxwell's distribution; hence, the streaming and collision cannot be interpreted as caused by displacement of single particles, but as packet of particles.

The BGK approximation is given by:

$$\underbrace{\mathbf{f}_a(\vec{x} + \vec{e}_a \Delta t, \mathbf{t} + \Delta t)}_{\text{Streaming}} = \underbrace{\mathbf{f}_a(\vec{x}, \mathbf{t}) - \frac{[\mathbf{f}_a(\vec{x}, \mathbf{t}) - \mathbf{f}_a^{\text{eq}}(\vec{x}, \mathbf{t})]}{\tau}}_{\text{Collision}} \quad (\text{A.15})$$

where e is the velocity along each direction a , τ is a relaxation time, and the collision factor corresponds to a relaxation towards local equilibrium (hence, f_a^{eq}). Further insight into the BGK approximation and some more complex ones are discussed in Succi, 2001.

APPENDIX B: SETUP AND MONITORING ALGORITHMS

The files provided in this section correspond to scripts developed for this dissertation, using PFC3D[®] built-in programming language “Fish”. These supporting algorithms set-up, controlled, and monitored the evolution of the simulations discussed in the dissertation.

In the files provided, comments were added for clarity. Such comments are recognized because they are preceded by a semicolon which PFC3D identifies as a non-executable line. Also, executable commands were underlined.

Solid specimen definition: “AfcWithBL_Run#.DVR”

This algorithm was divided in 7 steps that group similar specimen definition parameters, plus a 0-step in which generic functions are loaded, as follows:

- Step 0: Generic functions are loaded, so that they can be invoked to create the specimens. The “HandleBdry.FIS” file, highlighted in red (see an example of AfcWithBL_Run1.DVR, below), provides the logic to create a boundary layer that “wraps” around the main specimen. Moving restrictions are specified on the spheres that compose this layer to provide sliding of the entire sample in the injection direction. A description of the routines within “HandleBdry.FIS” is presented in a later section.
- Step 1: The net lengths of the specimen are specified here. A boolean parameter to indicate if the boundary layer is necessary is entered, too. The specimens that undergo

mechanical testing do not need the boundary layer.

- Step 2: The size and distribution of spheres is entered in this step.
- Step 3: The extra-boundary layer routine is invoked. If the boolean variable was set to one in the first step, the extra-layer is created.
- Step 4: Since the logic in the boundary layer routines have their own unique naming convention, the variables with the specimen dimensions are re-named to the convention of the self-contained PFC3D Fishtank logic.
- Step 5: Miscellaneous parameters needed for the wall stiffness, locked-in stress, and floater elimination logic are entered here (see section 4.3).
- Step 6: Strength/deformation parameters for the particles and the contact bonds are supplied in this step.
- Step 7: The actual genesis procedure is called, saving of intermediate specimens is activated, and control is returned to the main routine, either a calling parent file, or the main program prompt.

The implementation of the above algorithm is illustrated by the example presented below, corresponding to the file “AfcWithBL_Run1.DVR”. Enough comments have been added to explain the different sections of this driver file.

```
; Filename: AfcWithBL_Run1.DVR
;
; Description:
; Creates either a regular solid ready for mechanical testing, or
; a new solid material that has approximate core dimensions,
; i.e. 10x10x10 cm, but adding the extra-layer as a boundary. The
; extra-layer is created if the internal scope variable HB_AddBnd
; is set to one.
;
;
new
SET random ; for reproducibility
```

```

;
;=====
; Step 0: Loading facilities to create stable specimens:
;   Facilities from Itasca's Fishtank:
;     call %itascaFishTank%\FishPfc\md\md.FIS
;     call %itascaFishTank%\FishPfc3\et3\et3.FIS
;     call %itascaFishTank%\FishPfc\md\flt.FIS
;
;   Extra-layer fish functions in file HandleBndary.FIS, created by DM:
;     call %itascaFishTank%\FishPFC3\et3\My_et3\HandleBndry.FIS ;(DM)
;
; End Step 0
;=====
; Setting Run Name:
;   SET md_run_name = 'Run1'
;=====
; SPECIMEN GENESIS PROCEDURES CONTINUE BELOW:
;=====
; Step 1. Set specimen dimensions: 0.1*0.1*0.1 (m3) for this case:
;   SET HB_NetXlen=1e-1 HB_NetYlen=1e-1 HB_NetZlen=1e-1 HB_AddBnd = 1;
;
; Variables in line above
;   HB_NET[x,y,z]len = Net lengths
;   HB_AddBnd = Boolean to indicate addition of bndries.
;
; End Step 1
;=====
; Step 2: Set min. sphere size and ratio of max. to min. radii of spheres
;   Because same size spheres are desired the ratio is 1 (et3_radius_ratio).
;   Spheres diameter required for this test: 0.5 cm (et3_rlo):
;   SET et3_radius_ratio=1.0 et3_rlo=0.25e-2
;
; This results in a 20x20x20 spheres assembly approx. (8k balls)
;
; End Step 2
;=====
; Step 3. Add the extra-boundary:
;   HB_AddBndDim
;
; The above function adds the boundary length to the net length
;
; End Step 3
;=====
; Step 4. Return to the original set of variables names in the Fishtank to
;   avoid problems with the rest of the algorithm:
;   SET et3_xlen= @HB_TotXlen et3_ylen = @HB_TotYlen et3_zlen = @HB_TotZlen
;
; Injection along y-axis.
; End Step 4
;=====
; Step 5. Set rest of parameters, as specified originally:
;   wEcfac is multiplying factor for wall elastic modulus
;   req_isostr is isotropic locked-in stress (about 1/10th of expected peak strength)
;   flt_def is number of contacts admissible to declare that ball a floater
;   flt_remain is max. number of floaters admissible
;   SET md_wEcfac=1.1

```

```

SET tm_req_isostr=-3.0e5 tm_req_isostr_tol=0.50
SET flt_def=3 flt_remain=0.0
;
; End Step 5
; =====
; Step 6. Specify parameters that define a contact-bonded material
; a. For the Spheres:
    SET md_add_cbonds=1
    SET md_dens=2630.0
    SET md_Ec=7e9 md_knoverks=1.0
    SET md_fric=0.50
; Note that stiffness is not explicitly defined, but is defined by a relation in terms of Ec and Ball radius
; as discussed in section 4.4

; b. For the contacts:
    SET cb_sn_mean=1.0e7 cb_sn_sdev=0 ;For elastic test change sn_mean to 1e20
    SET cb_ss_mean=2.0e7 cb_ss_sdev=0 ;For elastic test change ss_mean to 1e20

; End Step 5
; =====
; Step 7. Call to genesis procedures and return to main prompt:
; Initialize variable et3_prep_saveall to save partial specimens during genesis :
    SET et3_prep_saveall=1

;Invoke specimen-genesis routines:
    et3_prep ; invoke the specimen-genesis procedures

; Give control back to the program, or calling file, after all processes have finished
    Return

; END OF FILE
; =====

```

Fluid definition: “Fl Inject Run#.DVR”

This algorithm was divided in 9 steps that group similar fluid definition parameters, plus a 0-step in which generic functions are loaded, as follows:

- Step 0: The solid specimen is reloaded. The grid fluid is to be defined on this solid assembly. The “InjThruPerf.FIS” file, highlighted in red (see an example of Fl_Inject_Run1.DVR, below), provides the logic to set up the fluid flow grid. A description of the routines within “InjThruPerf.FIS” is presented in a later section.

- Step 1: The confining stresses are defined, and the confining driver (“_Confine.DVR”; see description in a later section) is called to execute the routines that install the prescribed stresses.
- Step 2: The boundary condition of constant stress is defined.
- Step 3: Fluid parameters (density and viscosity), fluid/solid interaction parameters (poro/perm), grid specs (No. of cells in each direction), and injection position (i, j, k) are defined in this step
- Step 4: The extra-layer of spheres is restricted from sliding in the injection direction.
- Step 5: The fluid grid is created, and time counting is reset
- Step 6: Rate, time and pressure histories are created
- Step 7: Injection rate and ramp are entered; the boundary conditions for flow through a single point is invoked here.
- Step 8: Execution is started, and a routine to save intermediate files is activated.
- Step 9: The final specimen is saved and control is returned to the program or parent script.

The implementation of the above algorithm is illustrated by the example presented below, corresponding to the file “Fl_Inject_Run1.DVR”. Enough comments have been added to explain the different sections of this driver file.

```

; fname: Fl_Inject_Run1.DVR
;
; Description:
; Perform fluid injection upon a sample at constant confining stress
; =====
new
set random ; for reproducibility
; =====

```

```

; Step 0: Restore specimen and call fluid definition FISH functions
; Restore specimen
  Res C:\Afc-spc.sav
  call %itascaFishTank%\FishPFC3\MyDrvrs \InjThruPerf.FIS
;
; End step 0
; =====
; Step 1: Specify in situ stress parameters and set confining stress using the
;   _Confine.DRV driver file
  SET md_run_name='ID_1A'; Name, to differentiate between runs
  SET et3_knxfac=0.1 et3_knzfac=0.1 et3_knyfac=0.1
  SET et3_wsxx_req=-3.45e6 et3_wszz_req=-6.90e6
  SET et3_wsyy_req=-6.90e6 et3_ws_tol=0.01
  SET p_vel=2.0e-1
  SET pk_ci_fac=0.02 et3_servo_1=1
  call %itascaFishTank%\FishPfc3\et3\My_et3\_Confine.DVR

; Variables glossary:
;   For the Confinement routine (confine.DVR):
;
;   et3_kn[x,y,z]fac: fraction of average normal particle stiffness
;                   applied to the walls (wall stiffness = AvgKnParticles*fraction)
;   wsxx/yy/zz: Confining pressure
;   p_vel: platens velocity. For this case it is used only when the wall are not
;         'seated' on the sample, and provide a maximum velocity for them until
;         seating is achieved.
;   pk_ci_fac: fraction of the total number of cracks existing at peak load.
;             Arbitrary value that corresponds to crack-initiation stress.
;             i.e. it permits calculation of the crack initiation stress, after the triaxial
;             has been conducted, by calculating the stress at which this many cracks
;             existed.
;   et3_servo_1: indicates to move only one 'y' wall for servocontrol in y-direction

; End step 1
; =====
; Step 2: Set boundary stress conditions
  SET et3_servo_xon=1 et3_servo_yon=1 et3_servo_zon=1
  cyc 3000 ; cycles to 'initialize' the servocontrol B.C.
  HB SetBndry; Marks extra-boundary layer for visualization

; Variables et3_servo[x, y, z]on = 0 fixes wall. This is used to switch off the servocontrol along a
; specific direction, so that mixed B.C. can be specified, e.g. one direction with constant
; stress and two with fixed walls.

; End step 2
; =====
; Step 3: Specify fluid grid, properties, poro/perm, and injection position
  Config fluid; enables fluid flow module

;====FLUID FLOW (AND PORO/PERM) INPUT====
;-Fluid properties (density, viscosity)
  set et3_fl_dens = 1000 ; kg/m3
  set et3_fl_visc = 1 ; cp
  set et3_RPoro = 0.25 ; RPoro is rock's real porosity
  set et3_RPerm = 100 ; mD is Rock's real perm

```

```

;-Flow grid (cells along transversal hor. x, direction of flow y, transversal vert. z)
  set et3_fl_grx = 11
  set et3_fl_gry = 11
  set et3_fl_grz = 11

;===INJECTION POSITION===
;-Coordinates i, k; Note that j =0 because injection is on one end of the grid
  set et3_fl_InjCell_i = 6
  set et3_fl_InjCell_k = 6
;
; End step 3
;=====
; Step 4: Limit displacement of boundaries to keep entire sample from sliding
  group HB_FrYBndGr range FrYBnd
  ini yvel = 0 range group HB_BndGr
  fix y range group HB_BndGr

; End step 4
;=====
; Step 5. Call routines to create grid, initialize time counter and monitoring histories
  set_fluid
  set_ftime; initializes time count since injection starts

; End step 5
;=====
; Step 6. Set monitoring histories for fluid parameters
  history id 2001 frate
  history id 2002 ftime
  history id 2003 et3_fl_InjRate
  history id 2004 et3_fl_InjPress

; End step 6
;=====
; Step 7. Set injection parameters
  set et3_fl_InjRateInit = 7.5e-6 R_inc = 1e-6 ; initial rate and rate increment
  set_fvel; Starts flow through a single cell, i.e. fluid injection
; NOTE: R_inc= 0 indicates no rate increments during simulation

; End step 7
;=====
; Step 8. Set intermediate saves and start execution
  set_fishcall #FC BOND DEL SavePostCrack ; activate post-cracking saving routine
  run_time

; End step 8
;=====
; Step 9. Save final specimen at end of simulation, return control
  save_md_run_name; Changed the name to this one, which is more appropriate (011611)
  return
; EOF

```

Confining stress installation: “ Confine.DVR”

This algorithm is a modification of the triaxial testing script that is included with the

installation of PFC3D. It installs a servo-control mechanism on the specimen boundaries to maintain a constant stress, but first it uses the same servo-control to reach a prescribed confining stress condition. Only 3 steps that group similar stress confining parameters, plus a 0-step in which generic functions are loaded, were necessary in this driver, as follows:

- Step 0: Generic fish-files are loaded.
- Step 1: The initial stresses are set by invoking the “seattriax” routine; initial dimensions of the sample are recorded for subsequent strain calculations.
- Step 2: Monitoring variables for the solid are declared. The variables include stresses, strains, energies, and crack types and amount.
- Step 3: The displacements are reset, and the final specimen is saved. Control is returned to the program or parent script.

The implementation of the above algorithm is illustrated by the example presented below, corresponding to the file “_Confine.DVR”. Enough comments have been added to explain the different sections of this driver file.

```

; Filename: _Confine.DVR
; Description:
; This file brings a specimen to a prescribed confining stress.
;
; =====
; Step 0: Loading fishcall and crack monitoring functions:
      call %itascaFishTank%\FishPfc\md\fishcall.FIS
      call %itascaFishTank%\FishPfc\md\crk.FIS

; End step 0
; =====
; Step 1: Apply initial stresses:
      et3 wallstiff ; Wall stiffnesses are set, variables used are kn[x,y,z]fac
      et3 seattriax; Apply initial stresses.
      et3 sample_dimensions ;Calculates initial dimensions of sample

```

```

; End step 1
; =====
; Step 2: Simulation solid variables monitoring:
  crk_init ;crack tracking package
  history reset
  history nstep=20
  history id=1 crk_num ; microcracking
  history id=2 crk_num_cnf
  history id=3 crk_num_csf
  history id=4 crk_num_pnf
  history id=5 crk_num_psf
; wall-derived stresses & strains
  history id=10 et3_wexx ; wall-derived strains
  history id=11 et3_weyy
  history id=12 et3_wezz
  history id=16 et3_wevol
  history id=210 et3_sexx ; specimen-derived strains
  history id=211 et3_seyy
  history id=212 et3_sezz
  history id=216 et3_sevol
  history id=13 et3_wsxx ; wall-derived stresses
  history id=14 et3_wsyy
  history id=15 et3_wszz
  history id=17 et3_wsm
  history id=18 et3_wsd
  history id=110 et3_mexx ; averaged stresses & strains
  history id=111 et3_meyy ; from 3 measurement circles
  history id=112 et3_mezz
  history id=116 et3_mevol
  history id=113 et3_msxx
  history id=114 et3_msyy
  history id=115 et3_mszz
  history id=117 et3_msm
  history id=118 et3_msd
  trace energy on ; energy quantities
  history id=30 ; energy boundary
  history id=31 ; energy bond
  history id=32; energy frictional
  history id=33; energy kinetic
  history id=34; energy strain
  history id=35 et3_e_delstrain ; increment of strain energy

; End step 2
; =====
; Step 3: Finalization statements:
  prop xdisp=0.0 ydisp=0.0 zdisp=0.0 ; Reset displacements
  SET md_tag_name = '-cnf' ; Assign name to the confined specimen
  md_save_state; Saves confined specimen
  return; Returns control
; EOF

```

Extra-layer functions: "HandleBndry.FIS"

Two short functions take care of creating an extra-layer of spheres around the main specimen dimensions, and grouping them as an entity on which special boundary conditions may be specified. In the cases of this study, the spheres on the boundary layer were kept from displacing in the fluid injection direction, to prevent sliding of the entire sample.

The first function, “HB_AddBndDim”, calculates an extra-length to be applied in all directions. The extra-length is calculated as 1.5 times the diameter of the biggest sphere in the sample.

The second function, “HB_SetBndry”, compares the prescribed length of the specimen in each direction, with the current lengths. All the spheres beyond the prescribed length are marked and grouped as boundary layers, distinct of the spheres in the main body of the sample.

The implementation of these functions is presented below.

```

; Filename: HandleBndry.FIS
; PURPOSE: Functions to manage addition of ball boundaries to the sample.
;
; BY: David Martinez
; Date : Wed. Oct 10/07
; =====
;
;====FUNCTION 1: HB_SetBndry====
def HB_SetBndry

; ----Selects the range of balls beyond the 'net' dimension and groups them together.
;
; INPUT: HB_Net[X,Y,Z]len = Net lengths in x,y,z
; et3_rlo and et3_radius_ratio = min radius and ratio max/min radius, used
; to calculate the plane beyond which balls should be considered as part
; of the boundary
;
;

```

```

; OUTPUT: HB_BndGr = Group gathering all the boundary balls around the perimeter

; Calculate radius of largest balls
_MaxRad = et3_rlo * et3_radius_ratio

; if only the net length is taken as the limit, it would mark balls whose centroid
; is just beyond that line, as part of the boundary. Hence, the max radius was added
; to be sure that it marks as the boundary those balls that are completely
; beyond the net dimensions

_xlimUp = (HB_NetXlen/2) + _MaxRad ;/2 is necessary because the coordinate system
; is in the center of the parallelepiped. Fr = Front Bk = Back
_xlimLow = -_xlimUp
_ylimUp = (HB_NetYlen/2) + _MaxRad
_ylimLow = -_ylimUp
_zlimUp = (HB_NetZlen/2) + _MaxRad
_zlimLow = -_zlimUp
command
  range name FrXBnd plane dip 90 dd 90 ori @_xlimUp 0 0 above ;Fr/Bc = Front/Back
  range name BkXBnd plane dip 90 dd 90 ori @_xlimLow 0 0 below
  range name FrYBnd plane dip 90 dd 0 ori 0 @_ylimUp 0 above
  range name BkYBnd plane dip 90 dd 0 ori 0 @_ylimLow 0 below
  range name FrZBnd plane dip 0 dd 0 ori 0 0 @_zlimUp above
  range name BkZBnd plane dip 0 dd 0 ori 0 0 @_zlimLow below

  group HB_BndGr range FrXBnd any BkXBnd any FrYBnd any BkYBnd any FrZBnd any BkZBnd
any
end_command

end

;=====FUNCTION 2: HB_AddBndDim=====

def HB_AddBndDim
;
;
; -----Adds an extra 'layer' of balls to be used as the specimen boundary
;
; INPUT: HB_Net[X,Y,Z]len = Net lengths in x,y,z
;   HB_AddBnd = Boolean indicating to add a ball bndry when = 1
;   et3_rlo and et3_radius_ratio = min radius and ratio max/min radius, used
;   to calculate the extra layer length
;
; OUTPUT: HB_Tot[x,y,z]len = Total length after addition of extra layer

  if HB_AddBnd = 0 then ;no add bnd requested
    _Xtralen = 0
  else ; extra length is the diameter (radius*2) of the largest sphere * 2 (one at the top, one at the
bottom)

    _Xtralen = et3_rlo * et3_radius_ratio * 2 * 2
  ; The extra-length is increased by 50% to make sure the bdry. layer is well populated, with no holes.
    _Xtralen = _Xtralen*1.5
  end_if

```

```
HB_TotXlen = HB_NetXlen + _Xtralen
HB_TotYlen = HB_NetYlen + _Xtralen
HB_TotZlen = HB_NetZlen + _Xtralen
end

return

;END OF FILENAME: HandleBndry.FIS
```

Fluid injection control functions: “InjThruPerf.FIS”

Seven functions were created inside InjThruPerf.FIS. They are used to collect all the parameters that define the flow grid geometry and fluid parameters, launch and control the hydraulic injection simulation. Description of each function follows:

- Function “run_time”: An inside loop runs 3000 simulation timesteps at every iteration. Within a single iteration, a function to increase the rate is called, the 3000 timesteps are executed at that rate, and the resulting specimen status is saved if more than an incremental number of cracks are created during those timesteps. The crack increment used was 100 cracks. The loop ends when at least 1500 cracks have been created.
- Function “ramp_Rate”: The rate is increased within this function. It is called at the beginning of each iteration of the simulation loop discussed above.
- Function “set_fluid”: The fluid grid is generated, according to the parameters entered in the “Fl_Inject_Run#” driver. The viscosity and density are scaled within this function, according to the rules discussed in section 4.6.
- Function “set_fvel”: The injection point is defined inside this function.
- Function “set_ftime”: The current time is taken as the initial time of the simulation.
- Function “ftime”: Elapsed time, and history rate and pressure are recorded by this

function.

- Function “SavePostCrack”: It defines fixed number of cracks after which the specimen should be saved for posterior analysis.

The InjThruPerf.FIS file is presented below.

```
; fname: InjThruPerf.FIS

;=====FUNCTION 1: run_time → Launches and controls simulation=====

def run_time
loop while 1#0
ramp_Rate

command
cyc 3000
end_command

;-----Save specimen @ every new 100 cracks
if crk_num > (CrkCount100 + 100)
RT_SaveName = md_run_name + 'Cr' + string (crk_num) + '.sav'
command
save RT_SaveName
end_command
CrkCount100 = crk_num
end_if
;-----End of Save

;-----Termination criteria (1500 cracks have been reached)
if crk_num > 1500 ; et3_fl_InjRate >4.5e-5 this criterion was used to get a critically
; pressurized specimen, because I was getting cracks right
; after 4.5e-5 flowrate
exit
end_if

end_loop

;=====FUNCTION 2: ramp_Rate → Controls rate increase=====
def ramp_Rate
TotR_inc = TotR_inc+R_inc
et3_fl_InjRate = et3_fl_InjRateInit+TotR_inc-R_inc ;v_zero*(1+TotR_inc-R_inc)
set_fvel
end

;=====FUNCTION 3: set_fluid → Sets up flow grid and fluid properties =====
def set_fluid
;
;
; By: David Martinez
```

```

; Date: 082410
;
; Description: 'set_fluid' sets a flow grid on top of a DEM specimen, according to the
; number of cells prescribed by the user. The dimensions are set from the parame
; ters specified in the Fishtank genesis procedures (in this case, the modified
; HB_Net variables). In addition, all fluid properties are collected here, from user
; input ( i.e. density and viscosity)
;
; Input:      The outside input variables are passed to internal variables, which are prefixed
; by sf_ (for set_flow, the name of this function). This is done to limit the scope of
; the operations to that variable, from inside the function itself (i.e. the variables
; are declared local to the function). The name of the internal variable is enclosed
; in brackets ( ) in the following sections.
;
; **FLUID PROPERTIES
; et3_fl_dens --> fluid's density (sf_fl_dens)
; et3_fl_visc  --> fluid's viscosity (sf_fl_visc)
; et3_RPorosity --> Real rock's porosity (sf_RPorosity)
; et3_RPerm    --> Real rock's perm (sf_RPerm)
; _et3_porosity --> Specimen's porosity (sf_SPorosity) (calculated in file et3.fis)
;
; **FLOW GRID
; et3_fl_gr[x,y,z] --> number of cells along [x, y, z] directions (sf_fl_gr[x,y,z])
; HB_Net[X,Y,Z]len --> length along [x, y, z] directions (sf_fl_s[x,y,z])
;
; **SCALING VARIABLES
; These variables are calculated internally. They are used to scale the flow proper
; ties of the specimen, to that of the real rock, as described in the document
; "ScaleRules.docx".
; sf_Fk = Scaling factor for Carman-Kozeny term (i.e. Darcy's flow)
; sf_Ft = Scaling factor for turbulent term
; sf_AvgDiam = Particle average diameter, needed for scaling calculations
;
; The first term is introduced by multiplying it by viscosity prior to entering it into
; the grid generation scheme. The second term by multiplying it by density.
;
; sf_ScVisc = Viscosity multiplied by Fk
; sf_ScDens = Density multiplied by Ft
;
; Output:  Creation of the flow grid. Global variables related to dimensions are created, as
; follows.
;
; et3_fl_[height, depth, width] = Grid dimensions
;
; Comments: density and viscosity are scaled, according to Ergun's correlation. This scaling
; were implemented herein, so that the user enters the normal property values
;
; *****Collecting variables locally*****
;---Fluid Properties
sf_fl_dens = et3_fl_dens
sf_fl_visc = et3_fl_visc * 1e-3 ; 1 cp = 1e-3 Pa.S
sf_RPorosity = et3_RPorosity
sf_RPerm = et3_RPerm * 9.87e-16 ; (1 mD = 9.87e-16 m2 or 1D = 9.87e-13m2)
sf_SPorosity = _et3_porosity

```

```

;---Grid Cells
sf_fl_grx = et3_fl_grx
sf_fl_gry = et3_fl_gry
sf_fl_grz = et3_fl_grz
;---Grid dimensions
sf_fl_sx = HB_NetXlen
sf_fl_sy = HB_NetYlen
sf_fl_sz = HB_NetZlen

;*****Acquiring grid dimensions from ball boundary system (DM, Oct 10/07)*****
ylo = -1*sf_fl_sy/2
yhig = -1*ylo
xlo = -1*sf_fl_sx/2
xhig = -1*xlo
zlo = -1*sf_fl_sz/2
zhig = -1*zlo

et3_fl_width = yhig-ylo
et3_fl_depth = xhig-xlo
et3_fl_height = zhig-zlo

;*****Calculating scaling parameters*****
sf_AvgDiam = (et3_rlo + et3_rlo*et3_radius_ratio)/2 to calc avg ;*2 to convert to Diam
sf_Fk = (sf_SPoros^3*sf_AvgDiam^2)/(150*(1-sf_SPoros)^2*sf_RPerm)
sf_Ft = (sf_SPoros^3*sf_AvgDiam)/(sf_RPoro^(1.5)*(150*sf_RPerm)^(0.5))
sf_ScVisc = sf_Fk*sf_fl_visc
sf_ScDens = sf_Ft*sf_fl_dens

;*****Invoking grid genesis commands in PFC*****
command
fluid model xlo xhig ylo yhig zlo zhig size sf_fl_grx sf_fl_gry sf_fl_grz
fluid prop dens sf_ScDens visc sf_ScVisc
;fluid set tdel 5e-7 ;changed from 5e-4 by Yoshi's suggestion
fluid set tdel 1e-10 ; (DM090410): Flow DT is calculated automatically
fluid set por_re 0.0 ; (DM090410): Por. does not change in NS during flow calculation
fluid set buoy off
fluid set visterm on ; (DM090410): this activates viscosity term calculations
; ---Fix all velocity flow B.C. to be zero (except where point injection is to be installed)
fluid boundary vel 0 0 0 xl
fluid boundary vel 0 0 0 xu
;fluid boundary vel 0 0 0 yl
fluid boundary vel 0 0 0 yu ; yl not included because point inj. is set, via "set_fvel"
fluid boundary vel 0 0 0 zl
fluid boundary vel 0 0 0 zu
; ---Prescribe all flow Bdries to be non-symmetrical (except where point injection is to be
; installed)---
fluid boundary nonslip xl
fluid boundary nonslip xu
fluid boundary nonslip yu ;(DM090410): yl is not set 'cause vel. is to be prescribed in the
; routine "set_fvel", in order to create point injection.
fluid boundary nonslip zl
fluid boundary nonslip zu
end_command

end

```

```

;=====FUNCTION 4: set_fvel → Marks point injection through the desired location in the fluid
grid=====
def set_fvel
;
; By: David Martinez
; Date: 082810
;
; Description: 'set_fvel' sets fluid injection across one cell at the boundary of the flow grid.
; It sets a user-prescribed velocity in a user-selected cell, and sets zero velocity to
; the remaining cells on that grid's end. the local cell counters are numbered i, j, k,
; according to directions x, y, z, respectively. Because flow is assumed in Y-dir, the
; injection boundary end corresponds to coordinates i, 0, k. Thus, only the number
; of cells that are transversal to flow are required.
;
; Input: The outside input variables are passed to internal variables, which are prefixed
; by sfv_ (for set_fvel, the name of this function). This is done to limit the scope of
; the operations to that variable, from inside the function itself (i.e. the variables
; are declared local to the function). The name of the internal variable is enclosed
; in brackets ( ) in the following sections.
;
; et3_fl_gr[x,z] --> Number of cells along [x,z] directions (sfv_TrCells_[x,z])
; et3_fl_InjCell_[i,k] --> Injection cell position (sfv_Inj_[i,k])
; et3_fl_InjRate --> Injection rate, as ramped up from initial rate by function
; "ramp_Rate (sfv_InjRate)
; i, k --> Counters along x,z directions, respectively (Internal)
; sfv_InjVel --> Result of the calculation of velocity from flrate (Internal)
; sfv_InjZ, sfv_InjX, sfv_InjArea --> Injection height, depth and area (Internal)
; sfv_i_k_Vel --> loop variable that contains velocity for cell that got focus in that
; moment (Internal)
;
;
;*****Collecting variables locally*****
sfv_TrCells_x = et3_fl_grx
sfv_TrCells_z = et3_fl_grz
sfv_Inj_i = et3_fl_InjCell_i
sfv_Inj_k = et3_fl_InjCell_k
sfv_InjRate = et3_fl_InjRate

;*****Calculating injection velocity from flowrate*****
sfv_InjZ = et3_fl_height/sfv_TrCells_z
sfv_InjX = et3_fl_depth/sfv_TrCells_x
sfv_InjArea = sfv_InjZ * sfv_InjX
sfv_InjVel = sfv_InjRate/sfv_InjArea

;*****added by DM (Feb. 07)
;Updated for single cell injection (Apr. 10/07)
loop i(1,sfv_TrCells_x)
loop k(1,sfv_TrCells_z)
if k=sfv_Inj_k
if i=sfv_Inj_i
sfv_i_k_Vel=sfv_InjVel
end_if
else
sfv_i_k_Vel = 0
end_if

```

```

        command
        fluid boundary vel 0 sfv_i_k_Vel 0 at i 0 k
        end_command
    end_loop
end_loop

end

;=====FUNCTION 5: set_ftime → Logs current time as zero time=====
def set_ftime
    ftime0 = time
end

;=====FUNCTION 6: ftime → calculates current time, rate and injection pressure=====
def ftime

;*****Collecting variables locally*****
ft_TrCells_x = et3_fl_grx
ft_TrCells_z = et3_fl_grz

;*****Actual Process*****
ftime = time - ftime0
frate = 0.0
area = et3_fl_depth/float(ft_TrCells_x)*et3_fl_height/float(ft_TrCells_z)
loop i(1,ft_TrCells_x)
    loop k(1,ft_TrCells_z)
        frate = frate + fc_yvel(i,ny,k)*fc_por(i,ny,k)*area
    end_loop
end_loop

;History of pressure injection in the injection cell
et3_fl_InjPress = fc_pre(sfv_Inj_i, 1, sfv_Inj_k)

end

;=====FUNCTION 7: SavePostCrack → Saves the run after the creation of a fixed number of
cracks=====
def SavePostCrack
; Function to save after creation of a crack; saves occur not at every creation of a new crack,
; but at some specific ones
if crk_num > 0
if crk_num < 6
    SPC_SaveName = 'Post_' + md_run_name + '_Cr_' + string (crk_num) + '.sav'
    command
        save SPC_SaveName
    end_command
    exit
end_if
end_if

if crk_num > 30
if crk_num < 36
    SPC_SaveName = 'Post_' + md_run_name + '_Cr_' + string (crk_num) + '.sav'
    command
        save SPC_SaveName
    end_command

```

```
exit
end_if
end_if

if crk_num > 500
if crk_num < 506
  SPC_SaveName = 'Post_' + md_run_name + '_Cr_' + string (crk_num) + '.sav'
  command
    save SPC_SaveName
  end_command
  exit
end_if
end_if

if crk_num > 1200
if crk_num < 1206
  SPC_SaveName = 'Post_' + md_run_name + '_Cr_' + string (crk_num) + '.sav'
  command
    save SPC_SaveName
  end_command
  exit
end_if
end_if

end

;EOF
```